Modelling the Optical Properties of Semiconducting Nanostructures

Alexander Buccheri

Mansfield College, University of Oxford

A thesis submitted for the Degree of

Doctor of Philosophy in Materials

Trinity Term 2016

Contents

Abstract

Modelling the Optical Properties of Semiconducting Nanostructures

Alexander Buccheri, Mansfield College

A thesis submitted for the Degree of

Doctor of Philosophy in Materials Science, Trinity Term 2016

In this thesis we describe the development of a real-space implementation of the Bethe-Salpeter equation (BSE) and use it in conjunction with an empirical tight-binding model to investigate the optoelectronic properties of colloidal quantum-confined nanostructures. This novel implementation exploits the limited radial extent and small size of the atomic orbital basis to treat finite systems containing up to ~ 4000 atoms in a fully many-body framework.

In the first part of this thesis our empirical tight-binding model is initially benchmarked on zincblende CdSe nanocrystals, before subsequently being used to investigate the electronic states of zincblende CdSe nanoplatelets as a function of thickness. The band-edge electronic states are found to show minimal variation for a range of thicknesses and the results of our tight-binding model show good agreement with those predicted using a 14-band $\mathbf{k} \cdot \mathbf{p}$ model for a nanoplatelet of 4 monolayers (ML) in thickness. Optical absorption spectra were also computed in the independent-particle approximation. While the results of the tight-binding model show good agreement with those of the 14-band $\mathbf{k} \cdot \mathbf{p}$ model in the low-energy region of the spectrum, agreement with experiment was poor. This reflects the need for a many-body treatment of optical absorption in nanoplatelet systems.

In the second part of this thesis we apply our tight-binding plus BSE model to study the excitonic properties of CdSe nanocrystals and nanoplatelets. Simulations performed on CdSe nanocrystals examined an approximation of the BSE equivalent to configuration interaction singles (CIS), and found that both the optical gap and the low-energy spectral features were unaffected by the approximation. A

comparison of exciton binding energies with those predicted by CIS demonstrates the sensitivity of results to the exact treatment of dielectric screening and the decision of whether or not to screen exchange. Our model predicts optical gaps that are in strong agreement with average experimental data for all but the smallest diameters, but was not able to reproduce low-energy spectral features that were fully consistent with experiment. This was attributed to the absence of the spin-orbit interaction in the model.

Simulations performed on CdSe nanoplatelets investigate the optical gaps and exciton binding energies as a function of thickness. Exciton binding energies were found to reach $\sim$ 200 meV for the thinnest system, however, optical gaps were slightly overestimated in comparison to experiment. This is attributed to the reduced lateral dimensions used in our simulations and our bulk treatment of dielectric screening. A two-dimensional treatment of dielectric screening is expected to further increase binding energies. Calculations of the excitonic absorption spectrum reproduce the characteristic spectral features observed in experiment, and show strong agreement with the spectra of nanoplatelets, with thicknesses ranging from 3 ML to 5 ML.

Chapter 1

Introduction

1.1 Nanostructures and Quantum Confinement

Colloidal semiconductor nanocrystals, nanorods, nanoplatelets and multi-pods constitute a class of nanostructures with properties that vary from molecular to bulk-like as a function of size due to the quantum confinement effect[1]. Quantum confinement of electrons and holes in one, two or three dimensions[1] increases the optical gap of the system as a function of decreasing size in the confined dimension/s. Ekimov *et al.*[2] and Henglein[3] were the first to independently show that modification of quantum size levels subsequently changes the optical absorption and emission of nanocrystals, blue-shifting the features to higher energies as a function of decreasing diameter.

Optical spectroscopy provides a means of probing neutral excitations in semiconductor nanostructures, with optical absorption experiments on nanocrystals revealing low-energy spectral features dominated by excitonic effects. An exciton is defined as a bound state, comprised of a spatially correlated electron and hole. In covalent semiconductors, the dielectric function screens the Coulomb potential

[1] Corresponding to nanoplatelets, nanorods and nanocrystals, respectively.

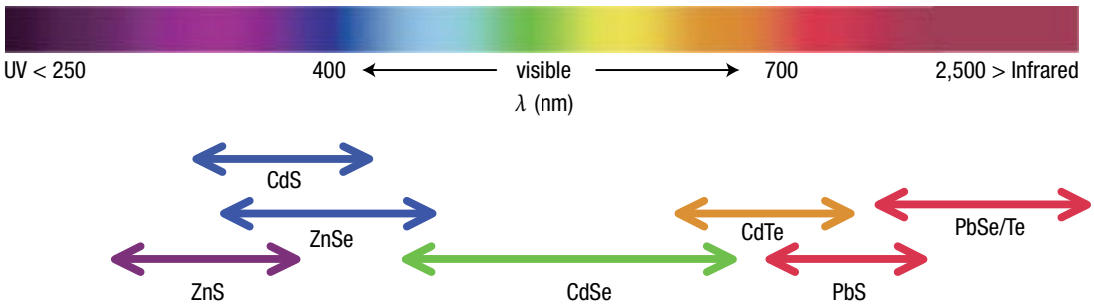

Figure 1.1: Nanocrystal emission wavelengths for a range of materials, shown in relation to the electromagnetic spectrum. Figure reproduced from reference[12].

between the electron and hole, resulting in weakly-bound excitons delocalised over many unit cells. These are referred to as Wannier-Mott excitons and comprise the excitonic species studied in this thesis[4]. In nanostructures, quantum confinement leads to an enhancement in the exciton binding energies as a consequence of increased electron-hole overlap and a reduction in dielectric screening relative to the bulk[5; 6]. Indeed, one can see enhancements of $\sim$ 60 times that of the bulk binding energy[7].

Colloidal nanostructures are synthesised with wet chemistry techniques that in general, produce systems with narrow size distributions, highly uniform morphologies and effective surface passivation[8]. Colloidal nanostructures are free-standing systems that retain their bulk crystal structure and lattice parameters down to sizes $\sim$ 1 nm in diameter[9].

CdSe nanocrystals represent the prototypical system for the study of quantum-confinement and its effects on optical properties as synthesis is highly reproducible in both the wurtzite and zincblende phases[10], with fine control over size distribution[2] across a range of diameters (1.5-10 nm)[11]. The band gap of spherical CdSe nanocrystals can be varied from 1.9 eV (652 nm) to 2.8 eV (443 nm) by reducing the diameter of the nanocrystal from 7 nm to 2 nm, effectively covering the range of the visible spectrum at room temperature[3].

[2]Less than 5% root mean square deviation in the diameters.
[3]See averages in Figure 10.13 of Chapter 10.

Cadmium chalcogenide nanocrystals are characterised by direct band gaps that are size-tuneable in the visible region and strong oscillator strengths. Properties which are broadly attributable to the II-VI semiconductors as a whole and which make them readily accessible with optical spectroscopy techniques, from which a plethora of electronic and optical properties can be discerned.

Heteorstructure engineering of binary and ternary systems has lead to additional improvements in quantum yields and photoluminescence stability, providing finer control over emission frequency, spatial localisation of charge carriers and radiative lifetimes[13]. The ability to control excitonic properties through size and composition have allowed colloidal nanocrystals to find applications as light emitters in LED displays[14], as light absorbers in solution-processed thin-films and photovoltaic cells[15; 16], and in photodetectors[17]. Nanoplatelets offer similarly exciting applications[18], with distinct optoelectronic properties that differ from their zero-dimensional counterparts. A summary of the optoelectronic properties of cadmium chalcogenide nanoplatelets is given in the following chapter.

Motivation

Cadmium chalcogenide nanocrystals have been studied since the 1980's[2; 3], resulting in a well-developed theory of the low-energy excitonic structure and dynamical processes that determine their optical properties[19–24]. Cadmium chalcogenide nanoplatelets, however, represent a much newer class of colloidal nanostructure with optical properties that distinctly differ from those of nanocrystals due to their quasi two-dimensional structure. A theoretical understanding of their low-energy excitonic structure is currently lacking. Furthermore, it will require a many-body treatment.

The emergence of colloidal nanoplatelets, amongst other nanoscale systems that exhibit strong excitonic effects[25], highlights the need to be able to apply many-body techniques to the simulation of nanostructures that contain thousands of atoms

but lack periodicity. Furthermore, the trend towards ternary and multinary systems, where material composition can vary at the scale of monolayers, indicates that these techniques will need to describe the electronic structure at the atomic scale.

Precise control over the thickness and increased control over the planar dimensions[26] results in distinct optical properties that make cadmium chalcogenide nanoplatelets a model system with which one can investigate the effects of dimensionality and confinement on the excitonic properties. A thorough understanding of the band-edge exciton structure is of fundamental physical interest and should also aid in device design. We therefore investigate the optoelectronic properties of the prototypical CdSe nanoplatelet using a many-body formalism, which we have novelly adapted to treat large, finite systems.

1.2 Computational Methods for Electronic Structure Calculations

One of the primary challenges in modelling colloidal nanostructures is that they can contain many thousands of atoms but are characterised by finite dimensions. The use of ab initio techniques in the calculation of both ground state and excited state properties is therefore not computationally feasible. As such, one must typically resort to the use of empirical models to compute the electronic structure of these systems. A semi-empirical model is broadly defined as a quantum mechanical model in which some quantity, such as the potential or basis, is parameterised, resulting in an accurate reproduction of the bulk properties of the material in question. This typically also removes the need for self-consistency. In the following section, we present a discussion of the main empirical models employed in the calculation of the electronic structure of nanoscale systems.

1.2.1 Envelope Function Methods

All envelope function methods are based on the effective mass approximation. In this approximation, the motion of an electron in a slowly varying potential is treated as a free electron with a renormalised, effective mass and the wave function is approximated as the product of the periodic Bloch function defined at the zone centre and a slowly varying envelope function.

$\mathbf{k} \cdot \mathbf{p}$ theory is the application of perturbation theory to extend the periodic Bloch solutions to other values of $\mathbf{k}$[27]. A typical $\mathbf{k} \cdot \mathbf{p}$ Hamiltonian is comprised of Bloch functions that describe the three highest valence bands and lowest conduction band, leading to an 8-band model in the presence of spin. One such example is the 8-band Pidgeon and Brown model[28], which accounts for valence-conduction coupling, and the effect of higher bands via second-order perturbation theory. This model is capable of accurately describing approximately 15% of the Brillouin zone in the proximity of the Γ point, for the bands in question[29].

Envelope function methods therefore treat the nanostructure as a confined bulk system and consequently lack explicit knowledge of the atomic structure however, envelope function Hamiltonians are still capable of capturing the atomistic symmetry of a nanostructure, given the inclusion of appropriate band coupling effects[30]. This means that calculation times are invariant with system size and results increase in accuracy as the system converges on the bulk. The lack of an explicit knowledge of the atomic structure does, however, impose some restrictions. Envelope models cannot explicitly describe surface reconstruction or surface passivation by ligands. They are also not well-suited for simulations of systems with small dimensions or that vary in composition at the monolayer scale.

1.2.2 Empirical Pseudopotential Models

Empirical pseudopotential models provide an atomistic description of the electronic structure. In an empirical pseudopotential model, the bulk crystal potential is expanded as the sum of local, atomic-like potentials. These are subsequently parameterised by fitting to a small number of low reciprocal lattice vectors that describe the bulk crystal and the Schrödinger equation is solved for the valence electrons in a plane wave basis. Alternatively, one can utilise a semi-empirical pseudopotential model. In this approach, the local atomic potentials are constructed from ab initio ionic pseudopotentials and modified to ensure good reproduction of bulk properties, such as the band gap. The non-local component of the ionic pseudopotentials is also added to the total crystal potential[31]

The atomistic nature of semi-empirical pseudopotential models means that they address many of the shortcomings associated with envelope function methods. They intrinsically capture the atomic symmetry of the system and produce wave functions of comparable quality to those found using density function theory (LDA), without the need for self-consistency. The use of a plane wave basis to treat nanoscale systems does, however, make pseudopotential models the most computationally-expensive of the empirical methods available to us[32].

1.2.3 Empirical Tight-Binding Models

Empirical tight-binding models provide an atomistic description of the valence electrons in solids in terms of localised atomic orbitals, giving an intuitive description of bonding in terms of on-site and inter-atomic orbital interactions[33]. Hamiltonian elements are parameterised and one can adjust the number of parameters by varying the radial extent of the orbitals or the size of the basis. In a minimal tight-binding model, one only considers the overlap between orbitals on adjacent atoms, resulting in a highly sparse Hamiltonian that can be efficiently stored and solved[34]. Empirical

tight-binding models therefore represent an efficient means of generating atomic wave functions for systems containing thousands of atoms[35].

In summary, the tight-binding model provides what we consider to be an ideal compromise between detail and efficiency. A minimal tight-binding model is capable of treating systems containing tens of thousands of atoms, whilst providing an atomic description of the system and of the wave functions. We therefore choose to model the electronic structure of CdSe nanocrystals and nanoplatelets using a tight-binding model.

1.3 Computational Methods for Many-body Calculations

In the final section of this chapter, we discuss the many-body formalism that we utilise to describe excitonic correlation. The GW[36; 37] and BSE[38] methods are currently recognised as two of the most reliable first-principles methods for the calculation of quasiparticle properties and two-body excitations, respectively[39]. Recent advances have seen both ab initio GW[40; 41] and BSE[42] calculations used to treat molecules and interfaces containing up to $\sim$ 400 atoms. Examples of applications include photosynthetic complexes[43; 44] and aqueous DNA[45].

Advancements in scaling can be attributed to basis set optimisation[42; 46], the use of localised basis sets[47; 48], schemes to reduce summations over empty states[49; 50] and improved parallelisation, however even with these advancements, calculations are still restricted to the molecular scale when performed from first-principles. We therefore develop and present a novel implementation of the BSE in conjunction with an empirical tight-binding model, which can be used to treat finite systems $\sim 10\times$ larger than those currently accessible with the most sophisticated ab initio methods.

There are, of course, other methods of treating excited states. For example, configuration interaction (CI) has frequently been applied to nanoscale systems[23; 51–54]. The fundamental drawback of CI calculations is, however, its scaling with system size. Indeed, in full CI calculations the basis determinants scale binomially with system size. Truncated CI schemes containing doubly, triply or quadruply excited determinants scale as N^6, N^8 and N^{10}, respectively, where N is the size of the basis[55]. To make the method tractable for nanoscale simulations, the basis is therefore typically restricted to single-substitution determinants[23]. This is called configuration interaction singles (CIS). BSE on the other hand, offers scalings of $N^3 - N^4$ depending on the specifics of the implementation[48].

Although CIS and BSE are derived in a completely different manner to one another, one can show that there is a formal connection between the two methods. It can be shown that the BSE includes additional coupling interactions that mix excitonic transitions. The BSE therefore includes correlation effects that are absent in CIS[56]. As such, we also take the opportunity to evaluate the results of CIS calculations for CdSe nanocrystals, against those of our BSE model.

In summary, we have presented a brief discussion of colloidal nanocrystal and nanoplatelet systems, addressing the physical properties that make them interesting to study and have outlined what we intend to contribute to the field. We have also presented a discussion of the methodologies that are typically used to treat these systems. In doing so, we explain why we opt to describe the electronic structure using a tight-binding model and why we intend to treat many-body excitations using the Bethe-Salpeter equation. What follows is a breakdown of the thesis chapters.

1.4 Structure of the Thesis

Chapter 2 proceeds with a review of the literature regarding the progress made towards understanding the optoelectronic properties of cadmium chalcogenide

nanoplatelets.

Chapter 3 reviews the use of the nearest neighbour (NN) sp^3s^* tight-binding model for the simulation of CdSe nanocrystals. The model's suitability and limitations are discussed.

Chapter 4 formally outlines the mathematical description of the NN sp^3s^* tight-binding model that we use to describe the electronic states of our nanostructures.

Chapter 5 gives a formal mathematical description of the BSE in transition space, detailing the construction of an effective two-particle Hamiltonian and how this can be used to simulate optical absorption spectra.

Chapter 6 presents the bulk properties of CdSe predicted with our tight-binding model and discusses some key model features including the sparse solver, orbital basis and surface passivation.

Chapter 7 describes the main features of our real-space implementation of the BSE, with a focus on the approximations made to the interaction kernel.

Chapters 8 and 9 present the results our tight-binding calculations on CdSe nanocrystals and nanoplatelets, respectively. These calculations are performed in the independent-particle approximation.

Chapters 10 and 11 present many-body calculations of the optical gaps, exciton binding energies and optical absorption spectra of CdSe nanocrystals and nanoplatelets, respectively. In both chapters, optical gaps and absorption spectra are compared with experiment, while exciton binding energies are compared with other theoretical results.

Chapter 12 summarises our results and conclusions, and suggests some extensions to the work presented.

Chapter 2

II-VI Colloidal Nanoplatelets

2.1 Cadmium Chalcogenides

Murray and coworkers were the first to demonstrate reproducible synthesis of spherical CdSe nanocrystals with a low size dispersion, using hot injection[11]. Peng and co-workers extended this synthesis technique to nanorods at high reaction temperatures, creating the first colloidal nanostructure with two-dimensional confinement[57]. In the same year, Manna *et al.* developed polytypic, multi-branched tetrapods[58], amongst several other exotic shapes.

The synthesis of ultra-thin structures with high reaction temperatures is however, intrinsically difficult due to a reduced control of growth rates along specific crystal planes and the increased risk of deformation. Ultra-thin, two-dimensional, cadmium-based colloidal nanostructures were therefore not realised until 2006 when Hyeon and co-workers synthesised nanoribbons from wurtzite seeds using a low-temperature, colloidal template method[63],[64]. This resulted in ultra-thin sheets $\sim$1.4 nm in thickness, with widths of 10-20 nm and lengths up to $\sim$ 1 micrometer.

The strong van der Waals interaction between organic ligands on adjacent ribbons

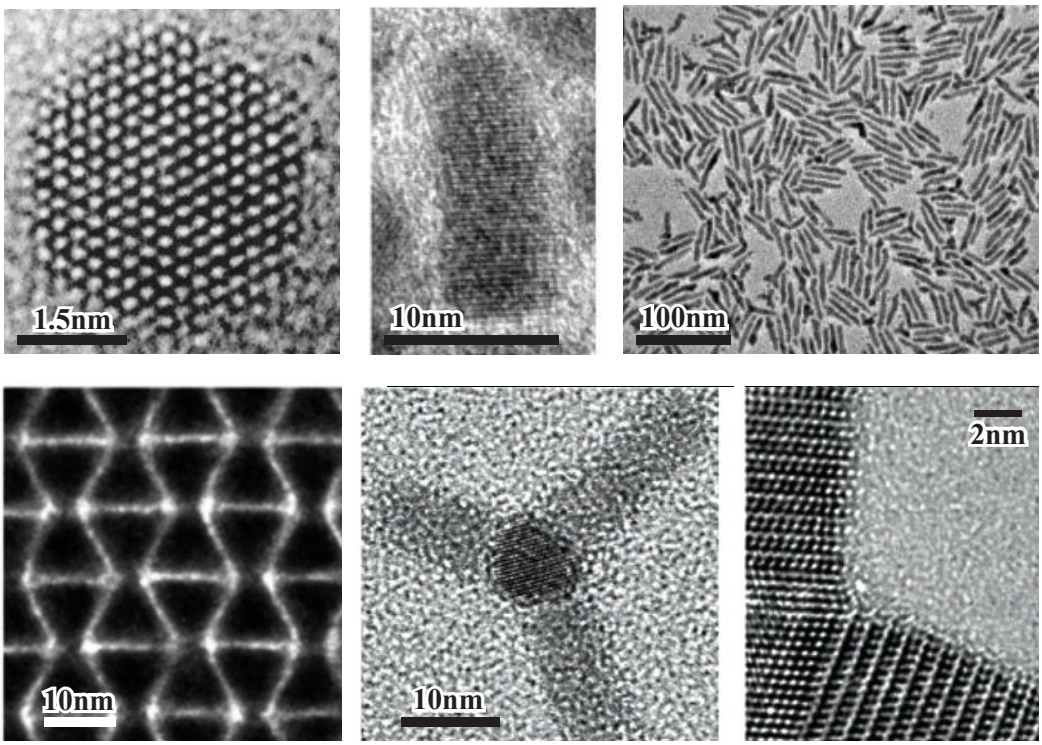

Figure 2.1: Various nanostructure morphologies. From top left to bottom right: A CdSe nanocrystal[59], a CdSe nanorod[57], an ensemble of CdSe nanorods[60], an array of CdSe tetrahedra[61] and a CdSe/CdS tetrapod at differing magnifications[62].

subsequently leads to self-assembly of laminar sheets and their large sizes make them prone to aggregation in solution[65].

The two-dimensional, zincblende analogue of CdSe nanoribbons was synthesised in 2008 by Ithurria and Dubertret[66]. Unlike nanoribbons, these nanoplatelets are characterised by polar surfaces and do not aggregate in solution. They offer greater control over the lateral dimensions and were the first two-dimensional colloids to be thickness-tuneable with atomic precision. These features are visible in transmission electron microscopy (TEM) images shown in Figure 2.2.

2.2 Cadmium Chalcogenide Nanoplatelets

Colloidal nanoplatelets are characterised by atomically flat, cubic morphology with the zincblende crystal structure[66]. They exhibit atomic thicknesses, beginning at

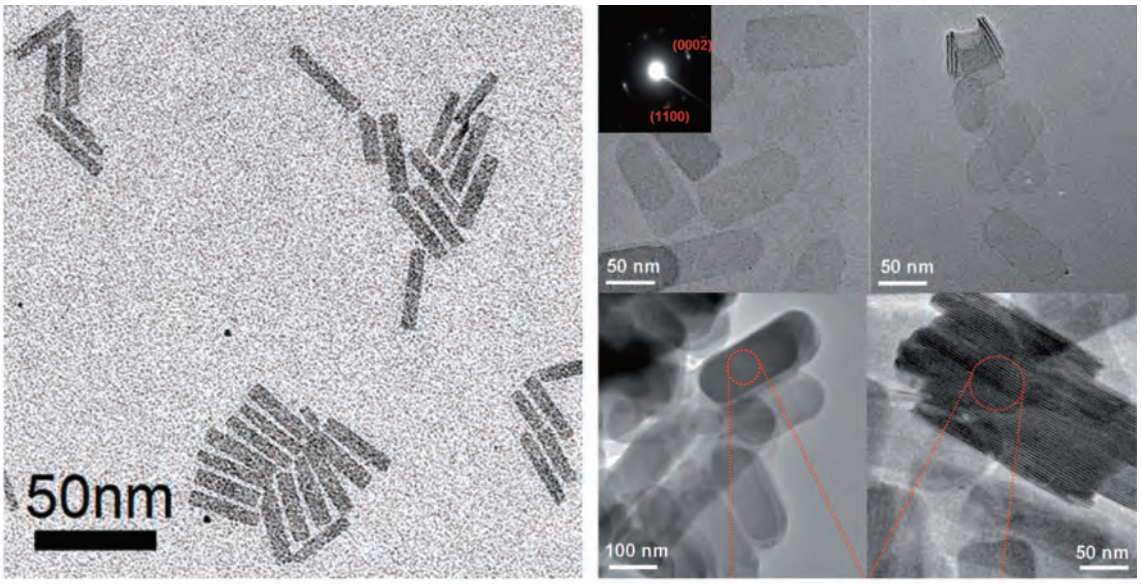

Figure 2.2: 2D Nanostructures. Left: TEM of CdSe nanoplatelets[67]. Top right: TEM of flat and rolled single-layered CdSe nanosheets, with SAED pattern inset. Bottom right: TEM pictures of laminar CdSe nanosheets[68].

two monolayers and can be tuned with monolayer precision, whereas the lateral dimensions vary from a few nanometers[69] to several hundred nanometers[70]. This results in quasi two-dimensional structures which strongly quantum confine the excitonic states in one dimension, producing optoelectronic properties comparable to epitaxial two-dimensional quantum wells[71].

Platelets are formed by continuous lateral growth of small nanocrystal seeds in the presence of acetate ions[1]. The seed dimensions therefore determine the platelet thickness, with both the top and bottom surfaces terminated with cadmium atoms and passivated with carboxylate alkyl groups[69], as depicted in Figure 2.3 (excluding a passivating species).

Nanoplatelets can be dispersed in hexane in low concentrations with minimal aggregation, facilitating single-platelet spectroscopy[67]. Quantum yields (QY), which is a ratio of emitted photons to absorbed photons, have been measured as high as ∼50% for single CdSe nanoplatelets at room temperature[72] and ∼ 80%

[1] Cd acetate, Zn acetate, etc.

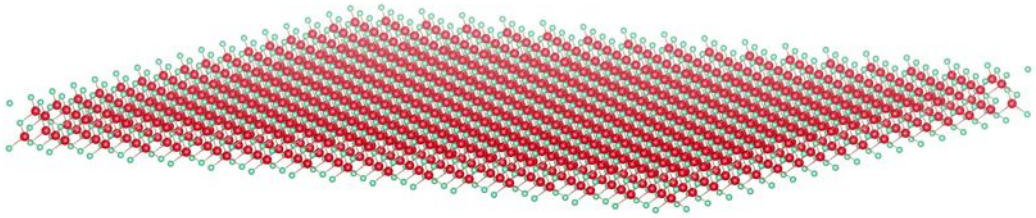

Figure 2.3: Ball and stick model of a CdSe nanoplatelet with lateral dimensions of 10 nm × 10 nm, and a thickness of two monolayers. Cd atoms are blue and Se atoms are red.

($\sim 100\%$) for CdSe/CdZnS platelets at room (cryogenic) temperature[73].

High QY for single-material platelets is likely to originate from a low surface defect density, reducing mid-gap trap states. The growth of a shell can further act to increase QY by reducing the overlap of the electron and hole wave functions with the surface[74], however this is strongly dependent on the shell quality. For example, CdSe/CdS nanoplatelets only exhibited $\sim 40\%$ quantum yield, which was attributed to the generation of interfacial defects[73].

The uniformity of surface thickness for both single platelets and throughout populations of platelets leads to optical absorption and emission features that exhibit reduced inhomogeneous broadening in single and ensemble measurements. For example, the full-width half-maximum (FWHM) of the emission maximum for CdSe nanoplatelets is typically < 10 nm (40 meV)[67], which is important for monochromatic light emission and the minimisation of reabsorption losses. Furthermore, the Stokes shift between the lowest absorption and emission maxima is ~ 1 nm, compared to ~ 10 nm in spherical nanocrystals.

The absorption spectrum of the cadmium chalcogenide nanoplatelets is characterised by two strong peaks at the absorption edge, attributed to transitions from the heavy-hole and light-hole states to the lowest conduction state, respectively. The absorption onset has been shown to redshift by ~ 1 eV when the platelet thickness is varied from 2 to 5[2] monolayers[72], as shown in Figure 2.4.

[2]The labelling in the left panel of Figure 2.4 has been assigned with effective mass calculations

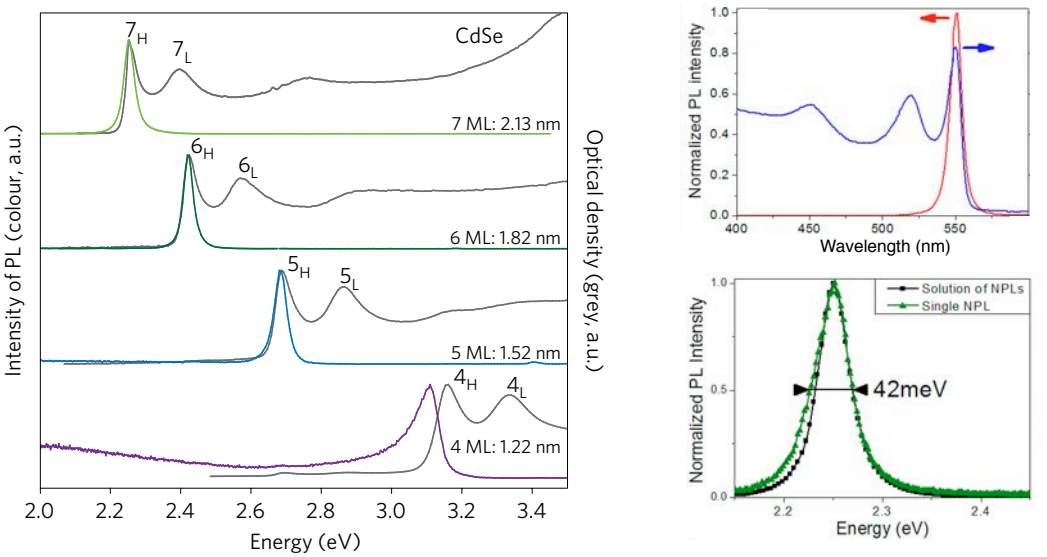

Figure 2.4: Left: Absorption (black line) as a function of thickness for CdSe nanoplatelets. Colour overlays show the respective photoluminescence peaks[72]. Bottom Right: Room temperature photoluminescence spectra of a solution of nanoplatelets and of a single nanoplatelet under air, on a glass substrate excited at 250 $W \cdot cm^{-2}$[67]. Top Right: Absorption (blue) and photoluminescence spectrum (red) of a solution of nanoplatelets[67].

2.2.1 Carrier Relaxation Dynamics

Upon photo-excitation, charge carriers are promoted to excited states before undergoing relaxation (cooling) to the band edges via non-radiative pathways. Pelton *et al.* inferred that for low pump powers, all carriers in CdSe nanoplatelets had relaxed to their lowest-energy excited states within 5 ps of excitation[75]. Sippel and coworkers elucidated these observations using time-resolved 2-photon photo-excitation at low excitation densities for CdSe and CdSe/CdS nanoplatelets[76]. Sub-40 femtosecond resolution allowed them to observe that the majority of excess carrier kinetic energy had been dissipated after 1 ps of excitation, in both systems. These results are in agreement with both Pelton *et al.* and Baghani *et al.*[77], the latter of whom also observed rapid carrier cooling decay within 10 ps of excitation.

and is now suspected to overestimate nanoplatelet thicknesses by 1-2 MLs.

2.3 Recombination Pathways

2.3.1 Nonradiative Decay Pathways

Multiple exciton complexes can also decay via non-radiative Auger recombination. In the case of nanocrystals, trion recombination (exciton plus excited carrier) is dominant and occurs at a rate which scales cubically. In nanorods however, bi-excitons are the prevalent species and recombine at a rate that scales quadratically[78]. Kunneman and coworkers fit kinetic rates to room-temperature photoluminescence decay spectra taken over 8 ns, for CdSe and CdSe/CdS/ZnS nanoplatelets[79]. In both instances they found rates that were fit better with quadratic rather than cubic exponents. Bi-exciton lifetimes of 14.3 ns and 8 ns, were subsequently found for 5 ML CdSe and CdSe/CdS/ZnS nanoplatelets, respectively.

Baghani and coworkers also examined photoluminescence decay over a shorter time period of 600 ps, in 4 ML CdSe platelets at room temperature[77]. They too found kinetics that were well-fit with a quadratic dependence and determined a bi-exciton recombination rate of 5 ns^{-1}: equivalent to lifetime of 200 ps. Differences with respect to the lifetimes reported by Kunneman *et al.* were attributed to the differing lateral and thickness dimensions used in the prior work. A comparable Auger lifetime of 500-600 ps was also reported in core/shell CdSe/CdS nanoplatelets by She *et al.*[80].

It is therefore evident that nanoplatelets exhibit Auger recombination rates that are at least an order of magnitude slower than those associated with spherical CdSe nanocrystals[51; 81–83], with bi-exciton Auger recombination rates comparable to those observed in CdSe nanorods[78; 84]; however lifetimes as large as 14 ns have yet to be corroborated. Indeed, it would be interesting to see Auger rates studied as a function of both the thickness and planar area.

2.3.2 Radiative Recombination Lifetimes

Radiative recombination rates (or equivalently, lifetimes) are generally well-fit to photoluminescence decay data with bi-exponential, and in some instances, tri-exponential functions. At room temperature, bi-exponential fits produce lifetimes comprised of a short component on the scale of picoseconds and a second component on the scale of nanoseconds.

The current consensus is that the nanoscale component corresponds to the radiative lifetime of the exciton, with reports varying from 4-8 ns for 5 ML CdSe platelets at room temperature[67; 69; 79; 85]. This assignment is justified on the basis of the correspondingly high QYs observed, variation as a function of temperature and that the application of a shell has been shown to reduce the proportional contribution of the fast decay component in the decay trace[73; 79]. The fast component could therefore be due to quenching by trap states, non-radiative Auger recombination or some other mechanism. As to which it is remains an open question. While growth of a shell reduces the overlap of the electron and hole wave functions with surface states, alloying of the hetero-interface is also known to reduce Auger recombination[86]. In some instances, a long-lived 3rd lifetime $\geq$ 50 ns is also reported. This long-lived component is consistent with carrier trapping in defect states[85].

At low-temperature, CdSe nanoplatelets exhibit photoluminescence intensity decays of mono-exponential character, with $\tau = 200 - 400$ ps[67; 72; 87]. Such lifetimes are considerably shorter than spherical CdSe nanocrystals emitting at similar wavelengths, with lifetimes in the range of $\sim$ 20-80 ns[88–90]. Naeem and coworkers argue, however, that PL decay taken over long acquisition times suffers from spectral diffusion and that the decay of non-resonantly excited platelets reflects the density dynamics mediated by phonon-scattering across all occupied exciton states. Subsequent radiative lifetimes must therefore be considered as upper bounds. By conducting transient resonant four-wave mixing measurements at low-temperature,

they instead find a radiative life of ∼1 ps for a 4 ML CdSe nanoplatelet[91]. A value that is consistent with homogeneous line widths of single NPL measured at low temperature (0.4 meV)[67].

Both core-only and core/shell nanoplatelets therefore exhibit a concurrent lifetime shortening and an enhancement of the fluorescence intensity (QY) as temperature decreases. A shortening of fluorescence decay time with decreasing temperature is usually associated with opening of non-radiative decay channels and a decrease in fluorescence intensity, however the increase in quantum yield and fast radiative recombination rates are not compatible with this.

Instead, fast single-exciton photoluminescence decay kinetics are attributed to the giant oscillator strength associated with the band-edge transition. It is thought from analogy with quantum wells, that the lowest excitonic state is delocalised in-plane and highly coherent due to the atomic precision of the surfaces coupled with the large lateral dimensions[1]. Indeed, a coherent phasing of dipoles over many unit cells has been shown to result in a correspondingly large dipole matrix element for the exciton, independent of thickness in quantum wells[92].

In-plane delocalisation of the exciton is supported by two-dimensional electron spectroscopy measurements taken by Cassette *et al.* Spectra show a symmetric 2D peak corresponding to the lowest excitonic transition, for both CdSe and core/shell CdSe/CdZnS nanoplatelets. If on the contrary, the exciton was localised, one would see an elongation of this peak along the diagonal of the spectrum[93].

2.3.3 Excitonic Binding Energy

Exciton binding energies are yet to be systematically investigated by way of experiment. Achtstein *et al.* predicted a range of values using effective mass calculations, varying from 100-400 meV depending on the platelet thickness and the dielectric constant of the surrounding material[87]. These values represent a

considerable enhancement over the bulk binding energy of 15 meV[94]. Calculations by Benchamekh and coworkers[95], which also include the use of image charges but construct the single-particle wave functions using tight-binding coefficients, find results which span a similar energy range.

Full many-body calculations of exciton complexes have yet to be done for nanoplatelet systems although the group of Even have done first-principles calculations of the surface passivation and its effect on the self-energy[3], giving a more realistic idea of the effect of the surface on the nanoplatelet states[96]. Their calculations show that the assumption of an abrupt dielectric interface and classically calculated image charge corrections overestimate the self-energy corrections, although this effect decreases with increasing thickness. For example, self-energy corrections for acetate-passivated surfaces of 2 ML CdSe NPLs peak at ~ 0.2 eV. Approximately half the size predicted using the classical theory.

The limited experimental data appears to coincide with the calculated values. Kunneman and coworkers inferred that the excitonic binding energy must exceed thermal energy at room temperature as rate equations consistent with bound excitons best fit their experimental data[79]. Furthermore, Grim *et al.* inferred a specific value of 132 meV $\pm$20 meV for 4 ML CdSe platelets[97].

2.4 Summary

This review demonstrates a maturing body of experimental work, focusing on measuring and understanding optical processes as a function of thickness, for both single-material CdSe and core/shell CdSe/CdS nanoplatelet systems. The effect of quantum confinement on the optical gap has been measured for a range of thicknesses and is found to change by $\sim$ 1 eV. Optical absorption spectra have

[3]Corrections to independent-particle energies arising from exchange and correlation.

been recorded for a range of thicknesses and have been shown to exhibit highly-reproducible, persistent spectral features. Furthermore, an initial assignment has been made to the two prominent band-edge optical transitions. Radiative lifetimes have also been quantified for several thicknesses and excitonic properties have been inferred from the photoluminescence.

What is currently lacking, however, is an accompanying theoretical description of the observed processes. We therefore intend to address some of these questions with our tight-binding plus BSE model. Using the tight-binding model, we are able to investigate the band-edge electronic states and observe how they vary with thickness. The band-edge states are important as they determine the dipole matrix elements of the lowest-energy transitions in the optical absorption spectrum. Dipole matrix elements subsequently provide information on the strength of transitions between states. Using this information, we can build up a picture of the absorption spectrum in the absence of the electron-hole interaction. Our BSE model then allows us to incorporate the electron-hole interaction, mixing the independent-particle transitions, which leads to excitonic properties.

Using our full model, we can quantify optical gaps and exciton binding energies as a function of thickness and lateral dimensions, and simulate the effect of the electron-hole interaction on the optical absorption spectrum. Indeed, the optical properties of CdSe nanoplatelets have not been studied with many-body calculations. Information regarding the structure of the lowest exciton states, their spatial distributions and the extent of independent-particle mixing can also be obtained from our formalism, however this constitutes future work. The following chapter subsequently reviews the application of the orthogonal NN sp^3s^* tight-binding model in the treatment of the optoelectronic properties of CdSe nanocrystals.

Chapter 3

A Review of Tight-Binding Model Applications

In this chapter we review applications of the orthogonal nearest neighbour sp^3s^* tight-binding model in the study of the electronic structure of group II-VI materials and discuss how many-body simulations of nanoscale systems have been approached in the past. We analyse the model's ability to reproduce the optical band-gap dependence on the diameter of CdSe nanocrystals, when used in conjunction with approximations for the exciton binding energy, and compare this to experimental data from the literature. Finally, we address some of the limitations associated with the model and comment on how this might affect our results.

3.1 Independent-Particle Calculations

The nearest neighbour (NN) sp^3s^* tight-binding model of Vogl and coworkers[34] has been extensively applied to nanostructures due to its ability to reproduce the valence bands, lowest conduction band high-symmetry points and subsequently the bulk band gap of direct-gap semiconductors, with the minimal number of empirical parameters. Indeed, Papaconstantopoulos and coworkers[98] have extensively investigated numerical parameter fitting for a variety of empirical tight-binding models and conclude that a two-centre NN sp^3s^* basis allows the accurate fitting of the four valence bands and an adequate reproduction of the band gap (although the dispersion of the conduction band is not accurate away from Γ).

Lippens and Lannoo performed the earliest studies of cadmium and zinc chalcogenide nanocrystals[99–101] using the sp^3s^* model. These studies provide the first calculations of band gap dependence as a function of size, for nanocrystals of up to 6 nm in diameter. Albe and coworkers[102] used the NN sp^3s^* model with a parameter set that was adapted from Lippens and Lannoo[100] to account for spin-orbit coupling. They investigate band gap dependence on size and the optical spectra of zincblende CdSe nanocrystals with diameters up to 5 nm. The introduction of spin-orbit coupling was shown to lead to better agreement with pseudo-potential calculations and experimental measurements for the band gap dependence on nanocrystal diameter, in comparison to the calculations of Lippens and Lannoo. Furthermore Albe and coworkers demonstrated that improved agreement can be obtained with experimental optical absorption spectra if one convolves a series of calculated spectra to account for the inhomogeneous broadening arising from the ensemble size distribution. Two examples are given in Figure 3.1.

Díaz and Planelles[104] explored the effect of morphology on the optical spectra of CdS triangular prisms and truncated tetrahedrons using the NN sp^3s^* model. The study demonstrated that the tight-binding model can capture subtle changes in

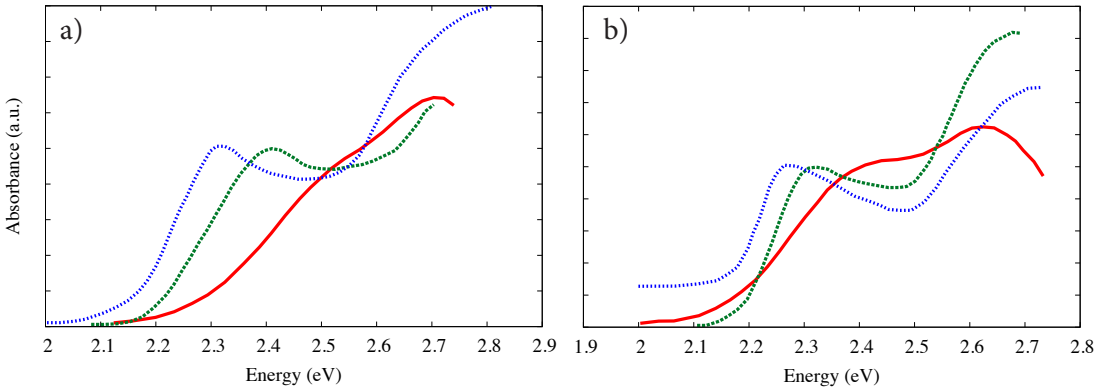

Figure 3.1: Optical spectra for CdSe nanocrystals of a) 3.4 nm and b) 3.6-nm diameter, adapted from reference [102]. In both panels, the absorption spectra are given for a single cluster (red, solid lines), a collection of clusters (dotted green, lines) with a mean diameter and experimental data[103](blue, dotted lines), respectively.

shape and crystal symmetry, highlighting the effect on the single-particle levels and corresponding band-edge transitions. Díaz and coworkers used the same model to simulate the band-edge transitions of CdS nanocrystals of 3-4 nm in diameter[105]. The predicted valence states were found to have envelope symmetries consistent with effective mass calculations, and the energy splittings and relative magnitudes of the lowest two transitions agreed with experiment. Furthermore, it was shown that CdS nanocrystals with wurtzite crystal structure exhibit band-edge optical spectra that show the same qualitative features as CdS nanocrystals with zincblende structure.

The ability of the NN sp^3s^* model to accurately predict the dependence of the band gap with nanocrystal size has been contentious. Sapra and Sarma[106] have argued that the sp^3s^* model of Lippens and Lannoo[101] overestimates the band gap for all II-VI materials however, their calculations explicitly include a passivating species whereas Lippens and Lannoo's simulations artificially remove mid-gap states, circumventing the need for an explicit passivating species. This passivating shell of atoms equates to a difference of one monolayer in thickness per nanocrystal, which Sapra and Sarma do not account for in their analysis. Furthermore, both Albe and coworkers[102] and Pérez-Conde and Bhattacharjee[107] have shown that an explicit

treatment of surface passivation in a NN sp^3s^* basis that also incorporates spin-orbit coupling, results in a model capable of reproducing the experimentally-determined optical band gap dependence on nanocrystal diameter.

3.2 Optical Band Gap as a Function of Nanocrystal Diameter

To demonstrate the NN sp^3s^* model's ability to reproduce the optical gap dependence on nanocrystal diameter, we compare tight-binding calculations by several groups with copious experimental data, shown in Figure 3.2. Red symbols represent several sets of tight-binding calculations, whereas blue symbols represent various experimental data. To facilitate the comparison, tight-binding calculations done at $T = 0\,\mathrm{K}$ are shifted down in energy, reproducing the effect of finite temperature on the band gap. The value of the shift has been determined using the Varshni equation[108], which is an empirical means of accounting for the effect of temperature on the band gap:

$$E_g(T) = E_g(0\,\mathrm{K}) - \frac{\alpha T^2}{\beta + T}, \tag{3.1}$$

where T is the temperature, (α, β) are fitted parameters and E_g is the band gap. Equation (3.1) predicts a 0.1 eV contraction in the band gap at a temperature of approximately 300 K. One notes that the magnitude of the change is dependent on the choice of parameters one uses in the Varshni equation. A room temperature shift was found to vary between 74 meV and 108 meV for the parameters given in [109] and references therein, and has therefore been rounded to an order of magnitude.

Tight-binding calculations can implicitly include the effect of temperature in the Hamiltonian by parameterising to a specific bulk band gap. A spread of values exist in the literature for the bulk band gap of zincblende CdSe, ranging from 1.7 eV to

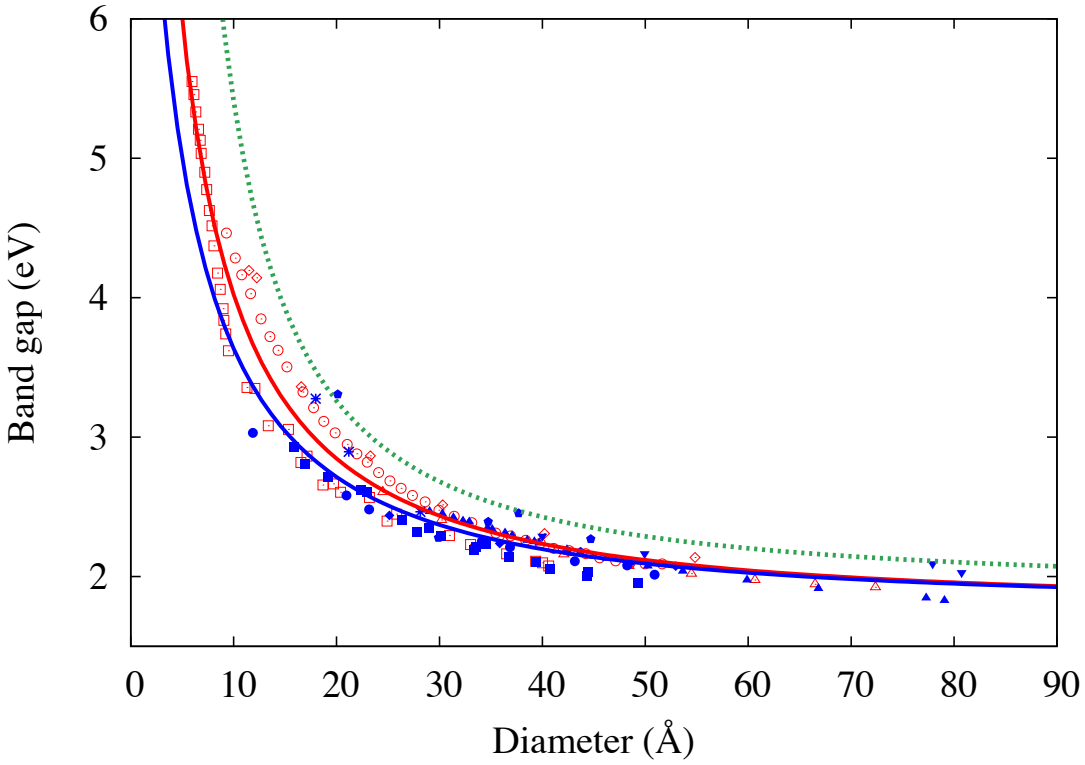

Figure 3.2: The optical band gap of a CdSe nanocrystal as a function of diameter. Tight-binding data are given by open, red symbols: Circles[100], diamonds[107], triangles[24] and squares[102]. Experimental data are given by solid, blue symbols: Stars[110], diamonds[111], inverted triangles[112], circles[11], pentagons[100], squares[113] and triangles[21]. The red line represents the best fit to the tight-binding data and the blue line represents the best fit to the experimental data. The single-particle band gap dependence predicted by our sp^3s^* model is also given by the green dashed line. Lines of best-fit are defined with Equation (3.2).

1.9 eV[113–117]. We assume a room temperature bulk band gap of 1.8 eV for zincblende CdSe. This corresponds to a value of 1.9 eV at T $\sim$ 0 K, using Equation (3.1). To facilitate comparison, we therefore only need to reduce the values of the open, red circles[100] and triangles[24] by 0.1 eV.

Pérez-Conde and Bhattacharjee's results[107] (open, red diamonds) show good agreement with Lippens and Lannoo[100] (open, red circles), even though the prior work contains spin-orbit coupling. This suggests that the energies of the lowest electron and hole states are only weakly affected by the inclusion of spin-orbit coupling in the model. The outlying tight-binding result given by open, red squares,

is that of Albe and coworkers[102]. Like the work of Pérez-Conde and Bhattacharjee, their calculations contain spin-orbit coupling and passivate the surface using pseudo-hydrogen atoms with an adjustable bond length. While Albe and coworkers cite the inclusion of spin-orbit coupling as the main reason for a difference in values when compared to Lippens and Lannoo[100], our opinion is that the difference is more likely explained by the different bulk band gap to which Albe and coworkers fit their Hamiltonian parameters and the choice of ligand bond length. Indeed, if we compare Albe and coworkers' data with the results of Pérez-Conde and Bhattacharjee's calculations for an equivalent ligand bond length, we find very strong agreement (see Figure E.1 in Appendix E). This highlights the sensitivity of the results to both the tight-binding parameterisation and the treatment of the surface passivation. Problems which are intrinsic to all empirical techniques[118].

Due to the spread in the data, we also display best-fits of the tight-binding (red line) and experimental (blue line) data in Figure 3.2. The single-particle results of our tight-binding model have been included as a point of reference (green dashed line). The optical band gap dependence is well-fit with a polynomial of the form[113; 119]:

$$E_g(d) = \frac{1}{a(d+\delta d)^2 + b(d+\delta d) + c} + E_{g,\text{bulk}}, \tag{3.2}$$

where d is the nanocrystal diameter, $E_{g,\text{bulk}} = 1.8$ eV and $(a, b, c, \delta d)$ are parameters to be determined by fitting. The fitting procedure is as follows. Equation (3.2) is initially used to fit the tight-binding data. δd is set to zero and is not used in this fit. As a result, we obtain a, b and c. The experimental data is then fit using δd as the only free parameter, with constants (a, b, c) found from the tight-binding fit. The parameter, δd, therefore corresponds to the average difference between experimental and simulated diameters, arising from experimental uncertainty and the length of the passivating species.

We find a value of 3.8 Å for this parameter, which reduces to 1.3 Å if we assume

a lower room-temperature bulk band gap of 1.7 eV. The order of magnitude is consistent with a bond length, suggesting that differences can reasonably be attributed to size uncertainty. The corresponding parameters are tabulated in Appendix E.

Inspection of the best-fits in Figure 3.2 reveals a difference of 0.13 eV at a diameter of 2 nm and a difference of 0.07 eV at a diameter of 3 nm. The error for larger diameter nanocrystals reduces to the meV. It is not expected that this model can reproduce experimental results in the molecular size limit, for systems containing $\leq$ 100 atoms. At this size, the lattice does not retain the bulk zincblende structure due to surface reconstruction (which comprises the majority of the structure)[120], and the properties of the ligands have a greater influence on the electronic structure[121]. Furthermore, the sp^3s^* basis cannot describe the L and X points with the same degree of accuracy as Γ, which can lead to errors if the lowest nanocrystal states are derived from a mixture of bulk states with different $\mathbf{k}$-vectors (valley-mixing)[122].

An analysis of the data presented in Figure 3.2 therefore demonstrates that the NN sp^3s^* tight-binding model is capable of reproducing the optical gap dependence on nanocrystal diameter, for diameters as small as $\sim$ 2 nm, within a reasonable level of uncertainty, when the excitonic binding energy is taken into account.

3.3 Many-Body Calculations

Building on the early work of Martin *et al.* on silicon nanocrystals[123], Pérez-Conde and Bhattacharjee[107] investigate excitonic effects in CdSe nanocrystals using a many-body treatment that parameterises on-site two-body integrals and approximates all other interactions with the monopole interaction (see Chapter 7). Corresponding optical gaps were found to be in good agreement with experiment, as shown in Figure 3.2.

Hill and Whaley were the first authors to do many-body calculations of the excitonic binding energy using pair products of tight-binding states expanded in an explicit basis of Slater orbitals, as the basis for configuration interaction calculations[124]. While comparison with experimental data on CdSe nanocrystals of 3 nm in diameter showed a quantitative disagreement, visual inspection of the results suggested that the qualitative trend was improved with respect to effective mass simulations. In our opinion, calculated values were systematically too large due to the small size of the two-particle basis and bulk screening.

This was improved upon by Lee and coworkers, who follow the same procedure but use more terms in their two-particle calculations and screen the Coulomb term with a modified dielectric function that accounts for the reduction in the average dielectric constant of smaller nanocrystals[24]. They find very good agreement between the calculated lowest optical transition and those determined from PLE experiments[21], in a diameter range of 3 nm to 6.5 nm. This is also shown in Figure 3.2.

Leung, Whaley and Pokrant also used the NN sp^3s^* model in conjunction with configuration interaction singles, including Coulomb and exchange terms, to investigate the optical properties of silicon[125] and CdSe nanocrystals[126]. They demonstrated that the model qualitatively predicted the long, finite lifetimes associated with the lowest exciton state of wurtzite CdSe nanocrystals, between 2 nm and 3.5 nm in diameter. Lifetimes of the lowest state varied from 10^{-4} s for nearly spherical NCs, to 10^{-2} s for prolate crystallites of 2 nm diameter[126].

This was subsequently contradicted by pseudopotential calculations carried out by Franceshetti *et al.*[23], who found that the lowest exciton state was optically forbidden for CdSe nanocrystals of a similar size to those of Leung *et al.* Tight-binding calculations by Pérez-Conde and Bhattacharjee[107] also find the lowest exciton state to be optically forbidden, for CdSe nanocrystals of 4 nm in diameter. They suggest that the disagreement with the tight-binding results of Leung *et al.*

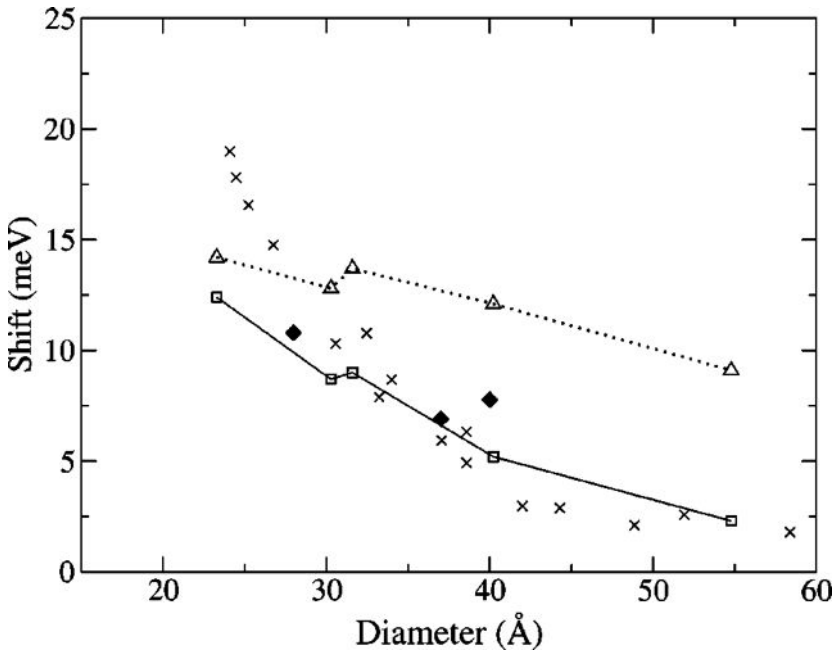

Figure 3.3: Resonant Stokes shift obtained from the energy position of the lowest energy peak of the computed absorption spectra, compared with the experimental measurements from Efros *et al.*[22] (crosses) and Chamarro *et al.*[103] (closed diamonds). The triangles connected by dotted lines correspond to a completely unscreened e-h exchange interaction, while the squares connected by solid lines correspond to a finite screening beyond the first neighbours. Figure taken from reference [127].

may be attributed to the differing treatment of the spin-orbit coupling. Leung *et al.* initially solve the single-particle Hamiltonian in the absence of spin-orbit coupling, then apply it as a perturbation to a subspace of band-edge states used to expand the two-particle Hamiltonian. However, spin-orbit coupling is of an order of magnitude larger than the average spacing of the single-particle levels. Pérez-Conde and Bhattacharjee therefore suggest that one can only reliably treat the lowest exciton state using pair-products constructed from the single-particle subspace, as the energy that the subspace spans is comparable in magnitude to changes in the lowest energy levels due to the addition of spin-orbit coupling. The exchange splitting dependence on size, computed by Pérez-Conde and Bhattacharjee, is shown in Figure 3.3.

Exchange splittings predicted by Leung *et al.*[126] were subsequently improved for

CdSe nanocrystals of $\leq$ 3 nm in diameter, by including surface reconstruction and partial passivation of the nanocrystal surface, consistent with experimental observations. In an additional publication, the authors also showed that the exchange splitting is insensitive to the bonding strength of the passivating species[128], in agreement with experiment observations[129]. An alternate explanation of the resonant Stokes shift dependence for nanocrystals of less than 2 nm in diameter was presented by Díaz and Bryant[130]. Using a tight-binding model with a sp^3d^5 basis, they showed that the lowest hole state is characterised by a P - state envelope in CdSe nanocrystals with diameters less than 2.3 nm. They therefore suggest that the resonant Stokes shift in small CdSe nanocrystals is actually a dipole-forbidden ($1P - 1S$ transition) as oppose to spin-forbidden.

3.4 Limitations of the sp^3s^* Model

Investigations by Boykin and coworkers[131] have shown that the NN sp^3s^* model is pathologically unable to reproduce the dispersion of the lowest conduction band away from the Γ-point, with the band dispersion remaining too flat along the direction $\Delta(\Gamma_1^c \rightarrow X_1^c)$. Indeed, this was recognised in the earliest calculations of Lippens and Lannoo[99] and will lead to errors in small crystallites and indirect-gap materials such as silicon.

Díaz and Bryant have subsequently systematically studied the effect of including d-orbitals in the basis of a nearest neighbour tight-binding model and compared the results to those produced with the sp^3s^* model[122; 127; 130]. A study of GaAs showed that the energetic position of the highest valence state predicted by the sp^3s^* model is in good agreement with that predicted by the $sp^3s^*d^5$ parameterisation of Jancu *et al.*[132] for a range of nanocrystal diameters, the smallest of which was 2 nm. An analysis of orbital contributions to the bulk bands showed that the inclusion of d-orbitals was not essential for a good description of the valence band-edge[122].

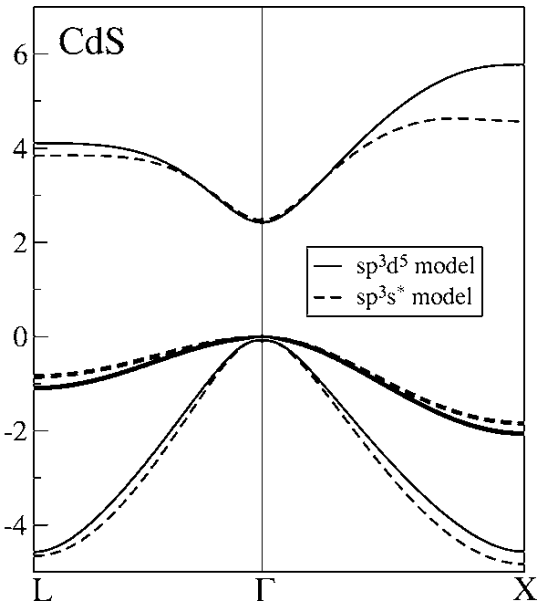

Figure 3.4: Bulk band structure for CdS along the $\Gamma - L$ (111) and the $\Gamma - X$ (100) directions, obtained with the sp^3d^5 model (solid line) and the sp^3s^* model using parameters from Lippens and Lannoo[100] (dashed line). Figure taken from reference [127].

Discrepancies in the lowest conduction states were, however, found between the two basis sets. This was attributed to a poor description of the the X and L-points in the lowest conduction band, which is particularly important in small GaAs nanocrystals where the lowest conduction state was shown to derive from bulk wave vectors at the edge of the Brillouin zone[122]. This subsequently led to a poor description of the band gap dependence as a function of size, by the sp^3s^* model. However, this was not found to be an issue in CdS, for which the L and X-points of the lowest conduction band are much higher in energy than the Γ-point (relative to GaAs)[127]. This argument can be extended to CdSe, as the lowest conduction band dispersion is very similar to that of CdS. Furthermore, it is shown in Figure 3.4 that the sp^3s^* and sp^3d^5 descriptions of the bulk band edges quantitatively agree within the vicinity of Γ and only show a large difference at X in the lowest conduction band[127].

3.5 Summary

The orthogonal NN sp^3s^* model is the least demanding empirical tight-binding model that can accurately reproduce the direct-gap of II-VI semiconductors. A review of the literature indicates that the NN sp^3s^* has been used successfully to describe the four highest valence bands across the Brillouin zone, the lowest conduction band about the Γ-point, as well as the band-edge effective masses in bulk CdSe and CdS. Its application to the II-VI class of nanocrystals has predicted absorption onsets, resonant stokes shifts and several exciton transitions in agreement with experimental data, indicating that the model is appropriate for the study of direct-gap nanostructures. In the following chapter, we present a formal, mathematical description of the tight-binding model and discuss the approximations used to construct the Hamiltonian in the NN sp^3s^* basis.

Chapter 4

Tight-Binding Theory

In this chapter, we start from the principal problem in solid states physics, how to solve the full many-body Schrödinger equation, and summarise the important approximations taken in order to make the problem tractable. The connection is then made between the semi-empirical tight-binding formalism and density functional theory, setting the tight-binding approach on quantitative grounds and elucidating the underlying approximations implicit to the formalism, before going on to discuss the specifics of the empirical tight-binding model used in this work.

4.1 The Many-Body Schrödinger Equation

The non-relativistic, many-body Schrödinger Hamiltonian in atomic Hartree units is[133]:

$$\left[-\sum_i \frac{\nabla_i^2}{2} - \sum_I \frac{1}{M_I}\frac{\nabla_I^2}{2} - \sum_{i,I} \frac{Z_I}{|\mathbf{r}_i - \mathbf{R}_I|} + \frac{1}{2}\sum_{i,j\neq i} \frac{1}{|\mathbf{r}_i - \mathbf{r}_j|} + \frac{1}{2}\sum_{I,J} \frac{Z_I Z_J}{|\mathbf{R}_I - \mathbf{R}_J|} \right] \tag{4.1}$$

where the terms from left to right are: the total electronic kinetic energy operator, the total nuclear kinetic energy operator, the attractive Coulomb potential between the electrons and the nuclei, the repulsive Coulomb potential between the electrons and the repulsive Coulomb potential between nuclei. (i, j) are electronic indices, (I, J) are nuclear indices, M_I are mass of the nuclei, Z_I represent the atomic numbers of the nuclei, and the coordinates $\mathbf{r}$ and $\mathbf{R}$ correspond to electrons and nuclei, respectively.

The study of optical excitations in nanostructures is primarily concerned with the properties of the valence electrons. It is therefore desirable to simplify Equation (4.1) until we are left with an expression that only describes this quantity, as it is incredibly expensive to solve for even the smallest systems and contains a lot of superfluous information. One can begin to simplify Equation (4.1) by treating the nuclei as stationary particles fixed at their equilibrium positions (the adiabatic approximation). This reduces the nuclear-nuclear repulsion to a constant. Furthermore, $M_I \gg m_i$ implies that the kinetic energy of the nuclei will be negligible, causing Equation (4.1) to simplify to:

$$\left[-\sum_i \frac{\nabla_i^2}{2} + \sum_i V_N(\mathbf{r}_i) + \frac{1}{2}\sum_{i,j\neq i} \frac{1}{|\mathbf{r}_i - \mathbf{r}_j|} \right] \Psi(\mathbf{r}_1, \mathbf{r}_2, ..., \mathbf{r}_N) = E\Psi(\mathbf{r}_1, \mathbf{r}_2, ..., \mathbf{r}_N), \tag{4.2}$$

where $V_N(\mathbf{r}_i) = -\sum_I \frac{Z_I}{|\mathbf{r}_i - \mathbf{R}_{I0}|}$ describes the Coulomb potential experienced by the

electrons due to the nuclei (the external potential), the third term describes the Coulomb repulsion between electrons, and the nuclear-nuclear repulsion has been absorbed into the total energy. Equation (4.2) therefore defines the many-body electronic Schrödinger equation for a set of nuclei fixed at their equilibrium positions $\mathbf{R}_{I0}$.

4.1.1 The Independent-Particle Approximation

The electronic kinetic energy and external potential of Equation (4.2) are local terms, whereas the Coulomb repulsion between electrons is non-local. If the Coulomb potential could be simplified to a local potential, then Equation (4.2) would reduce to the sum of N independent-particle equations:

$$\sum_{i}^{N}\left[-\frac{\nabla_i^2}{2}+V(\mathbf{r}_i)\right]\Psi(\mathbf{r}_1,\mathbf{r}_2,...,\mathbf{r}_N)=E\Psi(\mathbf{r}_1,\mathbf{r}_2,...,\mathbf{r}_N), \tag{4.3}$$

where $V(\mathbf{r}_i) = V_N(\mathbf{r}_i) + V_H(\mathbf{r}_i)$ is the effective crystal potential comprised of the external potential, $V_N(\mathbf{r}_i)$ and a local Coulomb potential, $V_H(\mathbf{r}_i)$. In this approximation, the many-body electronic wave function is equivalent to the product of single-particle states: $\Psi(\mathbf{r}_1,\mathbf{r}_2,...,\mathbf{r}_N) = \Pi_i^N\psi_i(\mathbf{r}_i)$ and the total energy reduces to the sum of independent-particle eigenvalues, $E = \sum_i^N E_i$. This simplification can be achieved by defining the Hartree potential, $V_H(\mathbf{r}_i) = \int d\mathbf{r}_j \frac{\rho(\mathbf{r}_j)}{|\mathbf{r}_i-\mathbf{r}_j|}$, which replaces the non-local Coulomb potential between electrons with a local, mean field generated by and felt by all electrons in the system[134; 135].

Exchange and Correlation

The Hartree approximation of the many-body problem can be improved with density functional theory (DFT), which introduces a correction to the Hartree potential via the non-local exchange and correlation potentials, $V_X(\mathbf{r},\mathbf{r}')$ and $V_C(\mathbf{r},\mathbf{r}')$, respectively. These account for the modification of the electronic potential due to the

antisymmetric nature of the many-body wave function and the Coulomb repulsion amongst electrons[136]. Density functional theory is however computationally demanding, scaling as N^3, where N is the size of the system. This is due to evaluation of the Hamiltonian matrix and the cost of imposing orthonormality amongst the Kohn-Sham functions (in a plane wave basis)[137]. Scaling can be improved by utilising a local orbital basis; however the increased efficiency is countered by a loss in accuracy, particularly for the unoccupied states. Furthermore, DFT simulations that use the most common approximations for the exchange-correlation functionals (LDA and GGA) underestimate the band gaps of a range of semiconductors[138], which is highly undesirable for the study of optical properties.

The electronic structure of the systems studied in the thesis are therefore treated non-self-consistently[1], using the Schrödinger equation for the valence electrons[2] in the independent-particle approximation, given by Equation (4.3).

4.2 The Tight-Binding Approximation

The tight-binding approximation provides an atomistic description of the electronic structure of solids. In the tight-binding approximation, electronic bands form from the overlap of localised atomic states, which occurs as the atoms of a solid are brought together. The electronic wave functions are therefore approximated by linear combinations of atomic orbitals[33].

Many models utilise the tight-binding approximation, ranging from first-principles models to empirical models. Any application that expands the Kohn-Sham wave functions in an orbital basis can be broadly classed as an ab initio tight-binding model. The most physically-complete models are fully self-consistent methods that

[1] The Hamiltonian is only solved once.

[2] Core electrons are sufficiently localised about the nuclei that they can be absorbed into the nuclear terms of Equation (4.1) to form ionic cores.

explicitly calculate the Hamiltonian matrix elements using atomic orbitals and the ionic potential. The local orbital code, Siesta[139], is one such example.

In contrast, we utilise an empirical tight-binding model, which treats the Hamiltonian elements as fitting parameters. This allows for an accurate reproduction of bulk properties, including the band gap, which is of utmost importance for optical calculations. Parameterisation and a small basis consequently reduce computational requirements, enabling an atomistic treatment of large systems. This makes empirical tight-binding models well-suited for the treatment of nanostructures. What follows is a formal description of the tight-binding method and the specific approximations we utilise in our empirical model.

4.3 A Secular Equation in an Orbital Basis

The following description of the tight-binding formalism is based upon the treatments of Cardona[140], Martin[141], and Chadi and Cohen[142]. An atomic orbital is defined as:

$$\phi_{\alpha,\gamma}(\mathbf{r} - \mathbf{r}_{j,\alpha}), \tag{4.4}$$

where the orbital γ is centred on atom α in the jth primitive unit cell. α spans the number of atoms per primitive unit cell and γ spans the valence orbitals of atom α. The atomic position vector, $\mathbf{r}_{j,\alpha} = \mathbf{T}_j + \mathbf{r}_\alpha$, is comprised of the position of atom α in the primitive unit cell plus a translation vector $\mathbf{T}_j$. The translational symmetry of the crystal allows one to construct Bloch functions for each atomic orbital per unit cell:

$$\Phi_{\alpha\gamma\mathbf{k}}(\mathbf{r}) = \frac{1}{\sqrt{N}} \sum_{j}^{N} e^{i\mathbf{k}\cdot\mathbf{r}_{j\alpha}} \phi_{\alpha,\gamma}(\mathbf{r} - \mathbf{r}_{j,\alpha}), \tag{4.5}$$

where N is the total number of primitive cells in the crystal. The eigenfunctions of the crystal can now be expanded as a linear combination of Bloch functions, over

all orbitals per unit cell [hence the sum runs over all (γ, α)]:

$$\Psi_{i\mathbf{k}}(\mathbf{r}) = \sum_{\gamma,\alpha}^{2N_{\text{basis}}} c_{\gamma,\alpha}(\mathbf{k})\Phi_{\alpha\gamma\mathbf{k}}(\mathbf{r}), \tag{4.6}$$

where $\mathbf{k}$ denotes the wavevector of the Bloch function and $\Psi_{i\mathbf{k}}(\mathbf{r})$ satisfies the Schrödinger equation given by Equation (4.3). In the usual manner, one multiplies the Schrödinger Equation (4.3) by the complex conjugate of one Bloch basis function and integrates over all space to obtain a secular equation:

$$\sum_{\gamma',\beta}\sum_{j'}^{N} e^{i\mathbf{k}\cdot(\mathbf{r}_{j'\beta}-\mathbf{r}_{j\alpha})}\Big[H_{\alpha\gamma,\beta\gamma'}(\mathbf{T}_{j'}) - E_{i\mathbf{k}}S_{\alpha\gamma,\beta\gamma'}(\mathbf{T}_{j'})\Big]c_{\gamma',\beta}(\mathbf{k}) = 0, \tag{4.7}$$

where $c_{\gamma',\beta}(\mathbf{k})$ are the tight-binding coefficients, and the Hamiltonian and overlap matrices are given by:

$$H_{\alpha\gamma,\beta\gamma'}(\mathbf{T}_{j'}) = \int \phi^*_{\alpha\gamma}(\mathbf{r}-\mathbf{r}_{j\alpha})H\phi_{\beta\gamma'}(\mathbf{r}-\mathbf{r}_{j'\beta})d\mathbf{r}, \tag{4.8}$$

$$S_{\alpha\gamma,\beta\gamma'}(\mathbf{T}_{j'}) = \int \phi^*_{\alpha\gamma}(\mathbf{r}-\mathbf{r}_{j\alpha})\phi_{\beta\gamma'}(\mathbf{r}-\mathbf{r}_{j'\beta})d\mathbf{r}. \tag{4.9}$$

We define the basis such that orbitals centred on different atomic sites are orthogonal, causing $S_{\alpha\gamma,\beta\gamma'}(\mathbf{T}_{j'}) = \delta_{\alpha\beta}\delta_{\gamma\gamma'}$.

4.4 The Nearest Neighbour Tight-Binding Hamiltonian

The locality of the atomic basis is expected to cause $H_{\alpha\gamma,\beta\gamma'}(\mathbf{T}_{j'})$ and $S_{\alpha\gamma,\beta\gamma'}(\mathbf{T}_{j'})$ to become negligible over several primitive unit cells[143]. In the interest of producing an efficient model with a maximally sparse Hamiltonian and the minimal number of unique matrix elements, one can restrict the Bloch summation to atoms in adjacent primitive unit cells, reducing the orbital overlap to orbitals centred on nearest neighbours. This allows the Hamiltonian to be described by a set of on-

site and nearest neighbour inter-atomic integrals: The so-called nearest neighbour approximation. In this approximation, the overlap between orbitals centred on neighbouring atoms is equivalent to the bonding in a diatomic molecule. As we shall see, this simplifies the definition of the parameters used to define the Hamiltonian matrix elements[143].

Restricting the orbital interactions to those between orbitals centred on adjacent atoms reduces the exponential summation in Equation (4.7) to:

$$\sum_{j'}^{N} e^{i\mathbf{k}\cdot(\mathbf{r}_{j'\beta}-\mathbf{r}_{j\alpha})} = [e^{i\mathbf{k}\cdot\mathbf{d}_1} + e^{i\mathbf{k}\cdot\mathbf{d}_2} + e^{i\mathbf{k}\cdot\mathbf{d}_3} + e^{i\mathbf{k}\cdot\mathbf{d}_4}], \tag{4.10}$$

where $\mathbf{d}_{1-4}$ define the displacement vectors between a central anion, α, and its four nearest neighbours in a tetrahedral configuration.

4.4.1 Hamiltonian Matrix Elements

The elements of the Hamiltonian, defined by Equation (4.8), can be split into two categories: on-site and inter-atomic. For on-site terms ($\alpha = \beta$) the energies reduce to those of isolated atoms, E_γ, in the nearest neighbour approximation. This results in $2N_{\text{basis}}$ on-site parameters, where N_{basis} is the size of the basis and the factor two reflects the need for a different set for the anion and cation.

The two-centre approximation (provided in Appendix A) results in inter-atomic overlaps between neighbouring orbitals that are equivalent to those found in a diatomic molecule, with cylindrical symmetry. The corresponding molecular orbitals are classified in terms of their azimuthal angular momentum about the axis that connects the two atomic centres, defined as $\mathbf{d} = (\mathbf{r}_\beta - \mathbf{r}_\alpha)$, and are symmetrically irreducible. In a basis containing s and p-orbitals, the corresponding molecular overlap parameters are: $V_{ss\sigma}$, $V_{sp\sigma}$, $V_{pp\sigma}$ and $V_{pp\pi}$, where σ and π denote $m = 0$ and $m = \pm 1$, respectively.

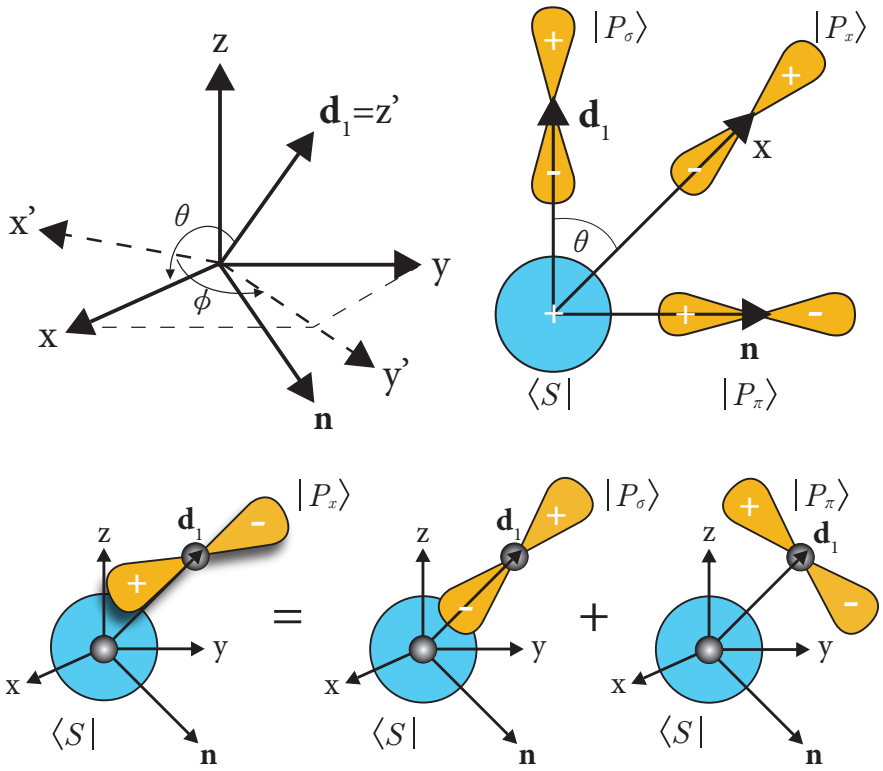

Figure 4.1: Schematic representation of the relation between the matrix element $V_{s,p_x} = \langle s|H|p_x\rangle$ defined between orbitals aligned along the (x, y, z) axes and molecular bonding orbitals aligned with respect to the displacement vector $\mathbf{d}_1$. The top diagrams shows the system coordinates and the planar projection of the orbitals whereas the bottom diagram shows V_{s,p_x} in terms of $V_{sp\sigma}$ and $V_{sp\pi}$.

The tight-binding basis is defined in terms of orbitals aligned along the Cartesian axes. A transformation is therefore required to express the inter-atomic elements in terms of molecular orbitals. This is achieved by applying rotations to the the angular component of the Cartesian orbital functions. We outline this procedure for the simplest non-trivial case of the inter-atomic element $\langle s|H|p_i\rangle$, where $i = x, y$ or z. An orbital $|p_i\rangle$ defined along one of the Cartesian axes can be written as a linear combination of p-orbitals aligned parallel and perpendicular to the $\mathbf{d}$ axis, as depicted in Figure 4.1. Formally, this is given as:

$$\begin{aligned} |p_i\rangle &= \cos(\theta)|p_d\rangle + \cos(90^\circ - \theta)|p_n\rangle, \\ &= \hat{\mathbf{e}} \cdot \hat{\mathbf{d}}|p_d\rangle + \hat{\mathbf{e}} \cdot \hat{\mathbf{n}}|p_n\rangle, \end{aligned} \tag{4.11}$$

where $\hat{\mathbf{n}}$ defines the unit vector normal to $\mathbf{d}$, $\hat{\mathbf{e}}$ defines the unit vector along the direction i and the corresponding subscripts indicate functions aligned in those directions. By definition, σ-bonded orbitals align parallel to the $\mathbf{d}$ axis and π-bonded orbitals align perpendicular to the $\mathbf{d}$ axis[140], allowing us to rewrite Equation (4.11) using molecular labelling:

$$|p_i\rangle = \hat{\mathbf{e}} \cdot \hat{\mathbf{d}}|p_\sigma\rangle + \hat{\mathbf{e}} \cdot \hat{\mathbf{n}}|p_\pi\rangle. \tag{4.12}$$

One can then directly substitute Equation (4.12) into the Hamiltonian element: $\langle s|H|p_i\rangle = \langle s_\sigma|H|[\hat{\mathbf{e}} \cdot \hat{\mathbf{d}}|p_\sigma\rangle + \hat{\mathbf{e}} \cdot \hat{\mathbf{n}}|p_\pi\rangle] = \hat{\mathbf{e}} \cdot \hat{\mathbf{d}}\langle s_\sigma|H|p_\sigma\rangle + \hat{\mathbf{e}} \cdot \hat{\mathbf{n}}\langle s_\sigma|H|p_\pi\rangle$. Finally, only elements with $m = m'$ are non-zero (see Appendix A), causing the second term to disappear. One is left with:

$$\langle s|H|p_i\rangle = \hat{\mathbf{e}} \cdot \hat{\mathbf{d}}\langle s_\sigma|H|p_\sigma\rangle = \hat{\mathbf{e}} \cdot \hat{\mathbf{d}}V_{sp\sigma}. \tag{4.13}$$

Upon substitution of the displacement vector, $\mathbf{d}_1$, and the tetrahedral bond length, $|\mathbf{d}| = \sqrt{3}a_l/4$, one obtains the tight-binding Hamiltonian elements in terms of the molecular orbital elements (4.14)-(4.17):

$$\langle s|H|s\rangle = V_{ss} \equiv V_{ss\sigma}, \tag{4.14}$$

$$\langle s|H|p_i\rangle = V_{sx} \equiv \frac{1}{\sqrt{3}}V_{sp\sigma}, \tag{4.15}$$

$$\langle p_i|H|p_i\rangle = V_{xx} \equiv \frac{1}{3}V_{pp\sigma} + \frac{2}{3}V_{pp\pi}, \tag{4.16}$$

$$\langle p_i|H|p_j\rangle = V_{xy} \equiv \frac{1}{3}V_{pp\sigma} - \frac{1}{3}V_{pp\pi}, \tag{4.17}$$

where the Hamiltonian elements between p-orbitals have been derived in the same manner as the element given by Equation (4.13) and the remaining Hamiltonian elements are obtained through symmetry considerations. The tight-binding Hamiltonian elements (4.14) to (4.17) are subsequently defined as parameters, which are found by fitting to bulk band structures. Finally we note that Equations (4.14)-

(4.17) are commonly quoted in terms of directional cosines, which are presented in Appendix A for completeness. The nearest neighbour, tight-binding Hamiltonian for the primitive unit cell of a zincblende semiconductor in the sp^3s^* basis therefore reads:

$$H = \begin{pmatrix} H_{aa} & H_{ac} \\ H_{ca} & H_{cc} \end{pmatrix}, \tag{4.18}$$

where a denotes anion and c denotes cation. The on-site sub-matrices are equal to:

$$H_{bb} = \left(\begin{array}{c|ccccc} & s,b & p_x,b & p_y,b & p_z,b & s^*,b \\ \hline s,b & E_s & 0 & 0 & 0 & 0 \\ p_x,b & 0 & E_p & 0 & 0 & 0 \\ p_y,b & 0 & 0 & E_p & 0 & 0 \\ p_z,b & 0 & 0 & 0 & E_p & 0 \\ s^*,b & 0 & 0 & 0 & 0 & E_{s^*} \end{array}\right), \tag{4.19}$$

where $b = a$ or c, and the inter-atomic sub-matrix is:

$$H_{ac} = \left(\begin{array}{c|ccccc} & s,c & p_x,c & p_y,c & p_z,c & s^*,c \\ \hline s,a & V_{ss}g_1 & V_{sp}g_2 & V_{sp}g_3 & V_{sp}g_4 & 0 \\ p_x,a & -V_{ps}g_2 & V_{xx}g_1 & V_{xy}g_4 & V_{xy}g_3 & -V_{ps^*}g_2 \\ p_y,a & -V_{ps}g_3 & V_{xy}g_4 & V_{xx}g_1 & V_{xy}g_2 & -V_{ps^*}g_3 \\ p_z,a & -V_{ps}g_4 & V_{xy}g_3 & V_{xy}g_2 & V_{xx}g_1 & -V_{ps^*}g_4 \\ s^*,a & 0 & V_{s^*p}g_2 & V_{s^*p}g_3 & V_{s^*p}g_4 & 0 \end{array}\right). \tag{4.20}$$

Using the Hermitian symmetry of the system, the other inter-atomic sub-matrix, H_{ca}, is given by the relation, $H_{ca} = H_{ac}^{\dagger}$. The $g_i(\mathbf{k})$ values in Equation (4.20) define a set of four phase factors that arise from the summation of the exponentials

in Equation (4.10):

$$g_1 = \frac{1}{4}[e^{i\mathbf{k}\cdot\mathbf{d}_1} + e^{i\mathbf{k}\cdot\mathbf{d}_2} + e^{i\mathbf{k}\cdot\mathbf{d}_3} + e^{i\mathbf{k}\cdot\mathbf{d}_4}], \tag{4.21}$$

$$g_2 = \frac{1}{4}[e^{i\mathbf{k}\cdot\mathbf{d}_1} + e^{i\mathbf{k}\cdot\mathbf{d}_2} - e^{i\mathbf{k}\cdot\mathbf{d}_3} - e^{i\mathbf{k}\cdot\mathbf{d}_4}], \tag{4.22}$$

$$g_3 = \frac{1}{4}[e^{i\mathbf{k}\cdot\mathbf{d}_1} - e^{i\mathbf{k}\cdot\mathbf{d}_2} + e^{i\mathbf{k}\cdot\mathbf{d}_3} - e^{i\mathbf{k}\cdot\mathbf{d}_4}], \tag{4.23}$$

$$g_4 = \frac{1}{4}[e^{i\mathbf{k}\cdot\mathbf{d}_1} - e^{i\mathbf{k}\cdot\mathbf{d}_2} - e^{i\mathbf{k}\cdot\mathbf{d}_3} + e^{i\mathbf{k}\cdot\mathbf{d}_4}]. \tag{4.24}$$

The signs of the exponential phase factors correspond to the specific position of the neighbouring cation relative to the central anion and arise from the positive and negative lobes of the bonding orbitals centred at the two sites. All of the tight-binding inter-atomic parameters, given by Equations (4.14)-(4.17), have been defined with respect to the bonding between the central anion and neighbouring cation at displacement vector $\mathbf{d}_1$. The appropriate phases of the remaining three interactions are then related to $\langle\phi_{\gamma'}(\mathbf{r}-\mathbf{r}_\alpha)|H|\phi_\gamma(\mathbf{r}-\mathbf{d}_1)\rangle$ by symmetry. An example is provided in Appendix A.

This concludes a complete description of the nearest neighbour sp^3s^* empirical tight-binding model. The secular Equation (4.7), defined by the Hamiltonian given in Equations (4.18) - (4.24), can be solved for finite systems containing thousands of atoms, generating eigenstates that contain atomistic detail and retain the underlying symmetry of the crystal structure. The use of this minimal model therefore provides us with the eigenvalues and eigenvectors necessary to compute the two-point and four-point polarisabilities of direct-gap nanostructures, in the cheapest manner possible. In the final section of this chapter we shall present the formalism with which one can compute independent-particle, inter-band transitions in an atomic orbital basis.

4.5 Independent-Particle Transitions

In the electric dipole approximation, the momentum of the photon is treated as negligible such that the electric field can be written as $\mathbf{E}(t) = \mathrm{Re}[\mathbf{E}_0 e^{-i\omega t}]$, where $\mathbf{E}_0$ is the electric field amplitude and ω is the frequency. This assumes that the electric field is uniform with respect to the length scale of the electronic states. The linear polarisability of the system in response to a real, uniform, external potential, $U(\mathbf{r}, t) = e\mathbf{E}_0 \cdot \mathbf{r}\cos(\omega t)$, is therefore given as (in SI units)[133]:

$$\alpha(\omega) = \frac{e^2}{\hbar} \sum_{v,c} |\langle v|\hat{\mathbf{e}} \cdot \mathbf{r}|c\rangle|^2 \left[\frac{1}{\omega_{vc} + \omega + i\gamma} + \frac{1}{\omega_{vc} - \omega - i\gamma} \right], \tag{4.25}$$

where $\mathbf{r}$ is the position vector, $\hat{\mathbf{e}}$ is the polarisation vector, e is the charge of an electron, $\omega_{vc} = (E_c - E_v)/\hbar$ is the interband transition frequency from a valence state, v, to a conduction state, c, and γ is the spontaneous decay rate of the excited conduction state. For absorption in finite systems, one is interested in the imaginary part of the polarisability:

$$\alpha_2(\omega) = \frac{\pi e^2}{\hbar\omega} \sum_{v,c} \omega_{vc} |\langle v|\hat{\mathbf{e}} \cdot \mathbf{r}|c\rangle|^2 \delta(\omega_{vc} - \omega), \tag{4.26}$$

which can be defined in terms of a dimensionless quantity f_{vc}, referred to as the oscillator strength:

$$f_{vc} = \frac{2m_e}{\hbar} \omega_{vc} |\langle v|\hat{\mathbf{e}} \cdot \mathbf{r}|c\rangle|^2, \tag{4.27}$$

such that the imaginary part of the polarisability is given as:

$$\alpha_2(\omega) = \frac{\pi e^2}{2\omega m_e} \sum_{v,c} f_{vc} \delta(\omega_{vc} - \omega). \tag{4.28}$$

The imaginary part of the polarisability is directly proportional to the absorption cross-section of the system, which defines the effective area of the system that

absorbs incident energy:

$$\sigma(\omega) = \frac{\omega}{\epsilon_0 c}\alpha_2(\omega), \tag{4.29}$$

where ϵ_0 is the static dielectric constant and c is the speed of light. The imaginary part of the linear polarisability is therefore used to describe the optical absorption spectra of finite systems in the electric dipole approximation.

4.5.1 Independent-Particle Transitions in an Orbital Basis

The independent-particle valence and conduction states can be expanded in the atomic orbital basis given by Equation (4.4). In bra-ket notation, one can rewrite expression (4.6) as:

$$|\Psi_i\rangle = \sum_{\alpha,\gamma}^{N} c_{i;(\alpha,\gamma)}|\alpha,\gamma\rangle, \tag{4.30}$$

where i is the independent-particle state index, α is the atomic index and γ is the local index of orbitals centred on atom α. The tight-binding coefficients are denoted as $c_{i;(\alpha,\gamma)}$ and the atomic orbitals are expressed as $\langle \mathbf{r}|\alpha,\gamma\rangle = \phi_\gamma(\mathbf{r}-\mathbf{r}_\alpha)$. Expanding the dipole matrix elements in the orbital basis gives:

$$\langle c|\hat{\mathbf{e}}\cdot\mathbf{r}|v\rangle = \sum_{(\alpha,\gamma),(\beta,\gamma')}^{N^2} c^*_{c;(\beta,\gamma')}c_{v;(\alpha,\gamma)}\langle\beta,\gamma'|\hat{\mathbf{e}}\cdot\mathbf{r}|\alpha,\gamma\rangle, \tag{4.31}$$

where:

$$\langle\beta,\gamma'|\hat{\mathbf{e}}\cdot\mathbf{r}|\alpha,\gamma\rangle = \int \phi^*_{\gamma'}(\mathbf{r}-\mathbf{r}_\beta)\hat{\mathbf{e}}\cdot\mathbf{r}\phi_\gamma(\mathbf{r}-\mathbf{r}_\alpha)\mathrm{d}\mathbf{r}, \tag{4.32}$$

is a dipole matrix element in the orbital basis, which describes transitions between orbitals γ and γ', centred on atoms α and β, respectively. In a local orbital basis with limited radial extent, it is useful to decompose the dipole operator into the sum of a position vector centred on a given atom, $\mathbf{r}_\alpha$, and a position vector relative to that atomic centre, $\mathbf{r}-\mathbf{r}_\alpha$. This allows the dipole matrix in the orbital basis, expression (4.32), to be decomposed into on-site and inter-atomic contributions, analogous to

the description of the tight-binding Hamiltonian[126; 144; 145]:

$$\begin{aligned}\langle\beta,\gamma'|\hat{\mathbf{e}}\cdot\mathbf{r}|\alpha,\gamma\rangle &= \langle\beta,\gamma'|\hat{\mathbf{e}}\cdot[\mathbf{r}_\alpha+(\mathbf{r}-\mathbf{r}_\alpha)]|\alpha,\gamma\rangle,\\ &= \langle\beta,\gamma'|\hat{\mathbf{e}}\cdot\mathbf{r}_\alpha|\alpha,\gamma\rangle+\langle\beta,\gamma'|\hat{\mathbf{e}}\cdot(\mathbf{r}-\mathbf{r}_\alpha)|\alpha,\gamma\rangle,\\ &= (\hat{\mathbf{e}}\cdot\mathbf{r}_\alpha)\delta_{(\alpha\beta)}\delta_{(\gamma\gamma')}+\langle\beta,\gamma'|\hat{\mathbf{e}}\cdot(\mathbf{r}-\mathbf{r}_\alpha)|\alpha,\gamma\rangle,\end{aligned} \tag{4.33}$$

where $(\hat{\mathbf{e}}\cdot\mathbf{r}_\alpha)$ is constant, allowing it to be moved outside of the corresponding integral, and $\delta_{(\alpha\beta)}\delta_{(\gamma\gamma')}=\langle\beta,\gamma'|\alpha,\gamma\rangle$ due to the orthogonality of the orbital basis. The independent-particle dipole matrix elements in an atomic orbital basis are therefore defined as:

$$\langle\beta\gamma'|\hat{\mathbf{e}}\cdot\mathbf{r}|\alpha\gamma\rangle=\sum_{\alpha,\gamma,\beta,\gamma'}c^*_{c;(\beta,\gamma)}c_{v;(\alpha,\gamma')}\Big[\hat{\mathbf{e}}\cdot\mathbf{r}_\alpha\delta_{(\alpha\beta)}\delta_{(\gamma\gamma')}+\langle\beta,\gamma'|\hat{\mathbf{e}}\cdot(\mathbf{r}-\mathbf{r}_\alpha)|\alpha,\gamma\rangle\Big]. \tag{4.34}$$

The first term in Equation (4.34) is the contribution to the dipole matrix elements from the tight-binding coefficients weighted by the position of the corresponding atomic site, whereas the second term in the brackets contains matrix elements between the operator $\mathbf{r}-\mathbf{r}_\alpha$ and the atomic orbitals. The two terms therefore correspond to contributions to the absorption spectrum from the global envelope of the wave function and the local variation of the atomic orbitals, respectively.

4.6 Summary

In summary, we have presented a tight-binding description of the valence electrons in tetrahedral, zincblende semiconductors. From a general formulation of the secular problem in an orbital basis, we have proceeded to make several approximations, leading to a minimal, nearest neighbour Hamiltonian. The nearest neighbour Hamiltonian in the sp^3s^* basis is given, along with the tight-binding parameters and periodic phase factors. These comprise all of the ingredients required to begin tight-

binding calculations. Finally, we have shown how one can use the eigenvalues and coefficients found by solving the tight-binding model to compute the independent-particle polarisability, the first step in describing absorption in finite systems. The following chapter extends on the optical theory presented here by introducing the Bethe-Salpeter equation as a means of describing two-body excitations in optical absorption spectroscopy.

Chapter 5

Many-Body Excitations

We begin by making the connection between linear response functions and optical absorption spectroscopy. The Bethe-Salpeter equation is presented as a response function containing electron-hole correlation and its connection to experimentally measurable quantities is shown. We present an expansion of the Bethe-Salpeter equation in a two-particle basis of independent-particle state products and show how it can be rewritten as an effective eigenvalue problem. Finally, we show how one can directly solve the Bethe-Salpeter equation for the first order change in the charge density and therefore efficiently compute the absorption cross-section of finite systems.

5.1 Spectroscopic Response Functions and The Bethe-Salpeter Equation

To first order, the change in the charge density in response to a local, time-dependent, external potential $U(2)$ is[37; 55]:

$$\delta\rho(1) = \int d2\ \chi(1,2)U(2), \tag{5.1}$$

where $\chi(1,2) = \chi(\mathbf{r}_1, \mathbf{r}_2, t_1 - t_2)$ defines the reducible polarisability[1] of the system:

$$\chi(1,2) = \frac{\delta\rho(1)}{\delta U(2)}. \tag{5.2}$$

Here, we have introduced the compact notation $1 = (\mathbf{r}_1, t_1)$, such that the spatial and temporal variables are encapsulated in the composite variable 1. More generally, the reducible polarisability can be regarded as a response function which contains information about how the electrons and holes behave in response to an external potential. For finite systems, the reducible polarisability yields the dynamical, linear polarisability tensor[55]:

$$\alpha_{ij}(\omega) = -\int U_i(1)\chi(1,2)U_j(2)d12, \tag{5.3}$$

where $i = (x, y, z)$ corresponds to the respective component of the external potential and ω is the photon frequency. Substituting for Equation (5.1) in Equation (5.3) and taking the imaginary part of the dynamical polarisability tensor, one obtains the photoabsorption cross-section:

$$\sigma_{ij}(\omega) = \frac{4\pi\omega}{c}\mathrm{Im}\Big[\alpha_{ij}(\omega)\Big], \tag{5.4}$$

[1] Reducible quantities are derivatives with respect to the external potential, whereas irreducible quantities are derivatives with respect to the total potential of the system (external potential plus the induced potential). Furthermore, $t_1 > t_2$ due to causality requirements.

where c is the speed of light. This defines the absorption spectrum of finite systems in the independent-particle approximation. Experimental absorption spectroscopy however, measures neutral excitations which are intrinsically two-body in nature due to the Coulomb attraction between the electron and hole. In order to treat excitonic correlation, we must therefore consider a different response function which accounts for electron-hole interaction:

$$L(1,2,3,4) = L_0(1,2,3,4) + \int d5678 L_0(1,2,5,6)K(5,6,7,8)L(7,8,3,4). \quad (5.5)$$

Equation (5.5) is the Bethe-Salpeter equation[38; 146] (BSE), a four-point response function that contains excitonic correlation. In Equation (5.5), $L_0(1,2,3,4)$ defines the motion of the independent electron and hole, whereas the second term contains an interaction kernel that mixes the formerly independent transitions. The interaction kernel, $K(1,2,3,4)$ in Equation (5.5), is defined as (see Appendix B for the derivation):

$$K(1,2,3,4) = v(1,3)\delta(1-2)\delta(3-4) - W(1,2)\delta(2-4)\delta(1-3), \quad (5.6)$$

where $v(1,3) = 1/|\mathbf{r}_1 - \mathbf{r}_3|\delta(t_1 - t_3)$ is the repulsive bare Coulomb interaction and $W(1,2) = \int v(\mathbf{r}_1, \mathbf{r}_3)\epsilon^{-1}(\mathbf{r}_3, \mathbf{r}_2, \omega)d\mathbf{r}_3$ is the attractive screened Coulomb interaction[147; 148]. The first and second terms of the kernel are referred to as the unscreened exchange term and the direct Coulomb term, respectively.

The Bethe-Salpeter Equation (5.5) shows that the initial response of the system to an external perturbation is the creation of an independent electron-hole pair, described by L_0. The propagation of the electron induces a change in the density which in turn generates an induced potential. The induced potential then self-consistently modifies the total potential of the system through the interaction kernel K, which couples the independent electron and hole, leading to either a renormalisation of independent-particle state energies or the creation of a bound excitonic state.

5.1.1 Connection to Experiment

Equation (5.5) describes the response of the system to an external potential and is therefore the two-particle analog of the reducible polarisability given by Equation (5.2). The two-point reducible polarisability $\chi(1,2)$ is therefore equivalent to a two-point contraction of $L(1,2,3,4)$[149]:

$$\chi(1,2) = L(1,1^+,2,2^+), \tag{5.7}$$

where $t_1^+ = t_1 + \delta$ and δ is an infinitesimal time increment, such that time ordering is preserved. Substituting Equation (5.7) into Equation (5.2) gives:

$$L(1,1^+,2,2^+) = \frac{\delta\rho(1,1^+)}{\delta U(2,2^+)}. \tag{5.8}$$

Unfortunately $L(1,1^+,2,2^+)$ cannot be written purely as a two-point quantity, $L(1,2)$, due to the arguments of the delta functions in the kernel given by Equation (5.6). We are therefore always required to solve a four-point equation.

5.2 Solving the Bethe-Salpeter Equation

In order to solve the Bethe-Salpeter equation one is required to project $L(1,2,3,4)$ onto the subspace of a given basis set. The physical picture of interacting electron-hole pairs suggests that it would be appropriate to expand the BSE in a two-particle basis constructed from pairs of independent-particle functions[2][150].

In general, any four-point function $S(1,2,3,4)$ can be expanded as[55; 151]:

$$S(\mathbf{r}_1,\mathbf{r}_2;\mathbf{r}_3,\mathbf{r}_4) = \sum_{n_1,n_2,n_3,n_4} \psi^*_{n_1}(\mathbf{r}_1)\psi_{n_2}(\mathbf{r}_2)\psi_{n_3}(\mathbf{r}_3)\psi^*_{n_4}(\mathbf{r}_4)S_{(n_1n_2)(n_3n_4)}, \tag{5.9}$$

[2]This assumes that four-particle and higher processes can be neglected in the formation of the excitation.

where:

$$S_{(n_1n_2)(n_3n_4)} = \langle n_1n_2|S(\mathbf{r}_1,\mathbf{r}_2;\mathbf{r}_3,\mathbf{r}_4)|n_3n_4\rangle, \tag{5.10}$$

defines the matrix elements of the function $S(\mathbf{r}_1,\mathbf{r}_2;\mathbf{r}_3,\mathbf{r}_4)$, expanded in a basis of pair-product states :

$$|n_1n_2\rangle = \psi^*_{n_1}(\mathbf{r}_1)\psi_{n_2}(\mathbf{r}_2). \tag{5.11}$$

Here, $\psi_{n_i}(\mathbf{r}_i)$ is an independent-particle state defined by the state index n_i and the spatial variable $\mathbf{r}_i$. These functions are supposed to form an orthonormal and complete set, although in practise, it is expected that only a limited number of electron-hole pairs will contribute to each excitation, and as such the basis size is treated as a convergence parameter[148]. To simplify matters, we can make the approximation that L depends only on the time differences $(t_2 - t_1)$ and $(t_4 - t_3)$. This enables the use of a Fourier transform to frequency space, such that L becomes a function of energy and the variables $1-4$ now relate to position only, $L \rightarrow L(1,2,3,4;\omega)$[148; 152].

Projecting L in the two-particle basis defined by Equation (5.11) gives:

$$L(1,2,3,4) = \sum_{n_1,n_2,n_3,n_4} \psi^*_{n_1}(\mathbf{r}_1)\psi_{n_2}(\mathbf{r}_2)\psi_{n_3}(\mathbf{r}_3)\psi^*_{n_4}(\mathbf{r}_4)L_{(n_1n_2)(n_3n_4)}. \tag{5.12}$$

The Bethe-Salpeter Equation (5.5) in transition space is therefore:

$$L_{(n_1n_2)(n_3n_4)} = L^0_{(n_1n_2)(n_3n_4)} + L^0_{(n_1n_2)(n_5n_6)}K_{(n_5n_6)(n_7n_8)}L_{(n_7n_8)(n_3n_4)}. \tag{5.13}$$

Rearranging Equation (5.13) such that L only appears on the left-hand side, one has:

$$L_{(n_1n_2)(n_3n_4)} = \left[\delta_{m_1,m_3}\delta_{m_2,m_4} - L^0_{(m_1m_2)(m_5m_6)}K_{(m_5m_6)(m_3m_4)}\right]^{-1} L^0_{(n_1n_2)(n_3n_4)}, \tag{5.14}$$

where the terms in the brackets collectively define the matrix:

$$\Pi_{(n_1n_2)(n_3n_4)} = \left[\delta_{m_1,m_3}\delta_{m_2,m_4} - L^0_{(m_1m_2)(m_5m_6)}K_{(m_5m_6)(m_3m_4)}\right]^{-1}_{(n_1n_2)(n_3n_4)}, \quad (5.15)$$

and m_i define a set of state indices. The four-point independent-particle polarisability is defined as[55]:

$$L^0(\mathbf{r}_1,\mathbf{r}_2,\mathbf{r}_3,\mathbf{r}_4) = \sum_{n_1,n_2}\frac{(f_{n_2}-f_{n_1})\psi^*_{n_1}(\mathbf{r}_1)\psi_{n_2}(\mathbf{r}_2)\psi_{n_1}(\mathbf{r}_3)\psi^*_{n_2}(\mathbf{r}_4)}{(E_{n_2}-E_{n_1}-\omega)}, \quad (5.16)$$

where f_{n_i} are occupation numbers, E_{n_i} are independent-particle eigenvalues and ω is the energy of the photon. Orthonormality of the basis means $L^0(\mathbf{r}_1,\mathbf{r}_2,\mathbf{r}_3,\mathbf{r}_4)$ is diagonal in transition space and reads:

$$L^0_{(n_1n_2)(n_3n_4)} = \frac{(f_{n_2}-f_{n_1})\delta_{n_1n_3}\delta_{n_2n_4}}{(E_{n_2}-E_{n_1}-\omega)}. \quad (5.17)$$

Substituting for $L^0_{(m_1m_2)(m_5m_6)}$ in Π using the definition given by Equation (5.17) and factorising the transition energy $(E_{m_2}-E_{m_1}-\omega)$, one obtains:

$$\Pi_{(n_1n_2)(n_3n_4)} = \left[\delta_{m_1m_3}\delta_{m_2m_4} - \frac{(f_{m_2}-f_{m_1})K_{(m_1m_2)(m_3m_4)}}{E_{m_2}-E_{m_1}-\omega}\right]^{-1}_{(n_1n_2)(n_3n_4)}, \quad (5.18)$$

$$\Pi_{(n_1n_2)(n_3n_4)} = \Bigg[(E_{m_2}-E_{m_1}-\omega)\delta_{m_1m_3}\delta_{m_2m_4} + (f_{m_1}-f_{m_2})K_{(m_1m_2)(m_3m_4)}\Bigg]^{-1}_{(n_1n_2)(n_3n_4)}(E_{n_2}-E_{n_1}-\omega), \quad (5.19)$$

such that the Bethe-Salpeter equation in transition space finally reads:

$$L_{(n_1n_2)(n_3n_4)} = \Pi L^0_{(n_1n_2)(n_3n_4)}. \quad (5.20)$$

It is now possible in principle, to directly solve Equation (5.20) for a set of discrete

frequencies $\{\omega_i\}$, however this requires the inversion of the interaction kernel at each frequency point in order to compute Π and therefore L. Hanke and Sham solved the BSE in this way using a localised orbital basis[153; 154] but matrix inversion quickly becomes too expensive for realistic systems. Fortunately, Equation (5.20) can be reformulated as an effective eigenvalue problem[155].

5.2.1 An Effective Two-Particle Hamiltonian

Defining an effective two-particle Hamiltonian[155]:

$$H^{2p}_{(m_1m_2)(m_3m_4)} \equiv (E_{m_2} - E_{m_1})\delta_{(m_1,m_3)}\delta_{(m_2,m_4)} + (f_{m_1} - f_{m_2})K_{(m_1m_2)(m_3m_4)}, \quad (5.21)$$

allows the matrix Equation (5.19) to be rewritten as:

$$\Pi_{(n_1n_2)(n_3n_4)} = \Big[H^{2p} - I\omega\Big]^{-1}_{(n_1n_2)(n_3n_4)} (E_{n_2} - E_{n_1} - \omega), \quad (5.22)$$

where I is the identity matrix. Furthermore, the transition energy multiplied by the independent-particle polarisability can be shown to reduce to the difference in occupation numbers:

$$\begin{aligned}(E_{n_2} - E_{n_1} - \omega)L^0_{(n_1n_2)(n_3n_4)} =& \frac{(E_{n_2} - E_{n_1})(f_{n_2} - f_{n_1})\delta_{(n_1,n_3)}\delta_{(n_2,n_4)}}{E_{n_2} - E_{n_1}}, \\ =& (f_{n_4} - f_{n_3}), \end{aligned} \quad (5.23)$$

such that the Bethe-Salpeter in transition space can be rewritten as:

$$\begin{aligned} L_{(n_1n_2)(n_3n_4)} &= \Pi_{(n_1n_2)(n_3n_4)}L^0_{(n_1n_2)(n_3n_4)}, \\ &\equiv [H^{2p} - I\omega]^{-1}_{(n_1n_2)(n_3n_4)}(f_{n4} - f_{n_3}). \end{aligned} \quad (5.24)$$

The effective, two-particle Hamiltonian is given explicitly as:

$$H^{2p}_{(n_1n_2)(n_3n_4)} =$$

$$\left(\begin{array}{c|cccc} {\scriptstyle (n_3n_4)\rightarrow \atop (n_1n_2)\downarrow} & \{v'c'\} & \{c'v'\} & \{v'\tilde{v}'\} & \{c'\tilde{c}'\} \\ \hline \{vc\} & H^{2p,res}_{(vc)(v'c')} & K_{(vc)(c'v')} & K_{(vc)(v'\tilde{v}')} & K_{(vc)(c'\tilde{c}')} \\ \{cv\} & -K_{(cv)(v'c')} & H^{2p,ares}_{(cv)(c'v')} & -K_{(cv)(v'\tilde{v}')} & -K_{(cv)(c'\tilde{c}')} \\ \{v\tilde{v}\} & 0 & 0 & (E_{\tilde{v}} - E_v)\delta_{(vv')(\tilde{v}\tilde{v}')} & 0 \\ \{c\tilde{c}\} & 0 & 0 & 0 & (E_{\tilde{c}} - E_c)\delta_{(cc')(\tilde{c}\tilde{c}')} \end{array}\right) \tag{5.25}$$

where $(v, v', \tilde{v}')$ and $(c, c', \tilde{c}')$ are indices for valence (occupied) and conduction (unoccupied) states, respectively. Here, we take $f_v = 1$ and $f_c = 0$ in Equation (5.21). The sub-blocks are defined by the resonant and the anti-resonant matrix two-particle Hamiltonians:

$$H^{2p,res}_{(vc)(v'c')} = (E_c - E_v)\delta_{vv'}\delta_{cc'} + K_{(vc)(v'c')}, \tag{5.26}$$

$$H^{2p,ares}_{(cv)(c'v')} = (E_v - E_c)\delta_{vv'}\delta_{cc'} - K_{(cv)(c'v')}, \tag{5.27}$$

and the coupling matrices, which are defined by the interaction kernel in the transition space as:

$$\begin{aligned} K_{(n_1n_2)(n_3n_4)} = 2 &\int \psi_{n_1}(\mathbf{r}_1)\psi^*_{n_2}(\mathbf{r}_1)v(1,3)\psi^*_{n_3}(\mathbf{r}_3)\psi_{n_4}(\mathbf{r}_3)d\mathbf{r}_1 d\mathbf{r}_3 \\ &- \int \psi_{n_1}(\mathbf{r}_1)\psi^*_{n_2}(\mathbf{r}_2)W(1,2)\psi^*_{n_3}(\mathbf{r}_1)\psi_{n_4}(\mathbf{r}_2)d\mathbf{r}_1 d\mathbf{r}_2. \end{aligned} \tag{5.28}$$

Here, (n_1, n_2) can take the following permutations of hole, v, and electron c indices: $(v, c), (c, v), (v, \tilde{v}), (c, \tilde{c})$.

The occupation numbers $(f_{n4} - f_{n_3})$ in Equation (5.24) mean that only elements where $n_3 \neq n_4$ will give non-zero contributions to the two-particle excitations. This corresponds to the first two columns of H_{2p}, where $(n_3, n_4) = (v'c'), (c'v')$, removing the hole-hole and electron-electron transitions. One is therefore left with inter-band transitions between electron and hole states:

$$H^{2p}_{(n_1n_2)(n_3n_4)} = \left(\begin{array}{c|cc} \substack{(n_3n_4)\rightarrow \\ (n_1n_2)\downarrow} & \{v'c'\} & \{c'v'\} \\ \hline \{vc\} & H^{2p,res}_{(vc)(v'c')} & K_{(vc)(c'v')} \\ \{cv\} & -\Big[K_{(vc)(c'v')}\Big]^* & -\Big[H^{2p,res}_{(vc)(v'c')}\Big]^* \end{array}\right), \tag{5.29}$$

where one has utilised the symmetry relations:

$$K_{(cv)(v'c')} = \Big[K_{(vc)(c'v')}\Big]^*, \tag{5.30}$$

$$H^{2p,ares}_{(cv)(c'v')} \equiv -\Big[H^{2p,res}_{(vc)(v'c')}\Big]^*, \tag{5.31}$$

to reduce the number of unique elements in the Hamiltonian. The resonant and anti-resonant terms, $H^{2p,res}_{(vc)(v'c')}$ and $-\Big[H^{2p,res}_{(vc)(v'c')}\Big]^*$, describe vertical transitions at positive and negative frequencies, respectively, whereas the interaction kernels that occupy the off-diagonal blocks act to mix positive and negative frequency transitions. A common approximation applied to the Hamiltonian, Equation (5.29), is the Tamm-Dancoff approximation. In this instance, one neglects the coupling terms resulting in $H^{2p}_{(n_1n_2)(n_3n_4)} = H^{2p,res}_{(vc)(v'c')}$ [156; 157]. This reduces the dimensions of Equation (5.29) by a factor 2 and results in a two-particle Hamiltonian with Hermitian symmetry.

5.2.2 The Interaction Kernel

The interaction kernel Equation (5.28) in the two-particle basis, $|vc\rangle$, is defined as $K_{(vc)(v'c')} = 2v_{(vc)(v'c')} - W_{(vc)(v'c')}$, with:

$$v_{(vc)(v'c')} = \int d\mathbf{r}_1 d\mathbf{r}_3 \psi_v(\mathbf{r}_1)\psi_c^*(\mathbf{r}_1)\frac{1}{|\mathbf{r}_1 - \mathbf{r}_3|}\psi_{v'}^*(\mathbf{r}_3)\psi_{c'}(\mathbf{r}_3), \tag{5.32}$$

and

$$W_{(vc)(v'c')} = \int d\mathbf{r}_1 d\mathbf{r}_2 \psi_v(\mathbf{r}_1)\psi_{v'}^*(\mathbf{r}_1)W(\mathbf{r}_1, \mathbf{r}_2, \omega)\psi_c^*(\mathbf{r}_2)\psi_{c'}(\mathbf{r}_2). \tag{5.33}$$

In Equation (5.33), the screened Coulomb potential is taken in the static approximation (no frequency-dependence):

$$W(\mathbf{r}_1, \mathbf{r}_2, \omega = 0) = \int d\mathbf{r}_3 \, \frac{1}{|\mathbf{r}_1 - \mathbf{r}_3|}\epsilon^{-1}(\mathbf{r}_3, \mathbf{r}_2, \omega = 0), \tag{5.34}$$

which is reasonable when the excitonic binding energies are smaller than the plasmon energies[150], or equivalently when the electron-hole scattering time is much longer than the characteristic screening time of the system. This approximation has been shown to be reasonable in simple semiconductors[158] and avoids the need to treat the calculation of Equation (5.24) self-consistently.

5.2.3 An Effective Two-Particle Eigenvalue Problem

Having constructed an effective two-particle Hamiltonian given by Equation (5.29), one is able to find its eigenvalues and eigenvectors as solutions of the effective eigenvalue problem:

$$H^{2p}_{(n_1n_2)(n_3n_4)}A_\lambda^{(n_3n_4)} = E_\lambda^{exc}A_\lambda^{(n_1n_2)}, \tag{5.35}$$

which can be solved using methods such as conjugate gradient, Arnoldi/Lanczos or Davidson-Jacobi[159] algorithms. The spectral representation of the excitonic Hamiltonian therefore replaces the problem of inverting a matrix at each frequency

with solving a linear set of equations once, for all frequencies. The two-particle coefficients, $\{A_\lambda\}$, and excitations, $\{E^{exc}_\lambda\}$, are not only solutions of Equation (5.35) but also of the Bethe-Salpeter equation in transition space (5.13).

The effective two-particle Hamiltonian therefore re-expresses the problem in terms of the mixing of different independent-particle transitions between the valence and conduction states of the one-particle Hamiltonian. This causes the resulting excitonic energies, E^{exc}_λ, to differ from the independent-particle transition energies $E_{n_2} - E_{n_1}$, with the mixing information contained within the two-particle coefficients A_λ. In a similar manner, we follow the alternative approach of Hübener[160] in which one solves a set of coupled linear equations of the general form:

$$[\mathbf{A} - \omega\mathbf{I}]\mathbf{x} = \mathbf{b}, \tag{5.36}$$

where $\mathbf{A} = H^{2p}$ is the two-particle Hamiltonian defined by Equation (5.29), $\mathbf{x} = \delta\rho$ is the change in the charge density given by Equation (5.1) and $\mathbf{b} = U$ is the external potential. Substituting for $\mathbf{A}$, $\mathbf{x}$ and $\mathbf{b}$ in Equation (5.36) leads to the explicit expression:

$$\left[\begin{pmatrix} H^{2p,res}_{(vc)(v'c')} & K_{(vc)(c'v')} \\ -\left[K_{(vc)(c'v')}\right]^* & -\left[H^{2p,res}_{(vc)(v'c')}\right]^* \end{pmatrix} - \omega \begin{pmatrix} \mathbf{1} & 0 \\ 0 & -\mathbf{1} \end{pmatrix}\right] \begin{pmatrix} \delta\rho^+ \\ \delta\rho^- \end{pmatrix} = \begin{pmatrix} - & \delta U \\ & \delta U \end{pmatrix}. \tag{5.37}$$

The unknown quantity in Equation (5.37) is the density response. As such, Equation (5.37) can be solved for $\delta\rho$ using iterative schemes, such as the conjugate gradient method. We favour this approach over that of solving an effective eigenvalue problem, as the solution to Equation (5.37) provides the quantity, $\delta\rho$, from which we can immediately and cheaply compute the two-particle absorption spectrum via Equations (5.1)-(5.3).

In the transition space, the dynamic polarisability tensor can be rewritten as:

$$\alpha_{ij}(\omega_k) = -U_k \cdot \delta\rho_k \tag{5.38}$$

where the index k corresponds to the transition frequency between the valence state v and the conduction state c. In the instance that the nanostructures of interest are randomly orientated, we compute the trace of the dynamic polarisability tensor:

$$\alpha_{\exp}(\omega_k) = \frac{1}{3}\Big(\alpha_{xx}(\omega_k) + \alpha_{yy}(\omega_k) + \alpha_{zz}(\omega_k)\Big). \tag{5.39}$$

5.3 Summary

In summary, we have presented a response function containing electron-hole correlation in the form of the Bethe-Salpeter equation, Equation (5.5). We proceed to expand Equation (5.5) in a two-particle basis, resulting in a transition space representation of the Bethe-Salpeter equation, given by Equation (5.20), which can be solved explicitly by direct inversion. Direct inversion of large matrices is however, never a desirable computational strategy, therefore we show how the transition space Bethe-Salpeter equation can be expressed in terms of an effective two-particle eigenvalue problem given by Equation (5.24). Equation (5.24) provides a physically intuitive interpretation of excitonic transitions which arise from the mixing of independent-particle transitions via the interaction kernel, Equation (5.28).

Finally, we have shown that it is possible to construct a set of coupled, linear equations (5.37), including the effective two-particle Hamiltonian and the external potential, which can be solved to efficiently obtain the first-order change in the charge density, from which we can directly compute the absorption spectra of finite systems. Chapters 6 and 7 will now address some of the key features of the empirical sp^3s^* tight-binding model and the approximations utilised in a real-space implementation of the Bethe-Salpeter equation, respectively.

Chapter 6

Implementation of the Tight-Binding Model

Having introduced the electronic structure formalism in Chapter 4, this chapter begins by discussing the bulk properties of zincblende semiconductors and presents the bulk properties of our sp^3s^* tight-binding model for CdSe. We then give a summary of the sparse eigenvalue solver, discuss the way in which we generate an explicit atomic orbital basis and outline the method that we utilise to passivate the dangling bonds of unterminated surface atoms.

6.1 The Zincblende Crystal Structure

Diamond and zincblende crystals are cubic structures comprised of a primitive unit cell containing two atoms at positions (0,0,0) a_l and $(\frac{1}{4}, \frac{1}{4}, \frac{1}{4})\, a_l$, where a_l is the lattice constant of the material. In this configuration each atom forms four sp^3 bonds with each of its nearest neighbours, leading to a network of tetrahedral bonding depicted in Figure 6.1. Zincblende differs from diamond in that it contains two atomic species and therefore each atom has four nearest neighbours of the opposite species, forming two interdigitated face-centred cubic lattices displaced by $\pm(\frac{1}{4}, \frac{1}{4}, \frac{1}{4})a_l$ with respect to one another. Zincblende crystals therefore adopt the Brillouin zone of the FCC lattice.

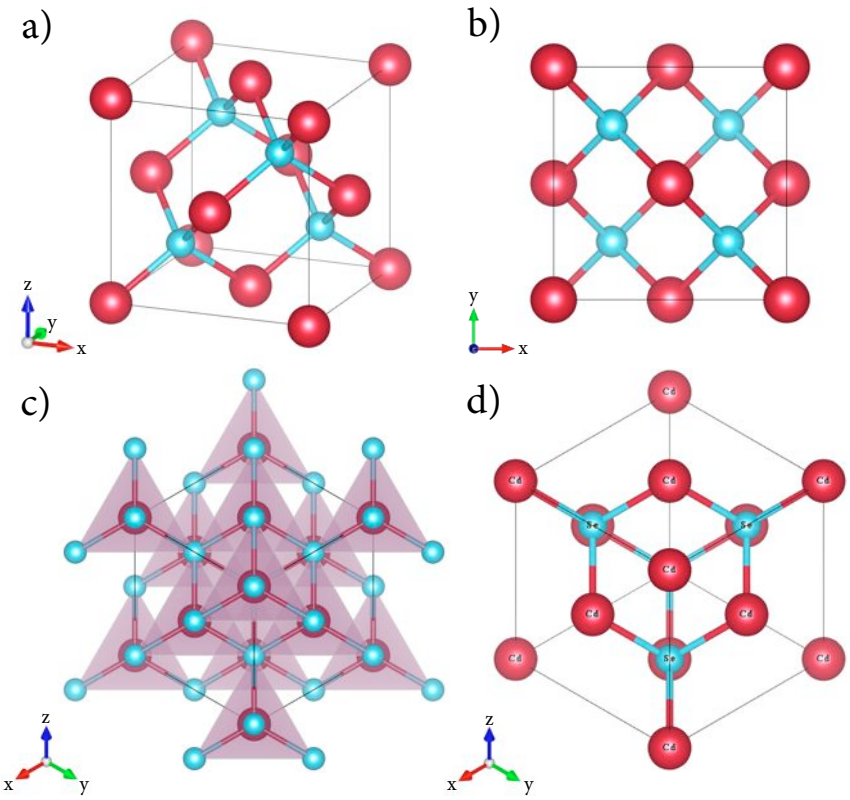

Figure 6.1: Tetrahedrally coordinated zincblende crystal lattice, displaying a) Isometric view, b) (001) plane, c) (111) plane with tetrahedra and d) (111) without tetrahedra. Cations are red and anions are blue.

Irreducible Representation		Class				
Mulliken	Koster	$\{E\}$	$\{3C_2\}$	$\{8C_3\}$	$\{6IC_4\}$	$\{6\sigma\}$
A_1	Γ_1	1	1	1	1	1
A_2	Γ_2	1	1	1	-1	-1
E	Γ_3	2	2	-1	0	0
T_2	Γ_4	3	-1	0	-1	1
T_1	Γ_5	3	-1	0	1	-1

Table 6.1: Character table for the T_d point group[161].

6.1.1 The Zincblende Bulk Band Structure

The zincblende structure belongs to the space group T_d^2, associated with the FCC translation group, and the tetrahedral point group T_d. The elements of a space group are themselves a combination of the translational symmetry of the unit cell and an element of a point group. If we restrict our analysis to the Γ-point ($\mathbf{k} = (0, 0, 0)$), which is the most physically relevant region of $\mathbf{k}$-space for direct-gap semiconductors, we can limit our discussion to the symmetry transformations of the T_d point group. The T_d point group is comprised of five classes and five irreducible representations, shown in Table 6.1.

In systems with cubic symmetry, one can approximate the symmetry about the Γ-point as spherical[162], which enables an analysis in terms of orbital angular momentum. In the absence of spin-orbit coupling, the basis states are chosen to be eigenfunctions of the orbital angular momentum operator $\hat{\mathrm{L}}$, leading to local Bloch functions, $|L, m_l\rangle$, defined by orbital angular momentum, L, and its azimuthal quantum number, m_l. In doing so, the Bloch functions are symmetrically equivalent to real orbitals. In the absence of spin, the conduction band minimum is non-degenerate and is described by a Bloch function with s-like symmetry, $|0, 0\rangle$, which is fully symmetric. From inspection of the character table for the T_d point group shown in Table 6.1, these symmetry properties are consistent with the Γ_1 irreducible representation (Koster notation), as it is unchanged under all operations.

The valence band top is described by Bloch functions with p_x, p_y and p_z-like

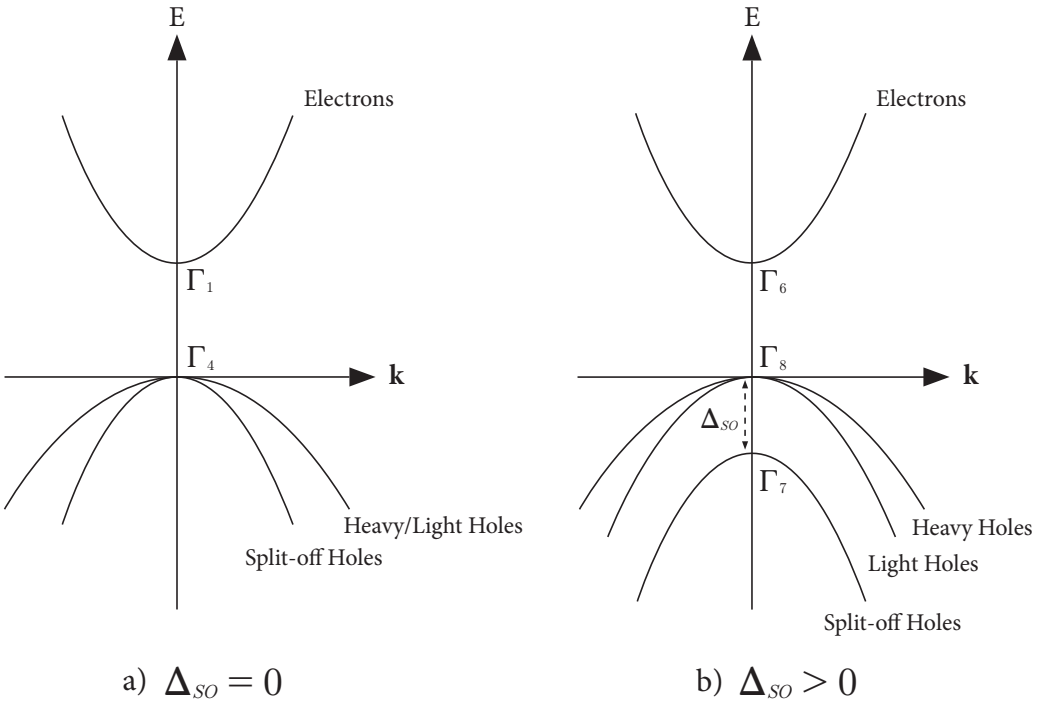

Figure 6.2: Schematic representation of the parabolic bulk bands of a zincblende semiconductor, a) without the influence of spin-orbit coupling and b) including spin-orbit coupling.

symmetries: $[|1,0\rangle, |1,-1\rangle, |1,1\rangle]$. As the valence band top is triply degenerate, these Bloch states must belong to the Γ_4 or Γ_5 irreducible representations because the degeneracy of an eigenstate is equal to the dimension of the irreducible representation to which it belongs[163]. Which representation the state belongs to can be established by calculating the character of the representing matrix generated by $L = 1$. Real p-orbitals have positive and negative lobes which change sign under the improper rotation IC_4. Inspection of the character table 6.1 indicates that the valence band top must therefore belong to the Γ_4 irreducible representation of the T_d group.

In spin-unpolarised calculations, the non-degenerate conduction band minimum and triply degenerate valence band maximum result in a lowest bulk exciton state that is three-fold degenerate. In spin-polarised calculations, in which one includes spin-orbit coupling, the degeneracy at the Γ-point is partially lifted, leading to a quadruply

	Orthogonal sp^3s^*	Experimental
E_g (eV)	1.90	1.76 eV [109], 1.77[165; 166], 1.83[115],*, 1.90[167]
m_{hh} (m_0)	0.475	0.45[168]
m_e (m_0)	0.128	0.12[163], 0.13[100]

Table 6.2: Bulk Properties of CdSe. ('*' Wurtzite structure).

degenerate valence band maximum, comprised of heavy hole and light hole states, and a doubly degenerate conduction band minimum. In this instance, the lowest exciton state is therefore eight-fold degenerate. Schematic, parabolic bulk band dispersions and symmetries at Γ are presented in Figure 6.2, both in the absence and presence of spin-orbit coupling.

The bulk band structure produced using our orthogonal tight-binding model is presented in Figure 6.3, in the absence of spin-orbit coupling. One can see how both the valence and conduction bands vary non-parabolically as one moves away from the Γ-point. Our tight-binding model therefore provides a more accurate representation of the bulk dispersion in relation to parabolic approximations. The corresponding band gap at zero temperature and effective masses of the electron and heavy hole bands are given in Table 6.2.

Spin-orbit coupling is relatively strong in CdSe, with a bulk splitting of 0.42 eV[164], however the electron-hole interaction is also very important in quasi two-dimensional systems. Bethe-Salpeter calculations with the inclusion of spin-orbit coupling represent a formidable challenge and to our knowledge, BSE Hamiltonians that include spin-orbit coupling have not been applied to finite systems. As one of the primary aims of this project was to model the excitonic properties of nanoscale colloids using the BSE, the decision was taken not to pursue the inclusion of spin-orbit coupling in the tight-binding model.

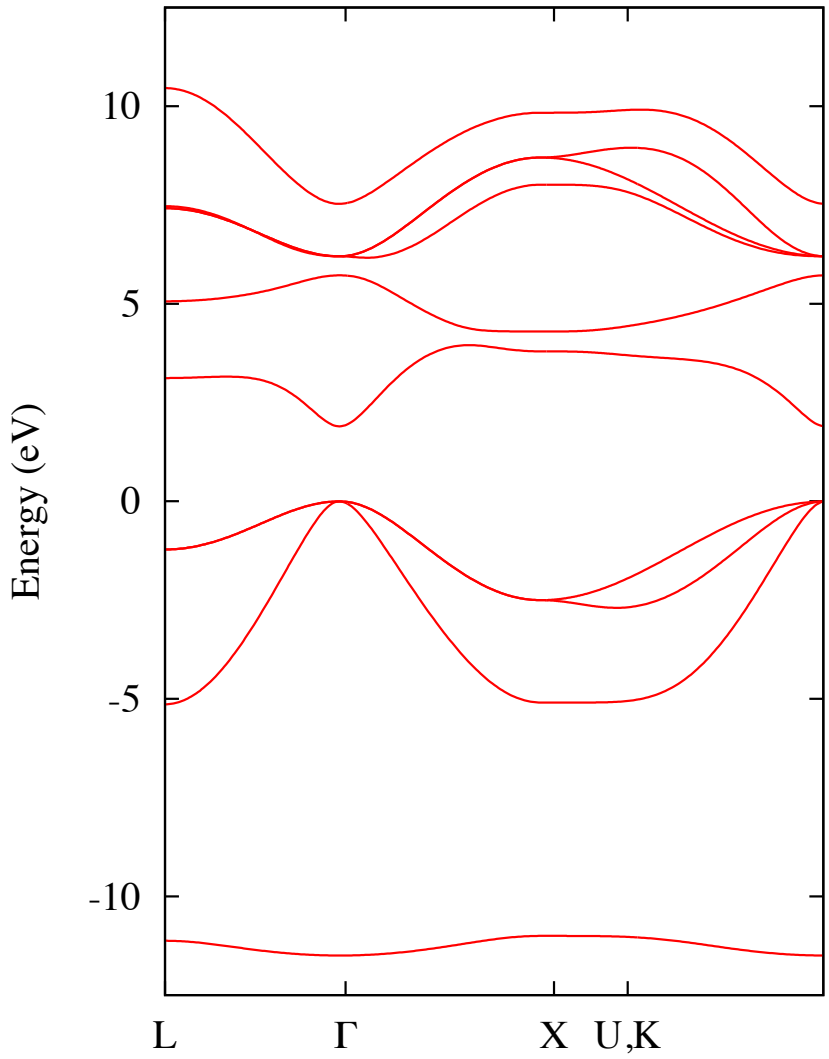

Figure 6.3: Bulk band structure of CdSe generated with the orthogonal NN sp^3s^* model, in the absence of spin-orbit coupling. The zero of the energy has been set to the top of the valence band, consistent with convention.

6.2 Solving the Standard Eigenvalue Problem

Obtaining the eigenstates of the bulk Hamiltonian requires one to solve the standard eigenvalue problem for a 10×10 matrix, which is computationally trivial. This is because the zincblende primitive unit cell only contains two atoms and the system is fully periodic. Solving the standard eigenvalue problem for systems comprised of large supercells containing many atoms however, forms a central point of electronic structure calculations. There are numerous methods for treating the eigenvalue

problem and one's choice of routine is highly dependent on the symmetry and size of the Hamiltonian. Small systems comprised of dense matrices are most efficiently treated with the LAPACK and BLAS linear algebra libraries[169]. The standard, symmetric eigenvalue problem is treated using QR decomposition of the Hamiltonian, which allows the problem to be solved without the need for matrix inversion. We utilise the LAPACK routine ZHEEV to compute all eigenvalues and eigenvectors, for systems containing up to ~ 1000 atoms. Beyond this size, one must turn to methods that more efficiently utilise memory resources.

6.2.1 FEAST Eigenvalue Solver

FEAST is an eigenvalue solver for sparse, symmetric and Hermitian matrices[170]. Unlike traditional Krylov subspace algorithms, FEAST uses contour integration to obtain eigenstates within a user-defined search interval. This has the advantage of being insensitive to spectrum structures and the ability to capture all eigenstate multiplicities. The method is still applied iteratively, however convergence is achieved in far fewer iterations than Krylov subspace algorithms. Specifically, FEAST utilises the Rayleigh-Ritz procedure[171] in which one obtains an approximate solution of the standard eigenvalue problem $AX = \epsilon X$ by iteratively solving a reduced eigenvalue problem of size m:

$$A_Q \Phi = \tilde{\epsilon} \Phi, \tag{6.1}$$

where $A_Q = (Q^T A Q)$ and Q defines a set of orthogonal basis vectors. The solutions of Equation (6.1) are given by the Ritz values, $\{\tilde{\epsilon}\}$, and the eigenfunctions $\{\Phi\}$. The approximate eigenvalues of the original problem are equivalent to the Ritz values, $\{\tilde{\epsilon}\}$, whereas the approximate eigenfunctions are given by $\tilde{X} = Q\Phi$. The Ritz pairs will be a good approximation of the true solutions of $AX = \epsilon X$ if the residual $(A\tilde{X} - \tilde{\epsilon}\tilde{X})$ has a small norm. Convergence on this criterion can then be achieved iteratively.

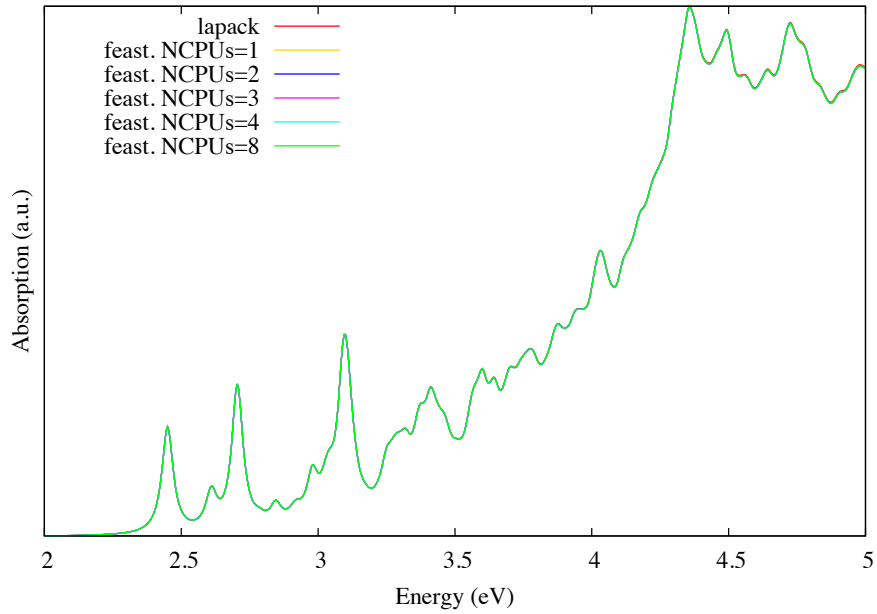

Figure 6.4: Absorption spectrum for a CdSe nanocrystal with a diameter of 4 nm, generated using a parallel implementation of the FEAST search interval.

As such, the FEAST algorithm allows one to compute a subspace of eigenstates from the energy region of interest, such as the band edges. Further details on the implementation can be found in Polizzi's original paper[170].

Scalability of the algorithm is achieved by distributing the energy range, containing m states, across multiple processes[172]. In Figure 6.4 we show the absorption spectrum of a CdSe nanocrystal with a diameter of 4 nm, computed using different subspace distributions. The spectra agree in all instances, indicating that the parallelisation scheme is suitable for the calculations we wish to present in later chapters. For specific details on the way in which one distributes the subspace, the reader is referred to Appendix C.

6.3 Choosing an Atomic Orbital Basis

An intrinsic problem of empirical tight-binding models is that in parameterising the Hamiltonian by fitting to a bulk band structure, one lacks an explicit description of the orbital basis functions. This creates an issue as orbital basis functions are

required to describe any physical quantity thats includes matrix elements involving the independent-particle states of the Hamiltonian. For example, orbital functions are required for the dipole matrix used in the calculation of the absorption spectrum and the kernel of the Bethe-Salpeter equation.

The need for an explicit form of the orbital basis therefore requires one to choose a set of functions to describe it. The only requirements placed upon the basis by the Hamiltonian is that the orbitals are atomic-like, as far as to say that they retain the symmetries of atomic orbitals and that they do not overlap with second-nearest neighbours. This suggests that the radial component of the basis should go to zero at half of the second-nearest neighbour distance and that the angular component can be described with spherical harmonics.

6.3.1 Numerical Radial Functions

The ab initio electronic structure code Siesta was used to generate the required radial functions[139]. Siesta's basis uses numerical, linear combinations of atomic orbitals. The sparsity of the Hamiltonian and overlap matrix is controlled through truncation of the radial extent.

It was initially assumed that through a combination of reducing the radial cut-off of the basis states and systematically removing elements of the Hamiltonian that correspond to interactions between more distant neighbours, that one might produce a first-principles band structure which could reproduce the band edges of the material of interest. The basis set used to generate this result would then correspond to a nearest neighbour approximation and could justifiably be transferred to the tight-binding model. In practise however, there proved to be no minimal basis that could reasonably reproduce the dispersion of the band edges of CdSe. As such, we have simply used Siesta as a tool to generate radial basis functions for CdSe, with a cut-off of $r_c = a_l/\sqrt{8}$, which prevents second-nearest neighbours from overlapping.

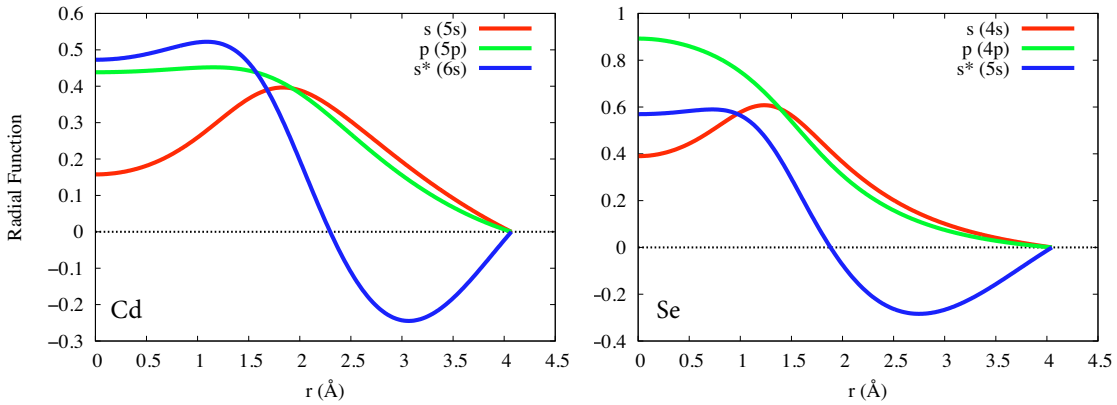

Figure 6.5: s, p and s^* numerical single-ζ radial functions for CdSe, generated using Siesta with a cut-off of 4.071 Bohr.

The smallest basis set used by Siesta to represent atomic valence orbitals is the single-ζ, which corresponds to a single function per atomic orbital. Using the scheme of Sankey and Niklewski[173],[174], single-ζ functions are found as solutions of a pseudo-atom in a spherical box of radius r. The input script used to generate the single-ζ radial functions shown in Figure 6.5 is given in Appendix C.

CdSe Radial Functions

The radial functions of the atomic valence orbitals, $(4s, 4p, 5s)$, where chosen for the sp^3s^* basis of selenium. The s^* orbital is viewed as an excited s-state, which is consistent with the interpretation of Vogl and coworkers[34]. In the case of cadmium, there are no p-orbitals in the valence: $(4d^{10}5s^2)$. As such, the orbitals $(5s, 5p, 6s)$ where chosen such that they retain the appropriate number of nodes. The radial functions for cadmium and selenium are plotted in Figure 6.5. Having defined the radial basis, the atomic orbitals are therefore given by:

$$\phi_\gamma(\mathbf{r} - \mathbf{r}_\alpha) = R_n^I(\mathbf{r} - \mathbf{r}_\alpha)Y_{l,m_l}(\theta, \phi), \tag{6.2}$$

where $\gamma = \{s, p_x, p_y, p_z, s^*\}$ is the orbital basis per atom, R_n^I are radial functions defined by $n = s, p, s^*$ for the atomic species $I = (a, c)$ (anion or cation), and Y_{l,m_l} are real spherical harmonics, defined by orbital and magnetic quantum numbers (l, m_l).

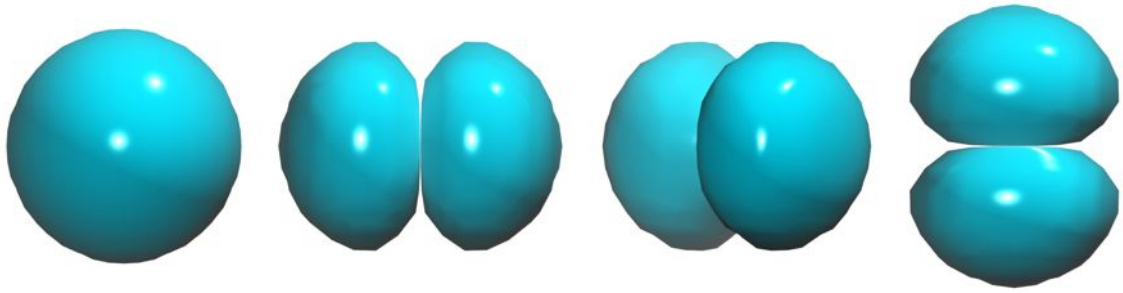

Figure 6.6: Isosurfaces of atomic orbtials $|\phi_s|^2$ and $|\phi_p|^2$, defined according to Equation (6.2). The radial components are given by the Siesta radial functions shown in Figure 6.5 (anion) and the angular components are defined by real harmonics.

Real orbitals are beneficial as they have no imaginary component and are defined with respect to the Cartesian directions (x, y, z), whilst maintaining their symmetry. This choice of basis is not unique in the sense that one could have chosen any set of functions which satisfy the symmetry of the Hamiltonian, however, in general one cannot do much better. Indeed, as discussed in Chapter 3, many prior studies of nanostructures using tight-binding models utilise Slater-type orbitals (STO) in conjunction with a Hamiltonian defined in an orthogonal basis[24; 125; 126; 145; 175; 176].

6.4 Surface Passivation

In finite structures, unterminated surface atoms lack a complete set of nearest neighbours. The resulting dangling bonds give rise to surface states with energies between that of the highest occupied state and lowest unoccupied state, and act to trap charge carriers. In the tight-binding formalism, one can passivate dangling bonds without having to explicitly include a passivating species[177; 178]. This can be achieved through an orthogonal transformation to a hybridised sp^3 basis, such that each hybridised orbital corresponds to a tetrahedral bonding direction. One is then able to passivate the bonds that lack neighbouring atoms, shifting the corresponding

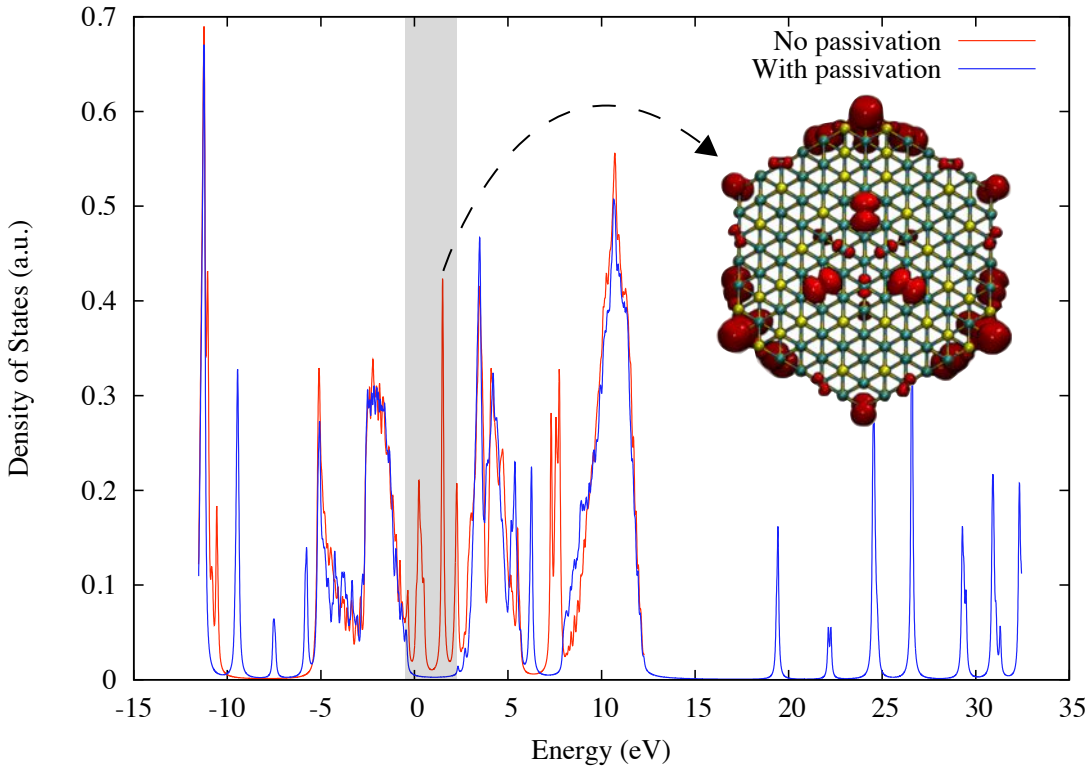

Figure 6.7: Density of states for a CdSe nanocrystal with a diameter of 3 nm. The red line represents the nanocrystal density of states in the absence of any passivation whereas the blue line represents the density of states of the passivated nanocrystal. The band gap region is indicated by the shaded box. Inset, we present the modulus squared wave function of a mid-gap state, indicated by the arrow in the DOS.

mid-gap states to arbitrarily higher energies. Physically, the procedure mimics the formation of bonding and anti-bonding states between a dangling bond and a passivating atom such as hydrogen[177]. We follow the procedure outlined in reference [177] and give the matrices of the passivated surface atoms in Appendix C.

Figure 6.7 demonstrates the effect of surface passivation on the density of states of a CdSe nanocrystal with a diameter of 3 nm. In the absence of any passivation (red line) there is a continuum of states between -5 eV and 12.5 eV, with surface states occupying the band gap region. Passivation of the nanocrystal leads to the removal of states from the band gap (blue line), with mid-gap states being shifted up to artificially higher energies, such that they do not interfere with the band edge states of interest. The inset in Figure 6.7 depicts the isosurface of a mid-gap state

from the unpassivated system. One can see that it is indeed localised to the surface, demonstrating that mid-gap states arise due to the dangling bonds of surface atoms.

6.5 Summary

In summary, we have presented a schematic representation of the bulk band structure for zincblende semiconductors, and discussed the symmetry of the valence band maximum and conduction band minimum at the Γ-point, in terms of the T_d point group. The bulk band structure, band gap and effective masses of the orthogonal NN sp^3s^* tight-binding model are presented for CdSe. We also give an overview of the routine used to find a subspace of eigenstates near the band edges and describe how we passivate the dangling bonds of unterminated surface atoms, such that our simulations are free of mid-gap states. In the following chapter, we shall outline our implementation of the Bethe-Salpeter equation for the calculation of two-particle excitations in optical absorption spectra.

Chapter 7

Implementation of the Bethe-Salpeter Equation in a Minimal Real-Space Basis Set

One of the goals of this project was to exploit the benefits of a minimal orbital basis in order to apply the Bethe-Salpeter formalism to large, finite systems. Drawing on the formalism outlined in Chapter 5, this chapter discusses the specifics of the Bethe-Salpeter implementation in an orbital basis, detailing the construction of the interaction kernel and the treatment of orbital integrals. We then go on to outline how a solution is found for the linear system defined by Equation (5.37)*, yielding the change in the charge density, and how this is used to efficiently construct the two-particle absorption spectrum in a parallel environment.*

7.1 Introduction

Our many-body calculations follow a simplified procedure, based on a common workflow utilised in ab initio calculations. Due to the scale of the systems of interest, we compute ground state eigenvalues and wave functions using an empirical tight-binding model, rather than DFT. The bulk tight-binding parameterisation is fit to the experimental bulk band gap and is therefore accurate by construction.

A large simplification to our approach is that we replace the microscopic dielectric function with the bulk dielectric constant. Indeed, one of the main difficulties in *GW* and BSE simulations is the calculation of the full dielectric response of the system due to the non-local and frequency-dependent nature of the dielectric function[55]. The full dielectric function can be computed in an empirical orbital model[179; 180], however it is known that the dielectric response in nanostructures is only modified near the surface[96; 181]. We therefore believe that static, bulk screening is appropriate as a first approximation and compute the screened Coulomb matrix in a static approximation.

What follows is an outline of the steps and approximations used to compute the kernel of the Bethe-Salpeter equation, given by Equations (5.32)-(5.33) in Chapter 5, in an orbital basis.

7.2 Expansion of the Bethe-Salpeter Kernel in an Orbital Basis

The exchange and direct terms of the interaction kernel, defined by Equations (5.32) and (5.33) in Chapter 5, can be written in an orbital expansion as:

$$v_{(vc)(v'c')} = \sum_{i,j,k,l} a_{(v;i)} a^*_{(c;j)} a^*_{(v';k)} a_{(c';l)} (ij|v|kl), \tag{7.1}$$

$$W_{(vc)(v'c')} = \sum_{i,j,k,l} a_{(v;i)} a^*_{(v';j)} a^*_{(c;k)} a_{(c';l)} (ij|W|kl), \tag{7.2}$$

where $a_{(v;i)}$ are tight-binding coefficients, (v, c, v', c') are independent-particle state indices, (i, j, k, l) are orbital indices each running over all orbital states in the system, with $i = (\gamma_i, \alpha)$, and the four-point orbital integrals are given as:

$$(ij|v|kl) = \int d\mathbf{r}_1 d\mathbf{r}_2 \phi_{\gamma_i}(\mathbf{r}_1 - \mathbf{r}_\alpha) \phi^*_{\gamma_j}(\mathbf{r}_1 - \mathbf{r}_\beta) \frac{1}{|\mathbf{r}_1 - \mathbf{r}_2|} \phi^*_{\gamma_k}(\mathbf{r}_2 - \mathbf{r}_\kappa) \phi_{\gamma_l}(\mathbf{r}_2 - \mathbf{r}_\lambda), \tag{7.3}$$

$$(ij|W|kl) = \int d\mathbf{r}_1 d\mathbf{r}_2 \phi_{\gamma_i}(\mathbf{r}_1 - \mathbf{r}_\alpha) \phi^*_{\gamma_j}(\mathbf{r}_1 - \mathbf{r}_\beta) W(\mathbf{r}_1, \mathbf{r}_2, \omega = 0) \phi^*_{\gamma_k}(\mathbf{r}_2 - \mathbf{r}_\kappa) \phi_{\gamma_l}(\mathbf{r}_2 - \mathbf{r}_\lambda). \tag{7.4}$$

To simplify the calculation of integrals involving the screened Coulomb potential, Equation (7.4), the microscopic, inverse dielectric function is replaced by the high-frequency, bulk dielectric constant ϵ_∞ such that:

$$W(\mathbf{r}_1, \mathbf{r}_2, \omega = 0) = \frac{1}{\epsilon_\infty |\mathbf{r}_1 - \mathbf{r}_2|}. \tag{7.5}$$

This corresponds to a static and uniform dielectric screening throughout the nanostructure, and is justified as a first approximation because the screening in the interior of the nanocrystal is bulk-like, with a differing dielectric response only expected close to surface[96; 181]. Importantly, this allows us the factorise the the dielectric constant such that we can rewrite Equation (7.4) in terms of Equation (7.3):

$$(ij|W|kl) = \epsilon_\infty^{-1} (ij|v|kl), \tag{7.6}$$

and subsequently expand the Bethe-Salpeter kernel in an orbital basis as:

$$\begin{aligned} K &= 2v + W \\ &= \sum_{i,j,k,l} \left[2 a_{(v;i)} a^*_{(c;j)} a^*_{(v';k)} a_{(c';l)} - \epsilon_\infty^{-1} a_{(v;i)} a^*_{(v';j)} a^*_{(c;k)} a_{(c';l)} \right] (ij|v|kl) \end{aligned} \tag{7.7}$$

7.2.1 Two-Centre Approximation for Orbital Integrals

In our initial implementation of the BSE kernel construction, Equation (7.7) was constructed as a four-point quantity, however, even when one restricts the summations over atoms β and λ to the nearest neighbours of α and κ, respectively, one is still required to perform $625 * N^2$ summations over each element of the kernel in the pair-particle basis. Furthermore, the integrals defined by Equation (7.3) were explicitly calculated in all instances. This approximation ultimately proved to be a severe bottleneck, restricting simulations to systems no larger than ~ 20 atoms.

It is however, possible to restrict four-point orbital integrals to at most, two unique centres as terms centred on three or four different sites are small in comparison[24; 125; 145; 176; 182; 183]. In restricting the atomic centres and orbital indices to two unique indices, the numerators of the four-point orbital integrands in Equations (7.3) and (7.4) reduce to:

$$\phi_{\gamma_i}(\mathbf{r}_1 - \mathbf{r}_\alpha)\phi^*_{\gamma_i}(\mathbf{r}_1 - \mathbf{r}_\alpha)\phi^*_{\gamma_j}(\mathbf{r}_2 - \mathbf{r}_\beta)\phi_{\gamma_j}(\mathbf{r}_2 - \mathbf{r}_\beta), \tag{7.8}$$

$$\phi_{\gamma_i}(\mathbf{r}_1 - \mathbf{r}_\alpha)\phi^*_{\gamma_j}(\mathbf{r}_1 - \mathbf{r}_\beta)\phi^*_{\gamma_i}(\mathbf{r}_2 - \mathbf{r}_\alpha)\phi_{\gamma_j}(\mathbf{r}_2 - \mathbf{r}_\beta), \tag{7.9}$$

$$\phi_{\gamma_i}(\mathbf{r}_1 - \mathbf{r}_\alpha)\phi^*_{\gamma_j}(\mathbf{r}_1 - \mathbf{r}_\beta)\phi^*_{\gamma_j}(\mathbf{r}_2 - \mathbf{r}_\beta)\phi_{\gamma_i}(\mathbf{r}_2 - \mathbf{r}_\alpha), \tag{7.10}$$

where Equation (7.8) is Coulomb-like in nature, and Equations (7.9) and (7.10) are exchange-like in nature. This terminology reflects the fact that in Equation (7.8) pairs of orbitals with the same orbital index are also defined by the same spatial variable, whereas in the exchange-like integrals, given by Equations (7.9)-(7.10), pairs of orbitals with the same orbital index are defined by different spatial variables.

At this point, we specify that the choice of orbital basis is real, such that we can drop the conjugate superscripts. In a real orbital basis, Equations (7.9) and (7.10) are equivalent, resulting in two two-centre orbital integrals. The Coulomb-like orbital

integral is:

$$(ii|v|jj) = \int_V d\mathbf{r}_1 d\mathbf{r}_2 \phi_{\gamma_i}(\mathbf{r}_1 - \mathbf{r}_\alpha)\phi_{\gamma_i}(\mathbf{r}_1 - \mathbf{r}_\alpha)\frac{1}{|\mathbf{r}_1 - \mathbf{r}_2|}\phi_{\gamma_j}(\mathbf{r}_2 - \mathbf{r}_\beta)\phi_{\gamma_j}(\mathbf{r}_2 - \mathbf{r}_\beta), \quad (7.11)$$

whereas the exchange-like orbital integral is:

$$(ij|v|ij) = \int_V d\mathbf{r}_1 d\mathbf{r}_2 \phi_{\gamma_i}(\mathbf{r}_1 - \mathbf{r}_\alpha)\phi_{\gamma_j}(\mathbf{r}_1 - \mathbf{r}_\beta)\frac{1}{|\mathbf{r}_1 - \mathbf{r}_2|}\phi_{\gamma_i}(\mathbf{r}_2 - \mathbf{r}_\alpha)\phi_{\gamma_j}(\mathbf{r}_2 - \mathbf{r}_\beta). \quad (7.12)$$

Applying the two-centre approximation to Equation (7.7) and factorising the tight-binding coefficients causes the BSE kernel to reduce to:

$$\begin{aligned} K_{(vc),(v'c')} = \sum_{i,j} & a_{(v;i)}a_{(c;i)}a_{(v';j)}a_{(c';j)}\left[2(ii|v|jj) - \epsilon_\infty^{-1}(ij|v|ij)\right] \\ & + a_{(v;i)}a_{(c;j)}a_{(v';i)}a_{(c';j)}\left[2(ij|v|ij) - \epsilon_\infty^{-1}(ii|v|jj)\right] \\ & + a_{(v;i)}a_{(c;j)}a_{(v';j)}a_{(c';i)}\left[2 - \epsilon_\infty^{-1}\right](ij|v|ij), \end{aligned} \quad (7.13)$$

where the screening is only applied to terms that derive from the direct term of the kernel in the pair-product basis, defined by Equation (7.2). An interesting consequence of applying the two-centre approximation to a real orbital basis is that the same set of tight-binding coefficients define the direct and exchange terms of the BSE kernel. An equivalent expression is given for $K_{(vc),(c'v')}$ in Appendix D.

7.2.2 Calculating Two-Centres Integrals

The orbital Coulomb and exchange-like integrals, defined by Equations (7.11) and (7.12), respectively, are explicitly computed for on-site and nearest neighbour interactions, giving two matrices, U_c and U_x. These define the Coulomb and exchange matrices, respectively, and are both symmetric in a real orbital basis. These matrices therefore possess the same symmetry as the tight-binding Hamiltonian given by Equations (4.19) and (4.20) in Chapter 4. In both instances,

U is analogously defined by four sub-blocks:

$$U = \begin{pmatrix} U^{aa} & U^{ac} \\ U^{ca} & U^{cc} \end{pmatrix}, \tag{7.14}$$

where a, c denote anions and cations, respectively. Calculated values are provided in Appendix D. In general, the on-site terms are largest, with the Coulomb elements $\sim 10 - 15$ eV and exchange elements an order of magnitude smaller. For nearest neighbour integrals, Coulomb terms are ~ 5 eV whereas exchange terms are ~ 0.01 eV. These observations are consistent with prior reports in the literature[24; 123; 124; 145]. For points in the integration where $\mathbf{r}_1 = \mathbf{r}_2$, we truncate the Coulomb singularity to a value equal to 0.1 times the bond length. This point is discussed further in Appendix D.

7.2.3 Multipole Expansion of the Coulomb Potential

For interactions between orbitals centred on atoms beyond those of nearest neighbours, we utilise the multipole expansion of the Coulomb potential to approximate Equation (7.11). This is justified because the exact details of the orbital structure are unimportant for well-separated charge distributions[184].

The spatial variables that define the Coulomb potential between two, well-separated, non-overlapping charge distributions can be decomposed in terms of the atomic positions at which the orbitals are centred and the radial distances that the orbitals extend to with respect to their atomic centres:

$$\begin{aligned} \mathbf{r}_1 - \mathbf{r}_2 =& \Big[\mathbf{R}_\alpha + (\mathbf{r}_1 - \mathbf{R}_\alpha)\Big] - \Big[\mathbf{R}_\beta - (\mathbf{r}_2 - \mathbf{R}_\beta)\Big] \\ =& \mathbf{R}_\alpha - \mathbf{R}_\beta + \mathbf{r}_{\alpha 1} - \mathbf{r}_{\beta 2}, \end{aligned} \tag{7.15}$$

where $\mathbf{r}$ is a spatial variable, $\mathbf{R}$ is an atomic centre and $(\mathbf{r} - \mathbf{R})$ is a local spatial variable with respect to the atomic centre. These vectors are schematically

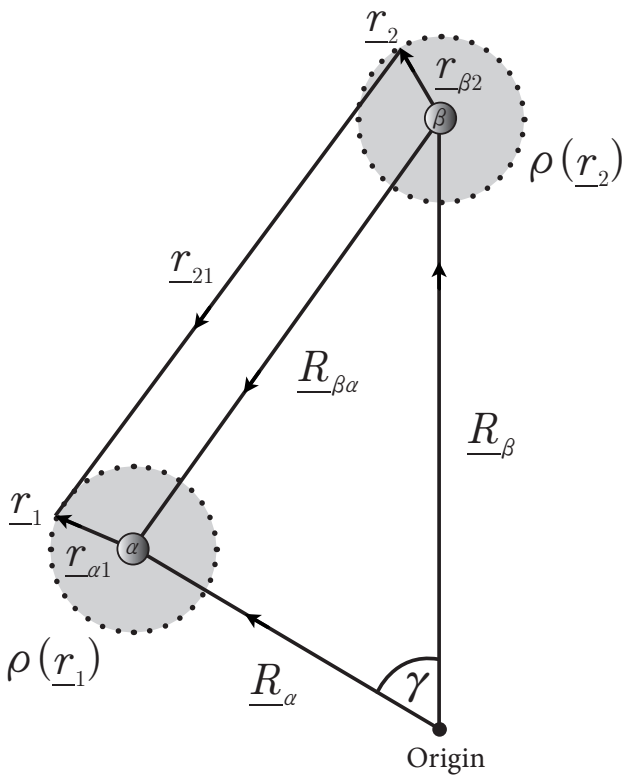

Figure 7.1: Vector diagram for two non-overlapping, orbital charge distributions.

represented in Figure 7.1. Using Equation (7.15), the Coulomb potential can therefore be written as:

$$\frac{1}{|\mathbf{r}_1 - \mathbf{r}_2|} = \frac{1}{|\mathbf{R}_{\beta\alpha} - (\mathbf{r}_{\beta 2} - \mathbf{r}_{\alpha 1})|}, \tag{7.16}$$

where the $\mathbf{R}_{\beta\alpha}$ defines the vector separating atoms α and β, and $(\mathbf{r}_{\beta 2} - \mathbf{r}_{\alpha 1})$ defines the difference in the spatial positions relative to the atomic centres. In the instance that $|\mathbf{R}_{\beta\alpha}| > |(\mathbf{r}_{\beta 2} - \mathbf{r}_{\alpha 1})|$, one can expand Equation (7.16) using the multipole expansion of the Coulomb potential[145; 176; 182; 183]. The multipole expansion is defined as[184]:

$$\frac{1}{|\mathbf{r}_1 - \mathbf{r}_2|} = 4\pi \sum_{l=0}^{\infty} \frac{1}{2l+1} \frac{r_<^l}{r_>^{l+1}} \sum_{m=-l}^{l} Y_{lm}^*(\theta', \phi') Y_{lm}(\theta, \phi), \tag{7.17}$$

where $r_>$ is the larger of the two radial magnitudes, $r_<$ is the smaller of the two

radial magnitudes and Y_{lm} are spherical harmonics defined by the quantum numbers (l, m). Taking $r_> = R_{\beta\alpha}$ and $r_< = |\mathbf{r}_{\beta 2} - \mathbf{r}_{\alpha 1}|$, the Hartree potential at a point $\mathbf{r}_1$ due to a charge distribution $\rho(\mathbf{r}_2)$ at point $\mathbf{r}_2$ is:

$$V_H(\mathbf{r}_1) = \frac{4\pi}{R_{\beta\alpha}} \sum_{l=0,m=-l}^{\infty,l} \frac{1}{2l+1} \frac{q_{lm}}{(R_{\beta\alpha})^l} Y_{lm}(\theta, \phi), \tag{7.18}$$

where q_{lm} define the multipole moments:

$$q_{lm} = \int Y^*_{lm}(\theta', \phi') |\mathbf{r}_{\beta 2} - \mathbf{r}_{\alpha 1}|^l \rho(\mathbf{r}_2) d\mathbf{r}_2. \tag{7.19}$$

The interaction energy between two non-overlapping charge distributions is defined as:

$$U^{\alpha,\beta}_{\gamma_i,\gamma_j} = \int V_H(\mathbf{r}_1) \rho(\mathbf{r}_1) d\mathbf{r}_1. \tag{7.20}$$

Expanding the Coulomb potential using the monopole moment, $q_{00} = \frac{1}{\sqrt{4\pi}} \int \rho(\mathbf{r}_2) d\mathbf{r}_2$, one obtains the following terms for the Hartree potential and the interaction energy:

$$V_H(\mathbf{r}_1) = \frac{1}{R_{\alpha\beta}} \int \rho(\mathbf{r}_2) d\mathbf{r}_2, \tag{7.21}$$

$$U = \frac{1}{R_{\alpha\beta}} \int \rho(\mathbf{r}_1) d\mathbf{r}_1 \int \rho(\mathbf{r}_2) d\mathbf{r}_2. \tag{7.22}$$

Substituting for the charge densities in Equation (7.22), one obtains the following expression for the two-centre Coulomb integral in the monopole approximation:

$$\begin{aligned} U_c =& \frac{1}{R_{\alpha\beta}} \int |\phi_{\gamma_i}(\mathbf{r}_1 - \mathbf{r}_\alpha)|^2 d\mathbf{r}_1 \int |\phi_{\gamma_j}(\mathbf{r}_2 - \mathbf{r}_\beta)|^2 d\mathbf{r}_2, \\ =& \frac{1}{R_{\alpha\beta}}. \end{aligned} \tag{7.23}$$

Similarly, the monopole term of the orbital exchange integral is:

$$\begin{aligned} U_x =& \frac{1}{R_{\alpha\beta}} \int \phi_{\gamma_i}(\mathbf{r}_1 - \mathbf{r}_\alpha)\phi_{\gamma_j}(\mathbf{r}_1 - \mathbf{r}_\beta)d\mathbf{r}_1 \int \phi_{\gamma_i}(\mathbf{r}_2 - \mathbf{r}_\alpha)\phi_{\gamma_j}(\mathbf{r}_2 - \mathbf{r}_\beta)d\mathbf{r}_2, \\ =& \frac{1}{R_{\alpha\beta}} \Big[S_{(\alpha\gamma_i)(\beta\gamma_j)} \Big]^2, \end{aligned} \tag{7.24}$$

however, as the exchange-like integrals are typically an order of magnitude smaller than the Coulomb integrals and decay exponentially with distance[24; 123; 124; 145], we neglect terms multiplied by $(ij|v|ij)$ in the kernel, beyond those of nearest neighbours and therefore do not utilise the monopole approximation for the exchange integrals.

7.2.4 Validity of the Monopole Approximation

To test the validity of the monopole approximation for second and third nearest neighbour Coulomb-like integrals, we explicitly compute the integrals defined by Equation (7.11) and compare the averages to the monopole value, given by Equation (7.23). The values are presented in Tables 7.1 and 7.2, respectively. Strictly speaking, $U_{\gamma,\gamma'} \neq U_{\gamma',\gamma}$, however we consider the differences to be negligible in this context and only distinguish between different orbitals to highlight how the orbital structure is not important as the interatomic separation increases.

Computed Element	min (eV)	max (eV)	Avg (eV)	$1/R_{\alpha\beta}$ (eV)
U^{aa}_{ss}	3.351	3.351	3.351	3.366
U^{aa}_{sp}	3.292	3.332	3.319	3.366
U^{aa}_{pp}	3.236	3.316	3.286	3.366
$U^{\mathrm{aa}}_{s^*p}$	3.285	3.325	3.312	3.366
U^{cc}_{ss}	3.364	3.364	3.364	3.366
U^{cc}_{sp}	3.309	3.378	3.355	3.366
U^{cc}_{pp}	3.260	3.402	3.347	3.366
$U^{\mathrm{cc}}_{s^*p}$	3.300	3.370	3.346	3.366

Table 7.1: Comparison of explicitly-calculated Coulomb integrals vs the monopole approximation, for second nearest neighbours at an inter-atomic separation of 4.28 Å.

Computed Element	min (eV)	max (eV)	Avg (eV)	$1/R_{\alpha\beta}$ (eV)
U_{ss}^{ac}	2.863	2.863	2.863	2.870
U_{sp}^{ac}	2.823	2.898	2.846	2.870
U_{pp}^{ac}	2.796	2.895	2.828	2.870
$U_{s^*p}^{\mathrm{ac}}$	2.816	2.892	2.839	2.870
U_{ss}^{ca}	2.863	2.863	2.863	2.870
U_{sp}^{ca}	2.823	2.898	2.846	2.870
U_{pp}^{ca}	2.796	2.895	2.828	2.870
$U_{s^*p}^{\mathrm{ca}}$	2.816	2.892	2.839	2.870

Table 7.2: Comparison of explicitly-calculated Coulomb integrals vs the monopole approximation, for third nearest neighbours at an inter-atomic separation of 5.02 Å.

The superscript of the elements in Tables 7.1 and 7.2 reflect the fact that the atom species of the neighbours depends on the species of the central atom. For second nearest neighbours, the atomic species of the neighbours are the same as the centre atom, hence anion-anion (aa) or cation-cation(cc). Alternatively, third nearest neighbours form anion-cation (ac) or cation-anion (ca) pairs with the central atom.

Data in Tables 7.1 and 7.2 show that both the atomic species and the orbital type do not have a large effect on the integral values for inter-atomic separations beyond that of nearest neighbours. We therefore consider the monopole approximation of the Coulomb potential to be consistent with this choice of atomic orbital basis and use it for two-centre integrals beyond that of nearest neighbours. An equivalent comparison is not made for exchange integrals because the radial cut-off of the basis causes the product $\phi_{\gamma_i}(\mathbf{r}_1)\phi_{\gamma_j}(\mathbf{r}_1) = 0$ for any pair of orbitals (i, j) centred on atoms beyond those of nearest neighbours. Having quantified the validity of the monopole approximation, we summarise how we treat the orbital integrals defined by Equations (7.11) and (7.12) in Table 7.3.

	Coulomb	Exchange
On-site	Explicitly calculated	Explicitly calculated
Nearest Neighbour	Explicitly calculated	Explicitly calculated
Beyond NN	Approximated using monopole term of multipole expansion	Neglected

Table 7.3: Summary of how the orbital Coulomb and exchange integrals are treated in our implementation of the BSE.

7.2.5 An Effective Two-particle Hamiltonian in a Real Basis

From Chapter 5, the effective two-particle Hamiltonian, given by Equation (5.29), in a real basis simplifies to:

$$H^{2p}_{(n_1n_2)(n_3n_4)} = \left(\begin{array}{c|cc} {\scriptstyle (n_3n_4)\rightarrow \atop (n_1n_2)\downarrow} & \{v'c'\} & \{c'v'\} \\ \hline \{vc\} & H^{2p,res}_{(vc)(v'c')} & K_{(vc)(c'v')} \\ \{cv\} & -K_{(vc)(c'v')} & -H^{2p,res}_{(vc)(v'c')} \end{array}\right), \tag{7.25}$$

where each sub-matrix has dimensions $\mathrm{N_{2p}} \times \mathrm{N_{2p}}$. Here, $\mathrm{N_{2p}} = \mathrm{N_v N_c}$ is the size of the two-particle basis, which is itself equal to to the number of valence states, $\mathrm{N_v}$, multiplied by the number of conduction states, $\mathrm{N_c}$, used in the two-particle expansion. Equation (7.25) is therefore fully defined by the kernels: $K_{(vc)(v'c')}$, $K_{(vc)(c'v')}$ and the independent-particle transition energies. Furthermore, as K is symmetric[55] such that $K_{(vc),(v'c')} = K_{(v'c'),(vc)}$, one only requires the lower (or upper) triangle of the two kernels (plus the transition energies) in order to be able to entirely reproduce H^{2p}, reducing the total number of unique elements to $\mathrm{N_{2p}}(\mathrm{N_{2p}} + 1)$.

7.3 Computing the Change in the Charge Density

In order to solve the linear system defined by Equation (5.37) in Chapter 5, one is required to compute the matrix-vector product of H^{2p} with an initial guess at

the density response $\tilde{\delta\rho}$, such that the resulting vector can be evaluated against the known solution. The guess at the density response $\tilde{\delta\rho}$ is then iteratively refined until it converges on $\delta\rho$ using a bi-conjugate gradient algorithm[185]1.

We therefore only need to consider two steps when discussing the MPI parallelisation of our Bethe-Salpeter implementation. In the first, the lower triangle of the coupling matrices, defined by Equation (7.13) is distributed amongst N_p processors using a row-wise block partitioning scheme. Each processor computes and stores a portion of the coupling matrices.

In the second step, the bi-conjugate gradient routine performs matrix-vector multiplication in order to evaluate the residuals. Parallelisation of matrix-vector multiplication is relatively straight-forward to implement as all elements in a given row of a matrix will contribute to the same element of the product vector. As such, each process can compute its contribution to the final vector independently and the full coupling matrices never need to be held in memory by any process. Each process therefore outputs its contribution to the matrix-vector product and these are summed to form the full vector on the master node.

Additionally, we note that the matrix-vector product routine is actually comprised of four products. One corresponding to each sub-matrix of the full two-particle Hamiltonian, given by Equation (7.25). Furthermore, the resonant two-particle Hamiltonian is only distinguished from the coupling matrix by the diagonal transition energies. These contributions are therefore added to output vector separately. The enthusiastic reader can find full details on all aspects of these routines in Appendix D.

The density response is solved in this manner for a discrete set of frequencies, corresponding to a subset of the lowest transitions in the absorption spectrum. At

[1]Bi-conjugate gradient utilises two sets of mutually orthogonal residuals, instead of one, enabling it to treat matrices which aren't symmetric, positive-definite[185] which is the case for Equation (7.25).

each frequency, the absorption cross-section is computed using Equations (5.38) and (5.4), defined in in Chapter 5.

7.4 Summary

In summary, we have described the details and approximations employed in our implementation of the Bethe-Salpeter equation, expanded in a real-space, orbital basis. In order the make the approach scalable, we utilise a two-centre approximation for the orbital integrals involving the bare Coulomb potential. This results in two specific types of orbital integral: The Coulomb-like integral and exchange-like integral. These are calculated on a dense grid once and tabulated for use in calculations. Two-centre Coulomb-like integrals between orbitals centred on atoms greater than a bond length apart are approximated using the monopole term of the multipole expansion. The validity of this approximation is tested.

We show how, using a real orbital basis, the BSE kernel factorises into a compact form in terms of the product of tight-binding coefficients and two-centre integrals, given by Equation (7.13). We then explain how symmetry allows us to describe the full two-particle Hamiltonian defined by Equation (7.25), using only the lower triangles of the kernels $K_{(vc),(v'c')}$ and $K_{(vc),(c'v')}$.

Finally, we outline how MPI parallelisation enables us to distribute the lower triangle of the kernels evenly amongst several processors and how this parallelisation scheme is utilised by a bi-conjugate gradient algorithm to compute the density response of a system to an external potential, from which we can cheaply compute the absorption cross-section of finite systems.

Chapter 8

Electronic and Optical Properties of Cadmium Chalcogenide Nanocrystals

In Chapters 3 and 4 we presented the general features of the empirical sp^3s^* tight-binding model and reviewed its application to cadmium chalcogenide nanocrystals, respectively. In this chapter we present our own results on CdSe nanocrystals. We benchmark the electronic structure as a function of diameter, present isosurfaces of the band-edge atomic wave functions and compare absorption spectra calculated in the independent-particle approximation to available experimental spectra.

8.1 Electronic Properties of Cadmium Chalcogenide Nanocrystals

In this chapter, we investigate the electronic properties of zincblende CdSe nanocrystals with approximately spherical shape, as depicted in Figure 8.1. By varying the nanocrystal size, one passes from the strong confinement to weak confinement, converging on bulk in the large-size limit. The level of confinement is defined by the nanocrystals radius, a, relative to the bulk Bohr radius of the exciton a_B, which is 5.6 nm for CdSe[90].

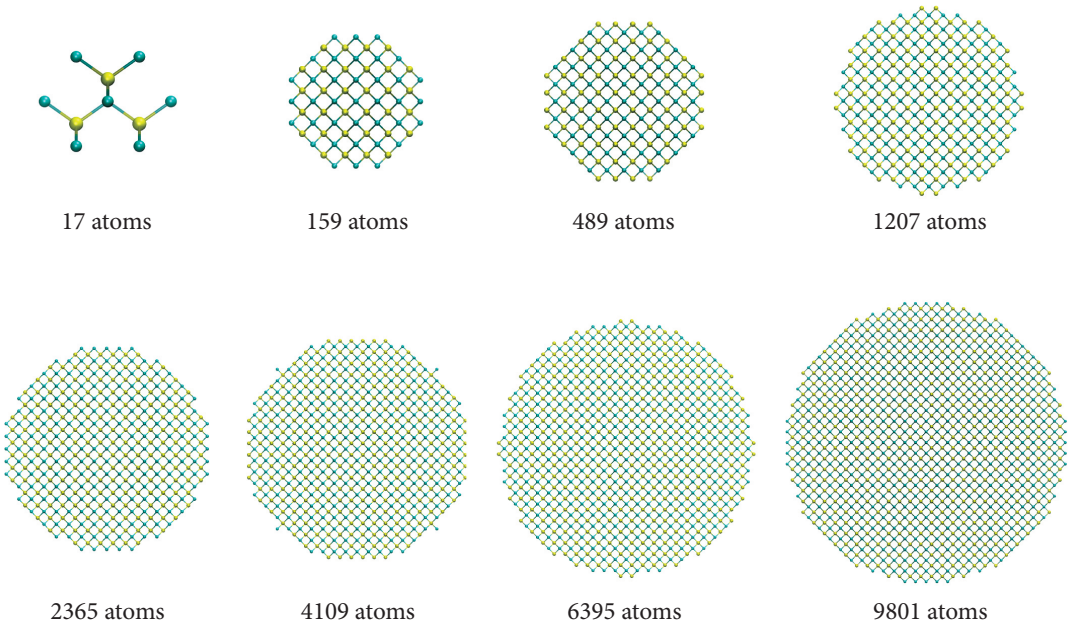

Figure 8.1: Ball and stick models of anion-centred, zincblende CdSe nanocrystals, with diameters ranging from 1 nm to 8 nm (top left to bottom right). Cd atoms are yellow and Se atoms are green. All nanocrystals are orientated with the $[0, -1, 0]$ axis coming out of the page, except for the smallest, which is orientated with the $[1, 1, 0]$ coming out of the page.

8.1.1 Independent-Particle Band Gap as a Function of Nanocrystal Diameter

Quantum confinement arises from the spatial confinement of carriers due to a reduction in the physical dimensions of the system and causes a widening of the electronic band gap in relation to the bulk band gap. One therefore sees an increase in the electronic band gap of the nanocrystal as a function of decreasing diameter. The independent-particle band gap dependence on the nanocrystal diameter predicted by three sp^3s^* basis sets is presented in Figure 8.2. Here, the red symbols represent our orthogonal model, the green symbols represent data from Lippens and Lannoo[100], and the blue symbols represent data from Lee and coworkers[24]. We avoid a comparison with experimental data at this stage, as these results do not include many-body effects. For example, we see that our tight-binding model predicts band gaps of 3.3 eV and 2.15 eV for nanocrystals with diameters of 2 nm and 7 nm, respectively, compared to the average experimental values of 2.8 eV and 1.9 eV quoted in Chapter 1. Optical gaps will be addressed in Chapter 10.

The excellent agreement between the data sets in Figure 8.2 is not surprising. Both ourselves, and Lee and coworkers utilise the same Hamiltonian parameters as Lippens and Lannoo, and all works exclude spin-orbit coupling. In reference [24], Lee and coworkers do not specify their choice of passivation parameters, however other work by the authors have referenced values as large as 100 eV[186; 187], which will shift mid-gap states well beyond the band edges. This treatment is therefore comparable to a complete removal of mid-gap states, which is the approach used by Lippens and Lannoo. We utilise a smaller passivation parameter of 25 eV, which is still sufficient to remove the mid-gap states far from the band edges (see Figure 8.3 and the discussion below) and has been cited in more recent simulations of CdSe nanocrystals by Korkusinski *et al.*[176] Consequently our band gaps are slightly contracted with respect to the other independent-particle references.

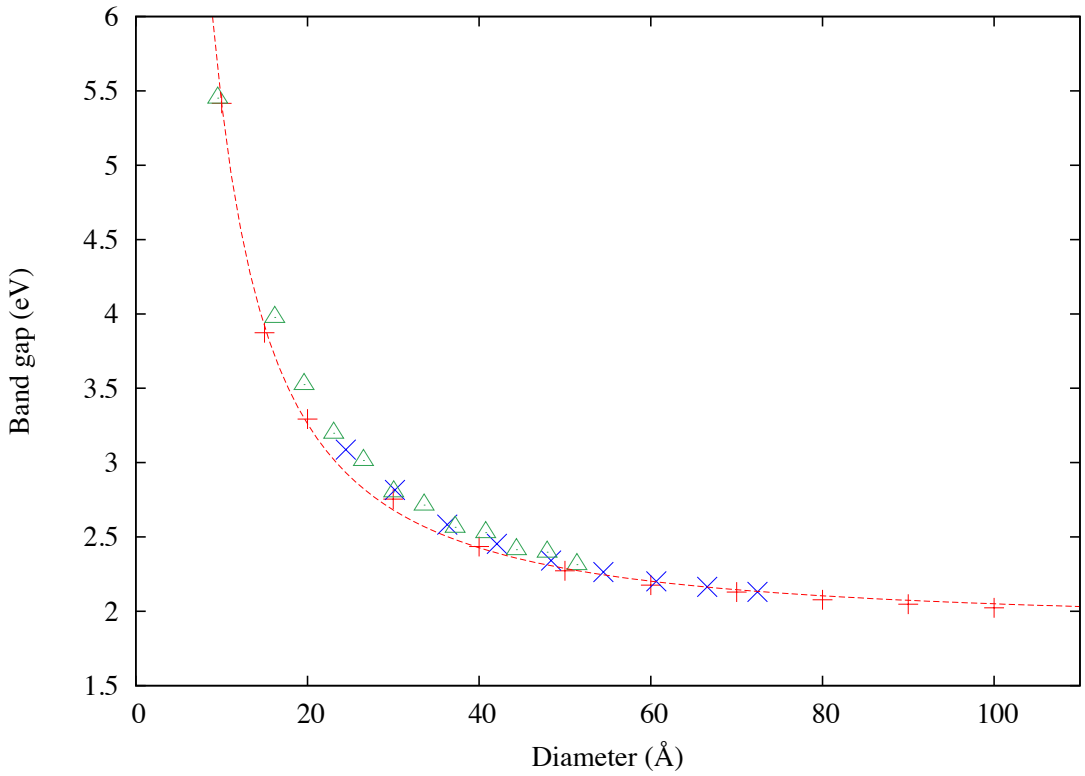

Figure 8.2: sp^3s^* independent-particle band gaps as a function of diameter. Our model is given by red pluses, green triangles represent data from Lippens and Lannoo[100] and the blue crosses represent data from Lee and coworkers[24]. Our model data is fit with an expression of the form $E_g(d) = 1/(ad^b) + E_{g,\text{bulk}}$.

Our data in Figure 8.2 have been fit using an expression for the confinement energy of a spherical nanocrystal in an infinite potential, as given by effective mass theory[188]. The energy of the lowest electron and hole levels is given by $E = 2\hbar^2\pi^2/m^*_{e,h}d^2$, where m^*_e (m^*_h) is the electron (hole) effective mass and d is the diameter of the nanocrystal. Fitting the data in Figure 8.2 with a function of the form, $E_g(d) = 1/(ad^b) + E_{g,\text{bulk}}$, we find a value of 1.37 for the exponent b, which differs from the $1/d^2$ scaling predicted by effective mass theory.

We attribute this to our model's correct description of the atomic T_d symmetry of the system, in comparison to the assumption of spherical symmetry (which is particularly important in the small-size limit), and to the more realistic bulk band structure dispersion of our tight-binding model in comparison to the parabolic band dispersion of the effective mass approximation.

8.2 Surface Passivation of Dangling Bonds

8.2.1 Band Gap Sensitivity to the Passivating Energy

Nanocrystals synthesised in solution utilise coordinating, organic ligands to terminate their growth and render them soluble in solvents. As well as their role in synthesis, ligands also act to passivate dangling surface bonds[189]. The dangling bonds of unterminated surface atoms lead to surface states with energies between that of the highest occupied state and lowest unoccupied state, and act to trap charge carriers, leading to poor quantum yields[59]. By saturating these dangling bonds, ligands therefore reduce the number of mid-gap trap states available as non-radiative recombination centres and improve the photoluminescence of the nanocrystal.

The tight-binding formalism facilitates the use of an orthogonal transformation to hybridised sp^3 orbitals, aligned along the bonding directions[178]. Mid-gap states can subsequently be passivated by the approximate formation of bonding and anti-bonding states between the dangling bonds and the vacuum at an energy determined by the passivation energy parameters given in Equations (C.4) and (C.5)[177] in Appendix C. The nature of the passivating species is not specified in this approach and the passivation energy parameters can be taken to be any values that clear the band gap of trap states. Indeed, it has been reported in the literature that interior states are insensitive to the choice of passivation energy[177; 190]. The specific choice of energy is therefore arbitrary and our model simulates an ideal nanocrystal surface, in which all dangling bonds have been fully passivated.

We seek to verify that the interior states are insensitive to the choice of passivation energy, specifically by investigating the effect of this parameter on the band edges. In Figure 8.3 we quantify the effect of the passivation energy on the independent-particle gap. In each calculation, the passivating energy is taken to be the same for all dangling bonds. It was found that for CdSe nanocrystals, passivation energies of

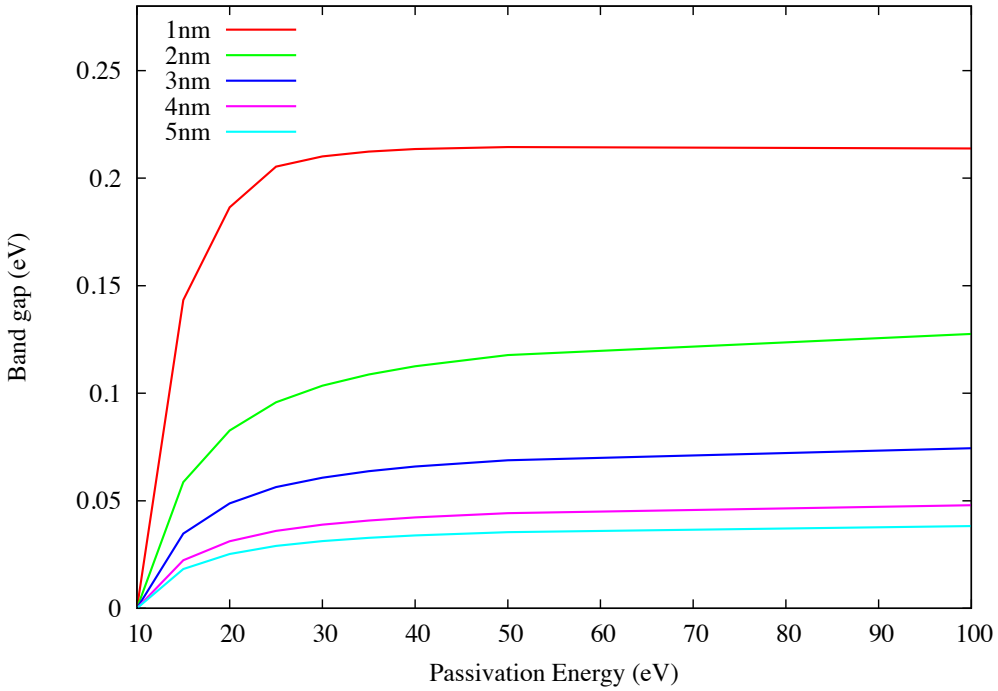

Figure 8.3: Independent-particle gap as a function of passivating energy. The y-axis zero is taken to be the value of the independent-particle gap for a passivating energy of 10 eV.

less than 10 eV were insufficient to fully remove trap states from the band gap and hence are not included in the figure.

Figure 8.3 shows that increasing the passivation energy parameter acts to widen the independent-particle gap, and that this widening saturates for large values. The sensitivity to the passivation energy parameter also decreases with increasing nanocrystal diameter, which we attribute to the decreasing surface to volume ratio. Interestingly, the rate of saturation in the independent-particle gap decreases with size in all but the smallest system.

Analysis of Figure 8.3 suggests that any value of passivating energy equal to or greater than 10 eV can be utilised. This offers some empirical flexibility when comparing to experimental results and provides a simple way in which to modify the surface potential to broadly account for the nature of the ligands and surface conditions of a given nanocrystal.

8.2.2 Effect of the Passivation on the Band-Edge Independent-Particle States

In Figure 8.4 we plot absorption spectra for nanocrystals with diameters of 2 nm (left panel) and 6 nm (right panel), as a function of passivation energy. In both panels, the spectra have been rigidly shifted such that the onsets line up, allowing for a better comparison of the spectral profiles (as we have shown in Figure 8.3, an increase in the passivation energy causes a widening of the independent-particle gap).

For a nanocrystal with a diameter of 2 nm, increasing the passivating energy from 10 eV to 20 eV causes an increase in the strength of the lowest transition in the optical absorption spectrum. There is also a change in the strengths of many of the low-energy transitions and this behaviour is observed as the passivating energy is increased from 25 eV to 50 eV, although the changes are less pronounced in this range. In general, consistent spectral features remain discernible for passivating energies of 25 eV and above.

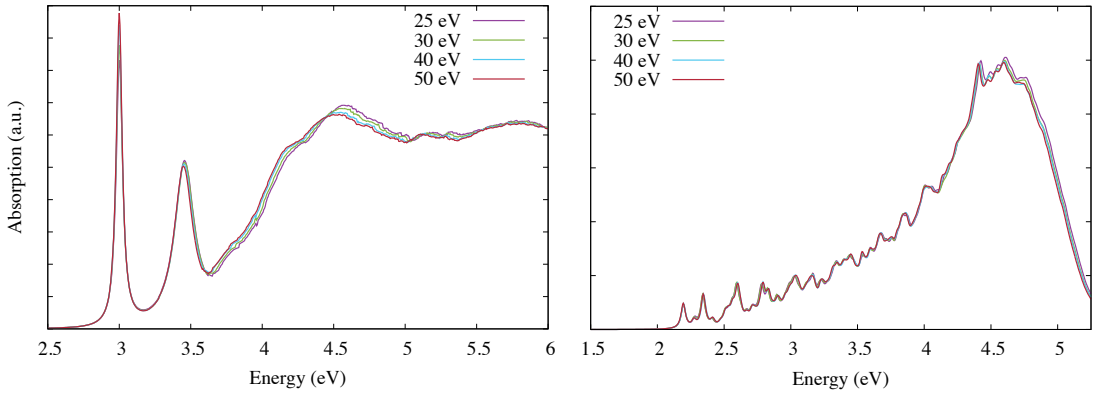

Figure 8.4: Absorption spectra for CdSe nanocrystals with diameters of 2 nm (left) and 6 nm (right), as a function of passivating energy. The FWHM of the spectral lines linearly increase from 40 meV to 400 meV between 3 eV and 4.5 eV in the left panel, whereas they are fixed at 40 meV in the right panel.

When an energy-dependent line width is utilised, small differences in transition strengths are smeared out, demonstrating that our choice of passivating energy does not affect our comparisons with experimental spectral profiles. This is shown for a nanocrystal with a diameter of 2 nm in the left panel of Figure 8.4. As one might expect, the sensitivity of the spectral features to the passivating energy diminishes as the nanocrystal size increases. For example, in a nanocrystal with a diameter of 6 nm, one finds the spectrum to be insensitive to passivation energies of 15 eV and above. The effect of the passivating energy on the spectrum of a nanocrystal with a diameter of 6 nm is shown in the right panel of Figure 8.4.

Inspection of wave function isosurfaces finds that the orientations of the wave functions are affected by the choice of passivating energy, however, the corresponding absorption spectra show only small differences in transition strengths (spectra with narrow line widths are not shown here) suggesting that the orbital angular momenta of the wave functions are conserved and the dipole matrix elements are unaffected. In summary, we find that the spectra of nanocrystals with diameters as small as 2 nm retain characteristic spectral features for passivating energies of 25 eV and above, which implies that the dipole matrix elements and therefore atomic wave functions must also be largely unchanged for the same range of passivating energies.

Values for the passivation energy used in tight-binding simulations have been found to vary from 25 eV[176] to 100 eV[105; 187] in the context of nanocrystals and self-assembled quantum dots. Having verified that the symmetries of the independent-particle states are insensitive to the choice of passivation energy parameter via analysis of the absorption spectra, we therefore choose the value that gives the best agreement with experiment where comparisons are made. This is taken to account for differences in our idealised treatment of the surface and the actual nanocrystal surface. Where comparisons are not made, we choose the lowest cited value of 25 eV.

8.3 Independent-Particle States

The independent-particle states of the tight-binding model are defined according to Equation (4.6) in Chapter 4. We show the lowest twenty occupied independent-particle states (blue) and the lowest ten unoccupied independent-particle states (red) for a nanocrystal of 6 nm in diameter, in Figures 8.5 and 8.6, respectively. In both of these figures, the radial functions of the atomic orbitals have been replaced by Gaussians to improve the aesthetic appearance. Wave functions constructed using atomic orbitals defined with a radial cut-off consistent with our tight-binding Hamiltonian are shown in Figures E.2 and E.3 in Appendix E.

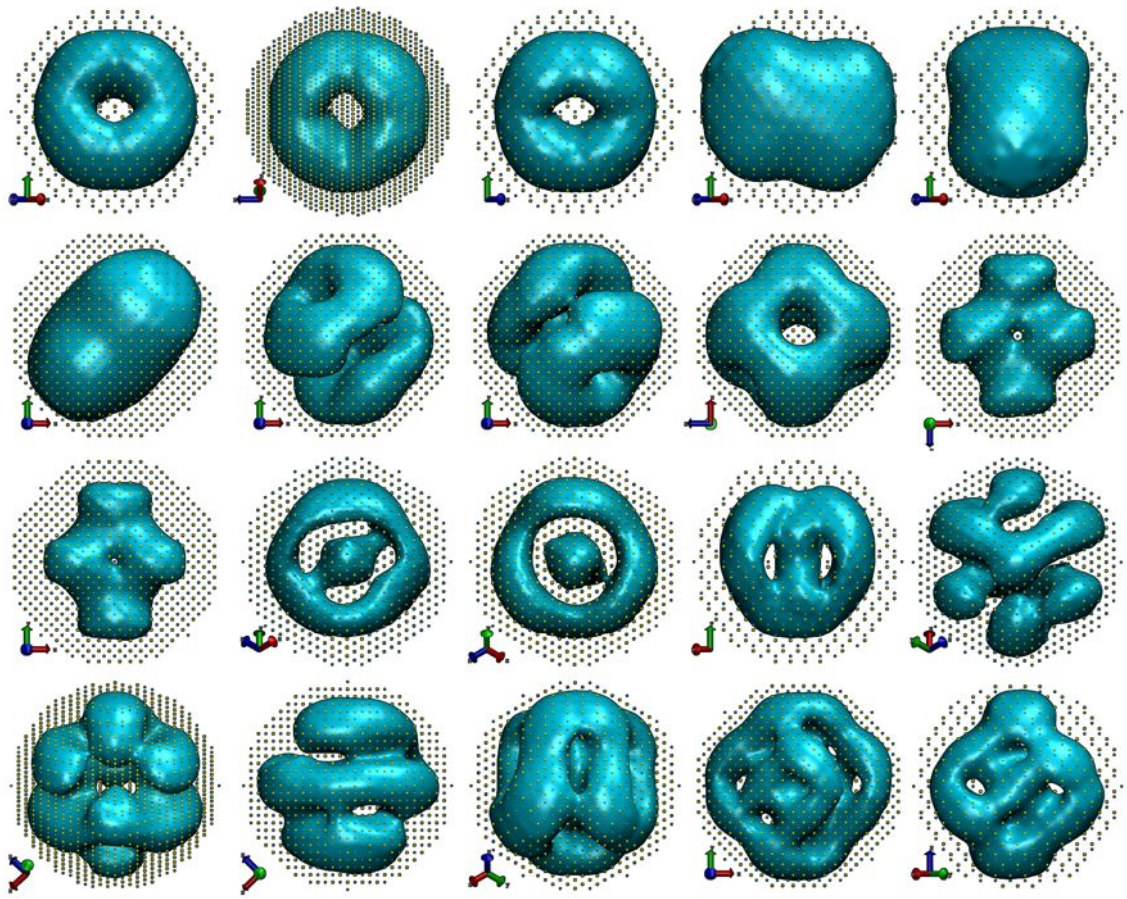

Figure 8.5: Isosurfaces, $|\Psi_i(\mathbf{r})|^2$, of the lowest twenty occupied states for a nanocrystal with a diameter of 6 nm. States are ordered from top left to bottom right.

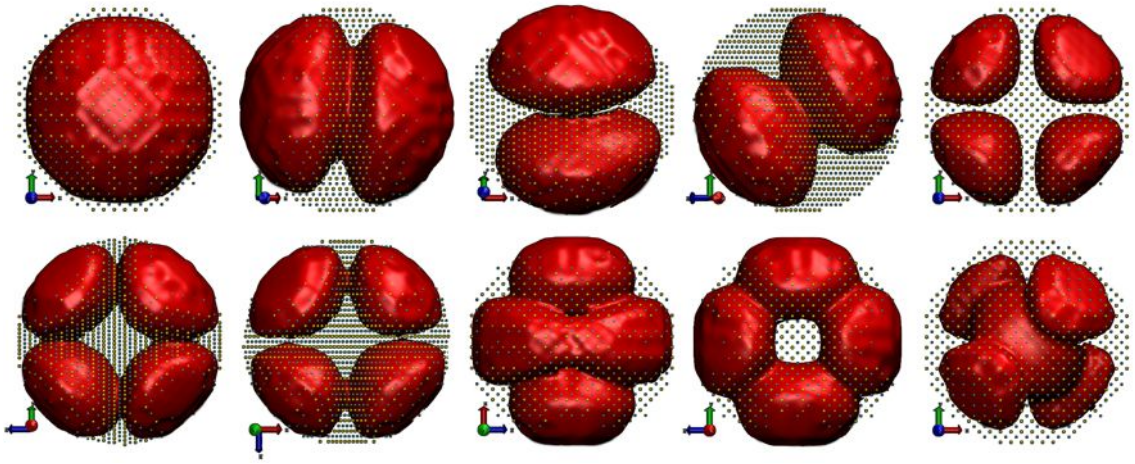

Figure 8.6: Isosurfaces, $|\Psi_i(\mathbf{r})|^2$, of the lowest ten unoccupied states for a nanocrystal with a diameter of 6 nm. States are ordered from top left to bottom right.

Figures 8.5 and 8.6 show wave functions that are delocalised throughout the volume of the nanocrystal and exhibit high symmetries. In Figure 8.7, we show the relative contribution of s and p orbitals to the functions presented in the prior figures, for a nanocrystal with a diameter of 6 nm. Figure 8.7 shows that the unoccupied states depicted in Figure 8.6 are predominantly comprised of s orbitals. This percentage decreases with increasing state index and reflects that higher unoccupied states are increasingly derived from **k**-points further from Γ. Figure 8.7 also shows that the occupied states depicted in Figure 8.5 predominantly derive from atomic p orbitals, although the exact ratio of $p_x : p_y : p_z$ varies between states. In both instances, these observations are consistent with what is found in bulk CdSe[191; 192]

8.3.1 Band-Edge Energy Levels

The presence of atomistic structure in our tight-binding model means that our Hamiltonian and its eigenstates capture the T_d crystal symmetry of the zincblende lattice. This gives us direct information regarding the energy level degeneracies that we expect to find in our nanocrystals. Indeed, the energy level degeneracy of a given

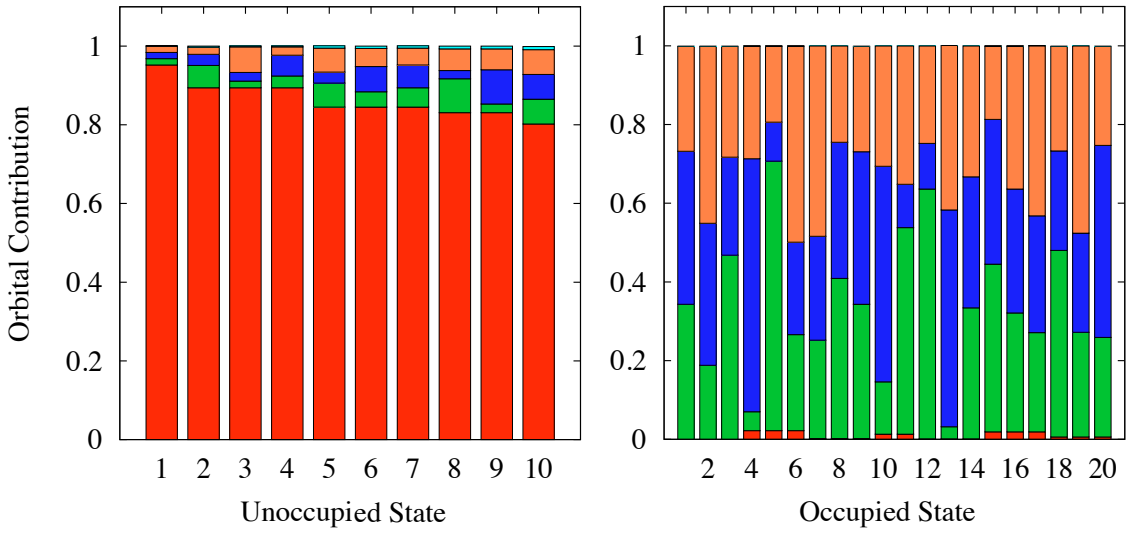

Figure 8.7: Orbital contributions to the lowest twenty occupied states and the lowest ten unoccupied states in a CdSe nanocrystal with a diameter of 6 nm. The key is as follows: s in red, p_x in green, p_y in blue, p_z in orange and s^* in cyan.

state is equal to the dimension of its irreducible representation[163][1]. The T_d character Table 6.1, given in Chapter 6, shows that the point group contains A, E and T irreducible representations, implying that CdSe nanocrystals with the zincblende structure will exhibit eigenstates that are singly, doubly and triply degenerate. This is observed in the quantum size levels presented in Figure 8.8.

All of our simulations have been done for nanocrystals with anion centres. It is expected that nanocrystals with cation centres will have the same symmetry and therefore degeneracies but slightly different state energies, whereas nanocrystals centred on the middle of bonds will exhibit symmetry breaking, lifting the state degeneracies and leading to small energy level splittings[187].

Figure 8.8 shows the energy levels of the lowest 20 occupied and 20 unoccupied states for a CdSe nanocrystal with a diameter of 6 nm. The labels to the left denote the state degeneracy and the labels to the right indicate the lowest angular momentum of the corresponding state. Coefficients with values less than 0.1 are not included in the symmetry assignments[116].

[1] An irreducible representation is a matrix containing information on the symmetry properties of the state.

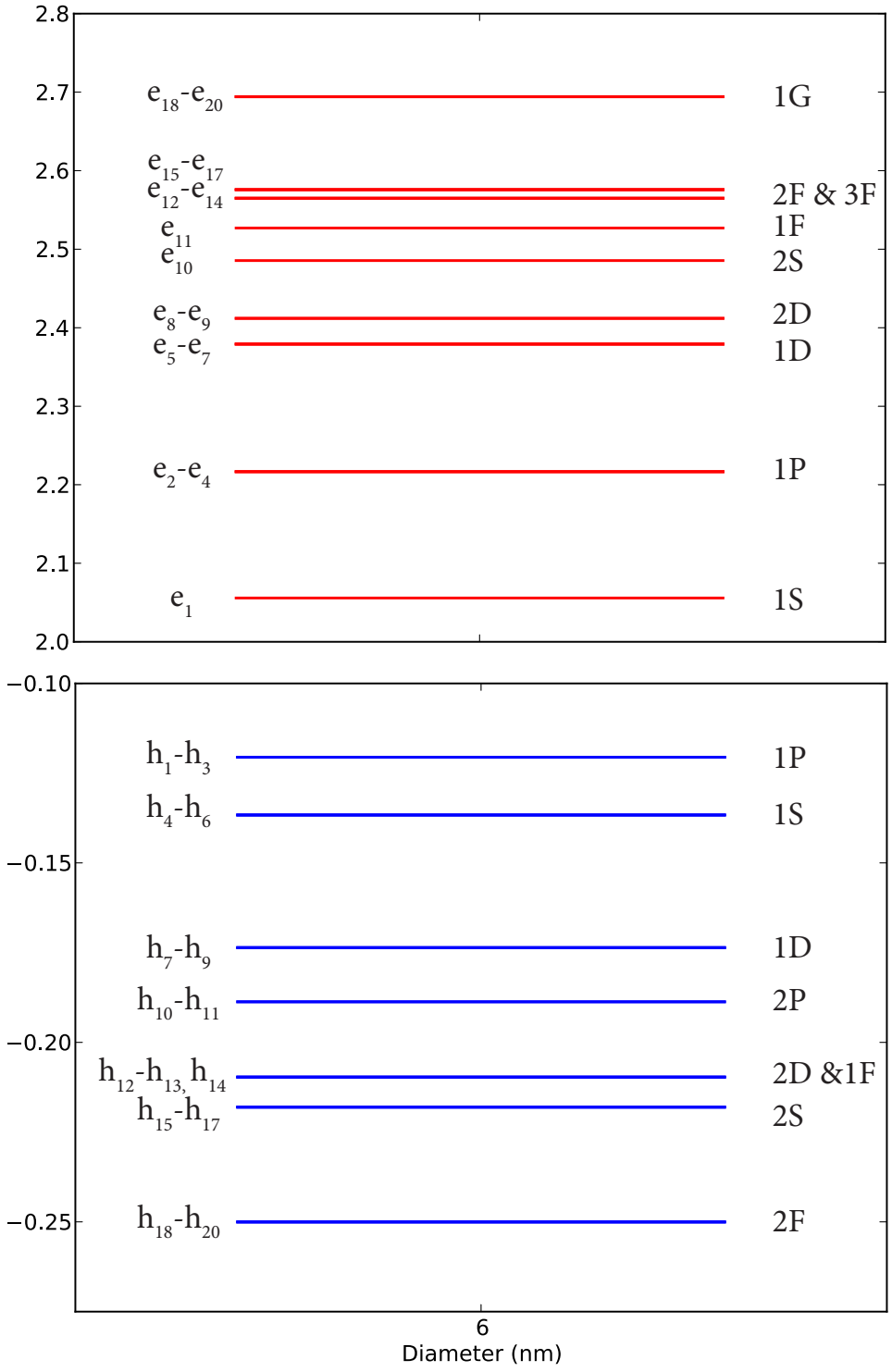

Figure 8.8: Level scheme for a CdSe nanocrystal with diameter of 6 nm. Level degeneracies are indicated on the left and the lowest angular momentum component is indicated on the right. h_i is used to denote occupied states whereas e_i is used to denote unoccupied states.

We quantify the global angular momenta that comprise each state by decomposing

State	Envelope Components
e_5	(D,1) (D,-1) (D,2) (D,-2)
e_4	(P,0) (P,-1) (P,1)
e_3	(P,-1) (P,1) (P,0)
e_2	(P,0) (P,-1) (P,1)
e_1	(S)
h_1	(P,0) (D,0) (P,-1) (P,1) (D,2) (D,-2)
h_2	(P,0) (P,-1) (P,1) (D,0) (D,2) (D,-2) (D,1) (D,-1)
h_3	(P,-1) (P,1) (P,0) (D,2) (D,-2) (D,0) (D,1) (D,-1)
h_4	(S,0) (P,-1) (P,1)
h_5	(P,-1) (P,1) (S,0) (P,0) (D,1) (D,-1) (F,3) (F,-3) (F,-2) (F,2)

Figure 8.9: A table showing the composition of global orbital angular momenta that comprise the lowest five occupied (h_i) and unoccupied (e_i) envelope states of a CdSe nanocrystal with a diameter of 6 nm. Spherical harmonics are denoted by their quantum numbers, (L, m_L), and are arranged in order of descending magnitude from left to right.

the globally-varying component of the atomic wave function, referred to as the envelope function, with a basis of spherical harmonics. The envelope component of the wave function is defined as the sum of the tight-binding coefficients at each atomic position. These envelopes can then be projected onto a spherical harmonic basis and the coefficients of this basis can be used to quantify how much each spherical harmonic, with angular momentum L, contributes to the envelope state. Orbital angular momenta for the envelopes of the lowest five occupied and lowest five unoccupied states are given in Table 8.9.

Figure 8.8 shows that the lowest unoccupied state is non-degenerate, with envelope angular momentum S and is followed by a triply-degenerate P state. Inspection of the lowest twenty unoccupied states reveals that the envelope functions are sequentially defined by the angular momenta: S, P, D, S, F, G. This was found to be characteristic of CdSe nanocrystals with diameters ranging from 3 nm to 6 nm and are consistent with what one finds with $\mathbf{k} \cdot \mathbf{p}$ theory[193].

Figure 8.8 also shows that the lowest occupied states are comprised of two sets of triply degenerate levels, followed by a large energetic gap. The triply-degenerate, lowest occupied state has angular momentum P and the next triply-degenerate

occupied state has angular momentum S. This is same for all CdSe nanocrystals studied, with diameters ranging from 3 nm to 6 nm.

There is, however, a question regarding the reliability of this envelope description for the occupied states. The summation of p orbital coefficients at any given atomic site can lead to numerical cancelations and create an erroneous representation of the envelope function at that point. With that said, the angular momenta that we obtain for the lowest six occupied states are consistent with what Lee and coworkers found using the sp^3s^* model[24]. Furthermore, a visual inspection of the corresponding isosurfaces in Figure 8.5 shows states that look broadly consistent with the assignments, rather than showing no similarities. We therefore adopt these assignments and examine whether they are consistent with the inter-band selection rule for optical transitions.

We note that the angular momenta assignments of the lowest six occupied states are, however, reversed in comparison to results found with pseudo-potential[116] and $sp^3d^5s^*$ tight-binding calculations[176]. Lee and coworkers suggested that this may be due to the absence of spin-orbit coupling in the model.

8.3.2 An Envelope Description of Inter-band Transitions

In this section, we proceed to use the orbital angular momentum assignments of the lowest occupied and unoccupied envelope functions to describe the band-edge transitions of CdSe nanocrystals. In spherically symmetric systems, the inter-band selection rules follow from the orbital angular momenta of the initial and final states that comprise the transition. Allowed transitions can only occur between initial and final states with the same orbital angular momentum[27; 194][2].

[2]The $\Delta L = 0$ selection rule can be shown if one assumes that the dipole matrix operator only operates on the Bloch component of the wave function, allowing the envelope function to be factorised such that, $|\langle u_{e,0}\chi_e|\mathbf{e}\cdot\mathbf{r}|u_{h,0}\chi_h\rangle|^2 \approx |\langle u_{e,0}\ |\mathbf{e}\cdot\mathbf{r}|u_{h,0}\rangle|^2|\langle\chi_e|\chi_h\rangle|^2$, and $|\langle\chi_e|\chi_h\rangle|^2 = \delta_{L,L'}$ via orthonormality.

Figure 8.10 shows the calculated absorption spectrum for a CdSe nanocrystal of 6 nm in diameter, both with and without spectral line broadening. The relative strengths of the transitions are indicated by the magnitudes of the red peaks and the lowest four transitions have been schematically depicted in a level diagram, given in Figure 8.12.

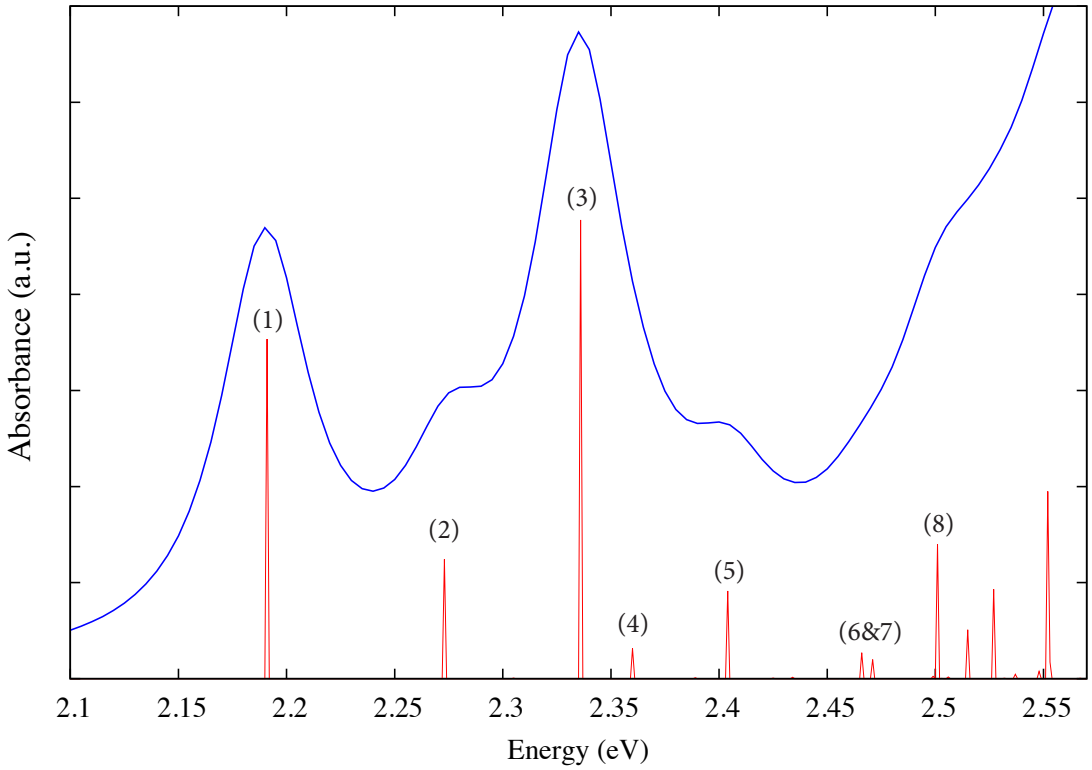

Figure 8.10: Absorption spectrum for a CdSe nanocrystal with a diameter of 6 nm. Red lines show the inter-band transitions and the blue line shows the same transitions convolved with Lorentzian functions (FWHM of 50 meV). The states involved in the labeled transition are schematically depicted in Figure 8.12 and given in Table 8.11.

The results depicted schematically in Figure 8.12 indicate that allowed transitions do indeed occur between initial and final states that share the same angular momentum. Inspection of Table 8.9 shows that there is a large amount of angular momentum mixing per state. The strength of a given transition is therefore determined by the percentage of angular momentum common to the initial and final states. Additionally, the intensities of the transitions are increased by the high level of

Allowed Transition	Hole States	Electron States	Lowest Envelopes
1	(h_4, h_5, h_6)	(e_1)	1S-1S
2	(h_{15}, h_{16}, h_{17})	(e_1)	2S-1S
3	(h_1, h_2, h_3)	(e_2, e_3, e_4)	1P-1P
4	(h_{30}, h_{31}, h_{32})	(e_1)	3S-1S
5	(h_{10}, h_{11})	(e_2, e_3, e_4)	2P-1P
6	(h_{18}, h_{19}, h_{20})	(e_2, e_3, e_4)	3P-1P
7	(h_{21}, h_{22}, h_{23})	(e_2, e_3, e_4)	4P-1P
8	(h_{24}, h_{25}, h_{26})	(e_2, e_3, e_4)	5P-1P

Figure 8.11: The first eight allowed transitions labelled in Figure 8.10, for a nanocrystal of 6 nm in diameter, predicted with our tight-binding model.

degeneracy in the occupied states, as indicated in Table 8.11. For example, the third transition is comprised of a triply degenerate occupied state and triply degenerate unoccupied state, leading to a nine-fold degenerate transition.

Despite the ordering of occupied states 1 to 6, shown in Figure 8.8, the lowest allowed transition remains 1S-1S, followed by 2S-1S and 1P-1P, which is in broad agreement with other models[21; 116; 195]. This is because the splitting between the two lowest unoccupied states is larger than the splitting between the two lowest occupied states.

In summary, the orbital angular momenta we find from decomposing our tight-binding envelope states are consistent with the inter-band selection rule and provide an intuitive explanation of the band-edge transitions in CdSe nanocrystal absorption spectra. Although a direct comparison with other models is unfortunately hampered by a lack spin-orbit coupling in our implementation, the basic S and P assignments are in broad agreement. This provides a method for the evaluation the transitions in CdSe nanoplatelets in terms of the orbital angular momenta of the envelope functions.

In the final section of this chapter, we compare nanocrystal spectra computed in the independent-particle approximation to available experimental spectra.

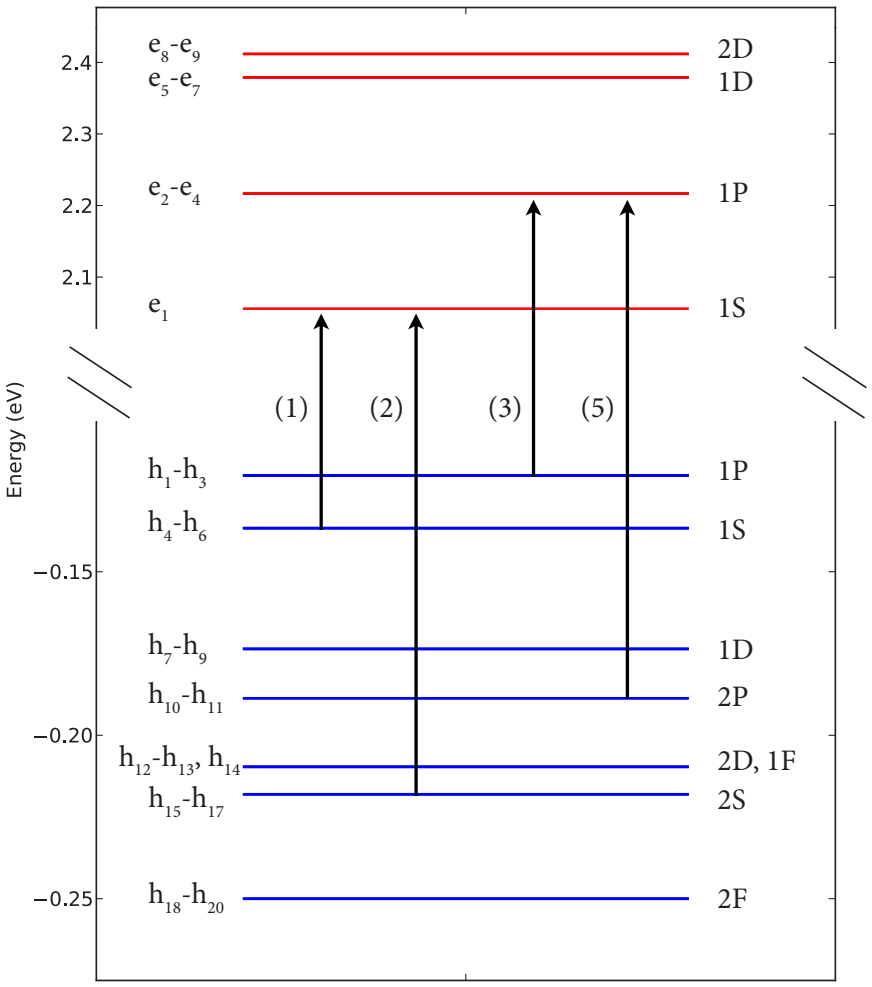

Figure 8.12: Schematic representation of allowed inter-band transitions between the lowest twenty occupied and twenty unoccupied levels of a CdSe nanocrystal, 6 nm in diameter. State degeneracies are noted by the labels to the left, whereas the lowest envelope angular momentum of each state is labelled on the right. The fourth, allowed transition is not listed as it involves higher occupied states.

8.4 Optical Absorption Spectra of CdSe Nanocrystals

8.4.1 Comparison to Experimental Spectra

Figures 8.13 and 8.14 show comparisons between experimental absorption spectra for CdSe nanocrystals of varying diameters and absorption spectra calculated using the sp^3s^* model, in the independent-particle approximation given by Equation (4.26)

in Chapter 4. All calculated data has been redshifted by 0.1 eV to account for the effect of temperature on the band gap, and a simple approximation for the Coulomb binding energy of lowest exciton state has also been applied to better-facilitate a comparison with the experimental data[188]. This redshifts the independent-particle spectra by an additional energy, $E_c = 3.572/(\epsilon_\infty d)$, where d is the nanocrystal diameter and $\epsilon_\infty = 6.23$ is the high-frequency dielectric constant of CdSe[102]. A polarisation vector, $\hat{\mathbf{e}} = (1, 1, 1)$, is used in all instances.

The calculated spectrum for a nanocrystal with a diameter of 6.8 nm is shown in green in Figure 8.13. The transitions are convolved with Lorentzian functions with FWHM of 50 meV to simulate spectral line broadening and the spectrum is normalised such that the lowest transition has the same magnitude as the lowest transition in the experimental spectrum. As one can see in the left panel of Figure 8.13, the position and profile of the absorption onset agrees well with the experimental spectrum, however, the relative intensities of all but the lowest peak in the calculated spectrum appear to be too large in relation to experiment.

The agreement between the calculated and experimental spectra can be significantly improved by utilising a line broadening that increases linearly as a function of transition energy[196]. This is shown by the blue line in the right panel of Figure 8.13. Variable broadening is justified as higher-energy transitions are dependent on nanocrystal shape, whereas the lowest-energy transitions only depend on the system volume[197]. In ensembles that exhibit both size and shape distributions, one would therefore expect to observe a spectral line width that increases with transition energy, particularly as the joint density of states also increases with transition energy.

A comparison of experimental and calculated absorption spectra for nanocrystals ranging in diameter from 3.1 nm to 6.8 nm is presented in Figure 8.14. All calculated spectra utilise energy-dependent line broadenings. This is applied linearly, ranging from 50 meV at the onset to a maximum of 500 meV at a transition energy of 4 eV

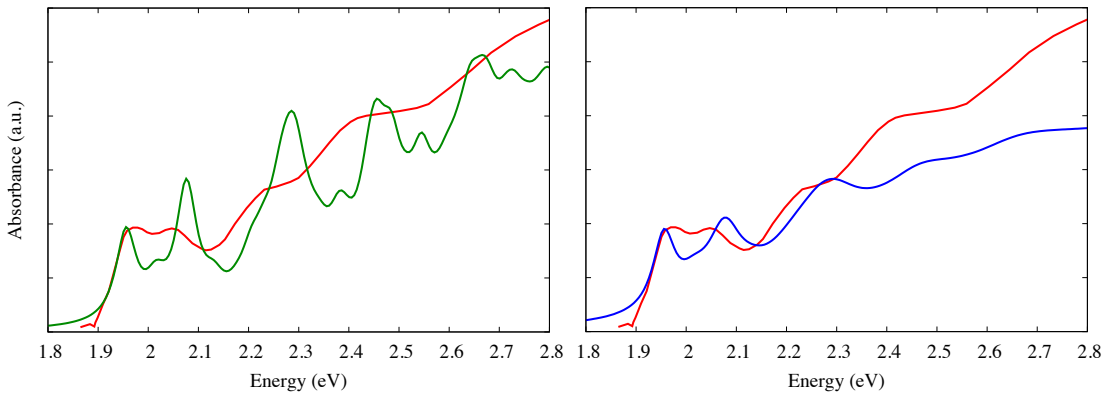

Figure 8.13: Comparison between an experimental absorption spectrum and the independent-particle absorption spectrum calculated using our sp^3s^* model ($\hat{\mathbf{e}} = (1, 1, 1)$), for a CdSe nanocrystal with a diameter of 6.8 nm. The red lines correspond to the experimental absorption spectrum [198], while the green and the blue lines correspond to absorption spectra computed using the sp^3s^* model. A FWHM of 50 meV is used for the green spectrum, whereas an energy-dependent FWHM varying from 50 meV to 300 meV is used in the blue spectrum.

(and fixed thereafter). The corresponding spectra computed with a fixed line width of 50 meV are presented in Figure E.5 of Appendix E. One could alternatively vary the line width nonlinearly, according to the scaling of the joint density of states with energy, however all treatments are arbitrary and we see a sufficient smearing of features with a line width that varies linearly with transition energy.

The comparisons reveal some general features of the sp^3s^* model. Figure 8.14 shows that for all sizes, our tight-binding model reproduces the characteristic features of the band-edge absorption spectrum: A large initial peak, a second peak that is smaller in magnitude than the first peak in the small-size limit and increases in magnitude as a function of increasing nanocrystal diameter, and a larger, broadened third peak.

The transition energy and profile of the first peak are well-reproduced for a range of nanocrystal diameters. This is found using passivating energies between 15 eV and 25 eV. We have, however, exploited size distributions $\sim 5\% - 10\%$, associated with nanocrystal ensembles, to improve agreement between the experimental and

computed onsets in some instances. It may be the case that the simple effective mass expression underestimates the magnitude of the excitonic binding energy for a range of sizes and that a many-body treatment will improve agreement in the optical gaps without the need to revert to size arguments.

The transition energy of the second transition peak is systematically overestimated in all spectra, although on average, this discrepancy reduces with increasing size. The size-dependent, rigid shift applied to the independent-particle spectra is, however, only valid for the lowest excitonic transition. One may observe a change in the energy separation between the first and second peak following the use of a many-body formalism.

There could be several reasons for the discrepancy in the energy and magnitude of the second peak. The most pertinent is the lack of spin-orbit coupling in our model. This effect is systemic rather than sample-specific, such as the choice of ligand species. Spin-orbit coupling has the effect of modifying the symmetry of the nanocrystal wave functions, which can consequently affect the dipole matrix elements that determine the optical transitions[194]. The change in symmetry will also lead to a splitting amongst degenerate, occupied states[199]. These effects may be sufficient to account for the differences observed in Figure 8.14.

Experiments have also shown that the choice of passivating species can affect both the magnitude and transition energy of the second absorption peak, while the first peak is relatively insensitive to the passivating ligands[200]. The same study showed that the transition energy of the second peak is less sensitive to the surface species as a the nanocrystal diameter increases, which is consistent with observations in Figure 8.14.

Finally, we observe that the oscillator strengths of transitions with energies above that of the second peak are underestimated by our tight-binding model. This could be a consequence of our expansion of the dipole matrix, which is used to calculate the

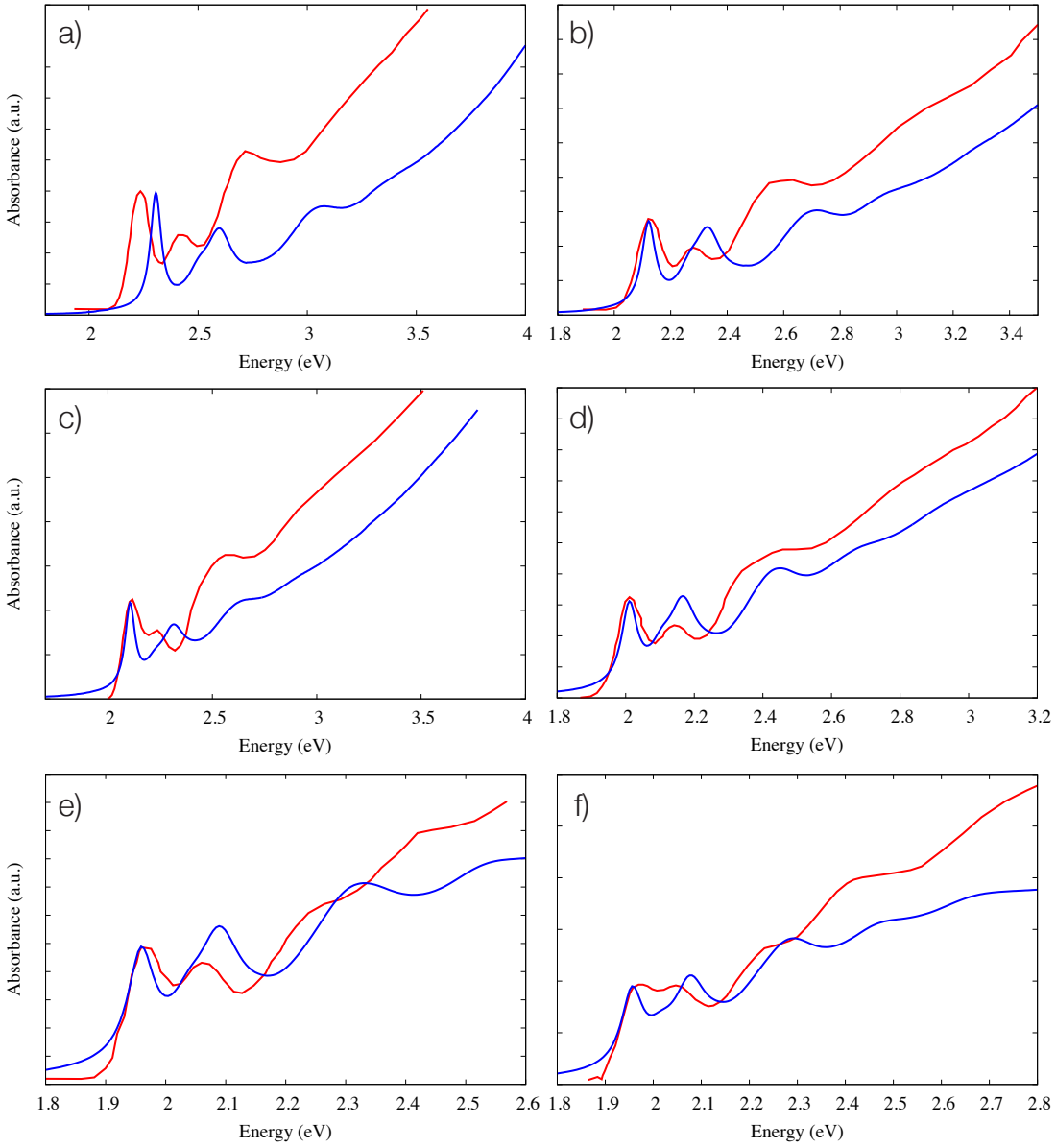

Figure 8.14: Comparison between experimental and calculated absorption spectra, for a range of nanocrystal sizes. Experimental spectra are shown in red whereas calculated spectra are shown in blue. All calculated spectra are redshifted by 0.1 eV to account for finite temperature and by an energy, $E_c = 3.572/(\epsilon_\infty d)$. Experimental spectra a), b), d) and e) are reproduced from reference [200] (zincblende nanocrystals), while experimental spectra b) and f) are reproduced from reference [198] (wurtzite nanocrystals). The plots correspond to CdSe nanocrystals with diameters: a) d_E=3.1 and d_C=3.5 nm (15 eV), b) d_E=4.1 and d_C=4.3 nm (15 eV), c) d_E=4.8 and d_C=4.8 nm (25 eV), d) d_E=5.2 and d_C=5.5 nm (15 eV), e) d_E=6.3 and d_C=6.3 nm (15 eV) and f) d_E=6.8 and d_C=6.8 nm (25 eV). Here, d_E is the experimentally-referenced diameter and d_C is the simulated nanocrystal diameter. The value in the brackets refers to the passivation energy used for each simulation.

transition strengths. Calculated spectra are computed using the product of the tight-binding coefficients with the atomic positions only, discarding local orbital variation (see Equations (4.31) - (4.34) in Chapter 4). Within this approximation, one only retains the global variation in the dipole matrix, which we refer to as the envelope component of the dipole matrix. It is possible that upon inclusion of more terms in the dipole matrix, one may see a greater increase in the oscillator strengths of high-energy transitions relative to lowest transition. This would improve agreement between calculated and experimental spectra, as we normalise to the strength of the lowest transition.

With that said, Schulz and coworkers find that for an orthogonal basis set, second-nearest neighbour contributions to the dipole matrix elements are negligible and that in general, orbital contributions to the dipole matrix elements are 30 times smaller than the envelope contribution, in III-V quantum dots[145]. We therefore would not expect the inclusion of orbital terms in the dipole matrix to change the overall form of the calculated spectra. Alternatively, it is plausible that the agreement in the high-energy region of the spectrum could also be improved with the inclusion of spin-orbit coupling.

8.5 Summary

In summary, we have demonstrated that our tight-binding model captures the T_d symmetry of the system with an analysis of the level degeneracies and orbital composition of the band-edge states. The unoccupied states were shown to have well-defined symmetries that are in agreement with other models, while the occupied states were shown to have mixed symmetries, as one would expect from pseudo potential and effective mass calculations.

A difference in the ordering of the two lowest sets of occupied states is found in comparison to other models and is attributed to the absence of spin-orbit coupling

in our calculations. This demonstrates the importance of comparing predictions with other models and methodologies. In the following chapter, we therefore make a direct comparison of our tight-binding calculations with $\mathbf{k} \cdot \mathbf{p}$ calculations in the absence of spin-orbit coupling to confirm the robustness of our predictions for CdSe nanoplatelets.

We have demonstrated the connection between the symmetry of the wave functions and the strengths of the dipole matrix elements, illustrating why a knowledge of the band-edge states is important in forming a description of low-energy transitions, and have shown that the spectral profiles of our calculated absorption spectra are insensitive to the choice of passivating energy, suggesting that our simplified treatment of surface passivation allows for a robust comparison with experimental spectra.

Spectral calculations show that the tight-binding model is capable of reproducing the characteristic features of the low-energy region of the optical absorption spectrum in the independent-particle approximation. Comparisons with experiment show good agreement for a range of sizes, following a rigid shift to account for the binding energy of the lowest exciton state. This suggests that the independent-particle properties of this model provide a suitable basis for two-particle calculations of the optical gap and the lowest excitonic transition energies, using our Bethe-Salpeter implementation.

Chapter 9

Electronic and Optical Properties of Cadmium Chalcogenide Nanoplatelets

In this chapter, we apply the sp^3s^* tight-binding model to the study of the electronic and optical properties of CdSe nanoplatelets in the independent-particle approximation. In analogy to studies of CdSe nanocrystals, we determine the independent-particle band gap dependence on nanoplatelet thickness, visualise the atomic wave functions of the band-edge states and perform the first calculations of the optical absorption spectrum. Tight-binding calculations are compared with a 14-band $\mathbf{k} \cdot \mathbf{p}$ model and with experiment.

9.1 Electronic Structure of CdSe Nanoplatelets

Introduction

Colloidal nanoplatelets represent a new class of quasi two-dimensional, zincblende, colloidal nanostructures[66]. Nanoplatelets exhibit atomically flat surfaces that can be tuned with monolayer precision and lateral dimensions that can vary from a few nanometers[69] to several hundred nanometers[70]. This results in structures that strongly quantum confine the exciton in the dimension perpendicular to the plane, producing optoelectronic properties that have been compared to epitaxial two-dimensional quantum wells[71].

While nanoplatelets have been grown using each of the cadmium chalcogenides, CdSe is the most well-studied of the three. This is because it was the first to have its growth process refined and its zero-dimensional counterpart is the most well-studied of the cadmium chalcogenide nanocrystals. Despite several experimental studies on the synthesis and spectroscopy of both single-material and heterostructure cadmium chalcogenide platelets (see Chapter 2), there has been relatively little theoretical work done[72; 87; 95; 96; 201] and only two atomistic treatments of optoelectronic properties[95; 96].

The results of Chapter 8 demonstrate that the orthogonal NN sp^3s^* model is capable of describing the band-edge properties of CdSe nanocrystals in the independent-particle approximation. In this chapter, we therefore use our tight-binding model to perform atomistic calculations that study the evolution of the band-edge states as a function of thickness, for CdSe nanoplatelets with realistic lateral dimensions. These states are important as they subsequently determine the strengths of the dipole matrix elements which govern the transition strengths of the absorption spectrum in the independent-particle approximation. This provides a means of understanding

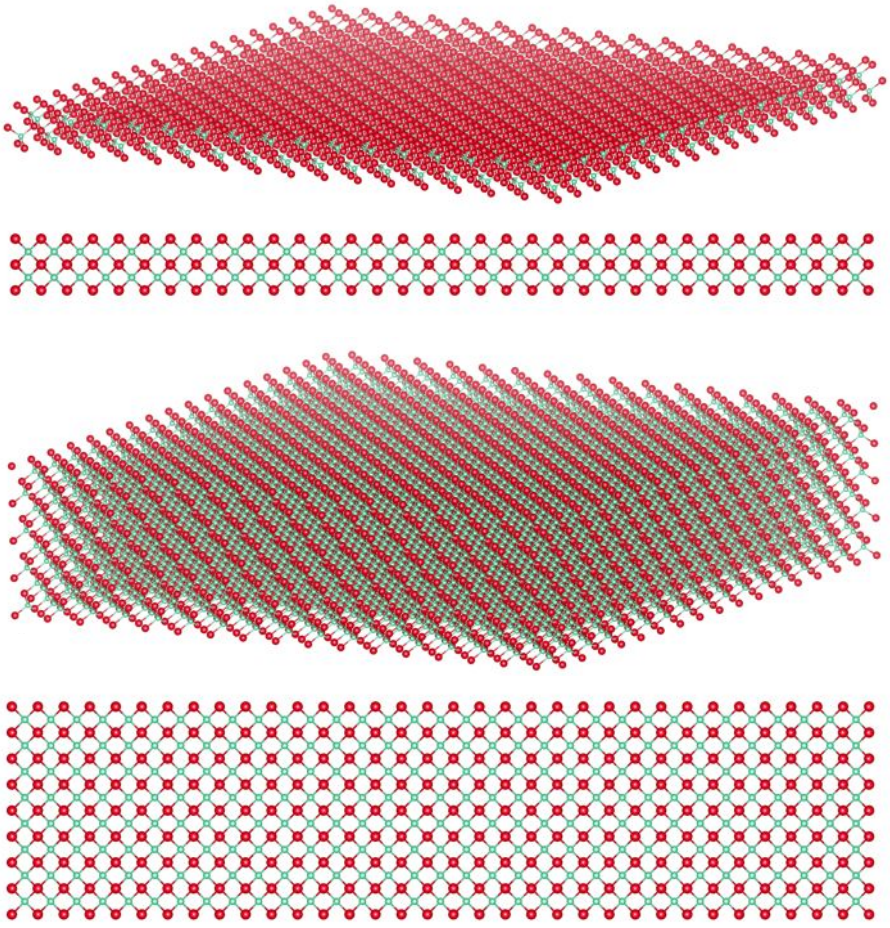

Figure 9.1: Ball and stick models of CdSe nanoplatelets with thicknesses of 2 and 8 monolayers, illustrating the smallest and largest systems considered in this study, respectively. We follow the established convention and define a monolayer as the distance between two planes of cadmium atoms.

the structure of the low-energy spectral features in the absence of the electron-hole interaction and forms a starting point with which we can begin to understand experimental observations from a theoretical perspective. This is the first theoretical study to address these features.

Our simulations define the nanoplatelet thickness in the [001] direction and terminate the basal planes with cadmium atoms, consistent with experimental observations[18]. In this study one considers systems with thicknesses in the range of 2 to 8 monolayers, with two such examples shown in Figure 9.1. Each monolayer is half the lattice constant of CdSe in thickness (a_l=0.606 nm[34]), leading to

nanoplatelets of thickness, $N_{ML}a_l/2$, where N_{ML} is the number of monolayers.

9.1.1 Effect of Finite Lateral Dimensions on the Band Gap

The large lateral extent of nanoplatelets and atomically precise surfaces make simulations well-suited to periodic boundary conditions, however while the lateral dimensions extend beyond 100 nm in some instances[70], optical studies have focussed on systems with lateral dimensions that vary between 6 nm and 35 nm[67; 79; 202]. We therefore explicitly consider nanoplatelets with finite lateral dimensions in this study.

Figure 9.2 quantifies the effect of the lateral extent on the independent-particle band gap. Quantum confinement is largest in the dimension corresponding to the nanoplatelet thickness. It is expected that the nanoplatelet will only experience weak confinement in the lateral dimensions once they exceed the two-dimensional bulk exciton Bohr radius.

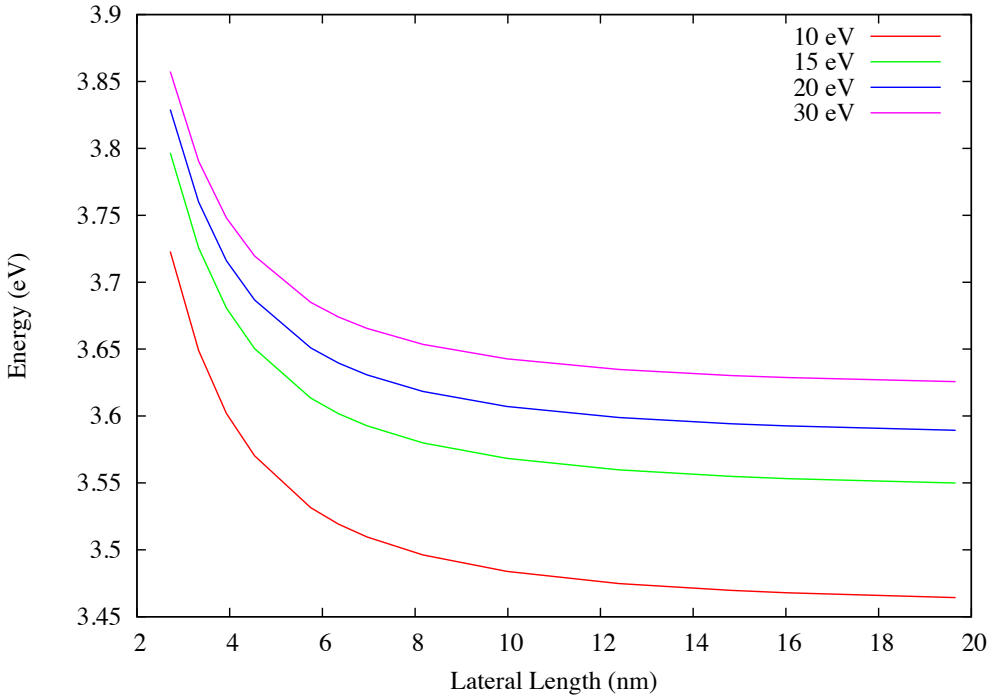

Figure 9.2: Variation in the independent-particle band gap as a function of lateral extent, for a CdSe nanoplatelet of 2 ML in thickness. Several passivation energies are included.

Thickness (ML)	Number of Atoms
2	2823
3	3946
4	5068
5	6191
6	7313
7	8436
8	9558

Table 9.1: Total number of atoms as a function of thickness, for nanoplatelets with laterals dimensions of 10 nm × 10 nm.

This is defined as $a_{B,2D} = \sqrt{(3/8)}a_{B,3D}$[67], where $a_{B,3D}$ is the three-dimensional bulk exciton Bohr radius. For CdSe the three-dimensional bulk Bohr radius is $a_{B,3D} = 5.6$ nm[203] which leads to a two-dimension value of $a_{B,2D} = 3.5$ nm.

The result of simulations examining the change in the independent-particle band gap of a two-monolayer platelet as a function of its lateral dimensions, for several passivating energies, is shown in Figure 9.2. In all cases, the lateral dimensions are equivalent such that we are simulating systems with a square planar area.

In Figure 9.2, the independent-particle band gap varies by $\sim$ 0.25 eV between 2.75 nm and 10 nm, then by an order of magnitude less between 10 nm and 20 nm. Inspection of the gradients in Figure 9.2 imply that the in-plane component of the exciton is only weakly confined for lateral dimensions of $\sim$10 nm and above. Based on these calculations we choose a value of 10 nm for the lateral dimensions of our simulated nanoplatelets. This value exceeds the two-dimensional, bulk Bohr radius and represents a realistic lateral area[204]. The total number of atoms in systems with these lateral dimensions are presented in Table 9.1, as a function of thickness. We also choose a passivating energy of 15 eV.

9.1.2 Independent-Particle Band Gap as a Function of Thickness

Figure 9.3 shows the independent-particle band gap predicted by our sp^3s^* model as a function of thickness, for CdSe nanoplatelets with lateral dimensions of 10 nm × 10 nm, and compares it to experimental data. As with the nanocrystal analysis, the effect of finite temperature on the band gap has been included using the Varshi equation given by expression (3.1) in Chapter 3. This corresponds to a 0.1 eV contraction in all calculated values. Only one experimental data point is plotted per monolayer as there is minimal variation in the values reported. A summary of values is given in Table 9.2.

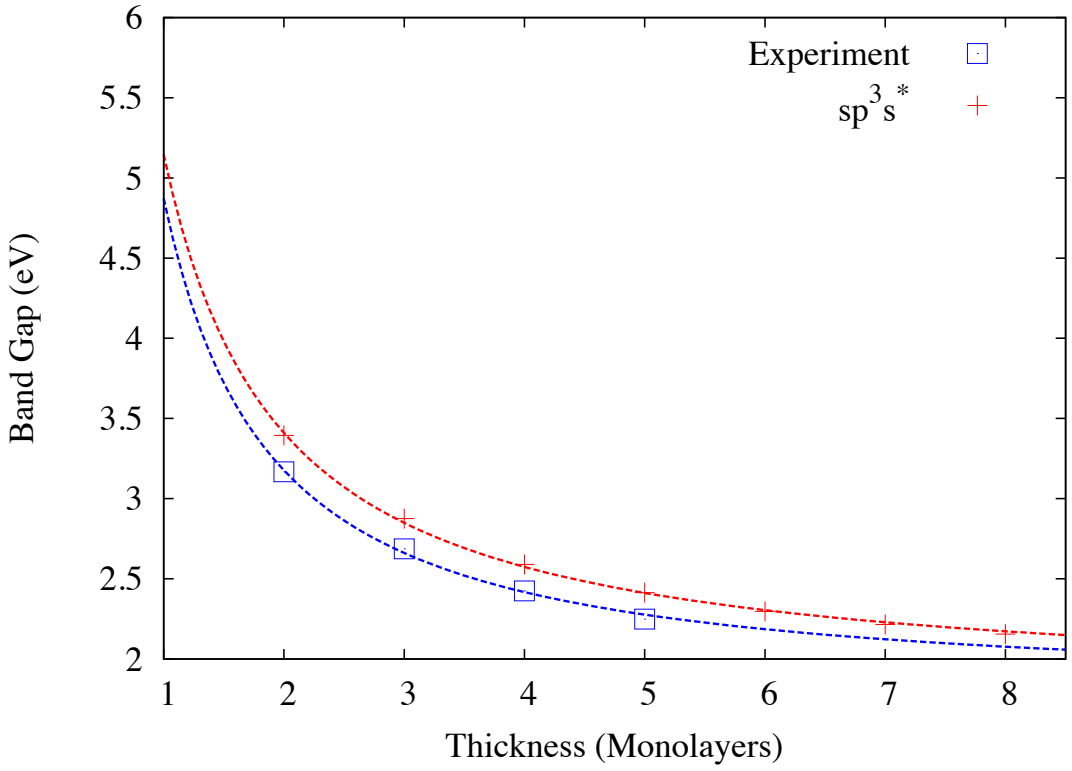

Figure 9.3: Independent-particle band gap as a function of nanoplatelet thickness, at room temperature. Red pluses represent our sp^3s^* model and the blue squares represent experimental data from reference [72].

Number of Monolayers	Wavelength (nm)	Energy (eV)
2	$391^{a,b}$	3.17
3	$461^{a,b}$	2.69
4	$511^{a,b}$, $512^{d,f}$, 513^{c}	2.42-243
5	$551^{a,b}$, $553^{c,e,f}$	2.24-2.25

Table 9.2: Experimentally-determined lowest excitonic transition for a range of CdSe nanoplatelets, all taken at room temperature: a[72](corrected for two monolayers),b[75], c[205],d[80], e[79] and f[202].

There is some controversy regarding the assignment of nanoplatelet thickness in relation to the observed optical gaps. The attribution of monolayer thicknesses was originally made using the results of an eight-band $\mathbf{k} \cdot \mathbf{p}$ model[72]. Improvements in synthesis have since lead to ensembles with greater homogeneity, making characterisation with TEM easier. Observations made by Mahler and coworkers using STEM suggest a systematic overestimation of two monolayers in thickness occurred as a result of using the $\mathbf{k} \cdot \mathbf{p}$ assignments[202]. This is contested by the group of Achtstein, who suggest that an overestimation of just one monolayer is more consistent with their TEM measurements[87]. The values given in Figure 9.3 and Table 9.2 represent the consensus in the literature and correspond to the assignment of Mahler and coworkers. This is discussed in more detail in Appendix G, following many-body calculations of the optical gap.

The red and blue curves in Figure 9.3 have been fit using an expression for the energy of confined charge carriers in a one-dimensional, infinite quantum well[66]. In this approximation, the transition energy is given by the expression:

$$\hbar\omega_n = \frac{\hbar^2 n^2 \pi^2}{2L^2}\left(\frac{1}{m_h^*} + \frac{1}{m_e^*}\right) + E_{g,\text{bulk}}, \tag{9.1}$$

where L is the thickness of the well, n denotes the transition, $m_{e,h}^*$ are the effective masses of the electron and hole, $E_{g,\text{bulk}}$ is the bulk band gap and ω is the frequency

Data	a	σ_a	b	σ_b
sp^3s^*	3.472	0.134	1.157	0.036
Experimental	3.153	0.222	1.291	0.074

Table 9.3: Fit parameters (a, b) and standard deviations (σ_a, σ_b) for the lines of best-fit plotted in Figure 9.3.

of the light, respectively. One therefore fits the band gap dependence using:

$$E(L) = \frac{a}{L^b} + E_{g,\text{bulk}}, \tag{9.2}$$

where (a, b) are fitting parameters. These are given in Table 9.3 for fits to the data shown in Figure 9.3. In both instances, we find an exponent for the well length which deviates from the effective mass prediction of 2. This is attributed to the atomic structure and symmetry of the system, and the nonparabolicity of the band edges[95].

9.2 Independent-Particle State Properties

CdSe nanoplatelets exhibit strong band-edge features in their optical absorption spectra. The character of the band-edge independent-particle states determines the strengths of these transitions and to a first approximation, the energies of the excitonic transitions. As such, a description of the independent-particle states forms the first step in understanding the optical properties of CdSe nanoplatelets.

In Figures 9.4 and 9.5, we present the atomic wave function isosurfaces for CdSe nanoplatelets with an even number of monolayers, ranging from 2 ML to 8 ML. Larger plots are shown for the 4 ML-thick nanoplatelet in Appendix F. In each case, the twenty lowest-energy states are presented, with their eigenvalues (in eV) given below each wave function. Unoccupied states are given in red whereas occupied states are given in blue. Atomic wave functions for nanoplatelets with an odd number of monolayers are not shown. This is because the eigenvalues of degenerate states in these systems are found to be numerically degenerate, therefore any linear

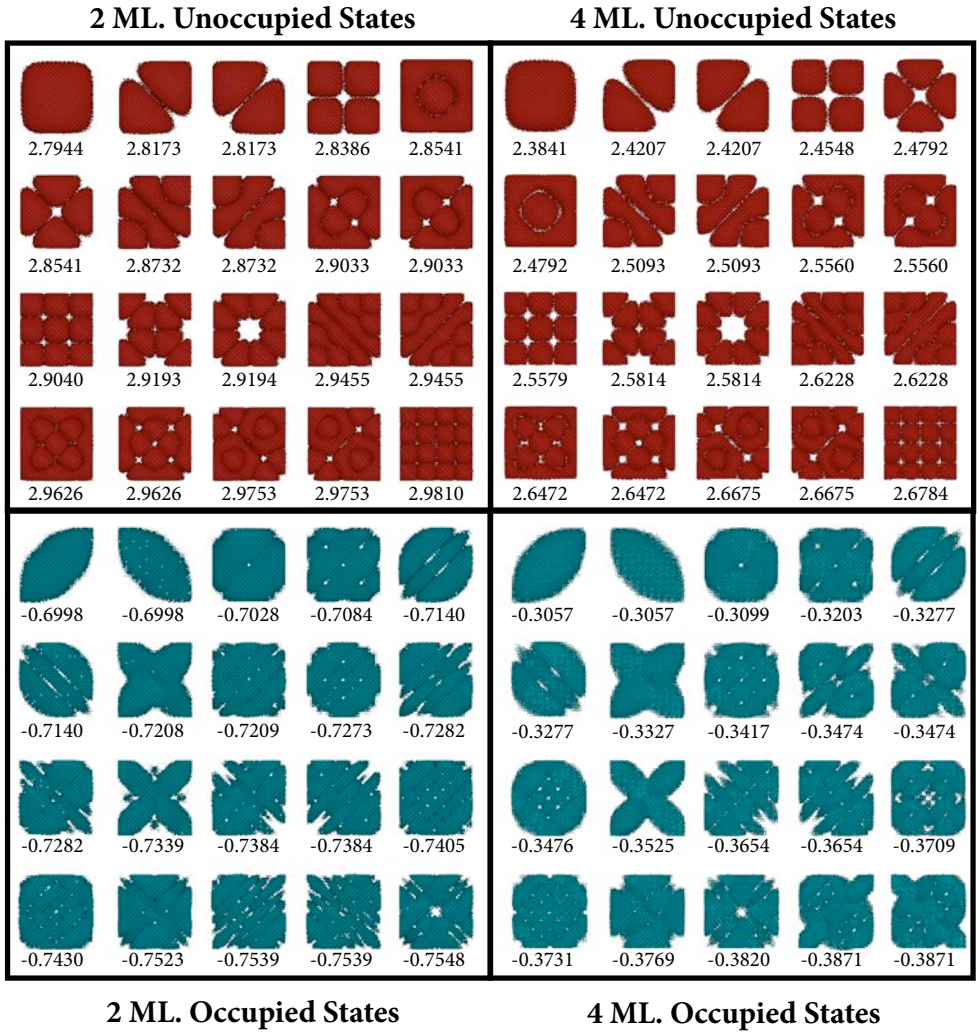

Figure 9.4: Atomic wave function isosurfaces, $|\Psi(\mathbf{r})|^2$, for the first twenty occupied states (blue) and unoccupied states (red) of nanoplatelets with thicknesses of 2 ML and 4 ML. In each panel, the states are ordered from top left to bottom right. The x and y axes point right and up, respectively, with z coming out of the page.

combination of their wave functions will also be a solution of the Schrödinger equation with the same energy. We find that these linear combinations vary arbitrarily depending on the specific subspace size used with the eigensolver. This hinders a visual comparison, and as the states are not required in order to understand the level evolution as a function of platelet thickness, we omit them to aid clarity. This is discussed further in Appendix F.

Inspection of Figures 9.4 and 9.5 reveal several energy level crossings that occur as a function of increasing thickness. As the thickness is increased from 2 ML to

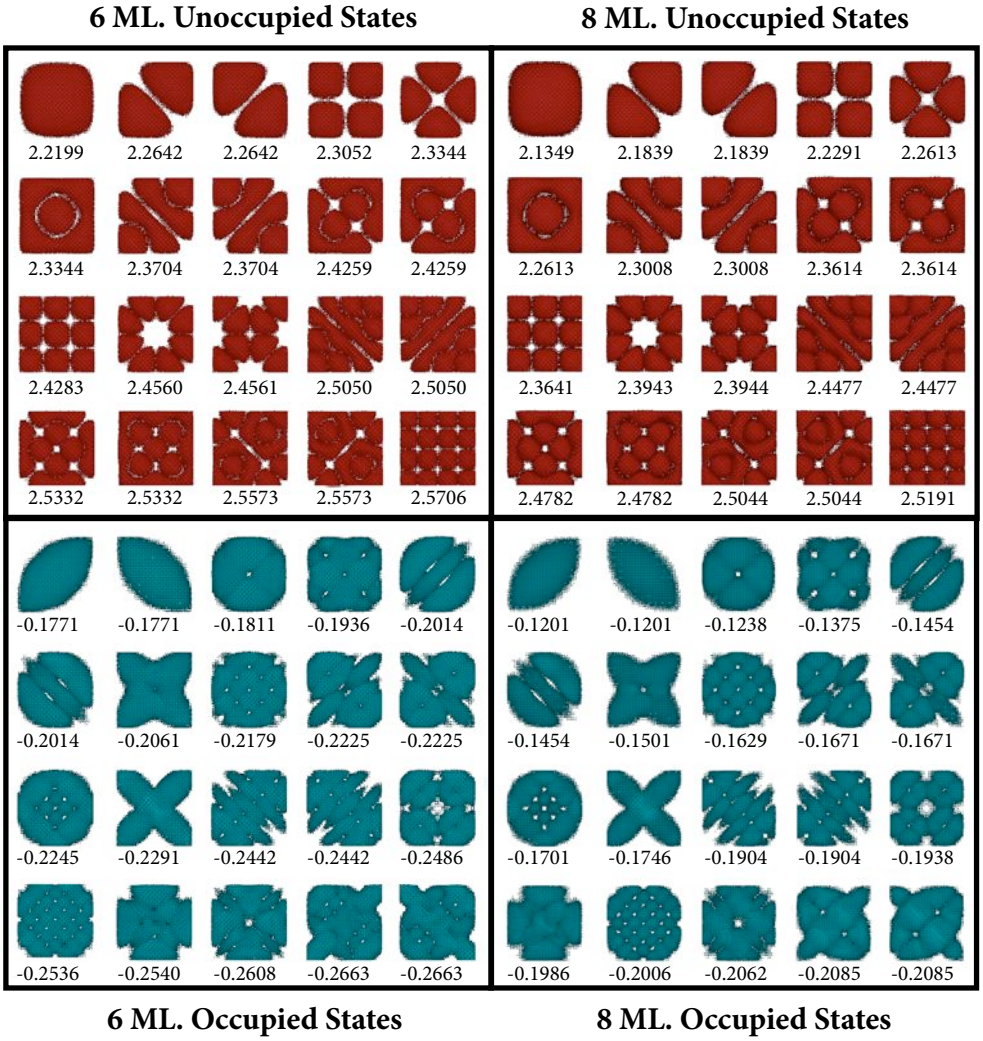

Figure 9.5: Atomic wave function isosurfaces, $|\Psi(\mathbf{r})|^2$, for the first twenty occupied states (blue) and unoccupied states (red) of nanoplatelets with thicknesses of 6 ML and 8 ML. In each panel, the states are ordered from top left to bottom right. The x and y axes point right and up, respectively, with z coming out of the page.

4 ML, unoccupied states 5 and 6 interchange positions. Occupied states 10 and 11 also increase in energy relative to state 9. The 10th and 11th occupied states in the 2 ML-thick platelet therefore become the 9th and 10th states in the 4 ML-thick platelet, while the 9th occupied state moves to the 11th state. An analogous move occurs between occupied states 18 and 19, and 20. We also observe a change in the 15th and 16th occupied states, however, it is difficult to say whether a level crossing occurs between 2 ML and 4 ML, or the wave functions change.

As the thickness is increased from 4 ML to 6 ML, unoccupied states 12 and 13

interchange positions, as do states and 16 and 17. There are no energy level crossings amongst the occupied states for this change in thickness. Finally, as the thickness is increased from 6 ML to 8 ML, occupied states 13 and 14 interchange positions, as do states 16 and 17 but no level crossings occur between unoccupied states.

The occurrence of energy level crossings is predominantly due to the presence of doubly degenerate states, which are a consequence of modelling our nanoplatelets with square planar areas. All of the level crossings between unoccupied states occur between doubly degenerate states, as do the majority of level crossings in the occupied manifold. The order in which degenerate states are given is inconsequential by virtue of the fact that they are degenerate. Furthermore, the energy spacing between the 9th and 11th occupied states following the level crossing that occurred when the nanoplatelet thickness increased from 2 ML to 4 ML, is only 0.25 meV. This indicates that the level crossings that occur between non-degenerate, band-edge occupied states correspond to changes in relative energies on the order of meV.

A visual inspection of Figures 9.4 and 9.5 reveals that the symmetries of the band-edge, occupied wave functions exhibit minimal differences as the thickness is increased from 2 ML to 8 ML, while the symmetries of the unoccupied states show no changes. In general, we can therefore say that the band-edge states of CdSe nanoplatelets are insensitive to changes in thickness over the range presented and that they exhibit C_2 symmetry. This implies that the low-energy features in the optical absorption spectrum should also be consistent for the range of thicknesses studied.

Effect of the Passivation Energy on the Independent-Particle States

As detailed in Chapter 8, we treat the nanoplatelet surface as an ideal surface with fully-passivated dangling bonds and eschew a specific ligand species, instead opting for a parameterised treatment of passivation. All calculations presented thus far have

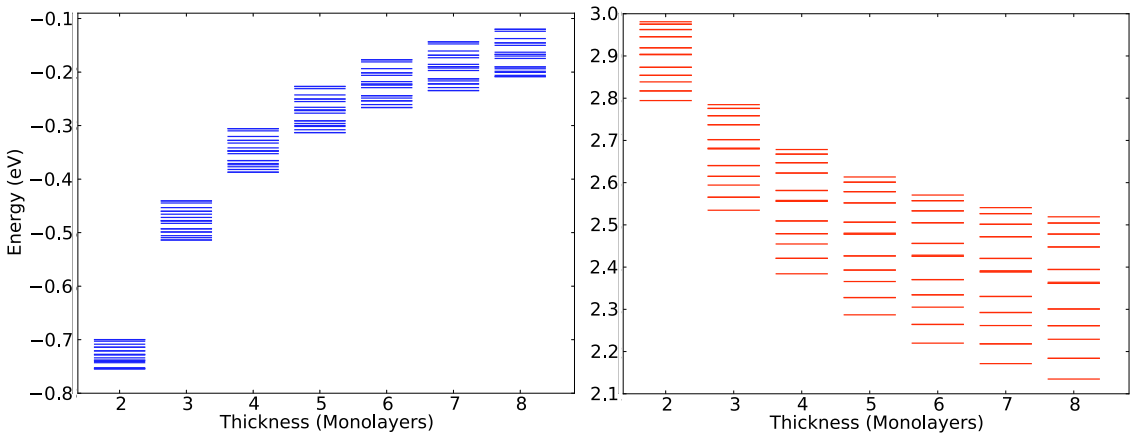

Figure 9.6: The lowest twenty occupied (blue) and unoccupied (red) states, as a function of thickness.

used a passivating energy of 15 eV. We have checked the extent to which our results depend on the specific value of this passivation parameter and present the details in Appendix F. We find that varying the passivation parameter has the greatest effect on the magnitude of the independent-particle gap, as shown in Figure 9.2. The appearance of the independent-particle wave functions are, however, insensitive to the choice of passivating energy and any subsequent change in the energy level spacings has a minimal effect on the spectral profile of the absorption spectrum, particularly when an energy-dependent line width is applied. We therefore continue to use a passivating energy of 15 eV for all subsequent nanoplatelet calculations.

9.2.1 Band-Edge Energy Levels

The eigenvalues of the twenty lowest occupied states and twenty lowest unoccupied states are presented in Figure 9.6, for CdSe nanoplatelets with thicknesses ranging from 2 ML to 8 ML. These states are the most relevant in any discussion of the low-energy region of the optical absorption spectrum. An analysis of the eigenvalues indicates that unlike CdSe nanocrystals, both manifolds are dense at the band edges. From Figure 9.6, we can see that twenty occupied levels are found within 0.1 eV of the highest occupied state, for all thicknesses considered.

In Figure 9.6, we observe an increase in the energy level spacing as a function of thickness in both the occupied and unoccupied states. This behaviour is the opposite of what one might initially expect from a simple understanding of quantum confinement in nanocrystals, which causes both the band gap and the energy level spacings to decrease as a function of increasing size. This behaviour can be explained if we treat the nanoplatelet as an infinitely confined quantum well with a separable solution. This results in a free-particle solution for the energies, with the particle mass replaced with an effective mass[27]:

$$E_{nml} = \frac{\hbar^2\pi^2}{2m_{\perp}^*}\left(\frac{l^2}{L_z^2}\right) + \frac{\hbar^2\pi^2}{2m_{\parallel}^*}\left(\frac{n^2}{L_x^2} + \frac{m^2}{L_y^2}\right), \tag{9.3}$$

where (n, m, l) are the quantum numbers for dimensions (x, y, z) with lengths (L_x, L_y, L_z), respectively and the effective masses for the components parallel and perpendicular to the plane are given by $m_{\parallel}$ and $m_{\perp}$, respectively. This solution leads to a series of discrete energy levels with quantum number l, that derive from the confined dimension. Each of these levels defines a sub-band, for which there exists a quasi-continuum of states defined by the lateral quantum numbers (n, m). This occurs because the lateral dimensions are much larger than the thickness dimension and the energy is inversely proportional to the square of the dimensions.

If we assume that the band-edge states shown in Figure 9.6 all belong to the lowest sub-band, for which the quantum number is $l = 1$, then the energy spacings must be governed by the second term in Equation (9.3). From this, we can infer that the in-plane effective masses of both the occupied and unoccupied states must decrease as a function of thickness for the level spacings to increase. This assumption is confirmed in reference [95].

We have been able to qualitatively reproduce the energy level behaviour using Equation (9.3) and the effective masses of the electron and heavy holes given in reference [95]. The larger increase in level spacings associated with the unoccupied

states is a consequence of smaller electron effective masses. Furthermore, the qualitative behaviour still occurs if the exponent of L in Equation (9.3) is less than 2, which we find from our fits to the data in Figure 9.3. We therefore find that the energy level spacings of the band-edge states of CdSe nanoplatelets increase as a function of increasing thickness, rather than decrease, the latter of which is observed in CdSe nanocrystals, and is a consequence of the system's geometry.

Orbital Composition of the Band-edge States

For nanoplatelets with a square planar aspect ratio, we find that the wave functions of the lowest twenty occupied states are almost entirely comprised of an equal amount of p_x and p_y orbitals, whereas the lowest twenty unoccupied states are predominantly comprised of s orbitals. Furthermore, while the relative contribution of p orbitals to the occupied states stays approximately constant as a function of the number of monolayers, the relative contribution from the s orbital to the lowest unoccupied states increases from 77% to 88% as the platelet thickness is increased from 2 ML to 8 ML.

9.2.2 Density of States

The density of states (DOS) for a nanoplatelet with a thickness of 4 ML is shown in Figure 9.7, along with the DOS for bulk, zincblende CdSe. The nanoplatelet DOS exhibits very sharp features as a consequence of quantum confinement in one dimension, and in contrast to nanocrystals, is characterised by not only a dense valence band edge but also a dense conduction band edge. Furthermore, the envelope of the nanoplatelet DOS closely modulates that of the bulk DOS. This is quite striking considering that the nanoplatelet only has a thickness of 1.2 nm, and provides some initial justification for the use of $\mathbf{k}\cdot\mathbf{p}$ theory on thin nanoplatelet systems.

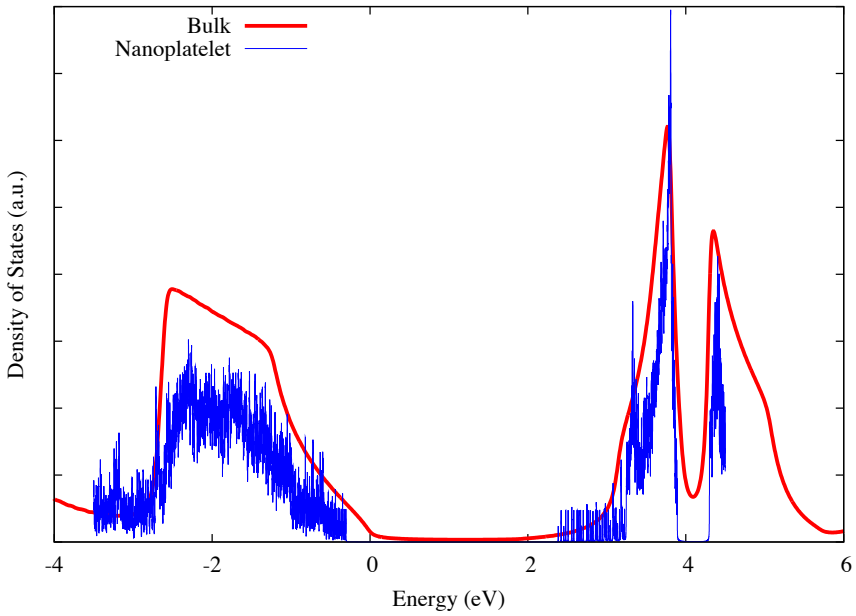

Figure 9.7: Density of states for a CdSe nanoplatelet with a thickness of 4 ML (blue) and for bulk, zincblende CdSe (red).

9.3 A Comparison with k · p Predictions

The goal of theory is to explain experimental observations or to make accurate predictions regarding some unmeasured physical properties of a system. This can often be harder in practise when multiple factors must be considered to explain experimental results but computational restrictions prevent such calculations. Comparing the results of different theoretical models therefore fulfils an important role in the validation of model results and can help to identify and address the shortcomings of any one theoretical approach.

All **k** · **p** calculations have been performed by Stanko Tomić at the University of Salford, England. His model is capable of constructing Hamiltonians including 8, 14 and 16 bands, both with and without spin-coupling. Tomić has shown that larger, multi-band **k** · **p** Hamiltonians can address the short-comings of those with fewer bands, such as yielding of the correct atomistic symmetry of the system[30].

Tomić has performed calculations on a CdSe nanoplatelet with a thickness of 1.2 nm,

which corresponds to 4 ML, and has kindly agreed that the results can be included in this thesis. This allows for a systematic comparison between envelope theory and atomistic theory, as well as experiment.

9.3.1 Independent-Particle States of the $\mathbf{k} \cdot \mathbf{p}$ Hamiltonian

The lowest six unoccupied and six occupied states calculated using 8, 14 and 16-band models, in the absence of spin-orbit coupling, are shown in Figure 9.8. There are some differences in the state orderings, both between the 8-band and 14-band models, and between the $\mathbf{k} \cdot \mathbf{p}$ and tight-binding models. As the number of bands is increased from 8 to 14, unoccupied states 2 and 3 interchange positions, as do unoccupied states 5 and 6. For the occupied states, we only see states 1 and 2 interchange positions.

A numerical analysis of the wave functions reveal that those generated by the 8-band model have C_{4v} symmetry where as those generated by the 14 and 16-band models have C_{2v} symmetry. The smallest $\mathbf{k} \cdot \mathbf{p}$ Hamiltonian that captures the symmetry of our atomic TB Hamiltonian is therefore the 14-band model, so this is what we shall compare our results to.

The 14 and 16-band $\mathbf{k} \cdot \mathbf{p}$ models predict degenerate energies for unoccupied states 2 and 3, occupied states 1 and 2, and occupied states 5 and 6. This is consistent with the level degeneracies predicted by our tight-binding model, however, the order of all degenerate pairs shown in Figure 9.8 are reversed with respect to the tight-binding states shown in Figure 9.4 (and Figures F.1 and F.2 in Appendix F).

Both methodologies, defined with very different basis sets, predict band-edge independent-particle state wave functions and degeneracies that are consistent with one another. The order in which degenerate states are found is unimportant as any linear combination of degenerate states is an allowed solution of the Schrödinger equation with the same energy. As such, physical observables, such as the optical

absorption spectrum are unaffected by these orderings. For example, we find that the ordering of degenerate states in our tight-binding simulations can vary with respect to changes in the passivating energy but the spectral features remain unchanged. This is shown in Appendix F.

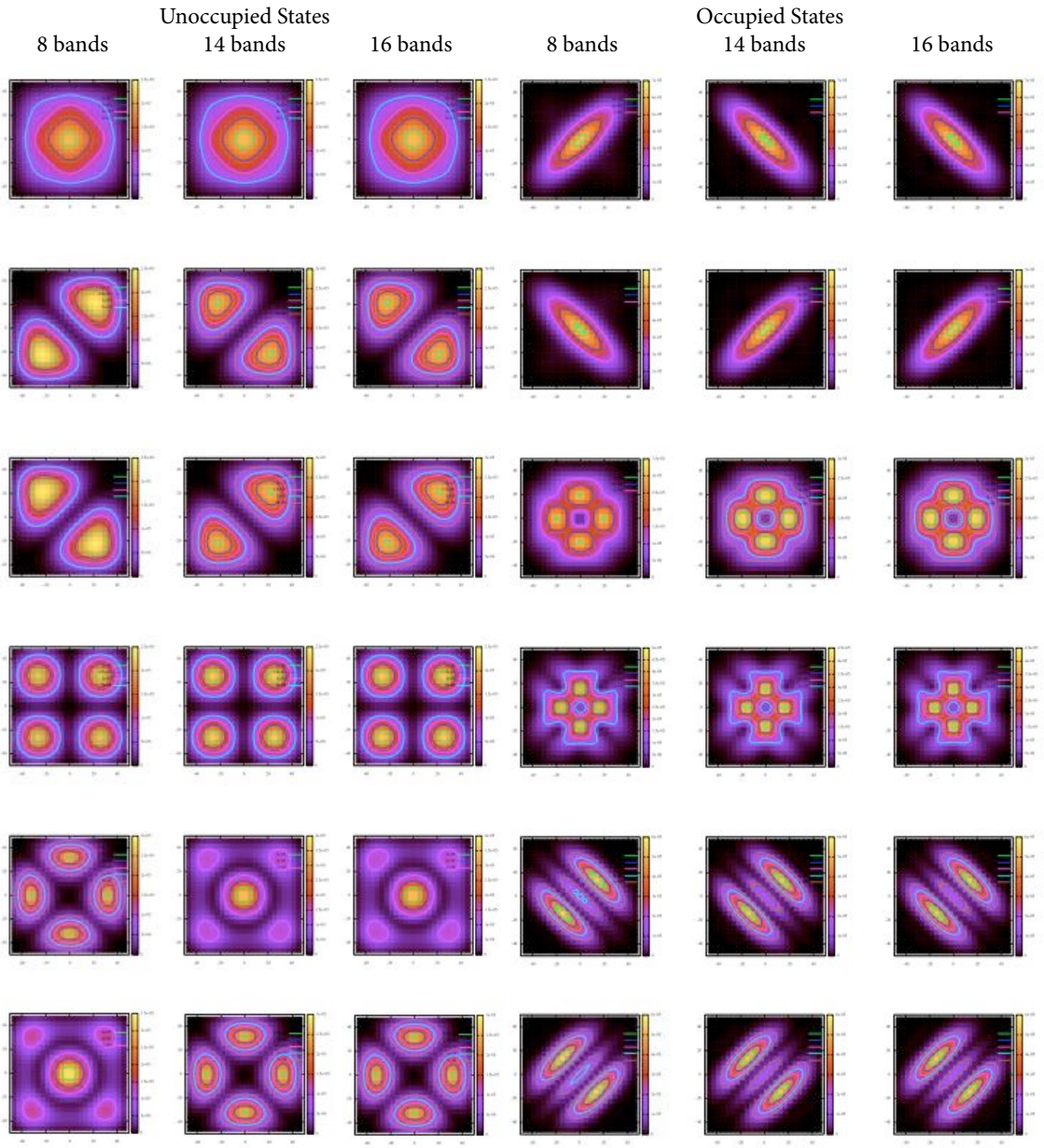

Figure 9.8: $\mathbf{k} \cdot \mathbf{p}$ envelope functions, $|\chi(\mathbf{r})|^2$, for the first six unoccupied and occupied states of a nanoplatelet with a thickness of 4 ML. The states are ordered from top to bottom per column, with the z axis is coming out of the page. The number of bands utilised in each calculation is indicated in the figure and all states have been computed in the absence of spin-orbit coupling.

9.4 Optical Absorption Spectra of CdSe Nanoplatelets

9.4.1 A Comparison with $\mathbf{k} \cdot \mathbf{p}$ Calculations

Having demonstrated the consistency in the band-edge wave functions generated by the two models, we proceed to compare the absorption spectrum computed using our tight-binding model to the spectrum computed with the $\mathbf{k} \cdot \mathbf{p}$ method. 8-band $\mathbf{k} \cdot \mathbf{p}$ models have previously been applied to CdSe nanoplatelets, with a focus on the evolution of the optical gap as a function of thickness[72; 87], however we are not aware of any studies of the optical spectra using either the tight-binding or $\mathbf{k} \cdot \mathbf{p}$ methods.

Here, we compare the results of our tight-binding model with those of a 14-band $\mathbf{k} \cdot \mathbf{p}$ model. This is the smallest $\mathbf{k} \cdot \mathbf{p}$ Hamiltonian capable of capturing the atomic symmetry of the system. An additional comparison of the differences in the spectra predicted by the 8-band and 14-band $\mathbf{k} \cdot \mathbf{p}$ Hamiltonians is presented in Appendix F. In Figure 9.9, we compare the independent-particle absorption spectra computed using the sp^3s^* tight-binding model and the 14-band $\mathbf{k} \cdot \mathbf{p}$ model, in the absence of spin-orbit coupling, for a nanoplatelet with a thickness of 4 ML. This represents one of the most well-studied nanoplatelet systems by experimentalists[72; 75; 80; 202; 205].

We remark that a larger passivating energy of 35 eV is required in order to achieve agreement in the onsets, and the tight-binding spectrum is normalised such that the magnitude of the first peak matches that of the $\mathbf{k} \cdot \mathbf{p}$ spectrum. This is required as the f-sum rule is not conserved in our calculations.

Many features in the tight-binding spectral profile are visible in the $\mathbf{k} \cdot \mathbf{p}$ spectrum, however there are differences in transition energies and oscillator strengths. There is strong agreement between the spectral profiles from the onset to 2.825 eV, with

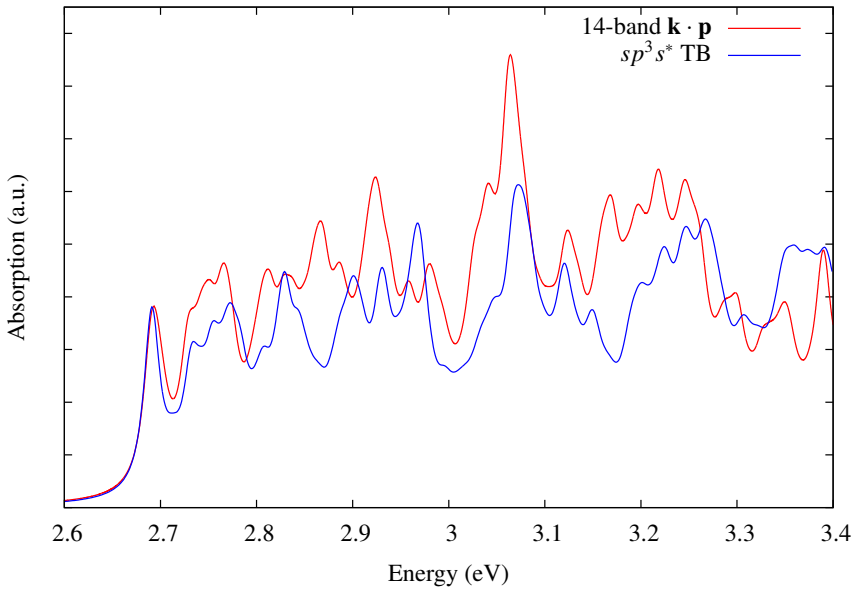

Figure 9.9: A comparison of the absorption spectrum of a 4 ML-thick nanoplatelet, computed in the independent-particle approximation, using our tight-binding model (blue) and Tomić's 14-band $\mathbf{k} \cdot \mathbf{p}$ model (red). The spectra are computed using a fixed line width of 20 meV (FWHM).

both spectra exhibiting an initial peak of comparable width followed by a large dip, then three peaks in close succession, followed by another dip. The magnitude of the structure in the TB spectrum that peaks around 2.825 eV is also comparable in magnitude to the corresponding $\mathbf{k} \cdot \mathbf{p}$ peak. The level of quantitative agreement in the transition energies of the peaks reduces beyond this point, however, the general, qualitative agreement between the spectral profiles is remarkably good. For example, both spectra exhibit a large dip at 3 eV, followed by a structure with a lip just prior to the peak with the strongest intensity in the low-energy region presented.

Using 2D electronic spectroscopy, Cassette and coworkers find that the second peak in the absorption spectrum exhibits a Gaussian line profile, indicating inhomogeneous broadening[93]. This could be a consequence of electron-phonon coupling or of the length scale of local disorder relative to the Bohr exciton radius, which varies between the excitonic states[206]. We therefore employ an energy-dependent line width to simulate the inhomogeneous broadening of transitions above

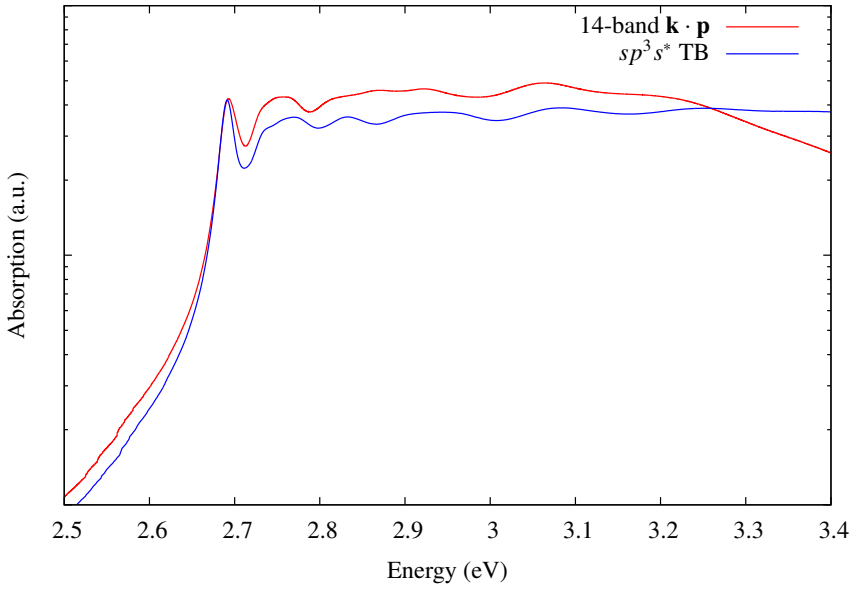

Figure 9.10: A comparison of the absorption spectrum of a 4 ML-thick nanoplatelet, computed in the independent-particle approximation, using our tight-binding model (blue) and Tomić's 14-band $\mathbf{k} \cdot \mathbf{p}$ model (red). Absorption has been plotted on a log scale and the line width (FWHM) of the spectra linearly increase from 20 meV to 200 meV between the onset and 3.4 eV.

the first peak. A comparison of the spectra generated with an energy-dependent line width is presented in Figure 9.10. Differences in the spectra are further minimised by plotting absorption on a log scale. A comparison between the spectra calculated with the two models, using a fixed line width and a log scale, is given in Appendix F. Line broadening results in spectra that retain the prominent, common features, whilst uncertainties regarding high-energy transitions are smeared out. The overall agreement between the spectral profiles predicted by the tight-binding and $\mathbf{k} \cdot \mathbf{p}$ models is very good for energies up to 0.7 eV above the absorption edge. The one noticeable difference is in the relative height of the spectral profiles, however, it could be that the tight-binding model predicts a stronger oscillator strength for the lowest exciton state and that normalising the spectra to this feature is misleading.

9.4.2 A Comparison with Experimental Spectra

The optical absorption spectra of CdSe nanoplatelets have been well-studied experimentally, for several thicknesses[69; 72; 87; 91; 202; 205]. It has been shown that nanoplatelets with thicknesses ranging from 2 ML to 6 ML exhibit persistent spectral features characterised by two well-defined peaks at the absorption edge[72; 75]. Representative, experimental absorption spectra are reproduced in Figure 9.11 for CdSe nanoplatelets with thicknesses of 4 ML and 5 ML, respectively.

The first peak defines the absorption onset and has a FWHM of the order of 40 meV[67]. The second peak is always smaller in magnitude, with a larger FWHM, and is centred between 130 meV and 170 meV higher in energy than the first peak[1]. A third peak, visible in the bottom panel of Figure 9.11, is sometimes observed, after which no other features are resolvable.

Studies concerned with the lateral dimensions have found that the features of the absorption spectrum are independent of lateral dimensions once they exceed the exciton Bohr radius[70; 207]. Yeltik and coworkers have shown that the transition energies of the two main peaks are insensitive to the ratio of the lateral dimensions. They also show that the relative intensity of the two peaks has a dependence on either the planar area or the lateral aspect ratio, with the intensity of the first peak increasing (or the intensity of the second peak decreasing) as the planar area increases. Unfortunately the aspect ratio increases with planar area, so one cannot distinguish between the two variables, however, this may be an observation of an increase in the oscillator strength of the lowest transition as a function of increasing exciton coherence area[92].

The experimental spectra shown in Figure 9.11 represent the two most-studied systems and illustrate the high reproducibility associated with nanoplatelet

[1]For thicknesses between 3 ML and 5 ML. In general, the separation decreases with increasing thickness.

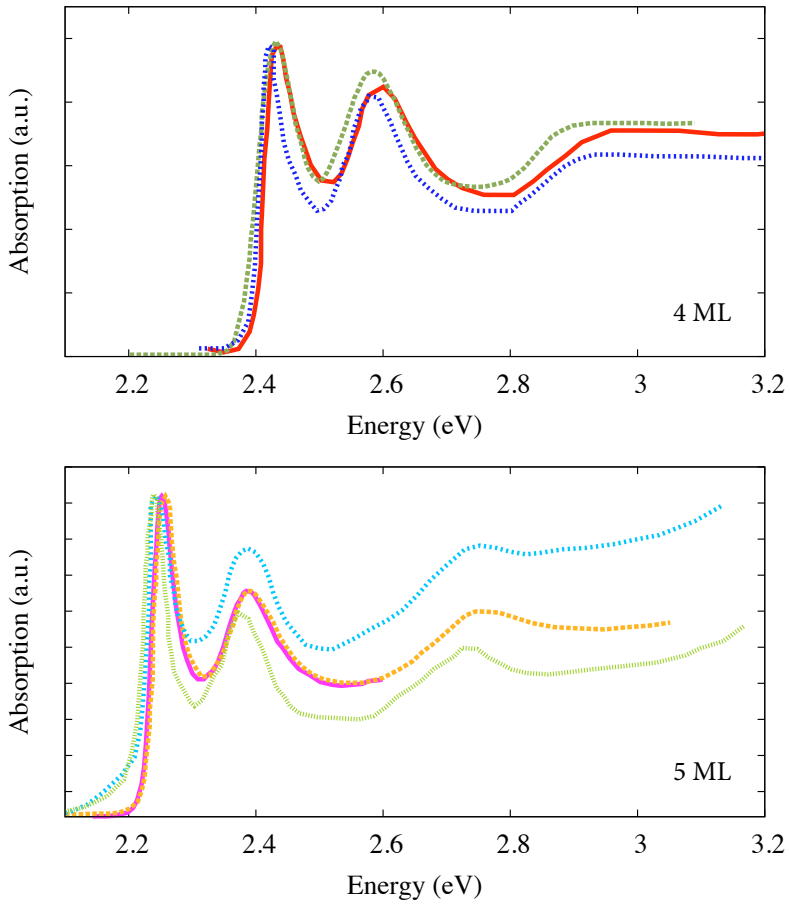

Figure 9.11: Experimental absorption spectra for CdSe nanoplatelets with thicknesses of 4 ML and 5 ML, respectively. The spectra have been directly reproduced from figures in the following references: red[208], green[97], blue[209], magenta[205], orange[67], light blue[207] and light green[207]. The comparison of data from multiple sources illustrates the high reproducibility of the spectral features, with well-defined transition energies. In all examples, the spectra have been normalised such that the magnitude of the first peak is constant.

absorption spectra. In Figures 9.12 and 9.13, we compare the experimental spectrum of a 4 ML-thick platelet to the spectrum computed using our tight-binding model. Equivalent plots are shown for a nanoplatelet of 5 ML in thickness in Appendix F, as the same conclusions apply. As discussed above, we model our platelets with lateral dimensions of 10 nm x 10 nm, such that they exceed the 2D exciton Bohr radius. We therefore do not expect differences between the lateral dimensions of our simulations and experimental systems to have a large effect on the absorption onset.

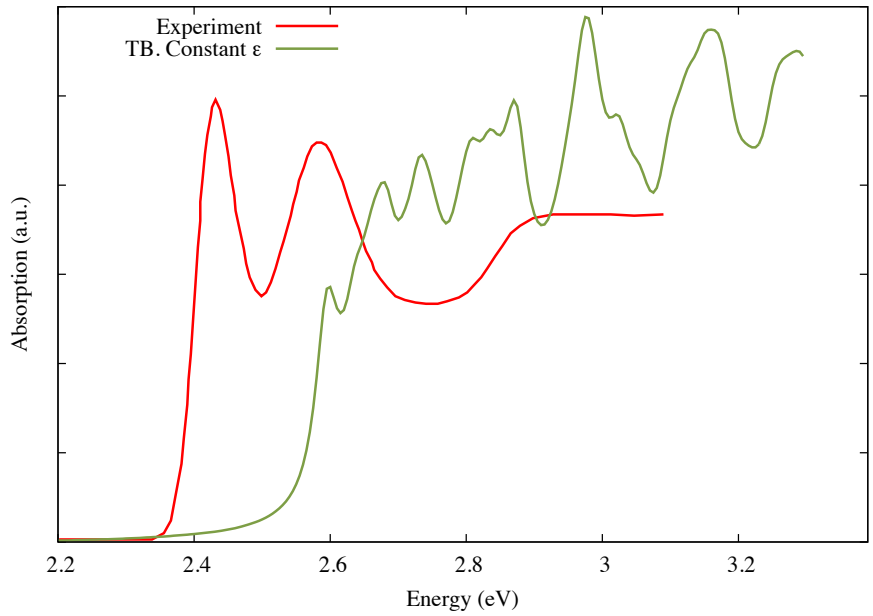

Figure 9.12: The absorption spectrum for a CdSe platelet of 4 ML in thickness. The experimental spectrum (red[97]) is compared to the tight-binding spectrum, computed in the independent-particle approximation (green). The tight-binding spectrum is computed using a fixed line width of 40 meV (FWHM).

Figure 9.12 compares the experimental absorption spectrum of the 4 ML-thick nanoplatelet (red) to the spectrum computed in the independent-particle approximation, using our tight-binding model (green). When comparing to experiment, all spectra are redshifted by 0.1 eV to account for the effect of temperature on the band gap. In all instances we have computed the spectrum using a polarisation vector, $\hat{\mathbf{e}} = (1, 0, 0)$. The square aspect ratio of the platelets simulated in this chapter cause them to exhibit the same spectra for the polarisation vector, $\hat{\mathbf{e}}_y$.

The overall agreement with experiment in Figure 9.12 is poor. The first clear difference is the strong redshift of the experimental spectrum in comparison to the calculated spectrum. This is indicative of a strong electron-hole interaction. The second striking difference is the large number of resolvable transitions present in the calculated spectrum that are not observed in the experimental spectrum. The spectrum predicted using the $\mathbf{k} \cdot \mathbf{p}$ model also shows a far larger number of

resolvable transitions in comparison to the experimental spectrum shown in Figure 9.12. The strong agreement between the calculated spectra displayed in Figure 9.9 reinforces the robustness of our tight-binding results and implies that some account for inhomogeneous broadening should be made when comparing to experimental spectra.

In Figure 9.13 we therefore compare the experimental spectrum to the tight-binding spectrum computed with a line width (FWHM) that linearly increases from 20 meV to 200 meV between the absorption onset and 3.3 eV[196]. The visual comparison is somewhat improved relative to Figure 9.12, however overall agreement is still poor. The width of the lowest peak in the independent-particle spectrum is approximately half that of the experimental peak and the separation between the first and second peaks in the independent-particle spectrum is much smaller than the peak separation in experiment. This would still be the case even if the line broadening was increased, causing the second and third peaks to merge into one broader peak. Finally, the large dip in the experimental spectrum, with a minimum at 2.75 eV, is completely absent in the calculated spectrum.

There could be several reasons for the observed discrepancies between experiment and our calculated results. Figures 9.12 and 9.13 exclude spin-orbit coupling and the electron-hole interaction. The electron-hole interaction should strongly red-shift the independent-particle spectrum and will mix the independent-particle transitions, leading to a redistribution of spectral weights.

In summary, the absorption spectrum for a nanoplatelet with a thickness of 4 ML, generated by sp^3s^* tight-binding model, shows strong agreement with the equivalent spectrum generated by the 14-band $\mathbf{k} \cdot \mathbf{p}$ model for the experimental region of interest. Both tight-binding and $\mathbf{k} \cdot \mathbf{p}$ predict a large number of spectral peaks that are not observed in the experimental spectrum, indicating the presence of inhomogeneous broadening. Even when inhomogeneous broadening is taken into

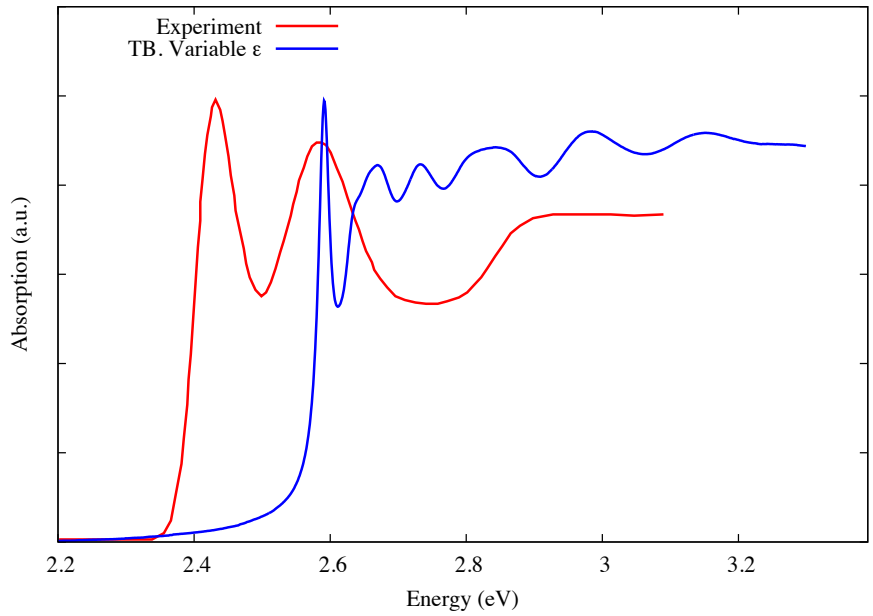

Figure 9.13: The absorption spectrum for a CdSe platelet with a thickness of 4 ML. The experimental spectrum (red) is compared to the tight-binding spectrum, computed in the independent-particle approximation (blue). The tight-binding spectrum is computed using a line width that linearly increases from 20 meV to 200 meV (FWHM) between the onset and 3.3 eV.

account, the independent-particle approximation fails to describe the main features of the experimental spectrum. We propose that the inclusion of the electron-hole interaction is therefore required for a proper description of the optical absorption spectra of CdSe nanoplatelets and seek to investigate its effect in Chapter 10. In the final section, we investigate which states comprise the lowest ten transitions in a nanoplatelet of 4 ML in thickness.

9.5 An Assignment of the Lowest Allowed Transitions

The two characteristic peaks that are observed experimentally in the optical absorption spectra of CdSe platelets lie within 0.3 eV of the onset in platelets with thicknesses of 3 ML, 4 ML and 5 ML. These features are of interest because the band-edge peak intensities are strong, indicating that CdSe nanoplatelets strongly

absorb at the corresponding transition energies/frequencies and the lowest exciton state emits with an energy approximately equal to the optical gap (the Stokes shift is ~ 1 nm).

From inspection of the experimental spectrum in Figure 9.12 and taking the zero of the energy as the onset, we infer that transitions in the range, 0 eV $\leq E_t \leq$ 0.1 eV, contribute to the first peak, whereas transitions in the range, 0.1eV $< E_t \leq$ 0.3eV, contribute to the second peak. In both instances, we are able to identify which independent-particle transitions contribute to these peaks, however we stress that the independent-particle picture does not necessarily directly transfer to the two-particle picture (and therefore experiment), as the strong electron-hole interaction will mix the independent-particle transitions, causing the structure of the independent-particle spectrum to be lost. With that said, the lowest excitonic transitions will be comprised of a mixture of independent-particle transitions with comparable energies and one can quantify the extent of the mixing. Investigating which transitions contribute to the two prominent spectral features in the independent-particle approximation therefore serves as a point of reference for two-particle calculations.

Figure 9.14 depicts the lowest transitions for a nanoplatelet of 4 ML in thickness, in the absence of any line broadening. As such, we are able to resolve individual transitions and establish how they contribute to the spectrum. We are also able to identify which electrons and holes contribute to each independent-particle transition. The lowest transitions are numerically labelled in Figure 9.14 and the corresponding states are listed in Table 9.4. We find that twelve allowed peaks[2] containing twenty four independent-particle transitions lie in the range, $0\,\text{eV} \leq E_t \leq 0.1\,\text{eV}$, and a further seventy three allowed peaks comprised of one hundred and forty transitions lie in the range, $0.1\,\text{eV} < E_t \leq 0.3\,\text{eV}$.

[2] An allowed peak is defined as the sum of degenerate transitions with a total oscillator strength greater than or equal to 0.01 times the oscillator strength of the first allowed peak and a transition is defined as degenerate when two of more transitions have energies that differ by less 0.1 meV.

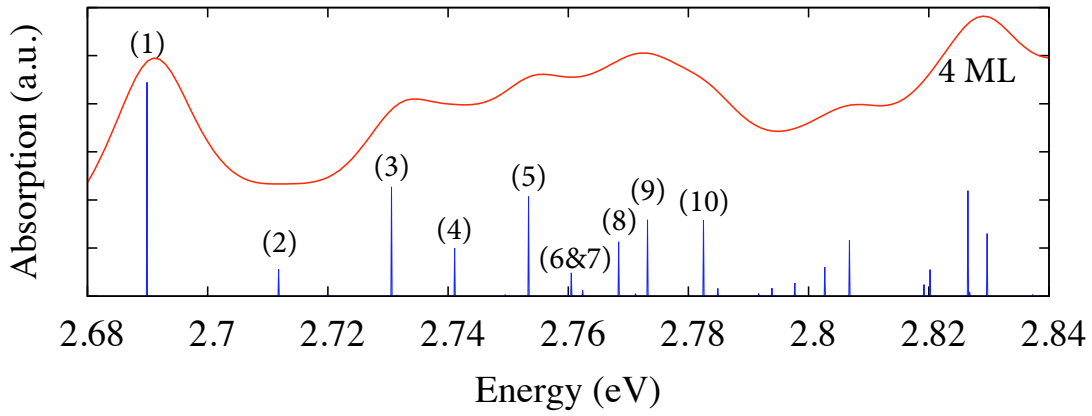

Figure 9.14: The lowest optical transitions calculated with the sp^3s^* model, in the absence of line broadening (blue) and with a constant line width of 20 meV (red), for a nanoplatelet with a thickness of 4 ML. The first ten allowed peaks are labelled in the figure and given in Table 9.4.

In the first interval the twelve allowed peaks are comprised of transitions containing twelve different hole states and six different electron states. Looking at the transitions that comprise the peaks, the smallest and largest hole states that contribute are 1 and 20, whereas the smallest and largest electron states that contribute are 1 and 6, respectively. The two strongest peaks, labelled as (1) and (3) in Figure 9.14, are both comprised of doubly-degenerate transitions that occur from hole states 1 and 2 to the lowest electron state, and from hole state 3 to electron states 2 and 3, respectively.

In the second interval the seventy three allowed peaks are comprised of transitions containing forty five different hole states and fourteen different electron states. Looking at the transitions that comprise the peaks, the smallest and largest hole states that contribute are 1 and 57, whereas the smallest and largest electron states that contribute are 2 and 15, respectively. The two strongest peaks are both comprised of quadruply-degenerate transitions that occur from hole states 27 and 28 to electron states 5 and 6, and from hole states 9 and 10 to electron states 5 and 6, respectively.

Delta Peak	Transition Energy	h_i	e_i	$\langle v\|\mathbf{e}\cdot\mathbf{r}\|c\rangle$ (Å)	$\|\langle v\|\mathbf{e}\cdot\mathbf{r}\|c\rangle\|^2$ (Å^2)
1	2.689877	1	1	-1.77	3.15
	2.689878	2	1	1.77	3.15
2	2.711837	5	1	0.629	0.396
	2.711837	6	1	0.629	0.396
3	2.730600	3	2	1.256	1.585
	2.730600	3	3	1.256	1.586
4	2.741072	4	2	-0.834	0.695
	2.741073	4	3	0.834	0.695
5	2.753411	7	2	-1.12	1.434
	2.753412	7	3	-1.12	1.433
6	2.760502	1	4	-0.579	0.335
	2.760502	2	4	-0.579	0.335
7	2.762405	8	2	0.29	0.0841
	2.762406	8	3	0.29	0.0841
8	2.768359	11	2	0.882	0.779
	2.768359	11	3	-0.882	0.779
9	2.773202	12	2	-1.044	1.090
	2.773202	12	3	1.044	1.091
10	2.782461	5	4	-1.041	1.084
	2.782461	6	4	1.041	1.084

Table 9.4: A table listing the atomic states which comprise the ten lowest delta peaks in the spectrum of a nanoplatelet with a thickness of 4 ML.

We have therefore identified which states and transitions contribute to the low-energy region in the absorption spectrum of a 4 ML-thick nanoplatelet, up to 0.3 eV above the onset. Further analysis would look to examine the degree of mixing between the independent-particle transitions presented here and quantify which independent-particle states contribute to the lowest exciton states. Information quantifying the amount of mixing is contained with two-particle coefficients and are found as solutions to the eigenvalue problem containing the effective two-particle Hamiltonian, given by Equation (5.21). We do not currently solve Equation (5.21) and therefore do not have access to the two-particle coefficients, however, we suggest how we would tackle this problem in Chapter 11.

9.6 Conclusion

In summary, we have investigated the optoelectronic properties of CdSe nanoplatelets in the independent-particle approximation, using our tight-binding model. We have presented how the band-edge energy levels vary as a function of thickness and visualised the corresponding atomic wave functions. Calculations show that the both the occupied and unoccupied states are very dense at the band edges, with level spacings on the order of meV. Nanoplatelets with square planar areas are found to exhibit both non-degenerate and doubly degenerate states. This symmetry is subsequently broken when the aspect ratio is changed from square to rectangular.

The atomic isosurfaces generated with our tight-binding model compare well visually with envelope functions found using a 14-band $\mathbf{k} \cdot \mathbf{p}$ model. Results show that the atomic wave functions of the CdSe nanoplatelets are delocalised across the planar area of the platelet, which is consistent with prior suggestions[72; 93]. We have produced the first calculations of nanoplatelet optical absorption spectra and compared results from our tight-binding model with those of the 14-band $\mathbf{k}\cdot\mathbf{p}$ model. We find very good agreement between the two models in the low-energy region of the spectrum.

A comparison of our calculated results with experimental absorption spectra found that in general, the independent-particle approximation not only overestimates the optical gap but also predicts fundamentally different spectral profiles. This analysis therefore suggests that a many-body treatment of the absorption spectrum is required in order to reproduce the features observed experimentally and that an energy-dependent, spectral line width should be applied due to the presence of inhomogeneous broadening.

Chapter 10

Many-Body Calculations of the Optical Properties of CdSe Nanocrystals

In optical absorption spectroscopy one probes neutral excitations due to the simultaneous creation of an electron and hole upon excitation of the system. Calculations done in the independent-particle approximation can provide an initial means of understanding such optical excitations in terms of non-interacting electron and hole pairs. In systems with weak excitonic properties, such as metals which exhibit strong dielectric screening[210], an independent-particle picture may suffice. In quantum-confined, semiconducting systems however, the electrons and holes are spatially confined in one or more dimensions, which can significantly modify the excitonic features with regards to the bulk[211]. In this chapter, we therefore present the results of many-body calculations on the excitonic binding energies and optical absorption spectra of CdSe nanocrystals using the Bethe-Salpeter equation implementation outlined in Chapters 5 and 7.

10.1 Introduction

CdSe represents the prototypical nanocrystal system, with well-studied optical and excitonic properties, both experimentally[1; 19–21; 89] and computationally[23; 24; 124; 126; 145; 176]. Using our Bethe-Salpeter equation implementation, presented in Chapters 5 and 7, we study the optical gap and excitonic binding energy as a function of system size.

Each term in the kernel is investigated and its relative contribution to the spectrum is identified. Comparisons are made with both experimental and computed values for the nanocrystal band gap dependence on diameter, initially presented in Figure 3.2 of Chapter 3.

The low-energy region of the absorption spectra of CdSe nanocrystals with diameters of up to 6 nm (4109 atoms) are studied and comparisons are made to experimental data, where available. The study of the optical absorption spectra of finite systems containing more than $\sim$ 50 atoms (above 1 nm in diameter) using the BSE, represents a recent advancement in the application of the formalism and reflects the maturity of the methodology in ab initio applications[48; 212].

10.1.1 Orbital Contributions to the BSE Kernel

The Bethe-Salpeter kernel is comprised of the exchange and direct terms, as defined by Equations (5.32) and (5.33), respectively in Chapter 5. In a real, orbital basis and using the two-centre approximation, both the direct and exchange terms are themselves comprised of tight-binding coefficients multiplied by Coulomb-like and exchange-like integrals. This is shown in Chapter 7. Evaluation of these integrals therefore requires a real-space description of the atomic orbitals. As discussed in Chapter 6, we define our basis using single-ζ radial functions, generated with the ab initio orbital code, Siesta[139]. These functions are defined with a radial cut-off that ensures no overlap between second-nearest neighbours, thus satisfying the

basic requirement of our tight-binding Hamiltonian. The choice of atomic orbital basis functions is otherwise arbitrary as they have no relation to the tight-binding parameters that define the Hamiltonian.

As the choice of tight-binding basis is not unique, it is necessary to quantify the sensitivity of the results to a specific choice. Schulz and coworkers state that the exact values of these integrals are not crucial[145]. Indeed, screened on-site Coulomb-like integrals and bare exchange-like integrals are of the same order of magnitude, and make a small contribution to the kernel in relation to the long-range part of the Coulomb operator. The contribution made to the diagonal elements of the screened Coulomb matrix, $W_{vc,vc}$, by the on-site integrals has also been quantitatively investigated by Lee and coworkers[24]. They do this by multiplying their on-site integrals by a scaling factor, thus allowing them to vary the integrals through a range of physically sensible values and measure the effect on $W_{vc,vc}$.

Like Lee and coworkers, and Schulz and coworkers, our implementation utilises a real-space orbital basis and employs the two-centre approximation in the calculation of both on-site and nearest neighbour integrals. As such, we believe that the conclusions of both studies should be applicable to our work. To validate this, we perform calculations of the the absorption spectrum of a small nanocrystal (2 nm in diameter) and a larger nanocrystal (4 nm in diameter), sequentially including terms in the kernel to investigate the relative contributions of on-site integrals, nearest neighbour integrals and terms beyond nearest neighbours, to the spectra.

It can be seen from panel a) in Figure 10.1 that the on-site contribution from the orbital Coulomb-like integrals is small in the 2 nm system. One sees a slight reduction in the oscillator strengths of the lowest three peaks and an incremental shift blueshift ~ 0.01 eV. There is a larger contribution from the on-site exchange-like orbital integrals, with a noticeable mixing of oscillator strengths, resulting in the emergence of higher-energy transitions. This is also accompanied by a small

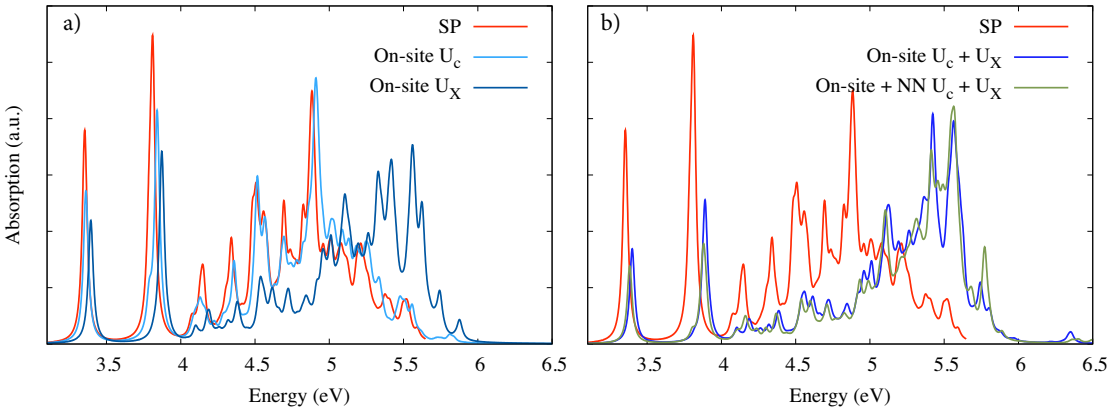

Figure 10.1: The absorption spectrum of a nanocrystal with a diameter of 2 nm. a) Only on-site terms are included in the interaction kernel. The Coulomb-like terms, U_c, and exchange-like terms, U_X, are given by the light-blue and dark-blue lines respectively. b) The cumulative contribution from the on-site terms (blue) is compared to the additional contribution from nearest neighbour terms (green). The energies of the largest electron and hole in the basis are 1225 meV and 1130 meV, respectively. In both plots, the single-particle spectrum is included as a reference in red.

blueshift in the onset. The greater contribution from the exchange-like integrals may be because the orbital Coulomb-like integrals only appear in the kernel once unscreened whereas the orbital exchange-like integrals appears twice in the kernel unscreened (see Equation (7.13) in Chapter 7).

Panel b) in Figure 10.1 shows that the inclusion of nearest neighbour terms in the kernel has a relatively small effect, even in such a small nanocrystal, with the most prominent change being a further reduction in the magnitude of the first two peaks of the spectrum. Figure 10.2 shows the contribution to the spectrum from interactions between orbitals centred on atoms with separations greater than the bond length. Not only do these terms strongly mix the oscillator strengths of the independent-particle transitions but they also lead to the expected redshift in the absorption spectrum onset, which one expects in direct-gap semiconductors.

In the case of the larger nanocrystal with a diameter of 4 nm, shown in Figure 10.3, we can see that the influence of on-site terms on the absorption spectrum is far smaller. Indeed, panel b) implies that interactions between orbitals centred on

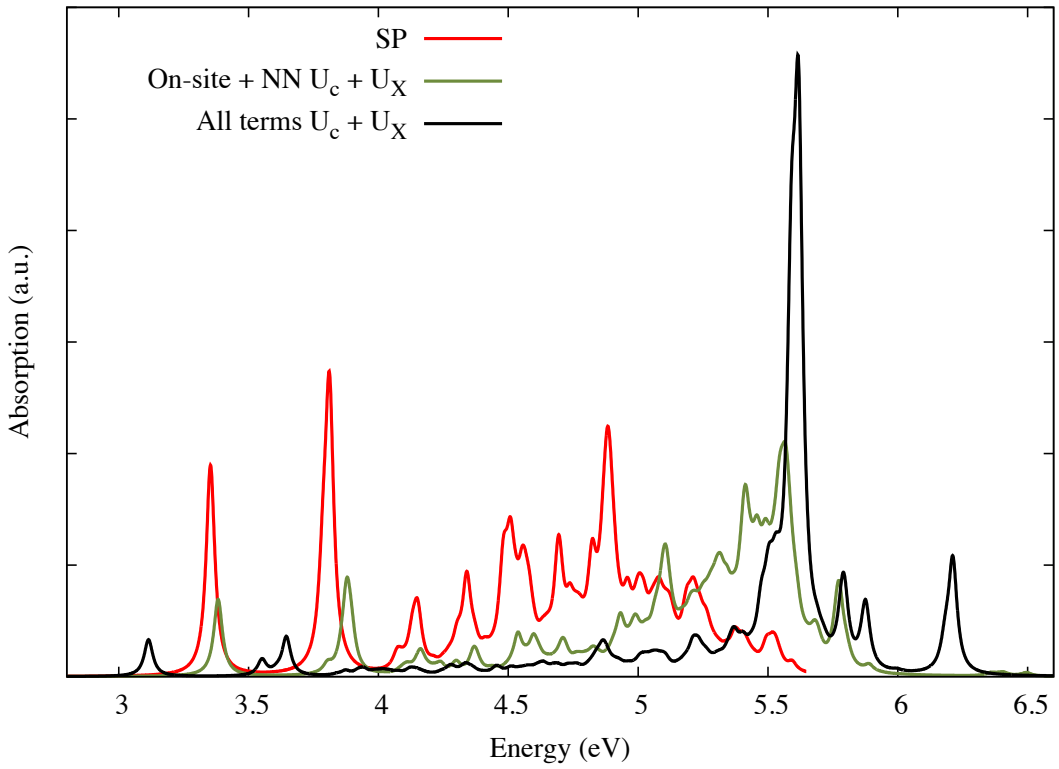

Figure 10.2: The absorption spectrum of a nanocrystal with a diameter of 2 nm. The black line shows the relative contribution of terms beyond those of nearest neighbours, to the spectrum. The energies of the largest electron and hole in the two-particle basis are 1225 meV and 1130 meV, respectively.

atoms with spacings greater than the bond length make the largest contribution to the interaction kernel and therefore the two-particle absorption spectrum.

The terms for which orbital integrals are explicitly calculated (on-site and nearest neighbour) have therefore been shown to contribute a smaller amount to the absorption spectrum than the monopole interaction between orbitals centred on atoms separated by more than the bond length. Furthermore, the sensitivity of the spectrum as a whole to the on-site terms decreases as a a function of increasing nanocrystal diameter. Both the spectral features and the absorption onset have been shown to be insensitive to the on-site terms of the kernel, for a nanocrystal of 4 nm in diameter.

This is because the number of two-centre interactions scales as N^2 where N is the number of orbital states in the system. Of these interactions, $N(N-25)$ are between

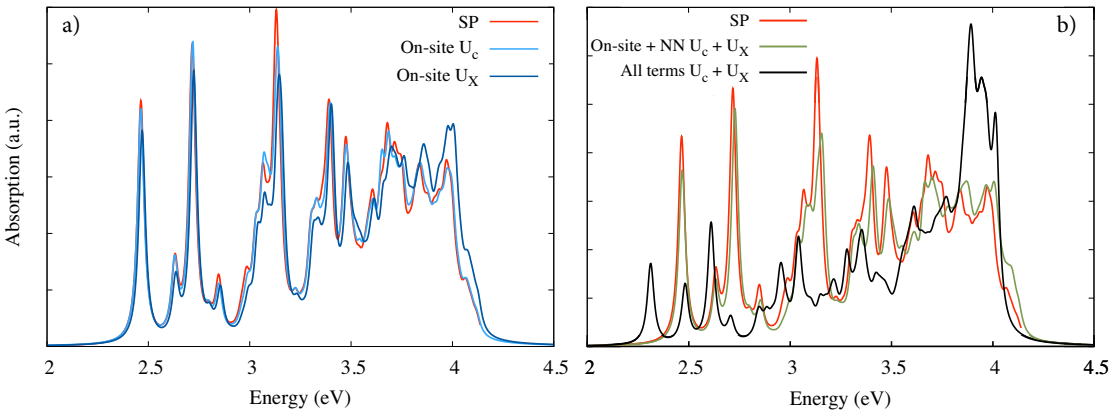

Figure 10.3: The absorption spectrum of a nanocrystal with a diameter of 4 nm. a) Only on-site terms are included in the interaction kernel. The Coulomb-like terms, U_c, and exchange-like terms, U_X, are given by the light-blue and dark-blue lines respectively. b) The cumulative contribution from the on-site terms plus nearest-neighbour terms (green) is compared to spectrum generated with the full kernel (black), with the single-particle spectrum included as a reference in red. The energies of the largest electron and hole in the basis are 1077 meV and 624 meV, respectively.

orbitals centred on atomic pairs with separations beyond nearest neighbours, compared to $5N$ on-site interactions and $20N$ nearest neighbour interactions. As N becomes large, the number of on-site terms therefore becomes negligible with respect to the total number of interactions.

These observations are consistent with those of Lee and coworkers[24], who additionally compare unscreened Coulomb and exchange integrals computed in a basis of Slater orbitals to those computed in a basis of Gaussian orbitals (commonly used in quantum chemistry packages). Unscreened Coulomb-like integrals varied by 10% when using the two sets of nonorthogonal basis functions. Orthogonalisation caused a further 10% variation in the integrals. Lee and coworkers therefore suggest that 20% constitutes an upper bound on the uncertainty of the on-site integrals[1].

[1]Lee and coworkers actually state an uncertainty of 20%-30%, and nearest neighbour exchange integrals were found to become negligible when orbital orthogonality between sites was enforced. This suggests that using a nonorthogonal basis set overestimates the contribution of nearest neighbour terms to the kernel and therefore the spectrum however, our results in Figure 10.1 b) show that such terms have a smaller effect on the spectrum than on-site terms. Hence we take the 20% upper bound associated with the on-site integrals to be reasonable.

Corresponding scaling tests revealed that a targeted accuracy of 10% in the energy of the Coulomb interaction could be achieved with a 20% uncertainty in the values of the on-site integrals, for a system of 2 nm in diameter[24]. The tolerable level of uncertainty in the orbital integrals rises as high as 50% for nanocrystals with a diameter of 6 nm. This is because terms beyond nearest neighbours make the largest contribution to the spectra of larger nanocrystals and in our implementation, as in Lee and coworkers, and Schulz and coworkers[145], these terms are approximated with the multipole expansion, for which the exact form of the atomic orbitals does not enter. As we utilise a basis set in which orbitals centred on different atomic sites are nonorthogonal, we expect a comparable amount of uncertainty in our calculations.

10.1.2 Approximations to the BSE Kernel

As well as investigating the contribution of interactions between orbitals with sequentially increasing separations to the BSE kernel and corresponding absorption spectrum, we also investigate the relative contribution of the exchange and direct terms to the kernel, as defined by Equations (5.32) and (5.33), respectively. Indeed, our choice of kernel is an approximation that corresponds to a specific choice for the form of the self-energy operator. We use the GW approximation of the self-energy, which is considered to give the best agreement with experiment in ab initio calculations[138; 213] (the derivation of the kernel is provided in Appendix B).

In Figure 10.4, we present several calculations of the optical absorption spectrum for a nanocrystal with a diameter of 4 nm, quantifying the contribution of each term to the kernel. The same behaviour was also observed for nanocrystals with diameters of 2 nm and 3 nm. By running separate calculations that only use the exchange term or the direct term, we are able to isolate the effect that each has on the spectrum. Inclusion of just the exchange term corresponds to retaining the bare Coulomb potential. As the bare Coulomb potential is defined as the derivative of the Hartree potential with respective to the charge density, this is referred to as

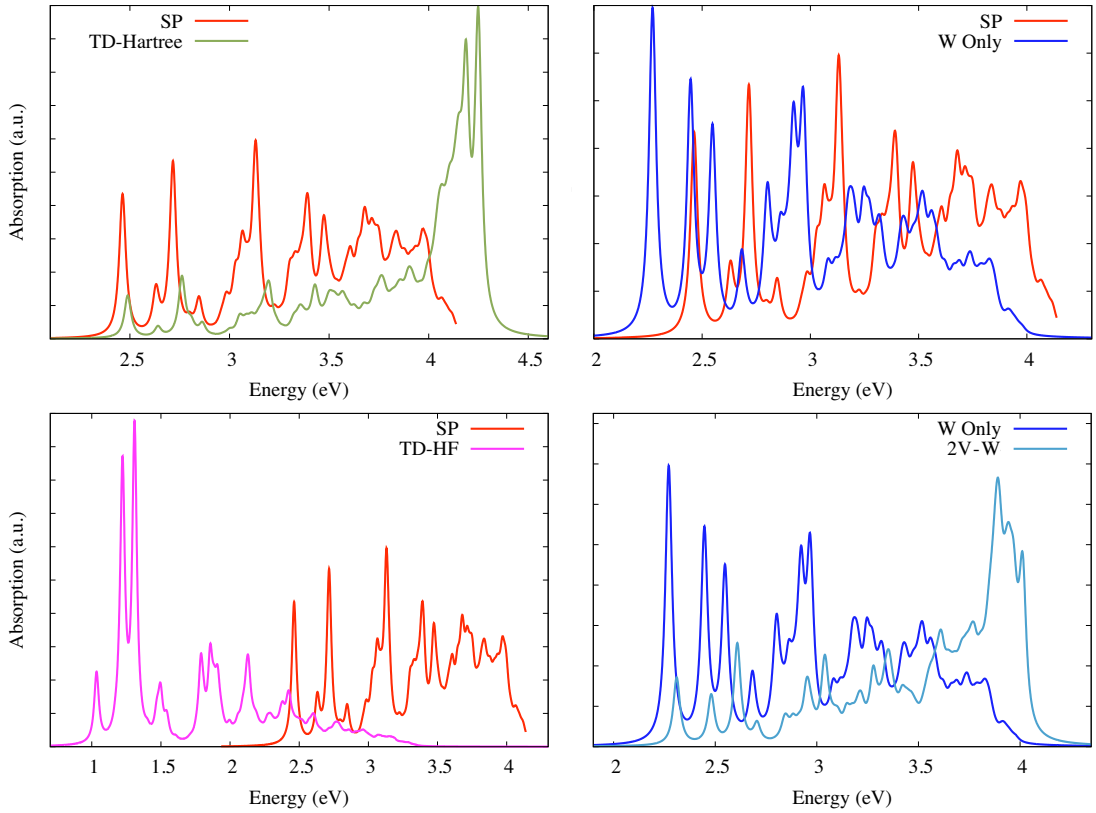

Figure 10.4: Spectra of a nanocrystal with a diameter of 4 nm, computed using different approximations of the BSE kernel. The top-left and top-right are computed using exchange only and direct only, respectively. The bottom-left is computed using exchange plus unscreened direct terms and the bottom-right compares spectra computed with the direct term only (dark blue) to the screened direct term plus exchange (light-blue). In all spectra, the energies of the largest electron and hole in the basis are 1077 meV and 624 meV, respectively. In several instances, the independent-particle spectrum is also included (red) as a point of reference.

the Time-dependent Hartree approximation (TDH). Alternatively, we can retain the direct term and neglect the exchange term (W only).

The spectra computed using only the exchange term and only the direct term are shown in the top left and top right panels of Figure 10.4, respectively. This shows us that the screened Coulomb interaction is responsible for the redshift of the absorption spectrum and the formation of a bound state in CdSe nanocrystals. Conversely, the TDH spectrum is blue-shifted in comparison to the independent-particle spectrum. The magnitude of the blueshift due to exchange is however, smaller than the magnitude of the redshift due to the direct term. We also observe a

large mixing of the independent-particle transitions, with an increase of the oscillator strengths of high-energy transitions in the TDH spectrum. This implies that the mixing of transitions, which results in high-energy transitions with strong oscillator strengths, and is observed in all spectra, is a consequence of exchange.

In the bottom-left panel of Figure 10.4 both the exchange and direct terms are included in the kernel however, both are unscreened. This is referred to as the Time-dependent Hartree-Fock approximation (TDHF). As Figure 10.4 shows, the TDHF approximation of the BSE kernel is not appropriate for semiconductors as it systemically overestimates the attraction between the electron and hole, therefore always resulting in a bound state. In contrast, the light-blue spectrum shown in the bottom-right panel of Figure 10.4 also includes the exchange and direct terms, however the direct term is screened in this instance (using the bulk dielectric constant). Screening of the direct term causes the absorption onset to differ by more than an eV in comparison to the spectrum computed in the TDHF approximation. This highlights the importance of dielectric screening in excitonic calculations.

Finally, we choose to compare spectra generated using $-W$ and $2V - W$ in the bottom-right panel of Figure 10.4. These kernels define the triplet and singlet Hamiltonians, respectively[150]. In the absence of spin-orbit coupling, the BSE Hamiltonian spin-singlet and spin-triplet configurations decouple, allowing them to be treated separately. Results show that the lowest triplet exciton state is lower in energy than the lowest singlet exciton state. For CdSe nanocrystals, recombination of the lowest triplet state is spin-forbidden [22], therefore all subsequent results are presented for the spin-singlet configuration as this contains the lowest, optically-active exciton state.

Connection Between the Bethe-Salpeter Equation and Configuration Interaction

We end this section by making the connection between the Bethe-Salpeter equation and the configuration interaction method, commonly used in quantum chemistry. An understanding of how the Hamiltonians are related enables us to make comparisons with prior calculations, particularly as configuration interaction has been used to treat the excitonic properties of nanocrystal systems in the past[23; 24; 119; 124–126; 145; 176; 196].

As detailed in Chapter 7, we approximate the direct term using static screening, specifically by replacing the microscopic, inverse dielectric function with the bulk, high-frequency dielectric constant. The use of static screening in the direct term is equivalent to the time-dependent, screened Hartree-Fock approximation of the BSE kernel[214] (TDsHF).

Prior authors have treated excitonic correlation in nanocrystals by expanding the Hartree-Fock Hamiltonian in a basis of single-excitation Slater determinants. This defines configuration interaction singles (CIS)[56; 125]. Upon inspection, the CIS two-particle Hamiltonian is equivalent to the resonant two-particle Hamiltonian of the BSE, taken in the limit of static screening[56] (see Equation (5.26) in Chapter 5).

Formally, configuration interaction singles is therefore equivalent to solving the Bethe-Salpeter equation in the Tamm-Dancoff approximation (TDA), with the kernel taken in the time-dependent, screened Hartree-Fock approximation[212]. Put more concisely, if the direct term is statically screened (TDsHF) and the coupling matrices are ignored (TDA) in the two-particle Hamiltonian given by Equation (5.29) in Chapter 5, then the solutions of the BSE are equivalent to those of CIS.

10.1.3 Spectral Convergence

In Figures 10.5 and 10.6, we present spectral convergence plots for a nanocrystal of 4 nm in diameter. The two-particle basis can be defined either in terms of the total number of electrons and holes included or by the energies of the N_e electron and N_h hole relative to the band extrema: $E_{i,\max} = E_{i_{N_i}} - E_{i_1}$, where i is the electron or hole index. It is convention in ab initio calculations to define the basis in terms of the maximum electron energy and set the maximum hole energy equal to this, such that $E_{h,\max} = E_{e,\max}$, however the band-edge holes exhibit a much higher density of states than the band-edge electrons in CdSe nanocrystals. This has the potential to hinder convergence as the number of hole states in the basis required to satisfy $E_{h,\max} \approx E_{e,\max}$ quickly becomes intractable as $E_{e,\max} \rightarrow$ large. In general however, we find that the low-energy spectral features are more sensitive to the maximum electron energy in the basis than they are to the maximum hole energy, therefore it is not crucial to ensure the condition, $E_{h,\max} = E_{e,\max}$, is met. This is demonstrated in Appendix G.

Fgure 10.5 shows that a moderate number of electron-hole pairs in the basis results in a low-energy spectral profile[2] with all the discerning features of a well-converged calculation. Subsequent convergence of the optical gap and oscillator strengths is relatively slow. Figure 10.6 shows that a doubling of the basis[3] leads to a change in the optical gap of $\sim$10 meV and demonstrates that we are able to converge the lowest features in the spectrum of a nanocrystal with a diameter of 4 nm to within a few meV, which is an order of magnitude smaller than the line width at room temperature. The convergence behaviour depicted in Figures 10.5 and 10.6 is representative of the entire range of nanocrystals in this study.

We find that basis convergence not only leads to the expected redshift of the

[2] 0.5 eV - 1 eV from the absorption onset.

[3] This is equivalent to increasing the energy cut-off from $(E_{h,\max}, E_{e,\max}) = (361, 906)$ meV to $(E_{h,\max}, E_{e,\max}) = (624, 1077)$ meV.

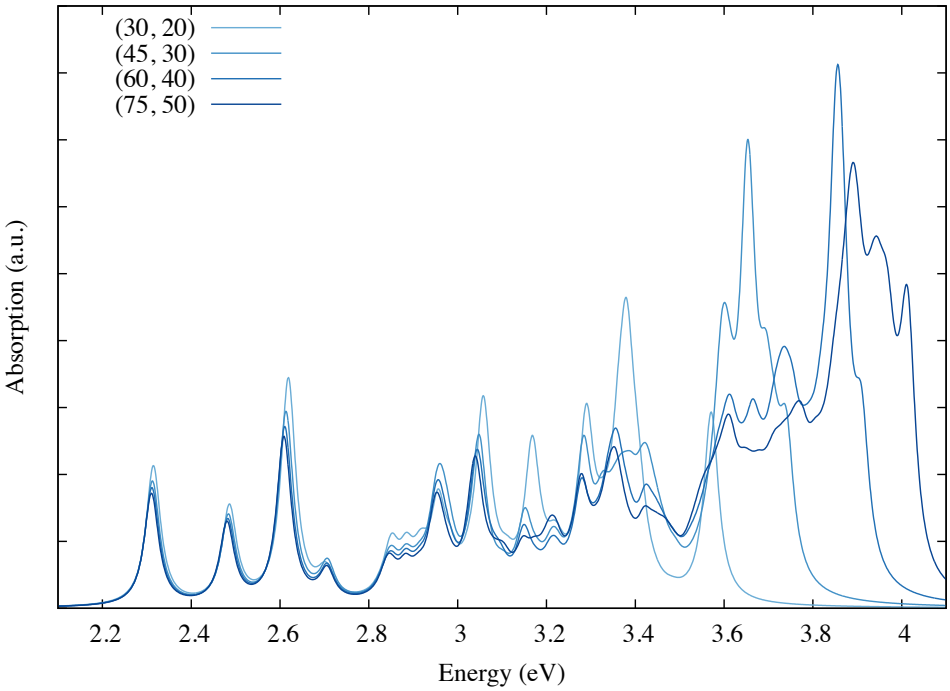

Figure 10.5: Spectral convergence of the absorption spectrum with respect to the two-particle basis containing (N_h, N_e) particles, where of N_h is the number of holes and N_e is the number of electrons in the basis. For a nanocrystal of 4 nm in diameter.

absorption onset but also results in a strong mixing of independent-particle transitions for all diameters treated, with a significant increase in the intensities of high-energy transitions. This is particularly noticeable in the absorption spectra of nanocrystals with small diameters, such as the one shown in Figure 10.2.

This redistribution of spectral weight was found to stem from the exchange term of the kernel. In bulk semiconductors the exchange interaction is comprised of a short range component and a long range component. The short range component is unscreened, whereas the long range component is screened with the bulk dielectric tensor[215]. Using a many-body treatment (configuration interaction singles), Franceschetti and coworkers have found that nanocrystals, including CdSe, also exhibit a long range exchange interaction[215]. They therefore use this phenomenological argument to justify their decision to screen the exchange interaction.

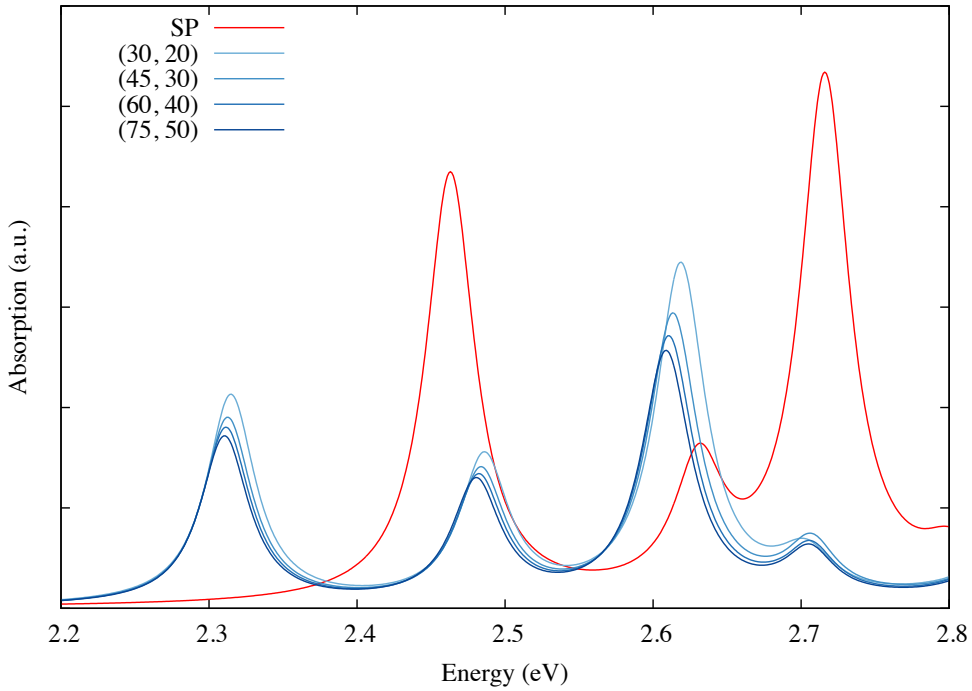

Figure 10.6: Convergence in the lowest-energy transitions of a nanocrystal with a diameter of 4 nm (blue lines). The independent-particle spectrum is included as a reference in red.

Conversely, the derivation of the BSE kernel using the *GW* definition of the self-energy results in an unscreened exchange term. As such, we do not screen the exchange interaction in our BSE implementation. There does, however, seem to be an empirical case for the screening of exchange and we suggest that this is something that could constitute further investigation.

10.2 Optical Absorption Spectra as a Function of System Diameter

In Figure 10.7, we present absorption spectra for CdSe nanocrystals with diameters ranging from 2 nm to 6 nm. One can see that the inclusion of many-body interactions not only leads to the well-documented, size-dependent redshift of the spectrum with respect to the independent-particle spectra but also a strong mixing of oscillator strengths. Specifically, we observe a large increase in the oscillator strengths of high-

energy transitions at the expense of the strengths of the lowest transitions. This effect is particularly prominent for nanocrystals containing less than 1000 atoms (below 4 nm in diameter).

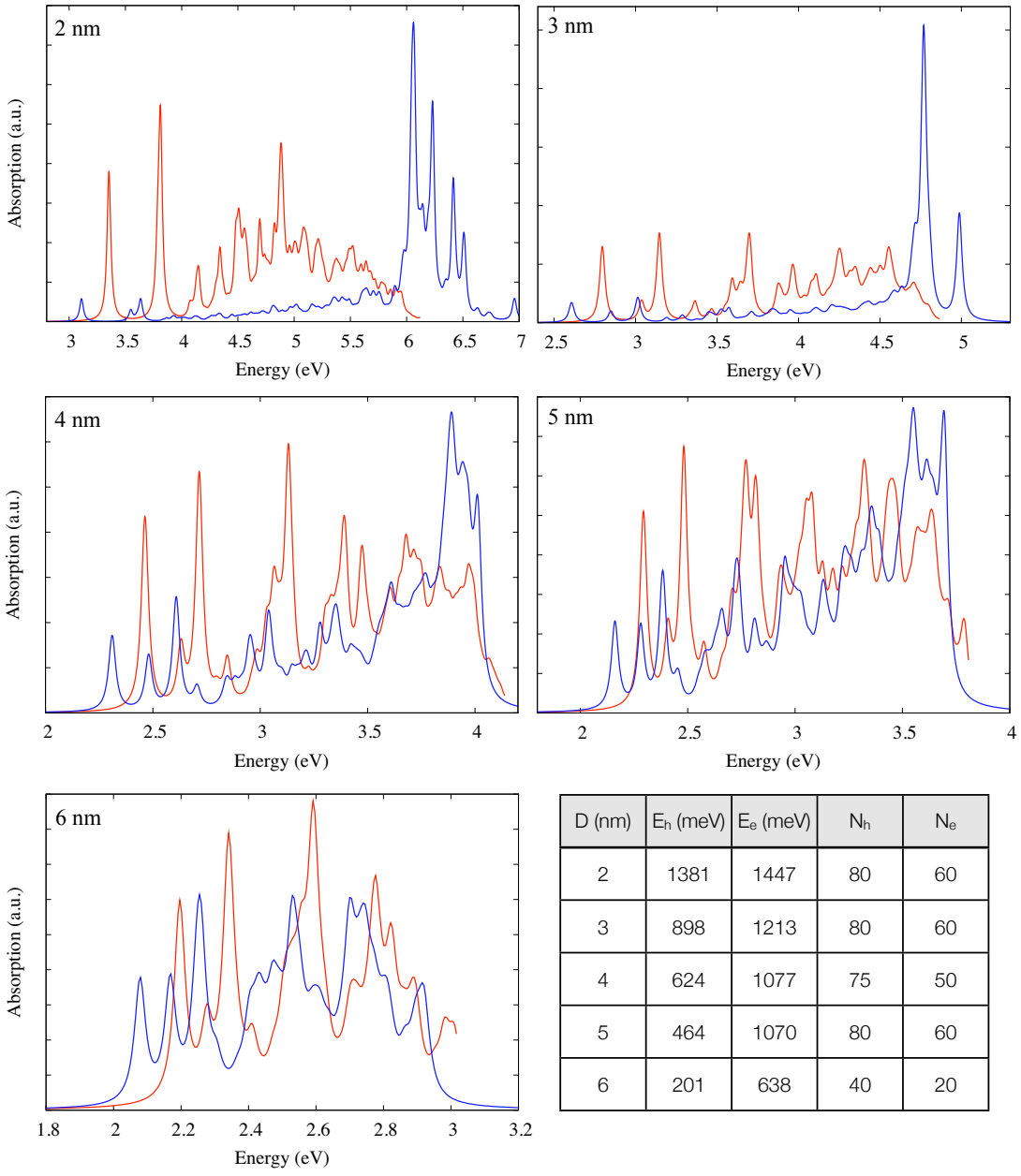

D (nm)	E_h (meV)	E_e (meV)	N_h	N_e
2	1381	1447	80	60
3	898	1213	80	60
4	624	1077	75	50
5	464	1070	80	60
6	201	638	40	20

Figure 10.7: A comparison of absorption spectra with (blue) and without (red) excitonic effects, for CdSe nanocrystals with diameters ranging from 2 nm to 6 nm. All spectra are convolved with Lorentizans, with fixed FWHM of 50 meV.

It is, however, difficult to distinguish whether this effect diminishes with increasing nanocrystal size or if one would see the same behaviour for larger nanocrystals, if their spectra were calculated using larger basis sets. This is investigated in more detail in Appendix G.

10.3 Optical Band Gap as a Function of System Diameter

The optical, excitonic gap is defined as the energy of the lowest, optically-active exciton state, which is equal to the quasiparticle band gap[4] plus the binding energy of the lowest spin-singlet exciton:

$$E_{g,opt} = E_g^{qp} + E_X, \tag{10.1}$$

where E_g^{qp} is the quasiparticle band gap and E_X is the binding energy of the lowest exciton state. The excitonic binding energy is negative, therefore the magnitude of the optical band gap is smaller than that of the quasiparticle band gap. In principle, E_g^{qp} should correspond to the quasiparticle band gap of the nanostructure, however, calculating the quasiparticle band gap is non-trivial. In ab initio calculations, the GW approximation of the self-energy operator provides the most accurate means of calculating quasiparticle energies for bulk and molecular systems[39], however this method is still currently too expensive to apply to nanoscale systems[41] and the details of GW calculations are beyond the scope of this thesis.

We therefore define E_g^{qp} using the independent-particle band gap predicted by our tight-binding model, which is defined as the difference in energies of the lowest unoccupied state and the highest occupied state. The tight-binding bulk band gap is fit to the bulk quasiparticle band gap and is therefore accurate by construction.

[4] A quasiparticle is an electron which is screened by the relaxation of all other electrons in the system.

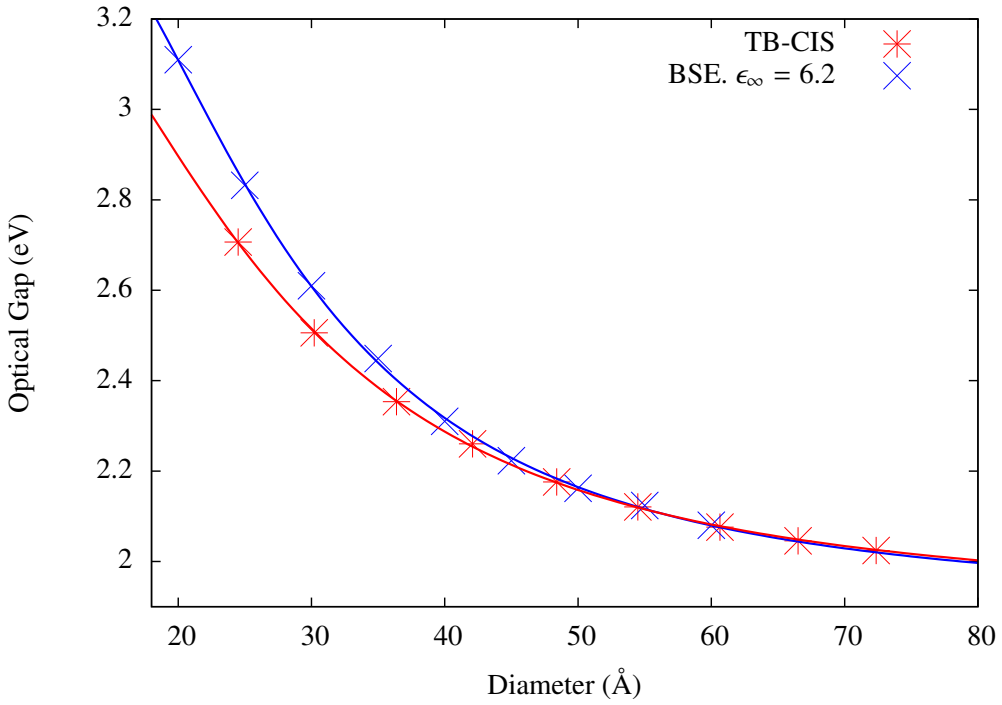

Figure 10.8: Dependence of the optical gap on nanocrystal diameter. The blue data is computed using our BSE implementation. Screening is approximated with the high-frequency dielectric constant. The red data is taken from reference [24] and is computed using CIS. In both sets of calculations, sp^3s^* eigenstates are used in the pair product basis.

Modifications to the band gap of the nanostructure, caused by polarisation charges at the surface are neglected.

All optical band gaps and excitonic energies presented in the following figures are determined by numerically identifying the first peak in the two-particle absorption spectrum. In doing so, we have been careful to confirm that the lowest peak is only comprised of one transition. One could alternatively diagonalise the two-particle Hamiltonian, however as we are interested in both the optical gap and the absorption spectrum, it is more efficient to determine the optical gap in this manner. All spectra are calculated with an energy spacing of 1 meV, so the error associated with spectral sampling is negligible. The exciton binding energy is then defined as the difference between the tight-binding band gap and the and optical band gap: $E_X = E_g - E_{g,opt}$.

The dependence of the optical gap and the exciton binding energy on the nanocrystal diameter are presented in Figures 10.8 -10.11, respectively. We compare our results to those of Lee and coworkers[24], who have computed excitonic optical gaps and binding energies using a very similar set of approximations to us. Like us, they work in a real-space implementation and construct the two-particle basis from tight-binding coefficients found using the orthogonal NN sp^3s^* model. Furthermore, the same set of approximations are made with regards to the orbital terms that comprise the kernel. This crucially means that any differences will be a result of approximations made in the two-particle calculations and not as a consequence of the independent-particle states.

Lee and coworkers perform their two-particle calculations using configuration interaction singles (CIS). As discussed above, this corresponds to the Tamm-Dancoff approximation (TDA) of our BSE implementation. They also introduce a phenomenological means of dielectric screening, which is used to screen both the direct and exchange terms.

In Figure 10.8 we compare the dependence of the optical gap on nanocrystal diameter calculated by Lee and coworkers, with the dependence calculated using our BSE implementation. In this instance, the full BSE Hamiltonian is used (the coupling matrices are included) and the direct term is screened with the high-frequency, bulk dielectric constant of CdSe. The exchange term is unscreened. The agreement in the optical gaps shown in Figure 10.8 is very good for nanocrystals with a diameter of 4 nm and greater, however we observe differences in the data for nanocrystals with smaller diameters. Furthermore, these differences become larger as the nanocrystal diameter gets smaller. At a diameter of 2 nm, our optical gap is ~ 0.2 eV larger than that predicted by Lee and coworkers.

This suggests that the differences stem from a size-dependent parameter. The obvious candidate is Lee and coworkers' choice of dielectric function, which varies

as a function of nanocrystal diameter, whereas we have used the same screening constant for all sizes considered in Figure 10.8.

10.3.1 Dielectric Screening in Nanostructures

To explain the discrepancies in the data presented in Figure 10.8, we begin by investigating the effect of dielectric screening. To retain a simple treatment of screening, we replace the microscopic dielectric function with the macroscopic dielectric constant of the nanocrystal. This approximation is justified on the basis that the Coulomb interaction is dominated by long-range terms[23]. The high-frequency, macroscopic dielectric constant of the nanocrystal is given by the modified Penn model for nanostructures[23; 216; 217]:

$$\epsilon_\infty(D) = 1 + (\epsilon_\infty^{bulk} - 1)\frac{(E_g^{bulk} + \Delta)^2}{(E_g(D) + \Delta)^2}, \tag{10.2}$$

where ϵ_∞^{bulk} is the high-frequency dielectric constant of bulk CdSe (6.2)[218], E_g^{bulk} is the bulk band gap, $E_g(D)$ is the independent-particle band gap of a nanocrystal with a diameter D, and $\Delta = E_2 - E_g^{bulk}$, where E_2 is the most pronounced peak in the bulk absorption spectrum. The size-dependence therefore enters via the independent-particle gap of the nanocrystal, calculated using our tight-binding model. The bulk band gap, $E_g^{bulk} = 1.9$ eV, is defined according to our bulk parameterisation.

A value of 5.72 eV is chosen for E_2, based on the position of the second peak of the bulk zincblende absorption spectrum, given in reference [219]. This results in a value of 3.82 eV for Δ. Evidently, this value could vary due to experimental uncertainties regarding the position of E_2 and the range of values reported in the literature for the bulk band gap (see table 6.2). We have tested the sensitivity of Equation (10.2) to physically sensible minimum and maximum values of Δ, and find that our choice of $\Delta = 3.82$ represents an average of two extremes, for the range of diameters investigated. The size-dependent dielectric constant defined using Equation (10.2)

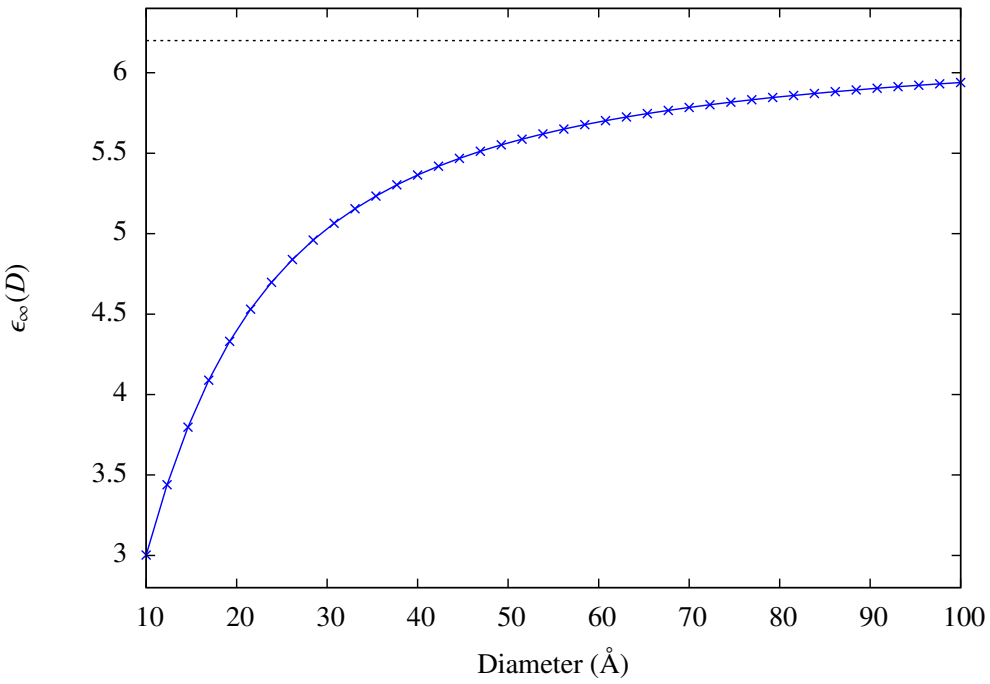

Figure 10.9: Size-dependence of the high-frequency dielectric constant, found using the modified Penn Model given by Equation (10.2).

is shown in Figure 10.9 and varies from 3 for a nanocrystal diameter of 1 nm, to ~ 6 for a diameter of 10 nm.

Such a model has been utilised several times in the literature[23; 24; 212], specifically in calculations of the exciton binding energy in CdSe nanocrystals. One could extend this further by including the ionic contribution to the dielectric screening[23], incorporating the dependence on the electron-hole separation[24], or accounting for the effect of the external dielectric environment, however all such models are phenomenological. We seek to illustrate the sensitivity of the results to the dielectric screening and get reasonable agreement for the optical gap as a function of diameter with Equation (10.2). To this extent, the use of Equation (10.2) is considered sufficient. This is discussed further in Appendix G.

Figure 10.10 compares the dependence of the optical gap on nanocrystal diameter, calculated by Lee and coworkers, with the dependence calculated using our BSE implementation. In this instance, we replace the bulk dielectric constant with the

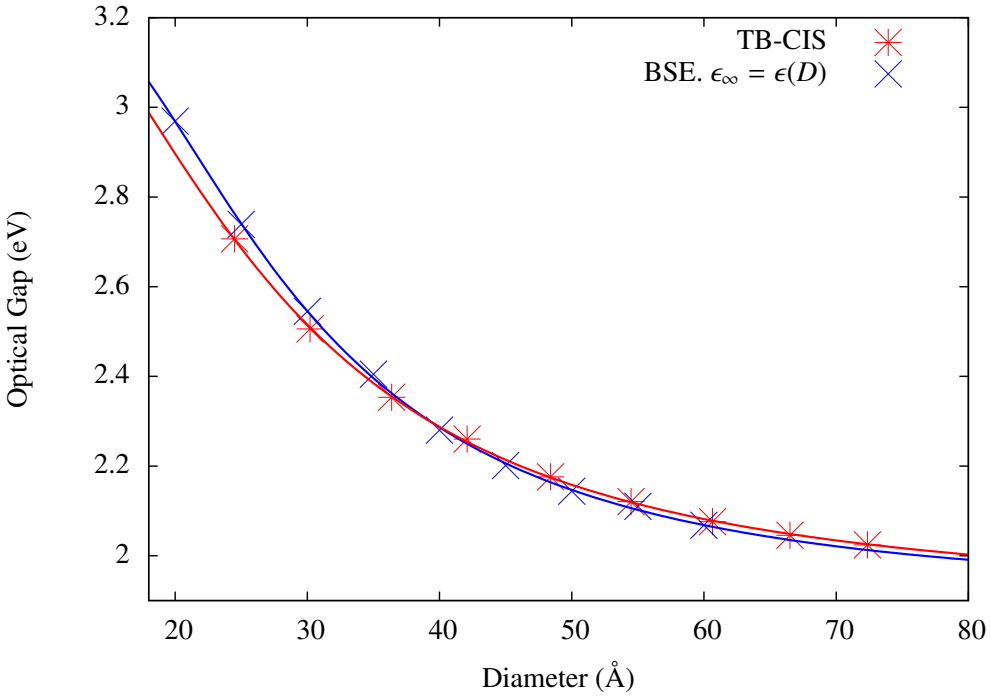

Figure 10.10: Dependence of the optical gap on nanocrystal diameter. The blue data are computed using our BSE implementation, with dielectric screening approximated by equation 10.2. The red data are taken from reference [24] and are computed using CIS. In both sets of calculations, sp^3s^* eigenstates are used in the pair product basis.

nanocrystal dielectric constant given by Equation (10.2). We would expect the optical gaps predicted by our model to be systematically lower in energy than that of Lee and coworkers, due to our choice of a smaller passivating energy. This is indeed the case for the optical gaps of nanocrystals with diameters above 4 nm. Agreement for nanocrystals with smaller diameters has also been considerably improved, although our corresponding optical gaps are still larger in energy.

A comparison of the two models can be made at the scale of meV by comparing the exciton binding energies (determined using Equation (10.1)). From Figure 10.11, we can see that the model of Lee and coworkers (red) systematically predicts larger excitonic binding energies than our BSE model (blue and green). Replacing the bulk dielectric constant with a phenomenological function, which essentially reduces the magnitude of the screening constant for smaller diameters, reduces the differences in

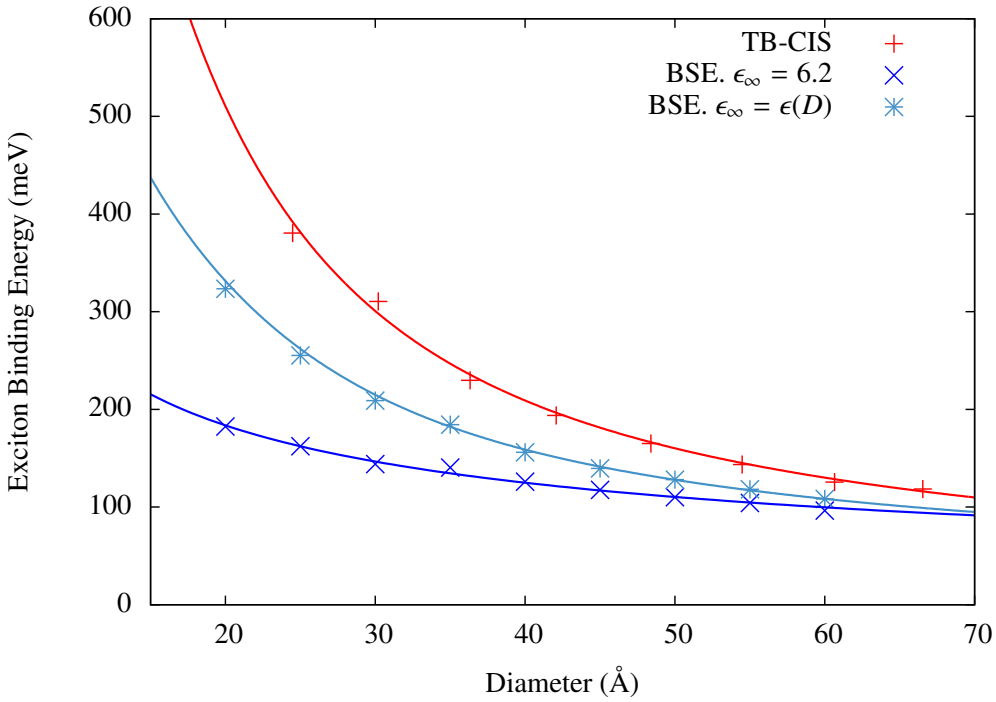

Figure 10.11: Dependence of the exciton binding energy on nanocrystal diameter for several sets of calculations: CIS using a size-dependent dielectric constant (red), BSE using the bulk dielectric constant to screen the direct term (blue) and BSE using a size-dependent dielectric constant to screen the direct term (turquoise).

our models by approximately half, on average. When comparing these data (red and turquoise) the differences in binding energies between 2 nm and 3.5 nm varies from 186 meV to 59 meV. For larger nanocrystals with diameters between 4 nm and 6 nm, the differences in binding energies vary from 54 meV to 24 meV, respectively. The size-dependent dielectric constant therefore does not fully account for the differences between our results and those of Lee and coworkers but it does illustrate the large effect that a reduction in the dielectric screening relative to the bulk can have on the exciton binding energy in nanostructures.

We propose several reasons for why we still observe differences between our results and those of Lee and coworkers. Screening of the exchange term will reduce the exchange energy and therefore increase the exciton binding energy. We infer from our kernel tests that the exchange term reduces the exciton binding energy by 80 meV and 30 meV in nanocrystals with diameters of 2 nm and 4 nm, respectively (see

Figure 10.4 in the latter case). As discussed above, the decision of whether or not to screen the exchange term in nanostructures is a controversial one.

Additionally, Lee and coworkers phenomenologically account for the electron-hole separation in their dielectric function. Short-range screening results in further reductions in the dielectric constant in comparison to the values given by Equation (10.2), which correspond to the long-distance limit. The subsequent effect would be larger on-site and nearest-neighbour orbital integrals. Figure 10.1 shows that these terms lead to a slight blueshift in the absorption spectrum, therefore it is possible that the inclusion of this effect may lead to a slight reduction in the exciton binding energies of the smallest nanocrystals studied.

The last point to consider is Lee and coworkers' choice of orbital basis, which differs from ours. The effect of the basis choice on the binding energy is also known to be size-sensitive, however as we have not performed calculations using Slater orbitals, we cannot comment on whether this will increase or decrease the values of the on-site and nearest-neighbour integrals.

In summary, it was not our aim to obtain perfect agreement with the results of Lee and coworkers but rather to assess the effect of dielectric screening on the exciton binding energy. These results suggest that in the absence of a microscopic dielectric function, some means of accounting for the reduction in dielectric screening experienced in quantum-confined nanostructures should be made, such that quantitative values can be predicted for excitonic binding energies. In the following sections, in which we compare our calculations with experiment, all results presented for CdSe nanocrystals will use Equation (10.2) to screen the direct term. The exchange term will be left bare, which is consistent with the consensus in the ab initio community[55; 220].

10.4 Effect of the Tamm-Dancoff Approximation

Aside from dielectric screening, a potential reason for the discrepancies between our calculated optical gaps and those of Lee and coworkers is that they use CIS, which is equivalent to solving the resonant, two-particle Hamiltonian block of our BSE Hamiltonian. This is commonly referred to as the Tamm-Dancoff approximation and corresponds to neglecting the coupling matrices that mix the resonant and anti-resonant transitions in our formalism.

This is a very attractive simplification to the full BSE formalism. Neglecting the coupling matrices reduces the number of matrix elements stored in memory by half. In simplifying the BSE Hamiltonian to the resonant, two-particle Hamiltonian, one is also able to exploit the Hermitian symmetry of the problem, reducing the effort required to solve Equation (5.37) (or the equivalent eigenvalue problem).

Its validity does however, appear to be problem-specific. Calculations have shown that in some systems, such as photoactive proteins[221] and carbon nanotubes[220], the TDA can predict erroneous optical gaps and optical spectra. On the contrary, calculations on silicon clusters demonstrated that the TDA had a negligible effect on the low-energy transitions of the spectra[222]. This warrants an investigation into the effect of the TDA on the optical spectra of CdSe nanocrystals, particularly as the vast majority of calculations to date have been done in an equivalent approximation.

We make the comparison between absorption spectra computed in the TDA to those computed using the full BSE Hamiltonian, for nanocrystals with diameters; 2 nm, 3 nm and 4 nm. The spectra corresponding to 2 nm and 4 nm diameters are presented in Figure 10.12. In both instances, the spectra exhibit minimal differences in their onsets. This shows that the TDA has a negligible effect on the optical gap of strongly-confined nanocrystals.

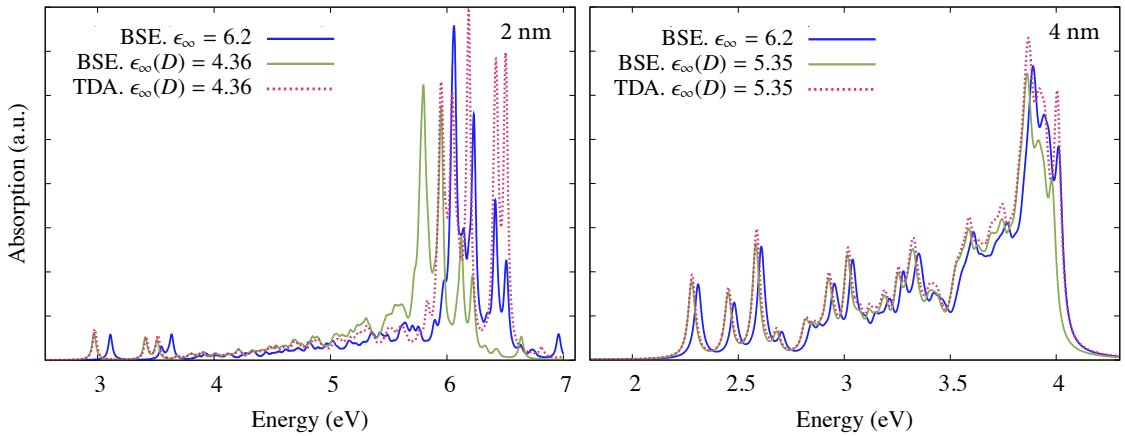

Figure 10.12: Absorption spectra for nanocrystals with diameters of 2 nm and 4 nm. Spectra are computed in three approximations: Full BSE with bulk dielectric screening (blue), full BSE with size-dependent dielectric screening (green) and TDA with size-dependent dielectric screening (dotted magenta).

Figure 10.12 also shows that transitions in the low-energy region of the spectra show no difference with regards to transition energy and only minor differences in oscillator strengths when computed in the TDA. We do however, see large shifts in the transition energies and strengths of the high-energy region of the spectrum for nanocrystals with diameters of 2 nm and 3 nm (the latter of which is not shown here). This effect is much less pronounced in the spectrum of the nanocrystal with a diameter of 4 nm but still present nonetheless.

From this analysis, we conclude that differences in the excitonic binding energies found using our formalism and that of Lee and coworkers are likely to largely be attributable to the reasons presented in the prior section and not the use of the TDA. Our results also suggest that full BSE calculations may be important in instances where one is interested in transitions greater than 1 eV above the lowest exciton state.

10.5 Experimental Comparisons

10.5.1 Optical Gap Dependence on Diameter

In Figure 10.13, we reproduce the data shown in Figure 3.2 of Chapter 3. Figure 3.2 presents best-fits to two sets of data for CdSe optical gaps as a function of diameter: The blue line represents the best-fit to experimental data[11; 21; 100; 110–113], whereas the red line represents the best-fit to tight-binding data[24; 100; 102; 107]. All lines of best-fit are defined with the expression[119]:

$$E_g = \frac{1}{ad^2 + bd + c} + E_{g,\text{bulk}}, \tag{10.3}$$

where d is the nanocrystal diameter, $E_{g,\text{bulk}}$ is the bulk band gap and (a, b, c) are fitting parameters. Figure 10.13 extends the prior plot by including the optical gap dependence on diameter computed with our BSE implementation (green line). Furthermore, the experimental data have been refit, such that all fits are now defined with Equation (10.3). The experimental data in Figure 3.2 were fit with Equation (3.2) in order to give an estimate for the average uncertainty in nanocrystal diameter. Details regarding the fitting process are discussed in Appendix G.

The agreement of the BSE calculations with the average optical gap as a function of diameter is very good. This may be somewhat fortuitous due to the spread in the values of the experimental data (see Figure G.5 in Appendix G), however the overall trend in the dependence is well-reproduced by our BSE calculations for a range of sizes. The empirical nature of our model means that quantitative agreement can be achieved for a specific set of data through the adjustment of fundamental parameters, such as the bulk band gap or the passivating energy. Agreement could also be improved below a diameter of 4 nm with a more rigorous treatment of the dielectric screening, as discussed in section 10.3.1.

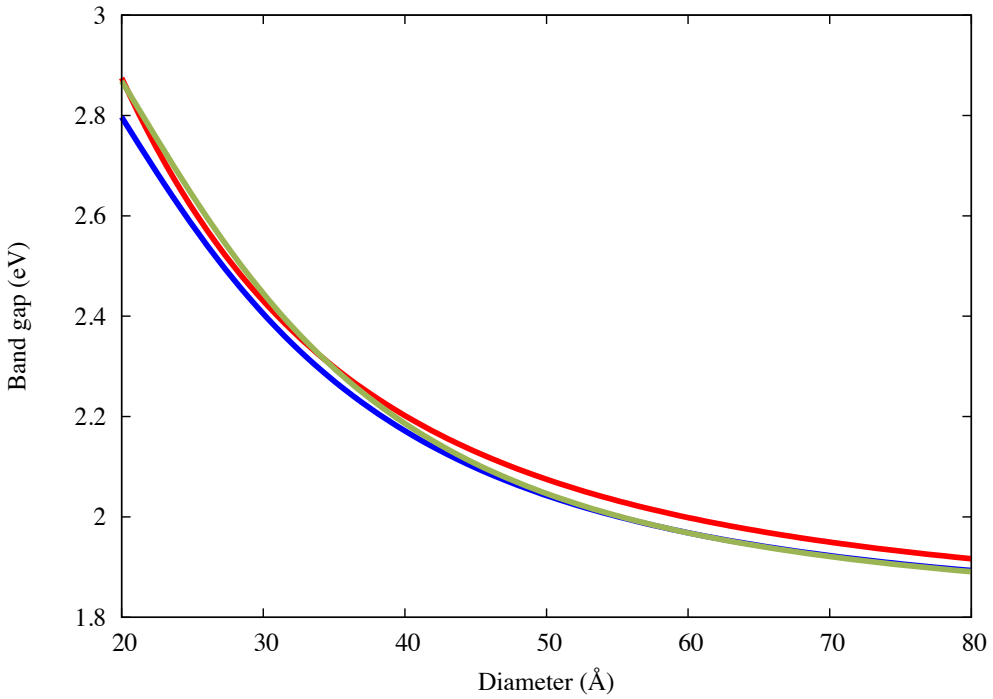

Figure 10.13: Lines of best-fit to the optical band gap of CdSe nanocrystals as a function of size: The experimental dependence on size is given by the blue line, the tight-binding dependence is given by the red line and the best-fit to our tight-binding+BSE results is given by the green line. All fits are produced with Equation (10.3).

10.5.2 Comparing Optical Absorption Spectra

Figure 10.14 compares experimental absorption spectra to those computed with our BSE implementation. The agreement of the onsets are much-improved for nanocrystals of all diameters, particularly those above 4 nm, when compared to independent-particle calculations shown in Figure 8.14 in Chapter 8. Indeed, the optical gaps can be accurately predicted without having to rely on size dispersion, as was the case previously. The agreement between the low-energy spectral features predicted by our BSE implementation and those observed in experiment is however, poor across the range of sizes investigated. While the predicted transition energy of the second peak is reasonable for nanocrystals with diameters of 4 nm and above, our BSE implementation predicts a splitting of the second peak that is not observed experimentally.

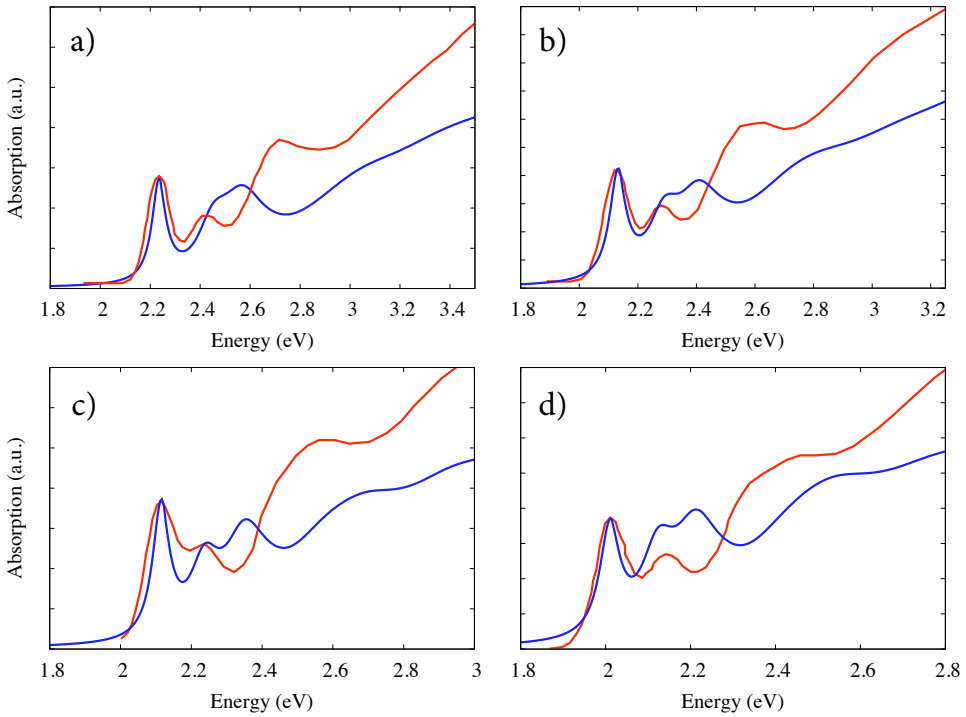

Figure 10.14: Comparison between the absorption spectra predicted with our BSE implementation and experiment, for CdSe nanocrystals with varying diameters. Experimental spectra are shown in red whereas calculated spectra are shown in blue. All calculated spectra are redshifted by 0.1 eV to account for finite temperature, except spectrum c), which is redshifted by 0.06 eV. The panels correspond to nanocrystals with diameters: a) d_E=3.1 and d_C=3.4 nm (15 eV), b) d_E=4.1 and d_C=4.1 nm (15 eV), c) d_E=4.8 and d_C=4.8 nm (25 eV), and d) d_E=5.2 and d_C=5.2 nm (15 eV), respectively. Here, d_E is the experimentally-referenced diameter and d_C is the simulated nanocrystal diameter. The value in the brackets refers to the passivation energy used for each simulation. The spectra in panels a) and b) were simulated with FWHM of 70 meV, whereas the spectra in panels c) and d) were simulated with FWHM equal to 60 meV.

The low-energy spectral features predicted by our BSE implementation are persistent for the range of sizes investigated. The fact that the discrepancies in the lowest spectral features are observed for the range of sizes suggests that the problem is systematic rather than size-dependent. For example, the size of the two-particle basis would not change this nor would a reduced value in our size-dependent dielectric constant.

The most fundamental physical effect that is missing from our model is spin-orbit

coupling. We know that the bulk zone-centre splitting in CdSe is 0.42 eV, which is comparable to the strength of the electron-hole interaction in strongly-confined nanocrystals (as indicated in Figure 10.11). We therefore suggest that agreement with experiment would most likely be improved via its inclusion in the two-particle model.

10.6 Conclusion

In conclusion, we have applied our BSE implementation to the prototypical CdSe nanocrystal system. We have looked at how the orbital terms contribute to the kernel and at what effect they have on the spectrum in Figures 10.1 - 10.3. In doing so, we have established that the long-range, Coulomb-like orbital interactions make the most significant contribution to the kernel and consequently to the optical spectrum. Furthermore, we have independently investigated the effect of the direct and exchange terms on the absorption spectrum. Figure 10.4 shows that the direct term is required in order to observe the redshift associated with quantum-confined, direct-gap semiconductors and that the magnitude of the shift is overestimated unless it is screened by the dielectric function. It also shows that the exchange term is responsible for a reduction in the Coulomb energy of the lowest exciton as well as mixing the oscillator strengths of the independent-particle transitions.

We have demonstrated in Figure 10.7 that our BSE implementation not only allows us to access information regarding the lowest exciton state but can also efficiently generate the optical absorption spectra of finite systems containing up to 4000 atoms. This opens the way towards studying the many-body properties of heterostructures, in which the spatial localisation of the electron and hole can be engineered, producing excitonic properties that are not achievable with single-material nanostructures[73; 74; 223].

Figure 10.12 demonstrates how the Tamm-Dancoff approximation of the two-particle

Hamiltonian has a minimal effect on the transition energies and oscillator strengths in the low-energy region of the optical absorption spectra of CdSe nanocrystals.

We have shown in Figure 10.13 that our BSE implementation is able to reproduce the average optical gap dependence on nanocrystal diameter and binding energies that are consistent with prior calculations. We have unfortunately, however, not been able to reproduce the lowest features observed in the optical absorption spectra of CdSe nanocrystals. Future work would therefore involve applying our model to a material in which the spin-orbit interaction is relatively weak, such as CdS. It would also be desirable to investigate a more complete independent-particle model that includes spin-orbit coupling and look at how this could be efficiently incorporated into the two-particle Hamiltonian.

In the final results chapter of this thesis, we apply our BSE implementation to CdSe nanoplatelets. The quasi two-dimensional nature of these systems is expected to result in excitonic binding energies in excess of those observed in CdSe nanocrystals. To date, no many-body calculations have been performed on the optical gaps or exciton binding energies as a function of thickness, and the effects of lateral confinement are only just beginning to be considered experimentally[207; 224]. We also investigate the optical absorption spectrum and compare simulation to highly reproducible experimental data. While our independent-particle model predicts numerous optical transitions, only two macroscopic peaks are observed experimentally. We therefore clarify to what extent the observed spectral features are a consequence of the electron-hole interaction.

Chapter 11

Many-Body Calculations of the Optical Properties of CdSe Nanoplatelets

In this final results chapter, we apply our BSE implementation to quasi two-dimensional CdSe nanoplatelets and provide the first many-body calculations of the optical gap and lowest exciton binding energy as a function of platelet thickness. In doing so, we find a binding energy dependence on thickness that differs in comparison to what has previously been found using a tight-binding plus effective mass model[95]. The optical absorption spectra of CdSe nanoplatelets with thicknesses of 3 ML, 4 ML and 5 ML are simulated. We find good agreement between experiment and theory, with our BSE implementation reproducing the main features of the experimental spectra.

11.1 Introduction

Excitonic effects are particularly important to consider in two-dimensional structures, where the exciton is strongly confined in one dimension. For example, BSE calculations have shown graphene to exhibit a binding energy of 600 meV for the lowest exciton state[210]. More recently, monolayer molybdenum disulfide (MoS_2) was found to have exciton binding energy ~ 1 eV[225]. One would also expect to find large binding energies for the lowest exciton state in quasi two-dimensional CdSe nanoplatelets due to the strong confinement perpendicular to the plane.

There are relatively few computational studies of exciton binding energies in nanoplatelets. Eight-band $\mathbf{k}.\mathbf{p}$ calculations by Achtstein and coworkers predict binding energies in the range $100 - 400$ meV for thicknesses of 3 ML - 7 ML[87]. Benchamekh and coworkers calculate the exciton binding energy using an effective mass wave function for the in-plane motion and define the thickness-dependent wave function with tight-binding amplitudes to capture the atomic variation[95]. In the absence of self-energy corrections, they find binding energies of the lowest exciton state equal to 168 meV for a 3 ML system, reducing to 93 meV for a 7 ML system. Given the growing interest in these quasi two-dimensional colloidal systems and their potential applications in light-emitting diodes[226] and lasing[80; 97] there is a clear need for accurate calculations of the exciton binding energy using a many-body formalism.

11.2 Optical Gap Dependence on Nanoplatelet Dimensions

The nanoplatelet calculations presented in this chapter are done with the smaller lateral dimensions of 7 nm $\times$ 7 nm, rather than the 10 nm $\times$ 10 nm used for the independent-particle calculations. We compromise on the lateral dimensions of

Thickness (ML)	Number of Atoms
2	1393
3	1946
4	2498
5	3051

Figure 11.1: Number of atoms in nanoplatelet systems considered in this study. The lateral dimensions are fixed at 7 nm × 7 nm.

the system to keep the calculations practical and ensure convergence. Indeed, an increase in the lateral dimensions from 7 nm to 10 nm corresponds to a doubling of the nanoplatelet planar area, approximately doubling the number of atoms in the system. The corresponding system sizes for nanoplatelets with lateral dimensions of 7 nm are given in Table 11.2.

11.2.1 Optical Gap Dependence on Lateral Dimensions

The exciton Bohr radius in a two-dimensional CdSe nanoplatelet is 3.5 nm (see Chapter 9). It is therefore expected that a reduction in lateral dimensions from 10 nm to 7 nm will lead to some enhancement in the in-plane confinement of the exciton, however this should not be large as we avoid entering the strong confinement regime.

We therefore quantify the effect of lateral confinement on the optical gap for a nanoplatelet with a thickness of 4 ML, in Figure 11.2. In the absence of a suitable, model dielectric function, we screen all calculations using the bulk high-frequency dielectric constant for CdSe. This is more appropriate than the static dielectric constant as the exciton binding energies are far in excess of the optical phonon frequencies (∼20 meV in CdSe). The line of best-fit is defined with Equation (10.3) in Chapter 10, where we have replaced the nanocrystal diameter with platelet lateral length ($L_x = L_y \equiv L$).

Th line of best-fit shown in Figure 11.2 is therefore defined using $E(L) = \frac{1}{aL^2+bL+c} + E_{g,4ML}$, where $(a, b, c) = (0.278,\ 0.165,\ 0.626)$ are best-fit parameters

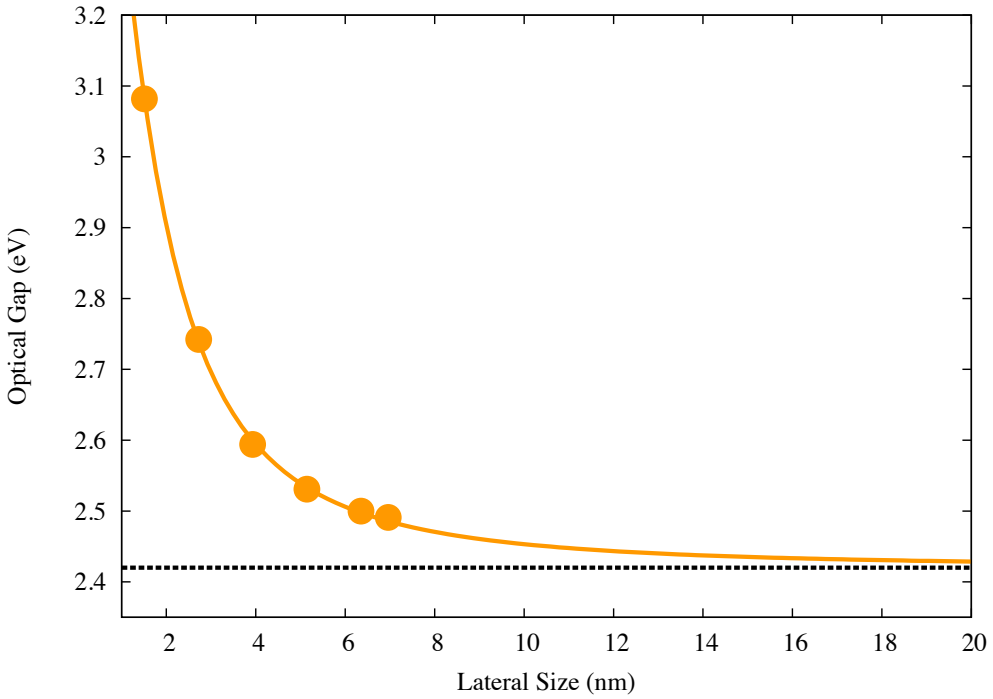

Figure 11.2: The dependence of the optical gap on lateral dimensions for a CdSe nanoplatelet with a thickness of 4 ML. BSE data are given in orange and have been corrected for temperature. All values have been calculated for platelets with a square aspect ratio. The dashed, black line corresponds to the experimental value of the optical gap.

and $E_{g,4ML} = 2.42$ eV is the experimental optical gap for a 4 ML-thick platelet, quoted in Table 9.2 of Chapter 9. This equation allows a better fit to the data than Equation (9.2) in Chapter 9 due to the additional degrees of freedom and demonstrates that the optical gap does not scale perfectly as $\frac{a}{L^2}$ with the lateral dimensions. This is also found to be the case for the optical gap as a function of thickness, which is discussed below.

Figure 11.2 also allows us to quantify the difference in the optical gap as a consequence of using smaller lateral dimensions in the calculations. For a fixed thickness of 4 ML, the difference in the optical gap of a nanoplatelet with lateral dimensions of 7 nm and a nanoplatelet with lateral dimensions of 10 nm is $\sim$ 20 - 40 meV, depending on the function used to fit the data. This increases to 50-60 meV when compared to a nanoplatelet with lateral dimensions of 20 nm.

11.2.2 Optical Gap Dependence on the Thickness

We compare the experimental and computed optical gaps for CdSe nanoplatelets in Figure 11.3. In the only prior tight-binding study by Benchamekh and coworkers, they find that the electron and hole self-energies approximately cancel the attractive image-charge interactions for the lowest exciton state (image charge interactions refer to the electron interacting with the hole image charge and the hole interacting with the electron image charge)[95]. This suggests that the optical gap is approximately equal to the independent-particle gap plus the electron-hole Coulomb (direct) and exchange energies. These findings support our choice not to include self-energy corrections for the lowest exciton state as a reasonable approximation.

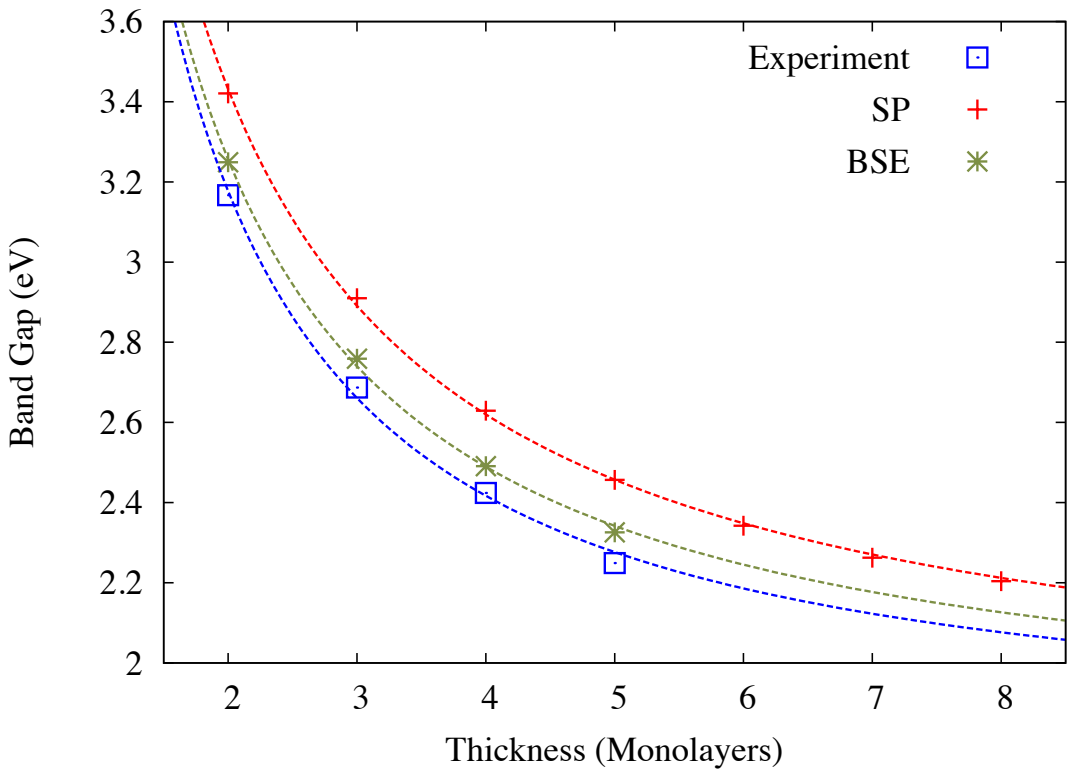

Figure 11.3: Band gaps as a function of thickness: Experimental optical gaps (blue squares/blue line), TB independent-particle gaps (red pluses/red dashed line) and TB+BSE optical gaps (green stars/green line). The experimental data is consistent with the values given in Table 9.2 and the computational data has been shifted down in energy by 0.1 eV to account for effect of temperature on the band gap. Nanoplatelet lateral dimensions are defined as 7 nm × 7 nm.

Figure 11.3 compares the experimentally-determined optical gaps (blue squares) listed in Table 9.2 in Chapter 9, to those predicted by our tight-binding model. The red pluses correspond to the independent-particle approximation whereas the green stars correspond to the tight-binding+BSE calculations. Benchamekh and coworkers have also computed the dependence of the optical gap on nanoplatelet thickness, however their results are systematically larger than ours and are therefore presented in Appendix G with a discussion, rather than here.

Figure 11.3 shows that our BSE calculations overestimate the experimental results. We suggest two reasons for this. Firstly, the cost of the many-body calculations forces us to compromise on the lateral dimensions of the nanoplatelets. As inferred from Figure 11.3, a 4 ML-thick nanoplatelet with lateral dimensions of 7 nm will have an optical gap ~ 0.05 eV larger than the same nanoplatelet with lateral dimensions of 20 nm. One would therefore expect a calculated value of 2.44 eV for the optical gap of a 4 ML-thick platelet with lateral dimensions of 20 nm. Much closer to the experimental value of 2.42 eV.

Secondly, we screen the direct term with the bulk high-frequency dielectric constant of CdSe, however we have seen that this overestimates the average screening in CdSe nanocrystals. It is reasonable to expect that it also overestimates the average screening in CdSe nanoplatelets, as the two systems exhibit comparable surface to volume ratios. These ratios are given in Table G.6 in Appendix G.

Despite the general overestimation of the experimental optical gaps by our TB+BSE model, the exponent of the fit to the TB+BSE data is very close to the exponent found from fitting the experimental data. The best-fit parameters and standard deviations for the lines shown in Figure 11.3 are given in Table 11.1. In all instances, the data is best fit with an exponent approximately equal to one, rather than an exponent of two, where the latter is associated with the thickness exponent in the expression for the energy of carriers confined in an infinite 1D quantum well.

Data	a	σ_a	b	σ_b
Experimental	3.07	0.152	1.16	0.0504
TB Independent-Particle:				
7 nm × 7 nm	3.25	0.0436	0.992	0.0115
10 nm × 10 nm	3.35	0.0728	1.056	0.0191
TB+BSE	3.07	0.0906	1.079	0.0295

Table 11.1: Parameters and standard deviations for the lines of best-fit plotted in Figure 11.3.

11.2.3 Exciton Binding Energy Dependence on Thickness

In Figure 11.4 we show the binding energy of the lowest exciton state as a function of nanoplatelet thickness. The results of Benchamekh and coworkers, in which image charge effects are excluded and a dielectric constant of $\epsilon_\infty = 6$ is used, have also been included[95]. The lack of theoretical details provided in their paper and the variety of effective mass methods described in the literature make it hard to comment on the exciton binding energies found by Benchamekh and coworkers, however we can make a comparison in terms of the dependence they find using a semi-classical approach and the dependence found using our many-body formalism. Despite the systematic disagreement in optical gaps as a function of thickness between our model and Benchamekh and coworkers', the differences in exciton binding energies predicted by the two models are much smaller.

Data points predicted by both models are available for nanoplatelets with thicknesses of 3 ML, 4 ML and 5 ML. For these thicknesses, there is reasonable agreement in the magnitude of the exciton binding energy found using the two formalisms, however the dependence of the binding energy on thickness found from fitting to equation (9.2) differs considerably between the two models.

If we fit the dependence assuming a scaling inversely proportional to the well thickness, we obtain an exponent of 0.304 (3 s.f.) for our BSE results and an exponent of 0.704 (3 s.f.) for the results of Benchamekh and coworkers. The difference in the exponents may partially be attributable to the exchange interaction,

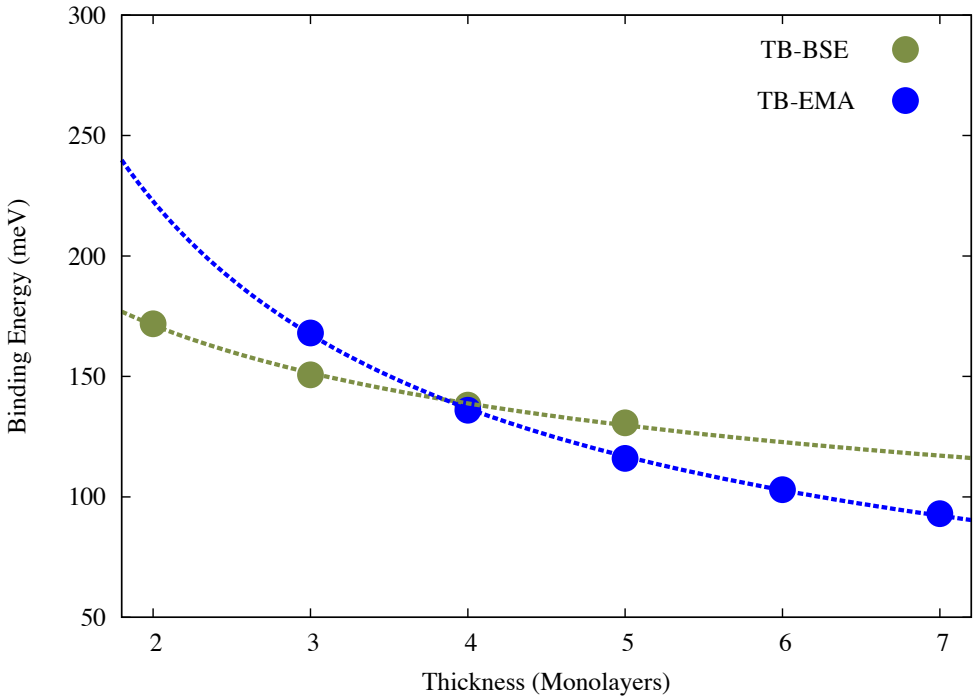

Figure 11.4: Binding energy of the lowest exciton state as a function of nanoplatelet thickness. Our tight-binding + BSE calculations are given in green whereas the tight-binding + effective mass calculations of Benchamekh and coworkers are given in blue. Lines of best-fit are given by Equation (9.2).

which is included in our calculations but absent in those of Benchamekh and coworkers, however it is more likely that it reflects the very different methodologies used to compute the binding energies.

At the timing of writing this thesis, a systematic experimental study of the exciton binding energy as a function of thickness has not been conducted. Kunneman and coworkers inferred that the excitonic binding energy of a CdSe nanoplatelet with a thickness of 5 ML must exceed thermal energy at room temperature (∼25-40 meV)[79]. All of our values are clearly well in excess of this. More specifically, Grim and coworkers inferred a binding energy of 132 meV ±20 meV for CdSe nanoplatelets with a thickness of 4 ML [97]. This is in strong agreement with our value of 138 meV (and Benchamekh and coworkers' value 136 meV). A systematic, experimental study of the exciton binding energy as a function of thickness is therefore desired to compare our predictions against.

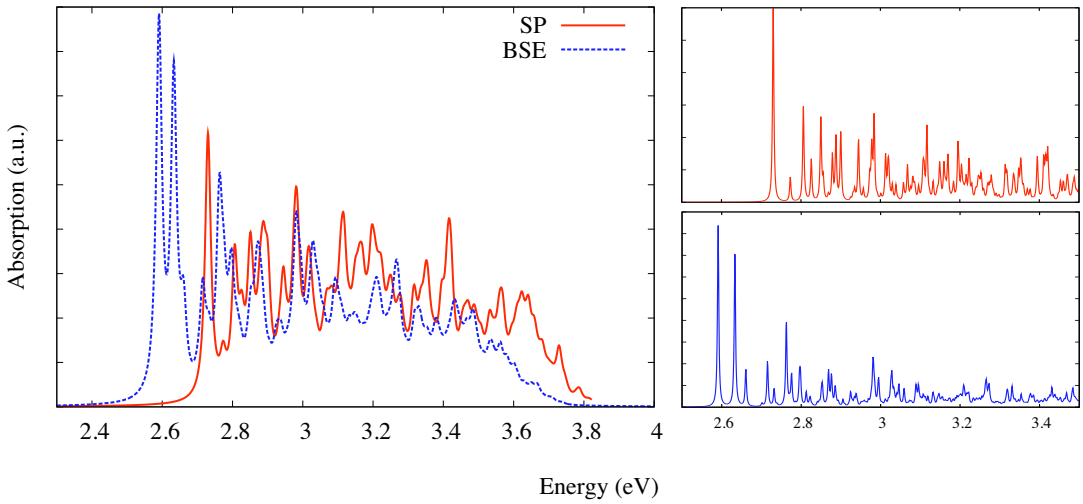

Figure 11.5: Absorption spectrum for a CdSe nanoplatelet of 4 ML in thickness. The independent-particle spectrum is presented in red, whereas the spectrum including excitonic effects is presented in blue. Spectra on the left are convolved with Lorentzians of 20 meV (FWHM), whereas those on the right have a minimal broadening of 4 meV (for an energy spacing of 1 meV).

11.3 Optical Absorption Spectra of CdSe Nanoplatelets

In Figure 11.5, we present the absorption spectrum for a nanoplatelet of 4 ML in thickness. The smaller panels of the figure correspond to the absorption onset with and without excitonic effects (blue and red spectra, respectively), highlighting the effect of the electron-hole interaction on the transitions.

The inclusion of excitonic effects in CdSe nanoplatelets using the BSE formalism has a very different effect on their absorption spectra in comparison to the effect it has on the absorption spectra of CdSe nanocrystals. Inclusion of many-body effects in the absorption spectra of CdSe nanocrystals led to a reduction in the oscillator strengths of the lowest transitions. Figure 11.5 shows us that the opposite occurs in CdSe nanoplatelets. In this system, we observe an enhancement of the lowest transitions in the absorption spectrum, as well as a redshift of the spectrum due to the formation of a bound exciton state.

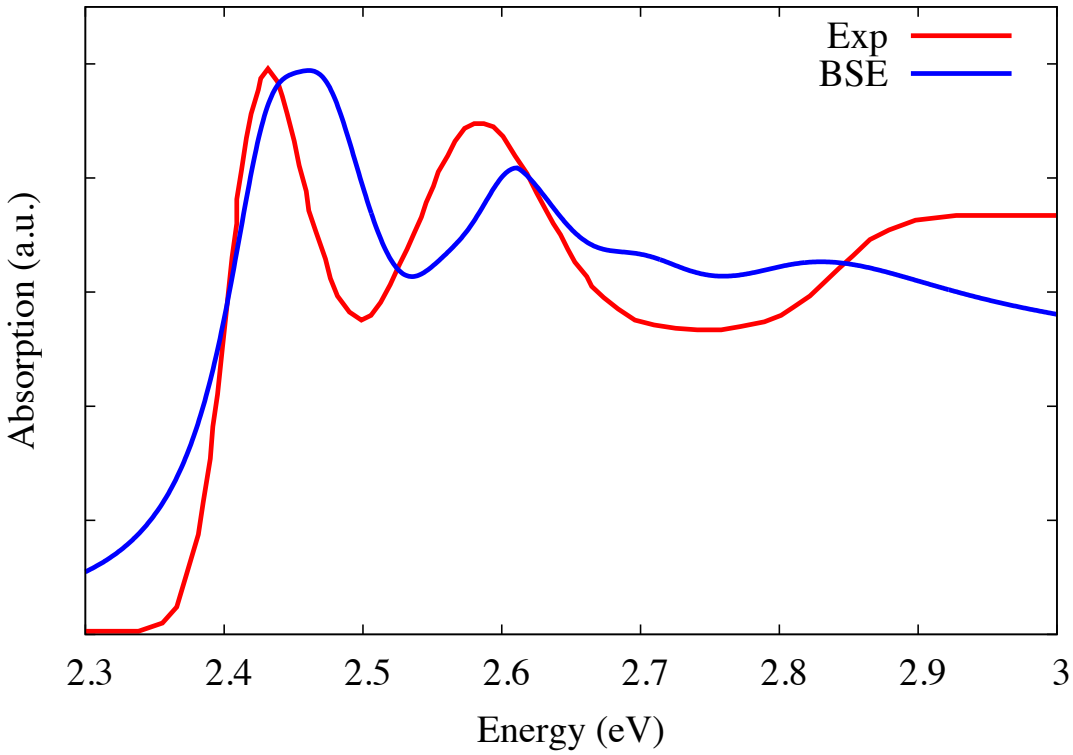

Figure 11.6: Absorption spectra for a CdSe nanoplatelet of 4 ML in thickness. The experimental spectrum in red is taken from reference [97]. The spectrum computed with our BSE implementation utilises an initial spectral line width with a FWHM of 80 meV. This linearly increases to 267 meV between the transition energies of 2.61 eV and 3 eV.

Far more features are visible in the calculated many-body spectrum in relation to the experimental spectrum. We therefore present the following many-body spectra with energy-dependent line widths. These are shown in Figures 11.6 - 11.8, along side their respective experimental spectra.

A Comparison with Experimental Absorption Spectra

In Figure 11.6, we have redshifted the calculated spectrum by 0.1 eV to account for the effect of temperature on the band gap. From inspection of Figure 11.2, we can see that the optical gap will contract by $\sim$ 50 - 60 meV when the lateral dimensions are increased from 7 nm to 20 nm. We therefore redshift the computed spectrum by an additional 60 meV to compensate for the effects of lateral confinement on the optical gap. We also compare computed absorption spectra for CdSe nanoplatelets

with thicknesses of 3 ML and 5 ML to experiment in Figures 11.7 and 11.8, respectively. All figures demonstrate that the main spectral features associated with the absorption spectra of CdSe nanoplatelets are captured with our tight-binding plus BSE model: Two prominent spectral peaks separated by an approximately parabolic profile, which is subsequently followed by a more pronounced spectral drop that then rises and smoothens off, with no further discernible features.

In each instance, empirical redshifts are required in order to achieve agreement with the experimental optical gaps (in addition to the temperature-related shift)[1]. This systematic overestimation was already seen in the optical gap dependence with thickness, shown in Figure 11.3. We suggest that this is attributable to our choice of lateral dimensions in each instance, as well as our decision to screen the electron-hole interaction with the high-frequency dielectric constant. In the prior chapter, we demonstrated that on average, this overestimated the dielectric screening in CdSe nanocrystals. Indeed, the macroscopic dielectric function has been shown to be nonlocal in 2D systems such as graphane, causing the Coulomb potential to converge on the unscreened 3D Coulomb potential at large in-plane separations[227]. Reduction in dielectric screening would consequently increase the binding energies of the exciton states and redshift the optical gap.

In Figures 11.6, 11.7 and 11.8 our calculations overestimate the width of the first peak and slightly underestimate the width of the second peak in relation to experiment. The spectral line width is a post-processing detail, achieved by convolving the transitions with Lorentzian profiles. This is approach is commonly employed as the calculation of spectral line widths requires a proper treatment of the frequency-dependence in the microscopic dielectric function, and is therefore very expensive.

A fixed line profile with a FWMH of 20 meV is used in the generation of the initial

[1] Empirical shifts of 80 meV, 60 meV and 90 meV for platelets with thicknesses of 3 ML, 4 ML and 5 ML, respectively.

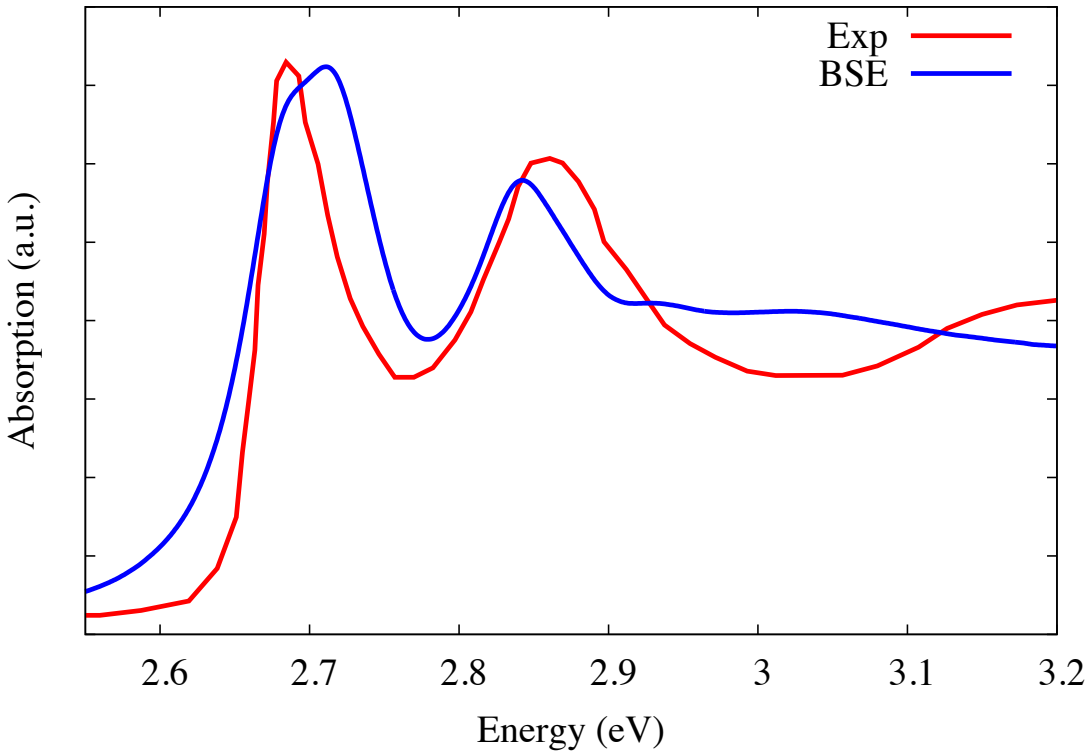

Figure 11.7: Absorption spectra for a CdSe nanoplatelet of 3 ML in thickness. The experimental spectrum in red is taken from reference [72]. The spectrum computed with our BSE implementation utilises an initial spectral line width with a FWHM of 60 meV. This linearly increases to 229 meV between the transition energies of 2.88 eV and 3.2 eV.

two-particle spectrum shown in Figure 11.5. With this setting, it is apparent that the lowest feature in the spectrum is actually comprised of two strong, closely-spaced excitonic transitions. The FWMH of the lowest peak in CdSe nanoplatelets is $\sim$ 45 meV at room temperature[228], however we find that a FWHM of more than 60 meV is required in order for the two lowest, closely-spaced transitions to be indistinguishable in our calculations.

The line profile of the lowest experimental peak is asymmetric for all thicknesses shown, which suggests the presence of a strong, band-edge transition followed closely in energy by a weaker transition. This implies that our calculations either overestimate the separation of the two, closely-spaced transitions or they overestimate the intensity of the second transition.

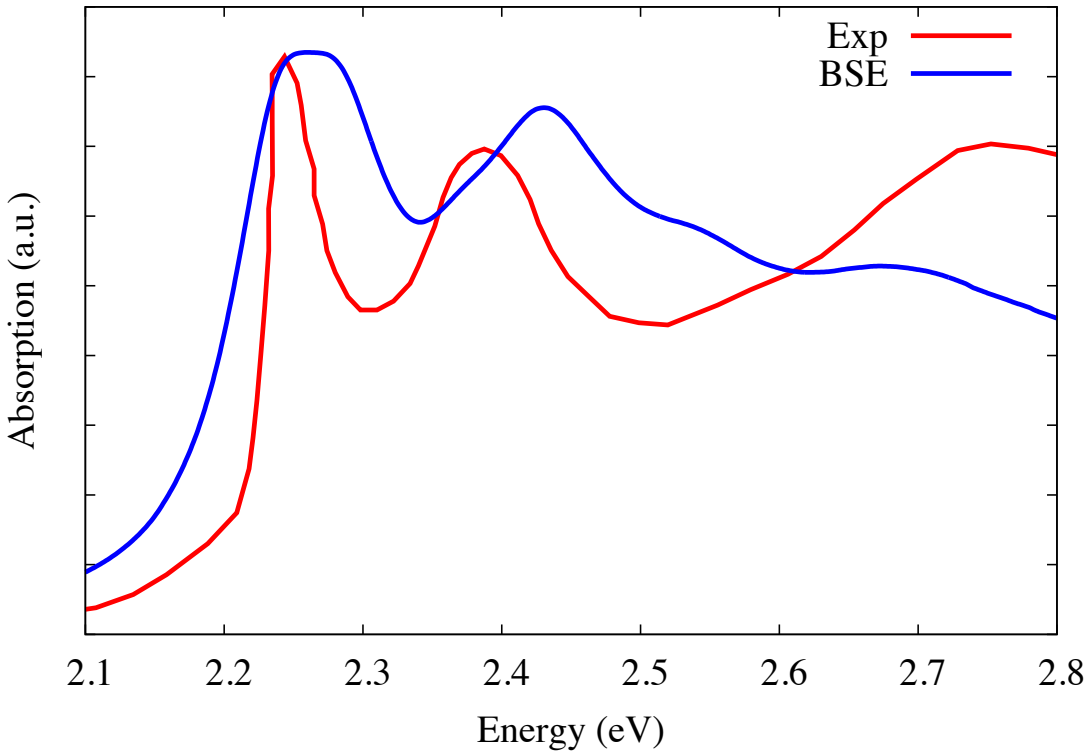

Figure 11.8: Absorption spectra for a CdSe nanoplatelet of 5 ML in thickness. The experimental spectrum in red is taken from reference [207]. The spectrum computed with our BSE implementation utilises an initial spectral line width with a FWHM of 80 meV. This linearly increases linearly to 193 meV between transition energies of 2.44 eV and 2.8 eV.

We suggest that the latter is more probable as our excitonic calculations are well-converged but lack spin-orbit coupling. A comparison of the spectra predicted by the 14-band $\mathbf{k} \cdot \mathbf{p}$ model, shown in Appendix F, demonstrates that the spin-orbital interaction redistributes the spectral weights of the low-energy features without modifying their transition energies. We therefore suggest that the inclusion of spin-orbit coupling may refine the agreement with experiment by redistributing some of the spectral weight associated with the lowest transitions.

One also observes slight differences in the intensities of the second peak predicted by our calculations when compared to those seen in experiment, in all three spectra. As shown in Figure 9.11, in Chapter 9, the relative intensity of the second peak observed in experimental spectra can be seen to vary between ensembles and must

therefore be a property relating to a given ensemble rather than a purely intrinsic property of a single nanoplatelet[207].

Finally, the drop in all spectral profiles experienced at high energies is not a physical effect. Rather, it reflects that a proportion of transitions with energies greater than $\min\{E_{e_{\max}} - E_{h_1}, E_{e_1} - E_{h_{\max}}\}$ are missing from the spectrum. This is because we construct our spectra with a finite number of band-edge wave functions from both manifolds. As a consequence, transitions with larger energies are missed if either the constituent hole or electron (or both) is not included in the subset of states used to construct the basis. Furthermore, as the electron-hole interaction mixes independent-particle transitions, higher-energy states that are absence from the basis may well be required to converge the highest transitions present in a given spectrum.

11.4 Conclusion

In conclusion, we have performed the first many-body calculations of the excitonic properties of CdSe nanoplatelets, using an atomistic tight-binding model that accounts for the finite lateral dimensions of the system and a real-space implementation of the Bethe-Salpeter equation. With this model, we have calculated the nanoplatelet optical gap as a function of both the lateral dimensions and the thickness. Figure 11.3 shows that our calculations overestimate the experimental, optical gap for the range of thicknesses considered and reasons have been suggested for why this might be the case.

In Figure 11.4 we have shown calculations for the binding energy of the lowest exciton state as a function of thickness and compared it to available computational data[95]. Our TB+BSE implementation predicts a different binding energy dependence on thickness in comparison to the data simulated with a tight-binding plus effective mass model. Coincidentally, both models predict very similar values for the only

binding energy for which we have an experimental reference. In this instance, our model strongly agrees with the inferred experimental value. More experimental data on exciton binding energies is therefore desirable to test current predictions against.

Finally, we present the first calculations of the optical absorption spectra of CdSe nanoplatelets with the inclusion of excitonic effects. Figure 11.6 - 11.8 demonstrate that our TB+BSE implementation captures the main features of the experimental spectra, reproducing the spectral profile. This shows the necessity for a many-body treatment of the electron-hole interaction in these quasi two-dimensional systems. In the final chapter of this thesis, we go on to summarise our results and discuss potential future work.

Chapter 12

Conclusions

The goals of this thesis were the development and application of a semi-empirical, nearest neighbour, sp^3s^* tight-binding model in conjunction with a real-space implementation of the Bethe-Salpeter equation, for the simulation of the optoelectronic properties of colloidal CdSe nanocrystals and nanoplatelets. This combination of methodologies reflects a growing desire to perform many-body calculations on large systems that lack periodicity, in a manner that is practical and scalable. The model is subsequently used to perform many-body calculations on colloidal CdSe nanocrystals and nanoplatelets, with an aim to investigate the effect of size and dimensionality on the electron-hole interaction, through the simulation of optical absorption spectra and excitonic binding energies.

12.1 Summary and Conclusions

Starting from the seminal work of Vogl and coworkers[34], we have written a semi-empirical, nearest neighbour (NN), sp^3s^* tight-binding model capable of treating finite systems containing up to $\sim$ 10,000 atoms[1]. The tight-binding model is subsequently used to generate the energies and wave functions required as inputs in many-body calculations. In order to perform many-body calculations, we have also written a real-space implementation of the Bethe-Salpeter equation (BSE) that exploits the limited radial extent of the atomic orbitals and the minimal basis size in order to efficiently calculate the excitonic properties of nanoscale systems. This implementation gives access to optical gaps, the exciton binding energy and excitonic absorption spectra.

We initially demonstrate that the tight-binding model is capable reproducing the band-edge states of CdSe nanocrystals, before applying it to CdSe nanoplatelets. The variation in the band-edge energies and wave functions are investigated as a function of thickness for CdSe nanoplatelets with realistic lateral dimensions and the optical absorption spectrum is simulated in the independent-particle approximation. For a nanoplatelet with a thickness of 4 ML, we find that our independent-particle calculations show good agreement in the low-energy region of the spectrum when compared to the spectrum generated using a 14-band $\mathbf{k} \cdot \mathbf{p}$ model. A comparison of our simulations with experimental absorption spectra, however, found that in general the independent-particle approximation both overestimates the optical gap and predicts fundamentally different spectral profiles. The conclusion from our analysis is that a many-body treatment of the optical absorption spectrum is required in order to reproduce the features observed experimentally.

Many-body calculations using our tight-binding plus BSE implementation were

[1]The FEAST sparse eigensolver and Siesta input routines represent the only third-party algorithms incorporated in our code.

initially performed on CdSe nanocrystals. The effect of the exchange and direct terms on the absorption spectrum were systematically tested and found to be consistent with prior observations, demonstrating that our implementation of the BSE kernel captures the physics necessary to describe excitonic properties. We also investigated the validity of the Tamm-Dancoff approximation (TDA) of the two-particle Hamiltonian. This is of particular interest because the TDA is formally equivalent to using configuration interaction singles[2] (CIS) and CIS has been widely used to calculate the optical properties of CdSe nanocrystals. We find that both the optical gap and the spectral features within $\sim$ 1eV of the absorption onset are unaffected by the TDA, whereas high-energy transitions are modified by the approximation.

Many-body calculations performed on CdSe nanocrystals predict values for the optical gaps that are in strong agreement with average experimental data for all but the smallest diameters. A comparison of exciton binding energies with those predicted by CIS demonstrates the sensitivity of results to the exact treatment of dielectric screening and the decision of whether or not to screen the exchange interaction. Calculated absorption spectra show partial agreement with experimental spectra. While the transition energies of the first and second peaks are in strong agreement with experiment, our model systematically overestimates the relative intensity of the second peak and predicts a close third peak that should not be present. We suggest that this is a consequence of not including spin-orbit coupling in our model, which is expected to redistribute the spectral weights of the band-edge transitions.

Many-body calculations performed on CdSe nanoplatelets predict optical gaps that are larger than those observed experimentally. This is shown to be a consequence of using lateral dimensions that are smaller than the those associated with the average nanoplatelet, introducing some in-plane confinement. Exciton binding energies were

[2]When screening is taken in the static limit.

found to vary from 172 meV to 131 meV for thicknesses ranging from 2 ML to 5 ML, respectively. There is, however, currently a lack of experimental data with which to compare to. Grim and coworkers have inferred a value of 132 meV for a nanoplatelet with a thickness of 4 ML, which is in strong agreement with our value of 138 meV. A systematic experimental investigation of binding energies in CdSe nanoplatelets is therefore desirable. Indeed, it is possible that the bulk high-frequency dielectric constant overestimates screening and that a reduction in screening would lead to an increase in the binding energies, most noticeably in the thinnest systems.

Finally, we have looked at the effect of the electron-hole interaction on the optical absorption spectra of CdSe nanoplatelets with thicknesses of 3 ML, 4 ML and 5 ML. We find that the inclusion of many-body effects causes a redshift in the spectra and strongly mixes the independent-particle transitions. This results in absorption spectra with low-energy spectral profiles that capture the characteristic features of the experimental spectra. In general, we find very good agreement between calculated and experimental optical absorption spectra, demonstrating the importance of a many-body treatment of the electron-hole interaction in colloidal nanoplatelets.

This thesis has therefore demonstrated the ability to treat large, finite systems with strong excitonic effects in a fully many-body manner and has presented results in quantitative agreement with experiment. We believe that this is an important step towards the study of larger, more complex heterostructures including core/shell/shell nanocrystals, core/shell nanoplatelets and core/crown nanoplatelets, with the ultimate goal of complete device simulation from the atomic scale.

12.2 Future Work

In this section, we discuss potential extensions to the work presented in this thesis and address what we consider to be interesting problems. These range from ideas

that can be implemented with immediate effect, to those that are more speculative.

First of all, it would be desirable to identify which independent-particle states contribute to the lowest excitonic transitions and quantify the amount of mixing experienced, both in CdSe nanocrystal and nanoplatelet systems. This information is contained within the two-particle coefficients that are found as solutions of the eigenvalue problem, given by Equation (5.35).

This problem can be simplified by replacing the full two-particle Hamiltonian, defined by Equation (5.29), with the resonant two-particle Hamiltonian defined by Equation (5.26). We have shown in Figure 10.12 that the low-energy region of the two-particle spectrum is well-described by the TDA, therefore it is reasonable to expect that the eigenstates of Equation (5.26) will also be a good approximation to solutions of the full Hamiltonian. In making this approximation, we replace a non-Hermitian matrix with a Hermitian matrix, reducing the number of elements stored in memory by half. The eigenvalue problem containing Equation (5.35) can then be solved in the standard way utilising Scalapack for a subset of the lowest eigenstates. Knowledge of these coefficients would also enable the construction and visualisation of the exciton wave functions, revealing their spatial distributions.

Certain aspects of our BSE implementation could be made more efficient. For example, the bi-conjugate gradient routine could be made more efficient by combining it with a multishift algorithm[160]. This solves the linear system in the absence of any frequency dependence. The residuals and coefficients found from the solution of this seed system are then related to the residuals and coefficients of linear systems with a frequency dependence via analytic recursion relations. One therefore replaces the need to compute the matrix-vector product at each discrete frequency with the evaluation of analytic expressions.

As we have discussed in the prior chapter, we screen the electron-hole interaction with the bulk dielectric constant in CdSe nanoplatelet simulations, however, we know

that dielectric screening is strongly modified in two-dimensional systems. Screening in two-dimensional materials has been shown to converge on the three-dimensional Coulomb potential, screened by the dielectric constant of the environment, for large in-plane separations[227]. One might be able to account for this in a simple manner by screening the direct term with the bulk dielectric constant at separations below a characteristic radius, and screening with the dielectric constant of the surrounding medium at distances in excess of the characteristic radius. A definition of the characteristic radius is provided in reference [227], or it could be treated empirically.

It would also be interesting to include the effect of spin-orbit coupling at the level of the tight-binding Hamiltonian. This would enable a more extensive comparison with the results of the $\mathbf{k} \cdot \mathbf{p}$ model and provide a complete independent-particle description of the band-edge properties of CdSe nanoplatelets. Inclusion of spin-orbital coupling at the two-particle level does, however, have the potential to be computationally expensive. If its magnitude is comparable to or greater than the electron-hole interaction, then the spin singlet and spin triplet configurations will mix, forcing one to treat the full spin-structure of the two-particle Hamiltonian. This will in principle, increase the size of both Hamiltonian dimensions by a factor of four.

Finally, there is an lingering desire to extend the model to the simulation of binary materials. Heterostructure engineering offers the possibility of finer control over the band gap and spatial localisation of the charge carriers, opening up a much larger phase space of excitonic properties to explore.

The development and implementation of novel numerical methods to address many-body problems in quantum systems continues to be both challenging and rewarding. It is hoped that the work in this thesis will contribute in some way to the ever-growing palette of methodologies that seek to shed light on neutral excitations in nanostructures.

Appendix A

Tight-Binding Theory

In this appendix we elaborate on the two-centre approximation of the tight-binding potential, and the derivation of the tight-binding parameters and phase factors. Slater-Koster parameters are presented in terms of directional cosines and the connection to the vector dot-product is made. With use of an example, we show how the $\pm$ signs of the exponential phase factors, given by Equations (4.21)-(4.24) in the Chapter 4, are related to the displacement vectors of the nearest neighbours.

A.1 The Two-Centre Approximation

The expectation value of the one-electron effective potential between orbitals γ and γ' centred on atoms α and β, respectively, can be expanded in terms of spherical atomic potentials:

$$\begin{aligned}\langle\beta\gamma'|V(\mathbf{r})|\alpha\gamma\rangle &= \langle\beta\gamma'|\sum_{\kappa} V(\mathbf{r}-\mathbf{r}_\kappa)|\alpha\gamma\rangle \\ &= \langle\beta\gamma'|V(\mathbf{r}-\mathbf{r}_\alpha)|\alpha\gamma\rangle + \langle\beta\gamma'|V(\mathbf{r}-\mathbf{r}_\beta)|\alpha\gamma\rangle \\ &+ \sum_{\kappa\neq\alpha,\beta}\langle\beta\gamma'|V(\mathbf{r}-\mathbf{r}_\kappa)|\alpha\gamma\rangle, \qquad \text{(A.1)}\end{aligned}$$

where $V(\mathbf{r} - \mathbf{r}_\alpha)$ are atomic potentials and κ is a generic, atomic index. In doing so, one can see that while all atomic potentials contribute to the potential energy between orbitals γ and γ', it is expected that the atomic potentials localised at the sites that orbitals γ and γ' are centred on will contribute the most, whereas atomic potentials centred further away, at $\kappa \neq \alpha, \beta$, will contribute less[229].

Slater and Koster acknowledged that in many cases, three-centre integrals are not negligible with respect to two-centre integrals[143] but neglecting them vastly simplifies the interpretation of inter-atomic integrals, allowing one to treat them as though they are equivalent to the bonding between two atoms which form a diatomic molecule. This subsequently enables the use of molecular bonding orbitals in the Hamiltonian and a reduction in the number of empirical parameters through symmetry considerations.

A.2 Tight-Binding Matrix Elements

In the two-centre approximation, the Hamiltonian has cylindrical symmetry and is therefore independent of the azimuthal angle. As such, the Hamiltonian commutes with the angular momentum operator, $\hat{\mathrm{L}}_{\mathbf{d}} = \hat{\mathbf{L}} \cdot \frac{\mathbf{d}}{|\mathbf{d}|}$, and the inter-atomic matrix elements vanish if the eigenvalues of the orbital angular momentum operator differ for the two orbitals under consideration.

The expectation of the commutator relation $[\hat{\mathrm{H}}, \hat{\mathrm{L}}_{\mathbf{d}}]$ is formally given as:

$$\langle \alpha\gamma | [\hat{\mathrm{H}}, \hat{\mathrm{L}}_{\mathbf{d}}] | \alpha'\gamma' \rangle = 0. \tag{A.2}$$

Explicitly expanding the commutator and using the definition $\hat{\mathrm{L}}_{\mathbf{d}} | \alpha\gamma \rangle = \hbar m | \alpha\gamma \rangle$, the expectation of the commutator can be shown to reduce to:

$$\langle \alpha\gamma | [\hat{\mathrm{H}}, \hat{\mathrm{L}}_{\mathbf{d}}] | \alpha'\gamma' \rangle = \langle \alpha\gamma | \hat{\mathrm{H}}\hat{\mathrm{L}}_{\mathbf{d}} | \alpha'\gamma' \rangle - \langle \alpha\gamma | \hat{\mathrm{L}}_{\mathbf{d}}\hat{\mathrm{H}} | \alpha'\gamma' \rangle, \tag{A.3}$$

$$= \hbar(m' - m) \langle \alpha\gamma | \hat{\mathrm{H}} | \alpha'\gamma' \rangle = 0. \tag{A.4}$$

The integral $\langle\alpha\gamma|\hat{\mathrm{H}}|\alpha'\gamma'\rangle$ therefore vanishes unless $m = m'$. The non-zero matrix elements between molecular orbitals are therefore given by $V_{ll'm}\delta_{m,m'}$. In a basis containing s and p-orbitals, the corresponding molecular overlap parameters are: $V_{ss\sigma}$, $V_{sp\sigma}$, $V_{pp\sigma}$ and $V_{pp\pi}$, where σ and π denote $m = 0$ and $m = \pm 1$, respectively.

A.3 Directional Cosines and Slater-Koster Relations

The Slater-Koster relations for all s and p matrix elements are:

$$V_{ss} = V_{ss\sigma}, \tag{A.5}$$

$$V_{sx} = lV_{sp\sigma}, \tag{A.6}$$

$$V_{xx} = l^2V_{pp\sigma} + (1 - l^2)V_{pp\pi}, \tag{A.7}$$

$$V_{xy} = lmV_{pp\sigma} - lmV_{pp\pi}, \tag{A.8}$$

$$V_{xz} = lnV_{pp\sigma} - lnV_{pp\pi}, \tag{A.9}$$

where (l, m, n) are directional cosines (not to be confused with the symbols denoting the orbital and azimuthal angular momenta above) which elegantly replace the vector dot products of Equation (4.12) in Chapter 4. All inter-atomic elements are defined between a central anion at the origin and a neighbouring cation at position $\mathbf{d}_1 = (1, 1, 1)\, a_l$. The directional cosines are therefore explicitly given as:

$$l = \cos(a) = \frac{\mathbf{d}_1 \cdot \hat{\mathbf{e}}_x}{|\mathbf{d}|}, \tag{A.10}$$

$$m = \cos(b) = \frac{\mathbf{d}_1 \cdot \hat{\mathbf{e}}_y}{|\mathbf{d}|}, \tag{A.11}$$

$$n = \cos(c) = \frac{\mathbf{d}_1 \cdot \hat{\mathbf{e}}_z}{|\mathbf{d}|}, \tag{A.12}$$

where $\hat{\mathbf{e}}_x = (1, 0, 0)$ with $\hat{\mathbf{e}}_y$ and $\hat{\mathbf{e}}_z$ defined equivalently. a is the angle between $\mathbf{d}_1$ and $\hat{\mathbf{e}}_x$, b is the angle between $\mathbf{d}_1$ and $\hat{\mathbf{e}}_y$, and c is the angle between $\mathbf{d}_1$ and $\hat{\mathbf{e}}_z$. The

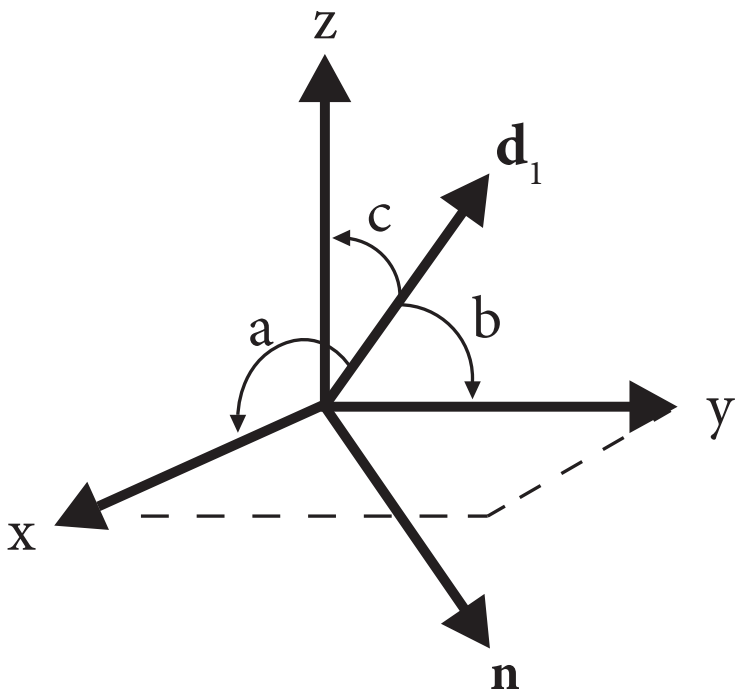

Figure A.1: Directional cosine angles relative to the atomic vector $\mathbf{d}_1$.

directional cosines are therefore equivalent to the (x, y, z) coordinates of the unit vector $\hat{\mathbf{d}}_1$. Upon substitution of the displacement vector, $\mathbf{d}_1$ and the tetrahedral bond length $|\mathbf{d}| = \sqrt{3}a_l/4$, one obtains the tight-binding Hamiltonian elements in terms of the molecular orbital elements (A.13)-(A.16):

$$V_{ss} = V_{ss\sigma}, \tag{A.13}$$

$$V_{sx} = \frac{1}{\sqrt{3}} V_{sp\sigma}, \tag{A.14}$$

$$V_{xx} = \frac{1}{3} V_{pp\sigma} + \frac{2}{3} V_{pp\pi}, \tag{A.15}$$

$$V_{xy} = \frac{1}{3} V_{pp\sigma} - \frac{1}{3} V_{pp\pi}, \tag{A.16}$$

where $V_{sx} \equiv V_{sy} \equiv V_{sz} = V_{sp}$, $V_{xz} \equiv V_{xy}$ and $V_{xx} \equiv V_{yy} \equiv V_{zz}$ via symmetry.

A.4 Determining the Signs of the Exponential Phase Factors

The signs of the exponential phase factors in Equations (4.21)-(4.24) correspond to the specific position of the neighbouring cation relative to the central anion and arise from the positive and negative lobes of the bonding orbitals centred at the two sites. All of the tight-binding inter-atomic parameters, Equations (4.14)-(4.17), have been defined with respect to the bonding between the central anion and neighbouring cation at displacement vector $\mathbf{d}_1$. The appropriate phases of the remaining three interactions are then related to $\langle\phi_{\gamma'}(\mathbf{r}-\mathbf{r}_a)|H|\phi_{\gamma}(\mathbf{r}-\mathbf{d}_1)\rangle$ by symmetry. An example is provided for the Hamiltonian element $\langle\phi_{p_x}(\mathbf{r}-\mathbf{r}_a)|H|\phi_{p_y}(\mathbf{r}-\mathbf{d}_1)\rangle$ (where $\mathbf{r}_a=(0,0,0)$):

A transformation from $\mathbf{d}_1=(1,1,1)$ to $\mathbf{d}_2=(1,-1,-1)$ transforms $|p_y\rangle$ to $-|p_y\rangle$ under rotation. One can see that $\langle p_x|$ is unchanged and there is no z-component in the element above. This results in a phase factor of $-e^{i\mathbf{k}\cdot\mathbf{d}_2}$.

A transformation from $\mathbf{d}_1=(1,1,1)$ to $\mathbf{d}_3=(-1,-1,-1)$ transforms the $\langle p_x|$ to $-\langle p_x|$ with $|p_y\rangle$ unchanged. This results in a phase factor of $-e^{i\mathbf{k}\cdot\mathbf{d}_3}$.

Finally, a transformation from $\mathbf{d}_1=(1,1,1)$ to $\mathbf{d}_4=(-1,-1,1)$ transforms both $\langle p_x|$ to $-\langle p_x|$ and $|p_y\rangle$ to $-|p_y\rangle$, resulting in no net change of phase for the exponential factor $e^{i\mathbf{k}\cdot\mathbf{d}_4}$.

The full phase factor associated with the parameter $\langle\phi_{p_x}(\mathbf{r}-\mathbf{r}_a)|H|\phi_{p_y}(\mathbf{r}-\mathbf{d}_1)\rangle$ is therefore $g_3=[e^{i\mathbf{k}\cdot\mathbf{d}_1}-e^{i\mathbf{k}\cdot\mathbf{d}_2}+e^{i\mathbf{k}\cdot\mathbf{d}_3}-e^{i\mathbf{k}\cdot\mathbf{d}_4}]$.

As such, the signs of the exponentials in the phase factors reflect the underlying, tetrahedral symmetry.

Appendix B

Many-Body Theory

B.1 The Bethe-Salpeter Kernel

In this appendix, we derive an approximation for the BSE kernel by choosing an explicit form for the self-energy operator. The kernel of the Bethe-Salpeter equation can be shown to be[38; 149]:

$$K(5,6,7,8) = i\frac{\delta V_H(5)}{\delta G(7,8)}\delta(5-6) + i\frac{\delta \Sigma(5,6)}{\delta G(7,8)}, \tag{B.1}$$

where V_H is the Hartree potential, Σ is the self-energy operator and G is the one-particle Green's function. The first term in the kernel given by Expression (B.1) can be simplified by noting that the charge density can be defined in terms of the one-particle Green's function[230]:

$$\rho(1) = -iG(1,1^+). \tag{B.2}$$

This subsequently allows one to write the Hartree potential in terms of the bare Coulomb interaction and the one-particle Green's function:

$$V_H(1) = -i\int d2v(1,2)G(2,2^+), \tag{B.3}$$

such that the derivative of Equation (B.3) with respect to the one-particle Green's function is:

$$i\frac{\delta V_H(5)}{\delta G(7,8)} = \int d2v(5,2)\frac{\delta G(2,2^+)}{\delta G(7,8)} \tag{B.4}$$

$$= v(5,7)\delta(7-8). \tag{B.5}$$

The second term of the Bethe-Salpeter kernel (B.1) still requires some choice for the self-energy. One such choice is the GW approximation, which was formulated by Lars Hedin in 1965[36]. In this approximation, Hedin replaced the bare Coulomb interaction with the screened Coulomb interaction W, motivated by the assumption that the dielectric screening between electrons would lead to a smaller, well-behaved interaction and faster convergence in the expansion of the self-energy. In the GW approximation, the self energy is given as[37]:

$$\Sigma(1,2) = iG(1,2)W(1^+,2). \tag{B.6}$$

Substituting for Equation (B.6) in the second term of Equation (B.1), one obtains:

$$-\frac{\delta G(5,6)W(5^+,6)}{\delta G(7,8)} = -W(5^+,6)\delta(6-8)\delta(5^+-7) - G(5,6)\frac{\delta W(5^+,6)}{\delta G(7,8)}. \tag{B.7}$$

The right-hand side of Equation (B.7) contains two terms however, only the first-order term is retained in order to simplify calculations[148; 231]. Therefore, upon neglecting changes in the screening due to the excitation, the Bethe-Salpeter interaction kernel in the GW approximation is:

$$K(1,2,3,4) = v(1,3)\delta(1-2)\delta(3-4) - W(1,2)\delta(2-4)\delta(1-3), \tag{B.8}$$

where $v(1,3)$ is the repulsive bare Coulomb interaction and $W(1,2)$ is the attractive,

screened Coulomb interaction[147; 148]. The first and second terms of the kernel are referred to as the unscreened exchange term and the direct Coulomb term, respectively.

Appendix C

Tight-Binding Implementation

In this appendix, we present details describing how we distribute the eigensolver subspace amongst multiple processes, and give additional details regarding basis state generation and surface passivation.

C.1 Subspace Distribution

The distributed intervals of the subspace require an estimate for the total number of eigenpairs per interval. A scheme that linearly distributes an initial guess at the total number of eigenstates in the subspace, m_0, such that $m_{0,\text{local}} = m_0/N_{\text{CPUs}}$ was initially implemented, however this is less than ideal as the total number of eigenvalues in the system is not linearly distributed with respect to the energy. Indeed this points to the density of states (DOS) as a more natural quantity for estimating $m_{0,\text{local}}$.

An issue with using the density of states is that it is not available prior to running a calculation. As such, we used the initial scheme to compute DOS for a range of system sizes, then use these DOS as inputs for the current scheme.

With the DOS reference distribution scheme, the subspace is then split into valence and conduction manifolds, such that it is possible to remove the band gap region

from the distribution. Indeed, inclusion of the band gap region in the calculations is redundant as it is known to be free from states and its inclusion actually hinders convergence on the process to which it is assigned.

After proportionally distributing the available processors between the valence and conduction states, one can define a local subspace guess (per processor), $\mathrm{m}^{v}_{\mathrm{local}} = \mathrm{m}^{v}_{0}/\mathrm{N}_{\mathrm{vp}}$, and in conjunction with a summation of the density of states, distribute the energy range amongst N_p processes. An algorithmic example is shown in Algorithm 1 for the valence states. An equivalent procedure is performed for the conduction states.

Algorithm 1 Approximately even distribution of of the subspace $[E_{\mathrm{min}} : E_{\mathrm{max}}]$ using DOS

```
1: subroutine DISTRIBUTE_ENERGY_SUBSPACE()
2:     ⋮
3:     j=1
4:     !elims(j,1:2) = energy limits per process j
5:     !Define start energy of process 1
6:     elims(j,1)=E_min
7:     sum=0.
8:
9:     !Loop over processes assigned to valence band
10:    for i=min,VBT do
11:        !Energy, starting at E_min
12:        eval=E_min+(i-1)*delE
13:        sum=sum+dos(i)
14:        !Evenly distribute [E_min : E_max] amongst N_vp
15:        if (sum ≥ m^v_local) then
16:            elims(j+1,2)=eval+delE
17:            elims(j,2)=eval
18:            j=j+1
19:            sum=0.
20:        end if
21:    end for
22:
23:    !Enforce end energy of process j
24:    elims(j,2)=E_max
25:    ⋮
26: end subroutine
```

C.2 Surface Passivation

A transformation between two orthogonal bases is formally given as:

$$A = UA'U^T, \tag{C.1}$$

where A is a sub-matrix of the Hamiltonian for a surface atom in the Cartesian orbital basis, A' is the same sub-matrix in the hybridised basis and U is an orthogonal matrix which defines the orthogonal transformation. The anion and cation transformation matrices are therefore given explicitly as[190]:

$$U_a^T = \frac{1}{2}\begin{pmatrix} 1 & 1 & 1 & 1 \\ 1 & 1 & -1 & -1 \\ 1 & -1 & 1 & -1 \\ 1 & -1 & -1 & 1 \end{pmatrix}, \quad U_c^T = \frac{1}{2}\begin{pmatrix} 1 & -1 & -1 & -1 \\ 1 & -1 & 1 & 1 \\ 1 & 1 & -1 & 1 \\ 1 & 1 & 1 & -1 \end{pmatrix}, \tag{C.2}$$

and surface-atom sub-matrix in the hybridised basis is:

$$A' = \left(\begin{array}{c|cccc} & |sp_a^3\rangle & |sp_b^3\rangle & |sp_c^3\rangle & |sp_d^3\rangle \\ \hline |sp_a^3\rangle & a & 0 & 0 & 0 \\ |sp_a^3\rangle & 0 & b & 0 & 0 \\ |sp_a^3\rangle & 0 & 0 & c & 0 \\ |sp_a^3\rangle & 0 & 0 & 0 & d \end{array}\right), \tag{C.3}$$

where (a, b, c, d) are the passivating energies associated with the hybrid orbitals of the same subscript, $|sp_{a-d}^3\rangle$. Only the diagonal elements correspond to the passivation of bonds aligned in the tetrahedral directions. Using this definition of the on-site matrix in the hybridised basis, Equation (C.3), and the orthogonal transform defined by Equation (C.1), one can then derive two expressions for the on-site matrix in the

Cartesian orbital basis, which includes terms for all four of the hybrid bonds:

$$A_a = \frac{1}{4}\begin{pmatrix} a+b+c+d & a+b-c-d & a-b+c-d & a-b-c+d \\ a+b-c-d & a+b+c+d & a-b-c+d & a-b+c-d \\ a-b+c-d & a-b-c+d & a+b+c+d & a+b-c-d \\ a-b-c+d & a-b+c-d & a+b-c-d & a+b+c+d \end{pmatrix}, \tag{C.4}$$

$$A_c = \frac{1}{4}\begin{pmatrix} a+b+c+d & -a-b+c+d & -a+b-c+d & -a+b+c-d \\ -a-b+c+d & a+b+c+d & a-b-c+d & a-b+c-d \\ -a+b-c+d & a-b-c+d & a+b+c+d & a+b-c-d \\ -a+b+c-d & a-b+c-d & a+b-c-d & a+b+c+d \end{pmatrix}, \tag{C.5}$$

where A_a is the on-site matrix for the anion and A_c is the on-site matrix for the cation. An on-site matrix with the elements initialised to zero represents an atom with all nearest neighbours. Dangling bonds can then be passivated by identifying which bonds, $|sp^3_{a-d}\rangle$, lack nearest neighbours and setting finite values for the corresponding energies (a, b, c, d) in Equation (C.4) and Equation (C.5). The s^* orbitals are not included as their intra-atomic (on-site) energies are typically larger than the band gap and therefore do not require passivating[177].

C.3 Basis Function Generation

Below, we provide an example input.fdf script for the ab initio code Siesta, which we used to generate single-ζ basis functions with the appropriate radial cut-off. All basis functions used in these calculations were generated with Siesta version 3.2.

Example fdf Input for CdSe

```
SystemName      CdSe
SystemLabel     CdSe
NumberOfAtoms   2
NumberOfSpecies  2

%block ChemicalSpeciesLabel
1 48 Cd
2 34 Se
%endblock ChemicalSpeciesLabel

%block PAO.Basis          # Define Basis set
Cd      4                 # Species label, number of l-shells
n=5 0 1                   # n, l, Nzeta, Polarization, NzetaPol
4.071
1.000
n=4 2 1                   # n, l, Nzeta
4.071
1.000
n=5 1 1                   # n, l, Nzeta
4.071
1.000
n=6 0 1                   # n, l, Nzeta
4.071
1.000
Se      3                 # Species label, number of l-shells
n=4 0 1                   # n, l, Nzeta
4.071
1.000
n=4 1 1                   # n, l, Nzeta, Polarization, NzetaPol
4.071
1.000
n=5 0 1                   # n, l, Nzeta, Polarization, NzetaPol
4.071
1.000
%endblock PAO.Basis

%block LatticeVectors
0.500 0.500 0.000
0.000 0.500 0.500
```

```
0.500 0.000 0.500
%endblock LatticeVectors

MeshCutoff          100.0 Ry

%block kgrid_Monkhorst_Pack
6 0 0 0.
0 6 0 0.
0 0 6 0
%endblock kgrid_Monkhorst_Pack

WriteKpoints T
save-hs T

LatticeConstant 11.43403431 Bohr

AtomicCoordinatesFormat ScaledCartesian
%block AtomicCoordinatesAndAtomicSpecies
0. 0. 0.          1 Cd 1
0.25 0.25 0.25 2 Se 2
%endblock AtomicCoordinatesAndAtomicSpecies

BandLinesScale pi/a
%block BandLines
1 1.000 1.000 1.000
20 0.000 0.000 0.000
25 2.000 0.000 0.000
30 2.000 2.000 2.000
%endblock BandLines
```

Appendix D

Implementation of the Bethe-Salpeter Equation

In this appendix, we provide additional information regarding the numerical details of the two-centre orbital integrals and details regarding the implementation and calculation of the matrix-vector product utilising MPI parallelisation. These details include the matrix partitioning scheme and distribution algorithm, and how we utilise the lower triangles of the coupling matrices (kernel) to compute all elements of the matrix-vector product via the symmetry of the two-particle Hamiltonian.

D.1 Two-Centre Orbital Integrals

In Equations (D.1)-(D.3), we present tabulated values for on-site and nearest-neighbour Coulomb-like and exchange-like, two-centre integrals. The integrals are computed with a grid spacing of 0.303 Å, using orbitals defined with numerical, single-ζ radial functions generated in Siesta and real harmonics for the angular component:

$$U^C_{aa} = \left(\begin{array}{c|ccccc} i\downarrow j\rightarrow & s,a & p_x,a & p_y,a & p_z,a & s^*,a \\ \hline s,a & 13.7 & 14.5 & 14.5 & 14.5 & 11.3 \\ p_x,a & & 16.6 & 15.0 & 15.0 & 11.7 \\ p_y,a & & & 16.6 & 15.0 & 11.7 \\ p_z,a & & & & 16.6 & 11.7 \\ s^*,a & & & & & 9.95 \end{array}\right), \; U^X_{aa} = \left(\begin{array}{c|ccccc} i\downarrow j\rightarrow & s,a & p_x,a & p_y,a & p_z,a & s^*,a \\ \hline s,a & 13.7 & 3.01 & 3.01 & 3.01 & 1.16 \\ p_x,a & & 16.6 & 0.738 & 0.738 & 0.685 \\ p_y,a & & & 16.6 & 0.738 & 0.685 \\ p_z,a & & & & 16.6 & 0.685 \\ s^*,a & & & & & 9.95 \end{array}\right), \tag{D.1}$$

$$U^C_{cc} = \left(\begin{array}{c|ccccc} i\downarrow j\rightarrow & s,c & p_x,c & p_y,c & p_z,c & s^*,c \\ \hline s,c & 10.7 & 11.1 & 11.1 & 11.1 & 10.4 \\ p_x,c & & 12.8 & 11.4 & 11.4 & 11.0 \\ p_y,c & & & 12.8 & 11.4 & 11.0 \\ p_z,c & & & & 12.8 & 11.0 \\ s^*,c & & & & & 10.4 \end{array}\right), \; U^X_{cc} = \left(\begin{array}{c|ccccc} i\downarrow j\rightarrow & s,c & p_x,c & p_y,c & p_z,c & s^*,c \\ \hline s,c & 10.7 & 2.52 & 2.52 & 2.52 & 0.942 \\ p_x,c & & 12.8 & 0.685 & 0.685 & 0.714 \\ p_y,c & & & 12.8 & 0.688 & 0.714 \\ p_z,c & & & & 12.8 & 0.714 \\ s^*,c & & & & & 10.4 \end{array}\right), \tag{D.2}$$

$$U^C_{ac} = \left(\begin{array}{c|ccccc} i\downarrow j\rightarrow & s,c & p_x,c & p_y,c & p_z,c & s^*,c \\ \hline s,a & 5.47 & 5.46 & 5.46 & 5.46 & 5.45 \\ p_x,a & 5.42 & 5.37 & 5.43 & 5.43 & 5.40 \\ p_y,a & 5.42 & 5.43 & 5.37 & 5.43 & 5.40 \\ p_z,a & 5.42 & 5.43 & 5.43 & 5.37 & 5.40 \\ s^*,a & 5.42 & 5.42 & 5.42 & 5.42 & 5.37 \end{array}\right), \; U^X_{ac} = \left(\begin{array}{c|ccccc} i\downarrow j\rightarrow & s,c & p_x,c & p_y,c & p_z,c & s^*,c \\ \hline s,a & 0.073 & 0.043 & 0.043 & 0.043 & 0.089 \\ p_x,a & 0.038 & 0.013 & 0.027 & 0.027 & 0.048 \\ p_y,a & 0.038 & 0.027 & 0.013 & 0.027 & 0.048 \\ p_z,a & 0.038 & 0.027 & 0.027 & 0.013 & 0.048 \\ s^*,a & 0.213 & 0.133 & 0.133 & 0.133 & 0.086 \end{array}\right). \tag{D.3}$$

Hard-Wall Cut-off of the Coulomb Singularity

In general, it is found that the on-site integrals are sensitive to the choice of truncation value for the Coulomb singularity, whereas the nearest neighbour integrals are not. A choice of 0.1 times the bond length for the denominator of the Coulomb potential at $\mathbf{r}_1 = \mathbf{r}_2$ results in integrals that are physical and consistent with values cited in the literature[24; 145]. Smaller coefficients (i.e. 0.01 and 0.001) result in values 2-4 times larger. We note that as the choice of basis is essentially arbitrary, we choose a truncated value that results in physical integrals and justify this decision a posteriori.

D.1.1 Coupling Matrix in an Orbital Expansion

The coupling matrices of the two-particle Hamiltonian, expanded in an orbital basis are given by:

$$\begin{aligned} K_{(vc),(c'v')} = \sum_{i,j} & a_{(v;i)}a_{(c;i)}a_{(v';j)}a_{(c';j)}\left[2(ii|v|jj) - \epsilon_\infty^{-1}(ij|v|ij)\right] \\ & + a_{(v;i)}a_{(c;j)}a_{(v';i)}a_{(c';j)}\left[2 - \epsilon_\infty^{-1}\right](ij|v|ij) \\ & + a_{(v;i)}a_{(c;j)}a_{(v';j)}a_{(c';i)}\left[2(ij|v|ij) - \epsilon_\infty^{-1}(ii|v|jj)\right], \end{aligned} \tag{D.4}$$

and

$$K_{(cv)(v'c')} = K_{(vc)(c'v')}. \tag{D.5}$$

D.2 Distributed Matrix-Vector Product

Several schemes exist for distributing and computing matrix-vector products. The most general and widely used consist of partitioning the matrix into stripes (vertically or horizontally) or rectangular fragments (blocks).

$$\begin{pmatrix} a_{11} & a_{12} & \dots & a_{1M} \\ a_{21} & a_{22} & \dots & a_{2M} \\ \vdots & & \ddots & \\ a_{N1} & a_{N2} & \dots & a_{NM} \end{pmatrix} \begin{pmatrix} X_1 \\ X_2 \\ \vdots \\ X_N \end{pmatrix} = \begin{pmatrix} b_1 \\ b_2 \\ \vdots \\ b_N \end{pmatrix} \tag{D.6}$$

Row-wise, block-striped matrix partitioning assigns a subset of matrix rows from Equation (D.6) to each process. Multiplication of each row of matrix A in Equation (D.6), with the column vector X corresponds to single element, b_i, of output vector b. Row-wise decomposition therefore results in each process computing a subset of elements $\{b_i\}$ of b, equal to the number of rows assigned to it, where b_i is given by:

$$a_{i1}X_1 + a_{i2}X_2 + \cdots + a_{iM}X_N = b_i. \tag{D.7}$$

Algorithm 2 Distribute Lower Triangle Matrix

```
1: subroutine DISTRIBUTE_LT(N, irow, Nrow)
2:     N_LT = N * (0.5 * (N − 1) + 1)          ▷ Number of elements in LT
3:     i = 0                                    ▷ Initialise row counter
4:     for ip = 1, N_p − 1 do
5:         N_av = N_LT / N_p                    ▷ Avg elements per process
6:         while N_av > 0 do
7:             i = i + 1                        ▷ Iterate row counter
8:             rs = N − (i − 1)                 ▷ Elements of row i
9:             N_av = N_av − rs
10:        end while
11:        Allocate row indices to process ip
12:    end for
13: end subroutine
```

Row-wise, block-striped matrix partitioning therefore allows the matrix to be distributed approximately linearly, with respect to the number of available processors but requires the multiplying vector to be fully defined on all processes.

D.2.1 Distributing the Lower Triangle

Distributing the lower triangular of a matrix is non-trivial as the rows vary systematically in size from 1 to $N_v N_c$. In order to distribute the rows such that the number of elements per process is kept approximately constant, the routine shown schematically in Algorithm 2 is utilised. It works by sequentially subtracting the number of elements per row, starting with the largest, from the average number of elements per process, until this value is less than or equal to zero. When this criterion is satisfied, the rows associated with the subtracted elements are assigned to process *ip* and the procedure repeats for all processes minus one. The final process is then assigned all remaining rows, such that the total number of rows is conserved.

D.2.2 Computing the Matrix-Vector Product with the Lower Triangle of the Interaction Kernel

The Bethe-Salpeter interaction kernel in the real basis of independent-particle pair products is symmetric. One is therefore only required to store the upper or lower

triangle of the kernels $K_{(vc)(v'c')}$ and $K_{(vc)(c'v')}$ in order to be able to fully describe the effective two-particle Hamiltonian. The matrix-vector product of the two-particle Hamiltonian with the vector X is initially treated by splitting the Hamiltonian given by Equation (7.25) into two parts, separating the diagonal transition energies from the interaction kernel elements:

$$H^{2p}_{(n_1n_2)(n_3n_4)} = \left(\begin{array}{c|cc} {\scriptstyle (n_3n_4)\rightarrow \atop (n_1n_2)\downarrow} & \{v'c'\} & \{c'v'\} \\ \hline \{vc\} & \epsilon_c - \epsilon_v - \omega & 0 \\ \{cv\} & 0 & -(\epsilon_c - \epsilon_v - \omega) \end{array}\right) \mathbf{I} + \left(\begin{array}{c|cc} {\scriptstyle (n_3n_4)\rightarrow \atop (n_1n_2)\downarrow} & \{v'c'\} & \{c'v'\} \\ \hline \{vc\} & K_{(vc)(v'c')} & K_{(vc)(c'v')} \\ \{cv\} & -K_{(vc)(c'v')} & -K_{(vc)(v'c')} \end{array}\right). \tag{D.8}$$

The transition energies are only defined on the diagonal of Equation (D.8), therefore they can be separated from the matrix-vector product and added to the solution independently. Each of the four kernel sub-matrices in Equation (D.8) is then decomposed into upper and lower triangular matrices. Using the property that $K_{(vc)(v'c')}$ is symmetric in a real orbital basis, each upper triangular matrix must be equal to the lower triangular matrix such that $L = L^T = U$. The right-hand side matrix in Equation (D.8) can therefore be schematically expressed in terms of the lower triangular matrices of the interaction kernels:

$$H^{2p} = \left(\begin{array}{cc|cc} \ddots & L_1 & \ddots & L_2 \\ L_1 & \ddots & L_2 & \ddots \\ \hline \ddots & -L_2 & \ddots & -L_1 \\ -L_2 & \ddots & -L_1 & \ddots \end{array}\right), \tag{D.9}$$

where L_1 denotes the lower triangle of $K_{(vc)(v'c')}$ and L_2 denotes the lower triangle of $K_{(vc)(c'v')}$. The solid lines in matrix (D.9) indicate the boundaries of the four interaction kernels, corresponding to the transitions: $\{v, c\} \rightarrow \{v', c'\}$ (top left),

$\{v, c\} \rightarrow \{c', v'\}$ (top right), $\{c, v\} \rightarrow \{v', c'\}$ (bottom left) and $\{c, v\} \rightarrow \{c', v'\}$ (bottom right). The dotted, diagonal lines separate each kernel into upper and lower triangles, where only the lower triangles of the top left and top right quadrants in Equation (D.9) are held in memory.

Dividing the terms in the matrix-vector product according to contributions from lower and upper triangular matrices, such that the complete matrix-vector product is defined as:

$$b = b^L + b^U, \tag{D.10}$$

where b^L (b^U) only contains contributes from the lower (upper)-triangular product, one has the following contributions from lower-triangular elements of the four quadrants of matrix (D.9):

$$\sum_{j=1}^{i} \left(L^1_{ij} X_j + L^2_{ij} X_{j+N_{2p}} \right) = b^L_i, \tag{D.11}$$

$$\sum_{j=1}^{i} \left(- L^2_{ij} X_j - L^1_{ij} X_{j+N_{2p}} \right) = b^L_{i+N_{2p}}, \tag{D.12}$$

where the row index i runs over the leading dimension of the resonant two-particle Hamiltonian, equal to the number of product states $\mathrm{N_{2p}}$, the column index j runs over columns of the lower triangular matrix L and X is the left-hand side column vector of length $2\mathrm{N_{2p}}$.

Contributions to the matrix-vector product from the upper triangular matrices of the four quadrants of (D.9) can be similarly expressed as:

$$\sum_{i=1, i\neq j}^{N_{2p}} \left(L^1_{ij} X_i + L^2_{ij} X_{i+N_{2p}} \right) = b^U_j, \tag{D.13}$$

$$\sum_{i=1, i\neq j}^{N_{2p}} \left(- L^2_{ij} X_i - L^1_{ij} X_{i+N_{2p}} \right) = b^U_{j+N_{2p}}, \tag{D.14}$$

where we have utilised the fact that $L_{j+N_{2p}, i+N_{2p}} = L_{ji} = L_{ij}$. The condition $i \neq j$ prevents double-counting of the diagonal elements. An implementation of Equations

Algorithm 3 Distributed Matrix-Vector Product 1

```
1: subroutine MVP_REALH(H,N2p,X,b)
2:     cnt=0
3:     for irow=rstart,rstop do
4:         for icol=1,irow do
5:             cnt=cnt+1
6:             !Top left and top right quadrants of H:
7:             !Lower Triangle
8:             b(irow)=b(irow)+L1(cnt)*X(icol)+f*L2(cnt)*X(icol+N2p)
9:             !Upper Triangle
10:            b(icol)=b(icol)+L1(cnt)*X(irow)+f*L2(cnt)*X(irow+N2p)
11:
12:            !Bottom left and bottom right quadrants of H:
13:            !Lower Triangle
14:            b(irow+N2p)=b(irow+N2p)-f*L2(cnt)*X(icol)-L1(cnt)*X(icol+N2p)
15:            !Upper Triangle
16:            b(icol+N2p)=b(icol+N2p)-f*L2(cnt)*X(irow)-L1(cnt)*X(irow+N2p)
17:
18:        end for
19:    end for
20: end subroutine
```

(D.11)-(D.14) is presented in Algorithm (3), where all of the symbols are defined as above, L_1 and L_2 are used in packed form[1], the row and column indices are denoted by irow and icol, respectively and $f = \pm 1$ determines whether one takes the product with H^{2p} or $(H^{2p})^\dagger$.

D.2.3 Computing the Transpose of the Two-Particle Hamiltonian

The biconjugate gradient algorithm requires the matrix-vector product $(H^{2p})^T X$ as well as $(H^{2p})X$, where $(H^{2p})^T$ is defined as:

$$(H^{2p})^T = \left(\begin{array}{cc|cc} \ddots & L_1 & \ddots & -L_2 \\ L_1 & \ddots & -L_2 & \ddots \\ \hline \ddots & L_2 & \ddots & -L_1 \\ L_2 & \ddots & -L_1 & \ddots \end{array}\right). \tag{D.15}$$

Upon comparison with the Hamiltonian defined in Equation (D.9), it can be seen that the two are related via a change of signs in the kernels which comprise the top

[1]The two-dimensional array is represented by a one-dimensional vector, with a composite index.

right and bottom left quadrants. The matrix-vector product with the transpose of the two-particle Hamiltonian can therefore be implemented by introducing a change of sign into Equations (D.11)-(D.14), which switches from $f = 1$ to $f = -1$ when the transposed Hamiltonian-vector product is required. This is shown in the pseudocode given by Algorithm (3).

Appendix E

Nanocrystal Supporting Information

E.1 Band gap Dependence on Nanocrystal Diameter

In this appendix we provide supporting material for the content of Chapters 3 and 8, regarding the properties of CdSe nanocrystals predicted by the sp^3s^* tight-binding model.

In Figure E.1, we demonstrate that two sp^3s^* models predict the same optical gap dependence on diameter when equivalent ligand bond lengths (therefore passivation parameters) are employed. This supports our assertion in Chapter 3 that it is the treatment of the surface states, rather than the inclusion of spin-orbit coupling, that leads to differences in the predicted band gap dependence on nanocrystal diameter between various sp^3s^* models. The primary source of difference arising from parameterising to different bulk band gaps.

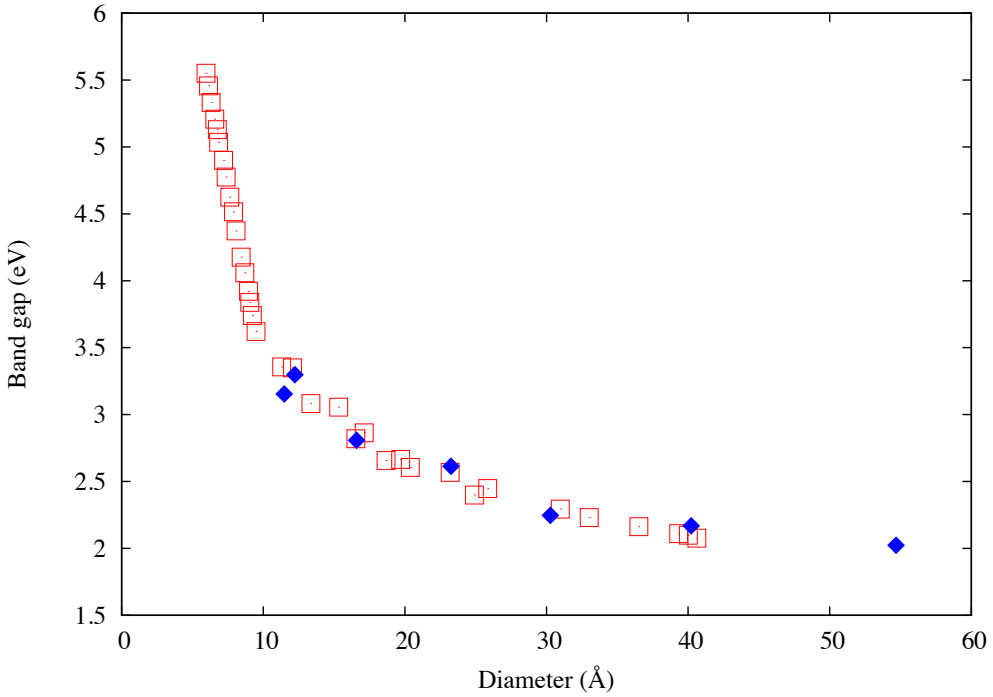

Figure E.1: A comparison of two sets of calculated optical gaps as a function of nanocrystal diameter. Both are generated with the sp^3s^* tight-binding model. The data of Albe and coworkers[102] is shown with red squares, whereas the data of Pérez-Conde and Bhattacharjee[107] is shown with blue diamonds. Albe and coworkers define their pseudo-Hydrogen bond lengths as $d_{Cd-H} = 1.76$ Å and $d_{Se-H} = 1.47$ Å, whereas Pérez-Conde and Bhattacharjee define theirs as $d_{Cd-H} = 1.71$ Å and $d_{Se-H} = 1.47$ Å.

Parameters for Lines of Best-Fit

Table E.1 gives the best-fit parameters to the tight-binding data in Figure 3.2, found from fitting with Equation (3.2). They are used to define the red line Figure 3.2, which shows the average, calculated optical gap dependence on nanocrystal diameter.

Table E.2 gives the best-fit parameters to our tight-binding data, given in red in Figure 8.2. They are subsequently used in the expression, $E_g(d) = 1/(ad^b) + E_{g,\text{bulk}}$, to define the independent-particle gap dependence on nanocrystal diameter, shown in Figure 8.2.

a	b	c	σ_a	σ_b	σ_c
5.53×10^{-4}	0.034	0.055	9×10^{-5}	6×10^{-3}	0.03

Table E.1: Parameters used to generate the tight-binding line of best-fit in Figure 3.2. σ_i represent the standard deviations.

a	b	σ_a	σ_b
0.0122	1.37	6.5×10^{-4}	0.021

Table E.2: Parameters used to define the line of best-fit in Figure 8.2. σ_i represent the standard deviations.

E.2 Independent-Particle State Properties

Figures E.2 and E.3 show the independent-particle states of the tight-binding model constructed with atomic radial functions, rather than Gaussian functions. The radial functions are defined with a cut-off consistent with the parameterisation of our tight-binding Hamiltonian, leading to the granular look of the wave function isosurfaces. We show the lowest ten unoccupied independent-particle states (red) and the lowest twenty occupied independent-particle states (blue) for a nanocrystal of 6 nm in diameter, in Figures E.2 and E.3, respectively.

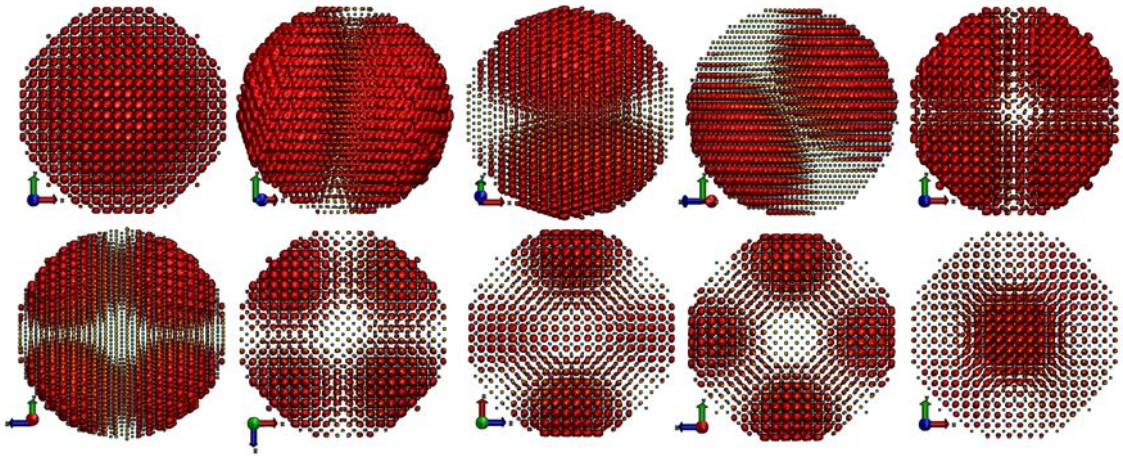

Figure E.2: Isosurfaces, $|\Psi_i(\mathbf{r})|^2$, of the lowest ten unoccupied, independent-particle states of a nanocrystal with a diameter of 6 nm. States are ordered from top left to bottom right. Red, green and blue arrows correspond to x, y and z directions, respectively.

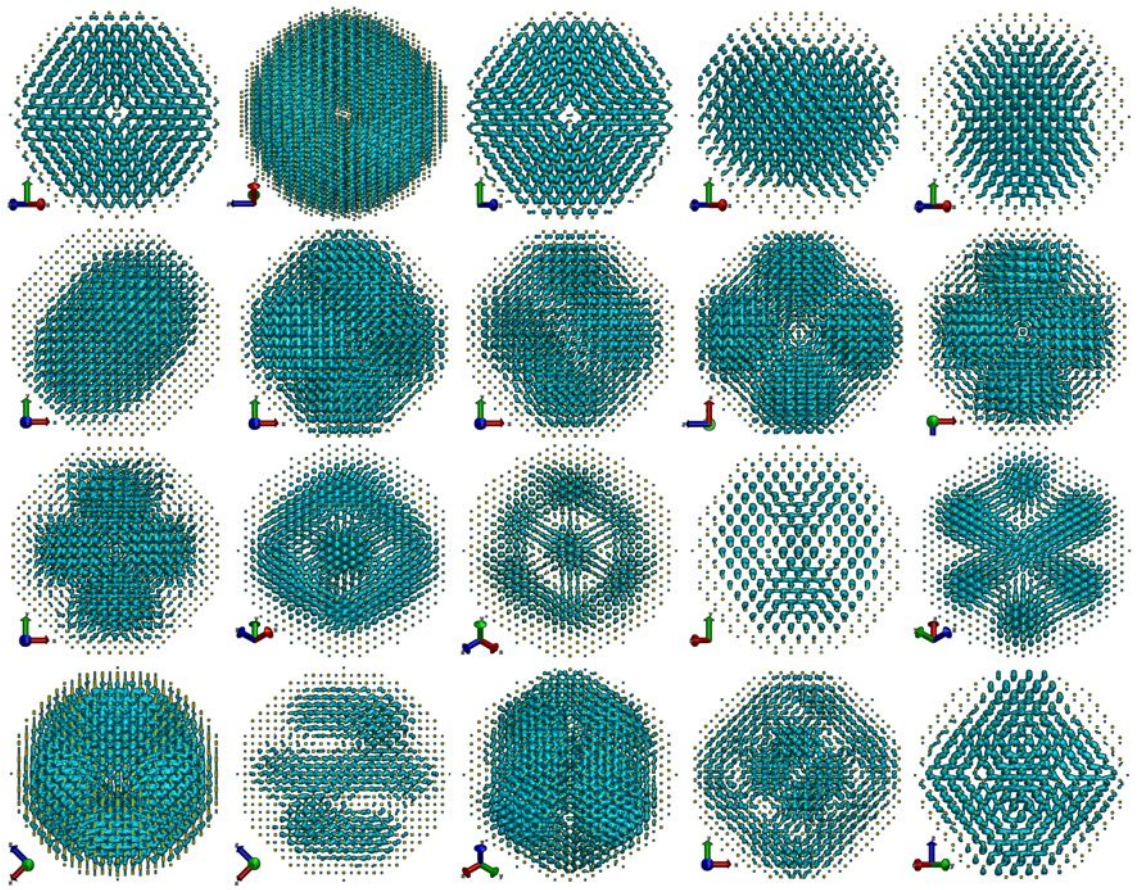

Figure E.3: Isosurfaces, $|\Psi_i(\mathbf{r})|^2$, of the lowest twenty occupied, independent-particle states of a nanocrystal with a diameter of 6 nm. States are ordered from top left to bottom right.

E.2.1 Energy Levels of the Lowest Occupied States

As the diameter is increased from 3 nm to 6 nm, we observe an overall reduction in the energy level spacings, however, the general characteristic level structure is retained between 3 nm and 6 nm. We show this in Figure E.4. The occupied level structure is characterised by the large spacing that separates the 1P and 1S states from the 1D and 2P states. This is followed by another spacing that separates the 1D and 2P states from the clustered 2D,1F and 2S states, which in turn is followed by another large gap between these and the 2F state.

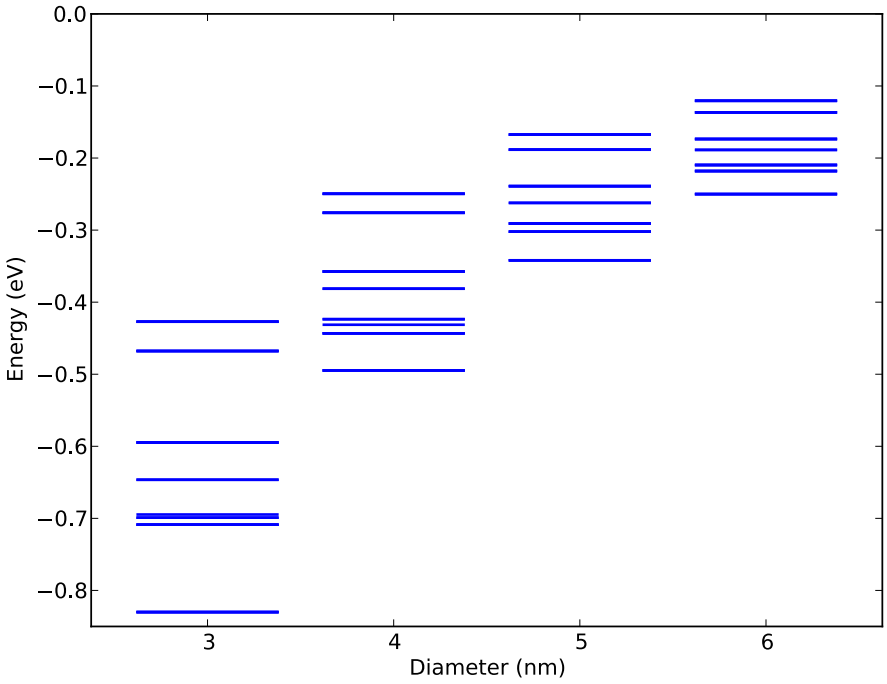

Figure E.4: Level ordering of the lowest twenty occupied states as a function of nanocrystal diameter.

E.3 A Comparison Between Experimental and Calculated Absorption Spectra

Finally, Figure E.5 compares absorption spectra computed in the independent-particle approximation using our tight-binding model, to experimental spectra taken from the literature. In every instance, the line widths of the computed spectra (given in green) are calculated with a fixed FWHM of 50 meV. As a result, many more transitions are resolved in the computed spectra in comparison to the experimental spectra, making the case for a spectral line width that increases as a function of the transition energy.

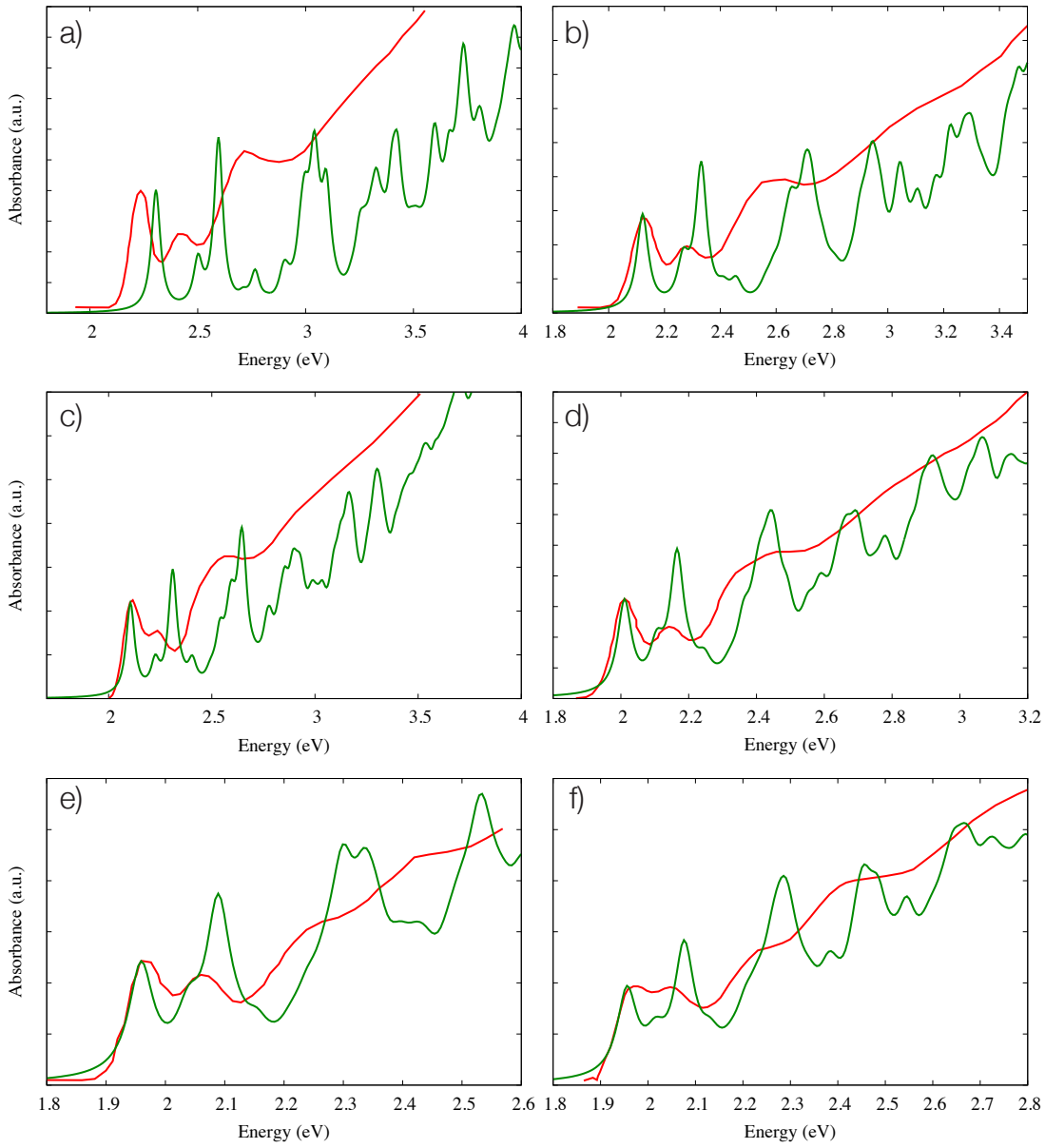

Figure E.5: Comparison between experimental and calculated absorption spectra, for a range of nanocrystal sizes. Experimental spectra are shown in red, whereas calculated spectra are shown in green. All calculated spectra are redshifted by 0.1 eV to account for finite temperature and by an energy, $E_c = 3.572/(\epsilon_\infty d)$. Experimental spectra a), b), d) and e) are taken from reference [200] (zincblende nanocrystals), while experimental spectra b) and f) are taken from reference [198] (wurtzite nanocrystals). The plots correspond to CdSe nanocrystals with diameters: a) d_E=3.1 and d_C=3.5 nm (15 eV), b) d_E=4.1 and d_C=4.3 nm (15 eV), c) d_E=4.8 and d_C=4.8 nm (25 eV), d) d_E=5.2 and d_C=5.5 nm (15 eV), e) d_E=6.3 and d_C=6.3 nm (15 eV) and f) d_E=6.8 and d_C=6.8 nm (25 eV). Here, d_E is the experimentally-referenced diameter and d_C is the simulated nanocrystal diameter. The value in the brackets refers to the passivation energy used for each simulation.

Appendix F

Nanoplatelet Supporting Information

F.1 Properties of the Independent Particle States

In this appendix, we present additional calculations regarding the independent-particle properties of CdSe nanoplatelets. The isosurfaces of the lowest twenty atomic wave functions from both manifolds are given for a nanoplatelet with a thickness of 4 ML, the effect of the passivation parameter on these functions is quantified and we examine the corresponding effect on the optical absorption spectrum. Independent-particle, tight-binding calculations for the absorption spectrum of a nanoplatelet with a thickness of 5 ML are presented. This system is shown in the appendix because of its similarity with the spectrum of a platelet with a thickness of 4 ML. Finally, we examine the results of the $\mathbf{k} \cdot \mathbf{p}$ calculations in more detail, comparing the absorption spectra predicted by the 8-band and 14-band models, before investigating the effect that spin-orbit coupling has on the spectrum.

F.1.1 Independent-Particle Wave Functions

Figures F.1 and F.2 show the band-edge isosurfaces of atomic wave functions for a CdSe nanoplatelet with a thickness of 4 ML in more details. Both sets of wave

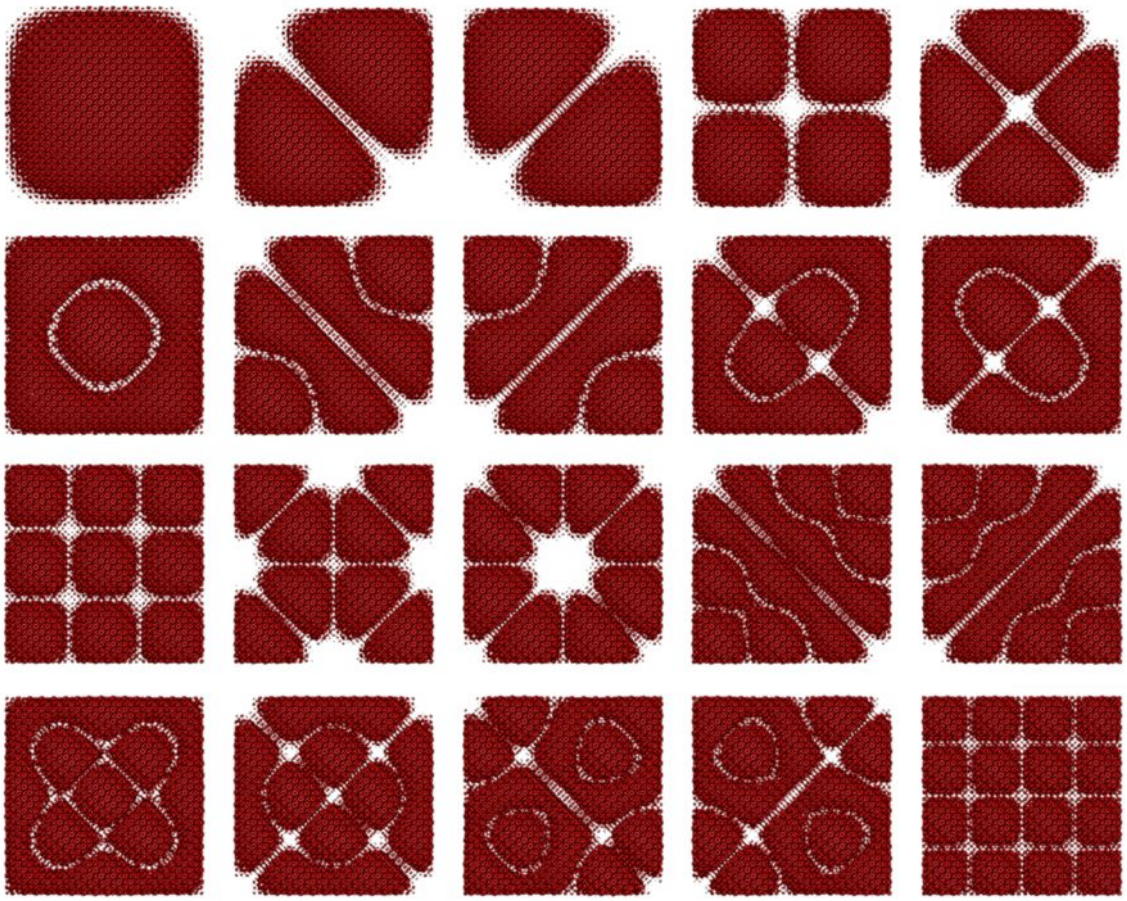

Figure F.1: Atomic wave function isosurfaces, $|\Psi(\mathbf{r})|^2$, for the first twenty unoccupied states of a nanoplatelet with a thickness of 4 ML. The states are ordered from top left to bottom right. The x and y axes point right and up, respectively, with z coming out of the page.

functions are representative of what one finds for platelets with thicknesses varying from 2 ML to 8 ML, although some energy level crossings do occur as the thickness is increased.

In Figure F.3, we plot the wave functions, rather than their moduli squared, for the lowest five unoccupied and occupied states of a nanoplatelet with a thickness of 4 ML. In each isosurface, we plot both the positive and negative components of the wave function at the same isovalue. Positive components of the wave functions are plotted in blue whereas negative components are plotted in red.

These plots show us how the atomic structure and local orbital basis contribute to the nanoplatelet wave functions. For example, the second and third unoccupied

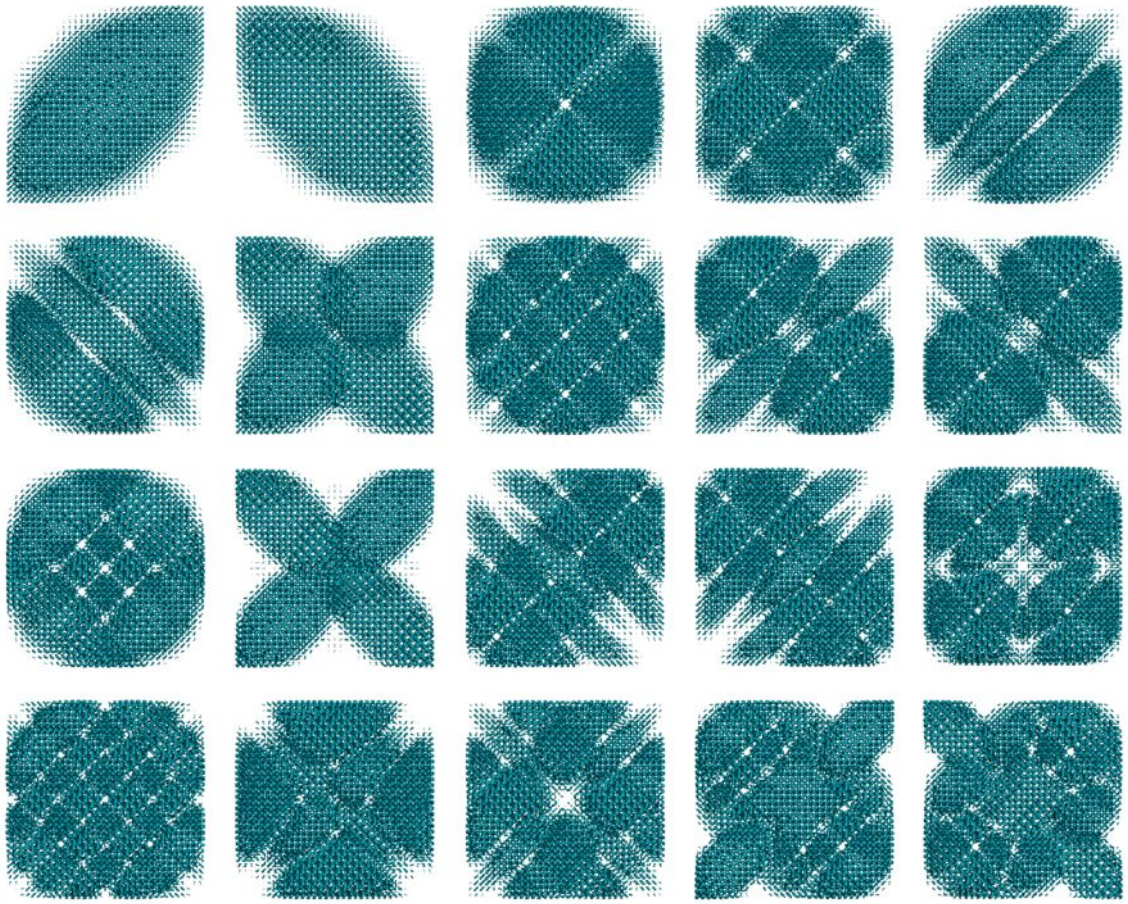

Figure F.2: Atomic wave function isosurfaces, $|\Psi(\mathbf{r})|^2$, for the first twenty occupied states of a nanoplatelet with a thickness of 4 ML. The states are ordered from top left to bottom right. The x and y axes point right and up, respectively, with z coming out of the page.

states are characterised by two well-defined lobes on the nanoscale, however, upon inspection both lobes are found to be comprised of a mixture of negative and positive atomic orbital components. The majority of the charge is distributed on the cadmium cations, which is consistent with the s orbitals deriving from the cadmium valence, while the relative contribution from the p orbitals centred on the selenium anions is much smaller. When averaged, this results in unoccupied functions with one lobe that is positive and one lobe that is negative. The same analysis applies to all unoccupied states shown in Figure F.1.

The picture is more complicated for the occupied states as the orbital composition results in a different local structure. Here, p orbitals from the cadmium and selenium

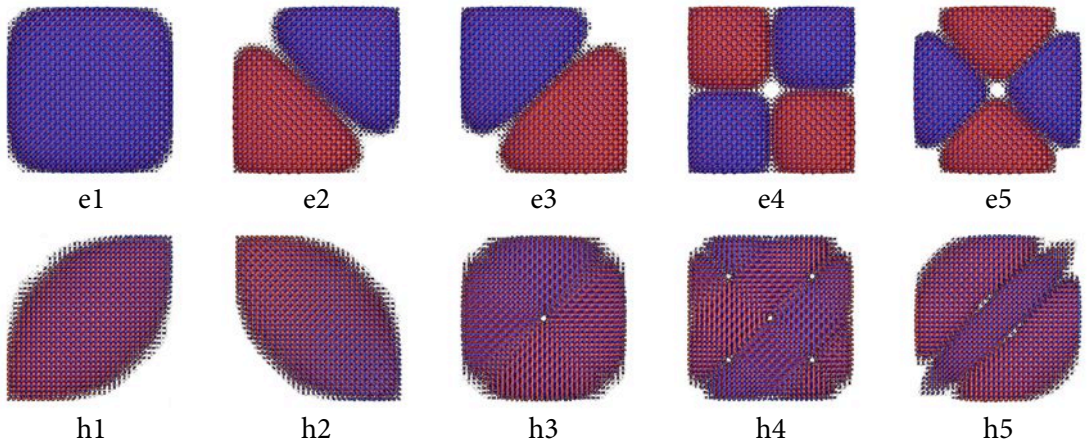

Figure F.3: Atomic wave function isosurfaces, $\Psi(\mathbf{r})$, for the first five occupied and unoccupied states of a nanoplatelet with a thickness of 4 ML. Blue signifies regions where the wave functions are positive, whereas red signifies negative.

valence contribute approximately equally to the nanoplatelet wave functions. This leads to wave functions that rapidly and systematically oscillate between positive and negative values at the atomic scale, both in the plane and perpendicular to the plane. Indeed, complex local variation is observed even at the band edge. For example, in the third occupied state, the orientation of the p orbitals rotates as one works around the planar area in a circular manner, leading to reversal in phase of the orbitals on either side of the (110) plane.

F.1.2 Odd-Monolayer Sensitivity to the Eigensolver

We simulate our nanoplatelets with equivalent lateral dimensions, leading to a square planar area. As a consequence, many states are doubly degenerate. We find that doubly degenerate states in systems with an even number of monolayers have eigenvalues with floating point differences. This is to be expected when using iterative methods of solving a Hamiltonian. Interestingly however, we find that the eigenvalues of doubly degenerate states in systems with an odd number of monolayers are numerically identical. As a consequence, we observe mixing between pairs of degenerate eigenvectors. The degree to which they mix varies with the subspace guess of the solver.

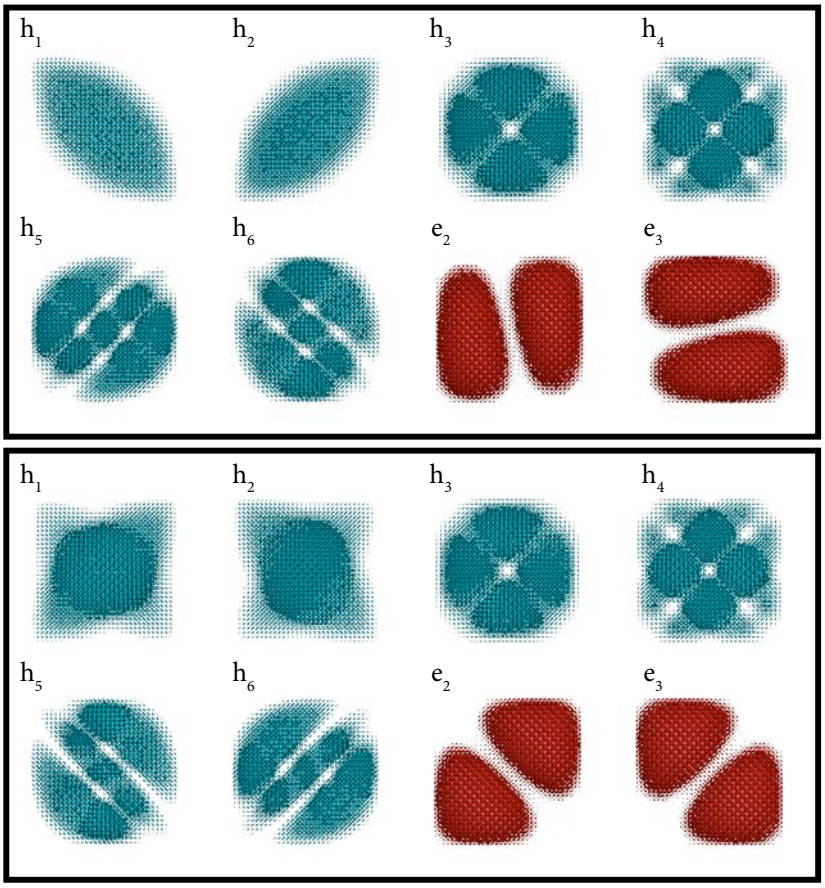

Figure F.4: Isosurfaces for the atomic wave functions, $|\Psi(\mathbf{r})|^2$, of a nanoplatelet with a thickness of 5 ML, computed using different-sized subspaces. The top panel corresponds to subspace 1 whereas the bottom panel corresponds to subspace 2, both of which are given in Table F.1.

The subspaces used in the following test cases are given in Table F.1. A mixing of eigenvectors is evident in the isosurfaces of the atomic wave functions. An example of this is shown in Figure F.4 for a system of 5 ML in thickness, for two different subspace guesses.

Subspace Guess	Lowest Eigenvalue (eV)	Largest Eigenvalue (eV)
400	-0.5	2.75
600	-0.75	3.0
1800	-1.0	3.25

Table F.1: Subspace sizes used to test the sparse solver. In each case, these subspaces were distributed amongst four processes.

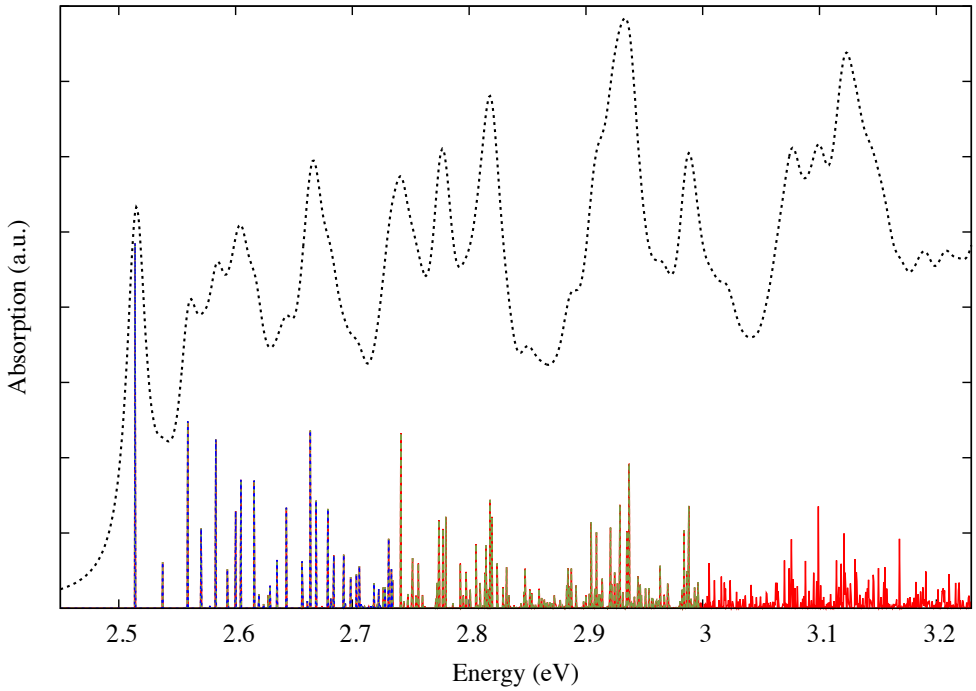

Figure F.5: Independent-particle absorption spectrum for a CdSe nanoplatelet with a thickness of 5 ML, computed using the three different subspaces stated in Table F.1 (blue=1, green=2 and red=3). In each instance, the magnitude of the dipole matrix element is conserved, resulting in the absorption spectrum shown in black.

We have verified that this is a consequence of the sparse FEAST solver and not a feature of the system or an artefact of our parallelisation scheme. Mixing of the eigenvectors was found to occur when we run FEAST in serial. Furthermore, if we replace the CdSe parameter set with one of our construction, for which the symmetry of the Hamiltonian is not perfectly conserved, we see a slight splitting of degenerate states and no mixing.

Despite a mixing of the eigenvectors for pairs of degenerate states, the total magnitude of each transition in the absorption spectrum is conserved. We have verified this in Figure F.5 for subspaces 1, 2 and 3 given in Table F.1.

F.1.3 Independent-Particle State Sensitivity to the Passivating Energy

We treat the nanoplatelet surface as an an ideal surface, with fully-passivated dangling bonds. As detailed in Chapter 8, this is achieved by an orthogonal transformation to hybridised sp^3 orbitals, aligned along the bonding directions, which can be interpreted as the approximate formation of bonding and anti-bonding states between the dangling bonds and the vacuum[177; 178]. The nature of the passivating species is therefore not specified in this approach and the passivating energy can be taken to be any value that clears the band gap of trap states.

In Figure 9.2 in Chapter 9, we showed the effect of the passivating energy on the magnitude of the independent-particle gap, as a function of lateral dimensions (with a thickness fixed at 2 ML). Here, we extend the investigation on the effect of the passivating energy to a subset of the lowest energy levels for a range of thicknesses, the appearance of the atomic wave functions and the independent-particle absorption spectrum. In the latter two cases, we simulate the nanoplatelets with a thickness of 4 ML, as this is most relevant to the results presented in Chapter 9.

Effect of Passivation on the Atomic Wave Functions

We investigate the sensitivity of these features for passivating energies ranging from 10 eV to 50 eV. A value of 10 eV represents the lowest passivating energy that clears the band-gap of states, whereas 50 eV represents a large confining potential. In Figure F.6 we present the same set of independent-particle state isosurfaces for a nanoplatelet of 4 ML in thickness and a planar area of 100 nm^2. These states contribute to the lowest 20 allowed transitions in the absorption spectrum. Simulations shown in the left panel of Figure F.6 utilise a passivating energy of 15 eV (the value used throughout Chapters 9 and 10 for nanoplatelet calculations) whereas simulations shown in the right panel utilise a passivating energy of 50 eV.

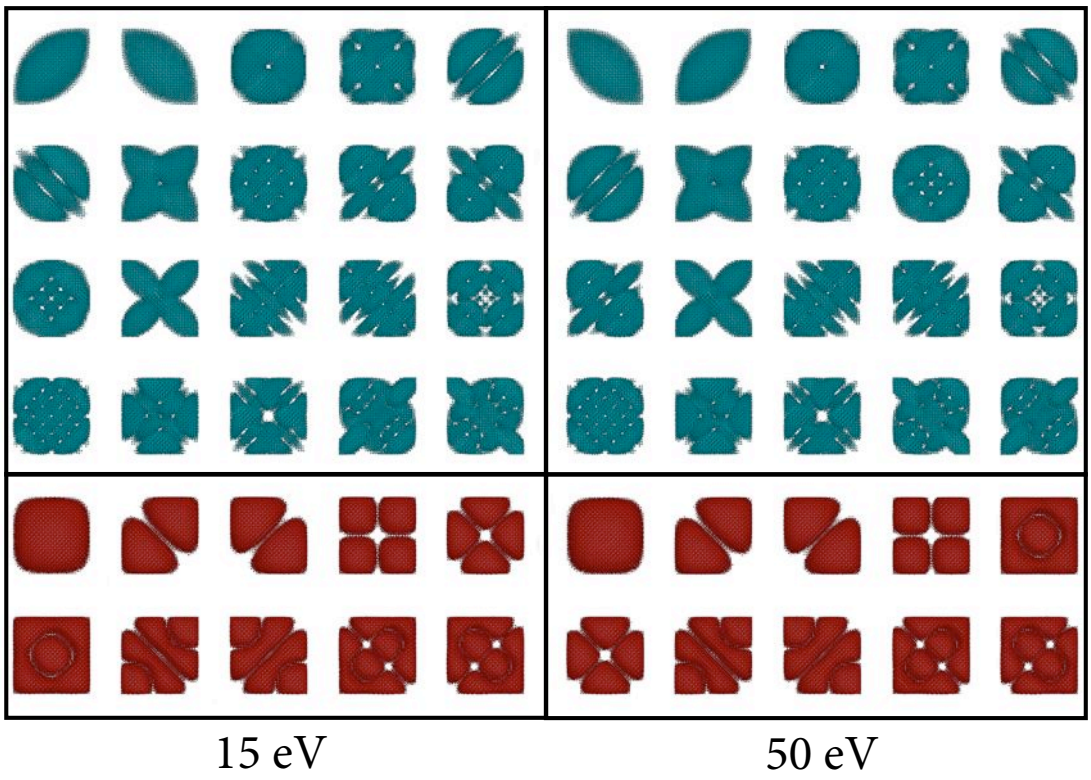

Figure F.6: Atomic wave function isosurfaces, $|\Psi(\mathbf{r})|^2$, for the first twenty occupied states (blue) and first ten unoccupied states (red) of a nanoplatelet with dimensions of 10 nm × 10 nm × 1.2 nm. Simulations have been done using passivating energies of 15 eV and 50 eV, for which the isosurfaces are shown in the left and right panels, respectively.

Figure F.6 shows that the appearance of the independent-particle states is unaffected by our choice of passivating energy, however, we do observe some state reordering. In all but one instance, the state reordering occurs between doubly degenerate pairs. The typical relative change in energy required for such states to change positions is less than a meV and will therefore not affect the transition energies of the absorption spectrum.

Effect of the Passivating Energy on the State Energy Levels

As Figure 9.2 has shown us in Chapter 9, an increase in the passivating energy acts to increase the independent-particle band gap. Figure F.7 reveals that an increase in the passivating energy actually acts to increase the energies of both the occupied and the unoccupied states, however the unoccupied states experience a more pronounced

shift than the occupied, leading to a net increase in the band gap as a function of the passivating energy.

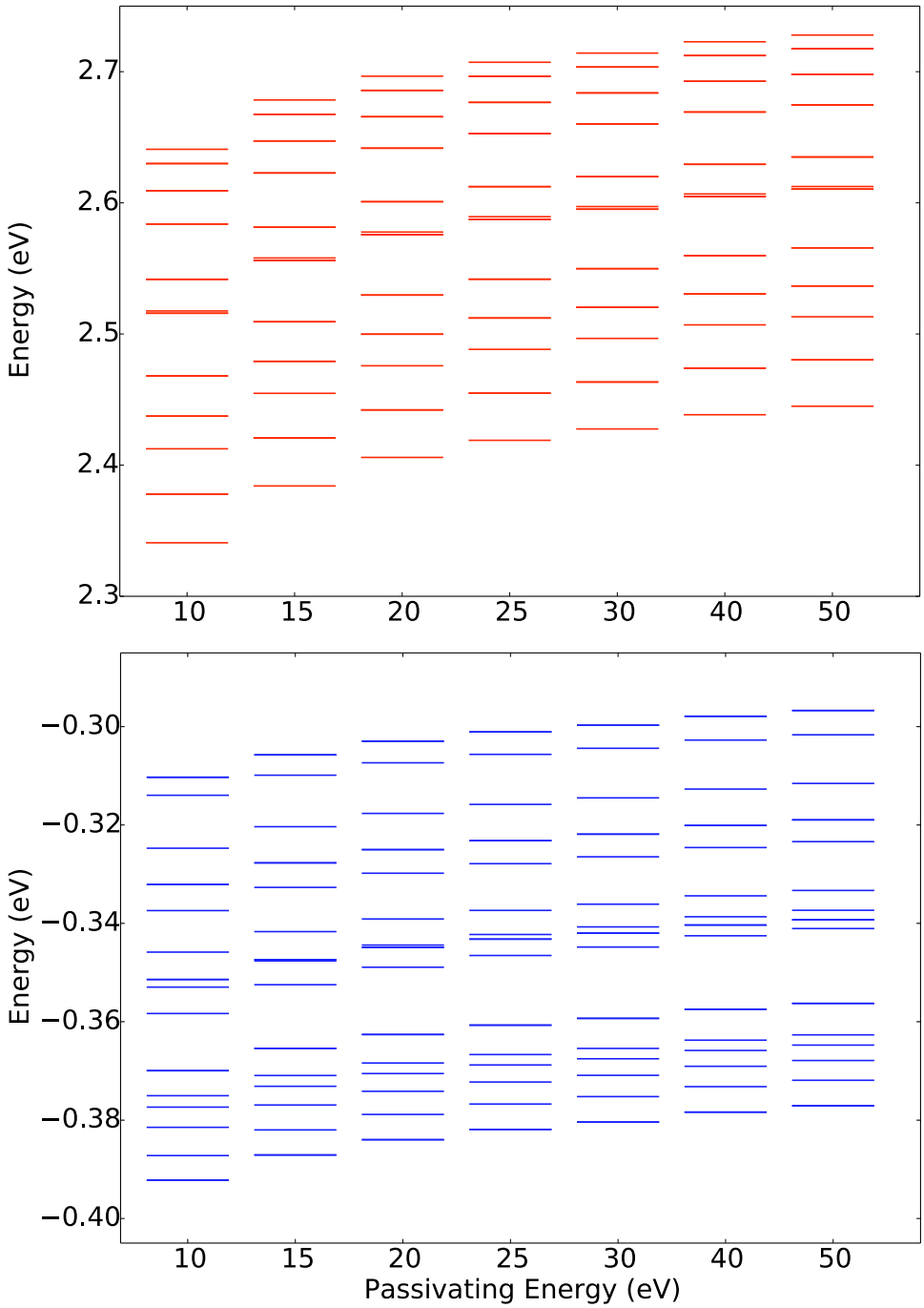

Figure F.7: Energy level digram showing the lowest twenty unoccupied energies (red) and lowest twenty occupied energies (blue) as a function of the passivating energy, for a nanoplatelet with a thickness of 4 ML.

Figure F.7 also reveals that the energy level spacings for this subset of band-edge states are relatively insensitive to the choice of passivating energy and appear to approximately experience a rigid shift. The exception being that we see some changes in the energy-level spacings for the third block of occupied states, which initially occupy the region [-0.34:-0.36] eV.

Effect of the Passivating Energy on the Absorption Spectrum

The absorption spectrum of a nanoplatelet with a thickness of 4 ML is presented in Figure F.8. The spectrum has been computed used passivating energies of 15 eV, 25 eV, 40 eV and 50 eV. The spectra have been computed using an energy-dependent line broadening[1] and in each instance, a rigid shift has been applied to the spectrum such that the onsets line up on a common value.

Small differences were observed in the absorption spectrum when computed with a fixed line broadening, with the level of disagreement increasing with transition energy. If we assume, based on Figure F.6, that the charge distributions of all atomic wave functions are unaffected by the passivating energy, then any differences observed in the absorption spectrum are more likely to be a consequence of changes in the absolute energies of the states (energy of the onset) and changes in energy level spacings, which in turn lead to relative changes in transition energies. Figure F.8 demonstrates that changes in the spectrum are however, largely smeared out by an increased spectral line width at higher energies, therefore our choice of passivating energy will not affect any comparisons with the spectral profiles of experimental spectra.

[1] Computed using an initial line width of 10 meV, which increases linearly up to 100 meV between the onset and 1.5 eV above the onset (constant thereafter).

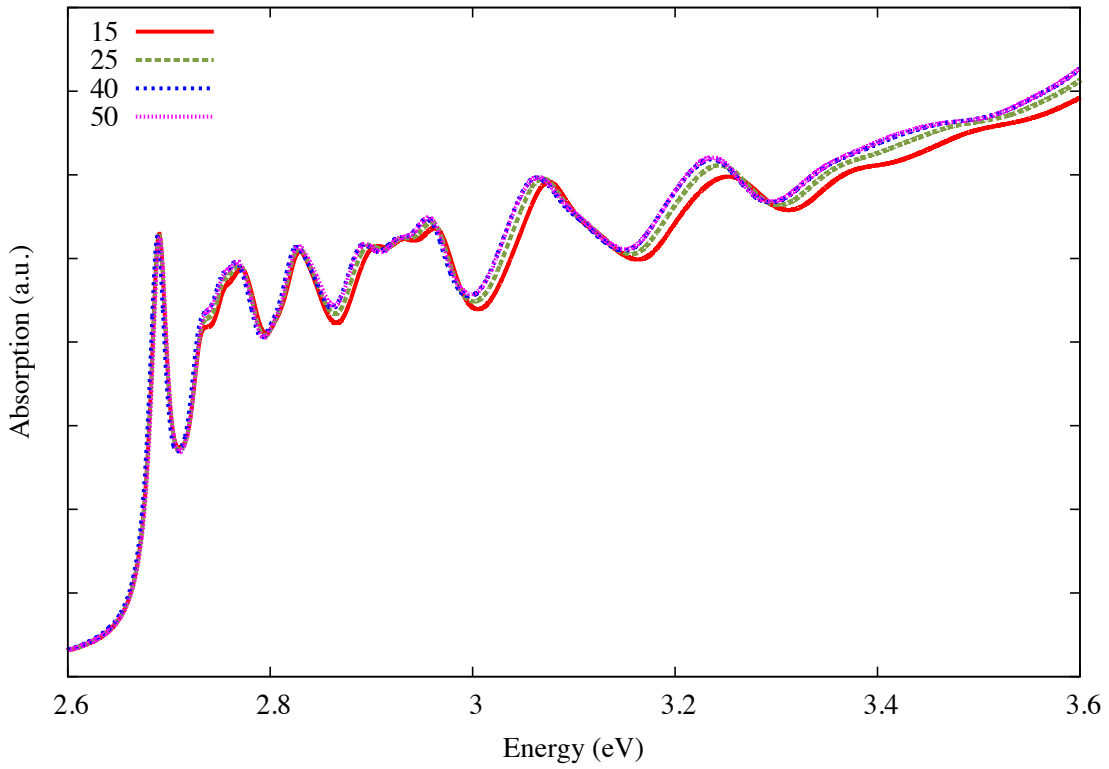

Figure F.8: Absorption spectra for a nanoplatelet with a thickness of 4 ML, computed using several passivating energies and an energy-dependent line width. Rigid shifts have been applied to the spectra such that their onsets line up, facilitating a comparison of the spectral profiles.

F.2 Absorption Spectrum of a Nanoplatelet with a Thickness of 5 ML

Figure F.9 compares the experimental absorption spectrum of the 5 ML-thick nanoplatelet (red) to the spectrum computed in the independent-particle approximation, using our tight-binding model (green). This is presented in the appendix because with the exception of the onset, the features of this spectrum do not significantly differ from those of the spectrum for a platelet with a thickness of 4 ML.

The overall agreement between spectra computed in the independent-particle approximation and experiment is poor. The use of an energy-dependent line width in the calculated spectrum is shown in Figure F.10. This improves the agreement

with experiment but in general, suffers from the same shortcomings as the 4 ML spectrum. The use of an energy-dependent line width has improved the magnitude of the second peak relative to the first and if one was to use a more aggressive broadening, such that the second and third peaks smeared into one, the width of the first and second peaks would be in reasonable agreement with experiment.

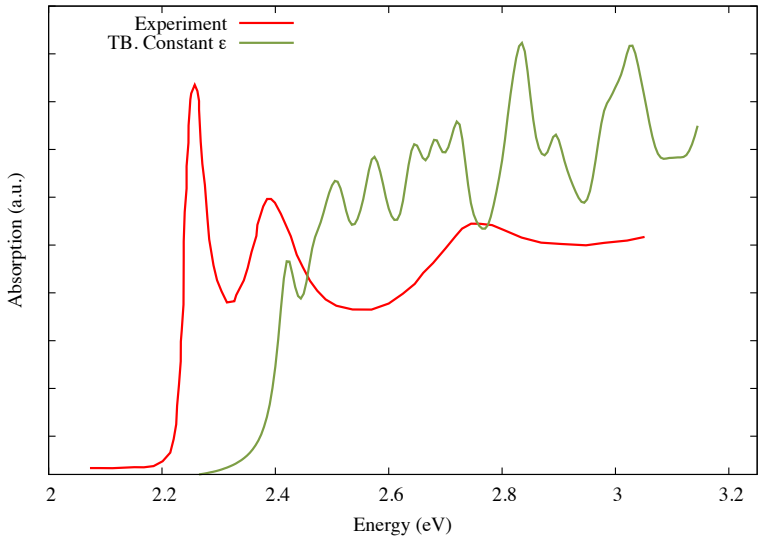

Figure F.9: The absorption spectrum for a CdSe platelet of 5 ML in thickness. The experimental spectrum (red[67]) is compared to the tight-binding spectrum, computed in the independent-particle approximation (green). The tight-binding spectrum is computed using a fixed line broadening of 20 meV (FWHM).

The calculated spectrum however, still does not capture the large dip in the experimental spectrum following the second peak. It is expected that inclusion of the electron-hole interaction will strongly mix the independent-particle transitions and improve the agreement with experiment.

F.3 Comparing $\mathbf{k} \cdot \mathbf{p}$ Simulations

The 8-band $\mathbf{k} \cdot \mathbf{p}$ model has been employed several times in the literature to explain experimental observations and make predictions regarding the opto-electronic properties of CdSe nanoplatelets[72; 87; 232]. In Figure F.11, we therefore present a comparison of the absorption spectra predicted by Tomić's 8-band and 14-band

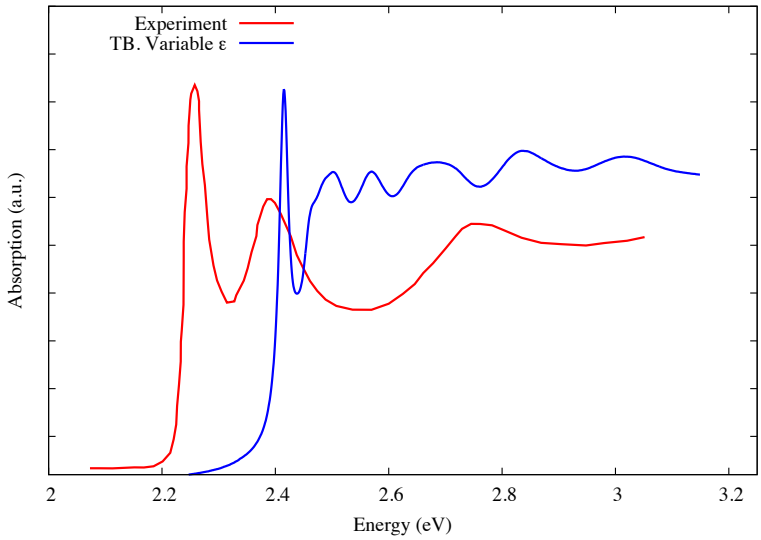

Figure F.10: The absorption spectrum for a CdSe platelet of 5 ML in thickness. The experimental spectrum (red) is compared to the tight-binding spectrum, computed in the independent-particle approximation (blue). The tight-binding spectrum is computed using a line broadening that linearly increases from 10 meV to 200 meV in the energy range $[2.5 : 4.1]$ eV.

$\mathbf{k} \cdot \mathbf{p}$ models, given in red and blue, respectively. In both instances, the spectra are computed in the absence of spin-orbit coupling and using a polarisation vector, $\hat{\mathbf{e}} = (1, 0, 0)$.

The transition energies of the first three macroscopic peak structures are in perfect agreement, however beyond this, the absorption spectra predicted by the two models show little agreement to one another. We suspect that this occurs for two main reasons: Firstly, the two Hamiltonians predict different energy-level spacings for the envelope states. This will lead to transitions with different energies. Secondly, the two Hamiltonians exhibit different symmetries which will lead to envelope states with different symmetries. This consequently affects the strengths of the transitions. Furthermore, we expect that differences between the envelope states of the two models increases as one moves further from the band edges, leading to absorption spectra that disagree more as the transition energy increases.

An analysis of Figure F.11 and the comparison of the 14-band model with our tight-binding model, shown in Figure F.12, therefore suggest that the 14-band $\mathbf{k} \cdot \mathbf{p}$ model

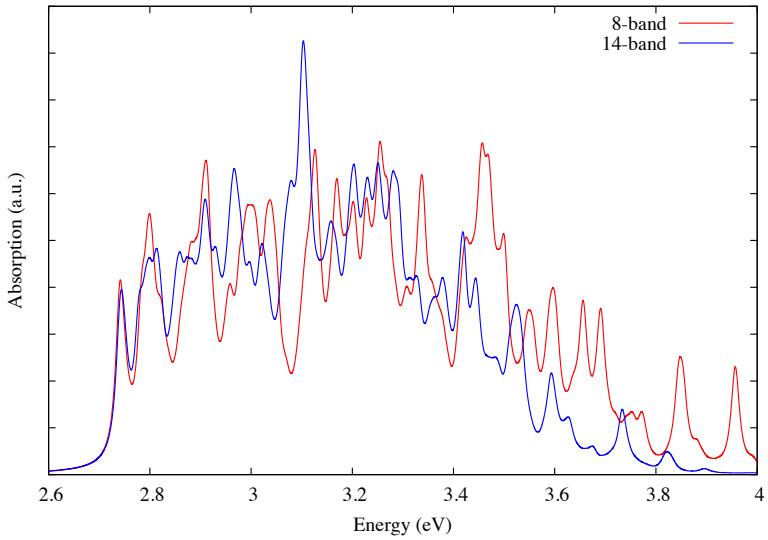

Figure F.11: Absorption spectra of a nanoplatelet with a thickness of 4 ML, computed using $\mathbf{k} \cdot \mathbf{p}$ Hamiltonians comprised of eight (red) and fourteen (blue) bands, respectively.

is required in order to predict opto-electronic properties in agreement with those predicted by a minimal atomistic model.

F.3.1 The Influence of Spin-Orbit Coupling on the Absorption Spectrum

As our tight-binding model lacks spin-orbit coupling, we are unable to directly investigate its effect on the spectrum, however Stanko Tomić's $\mathbf{k} \cdot \mathbf{p}$ model does support the inclusion spin-orbit coupling. Figure 9.9 in Chapter 9 shows that there is good agreement between the tight-binding and 14-band $\mathbf{k} \cdot \mathbf{p}$ models for the low-energy region of the absorption spectrum. We therefore believe that the 14-band $\mathbf{k} \cdot \mathbf{p}$ model will give a useful indication of the effect of spin-orbit coupling on the region of the spectrum that interests us.

A numerical analysis of the lowest transitions reveals that in the absence of spin-orbit coupling, there are twenty one allowed transitions in the region, $0\,\text{eV} \leq E_t \leq 0.1\,\text{eV}$, where E_t is defined relative to the onset, and a further seventy eight transitions in the range, $0.1\,\text{eV} < E_t \leq 0.3\,\text{eV}$. These are comparable to our tight-binding results,

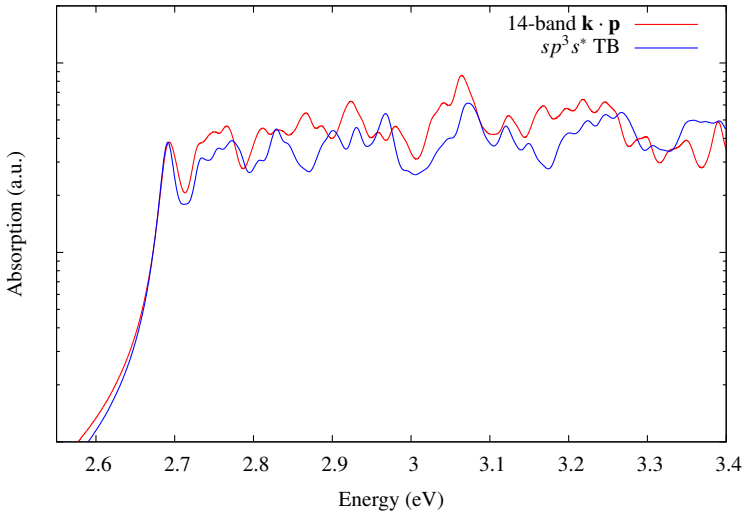

Figure F.12: A comparison of the absorption spectrum of a 4 ML-thick nanoplatelet, computed in the independent-particle approximation, using our tight-binding model (blue) and Tomić's 14-band $\mathbf{k}\cdot\mathbf{p}$ model (red). The spectra are plotted on a log scale and computed using a fixed line width of 20 meV (FWHM).

which find twelve and seventy three transitions in the same intervals, respectively. Discrepancies may be due to differences in the tight-binding wave functions and the $\mathbf{k}\cdot\mathbf{p}$ envelope functions, consequently affecting the respective dipole matrix elements. Differences in energy-level spacings and the arbitrary criterion used to define an allowed transition are also contributing factors.

When spin-orbit coupling is included in the $\mathbf{k}\cdot\mathbf{p}$ model however, the number of allowed transitions in the region, $0\,\text{eV} \leq E_t \leq 0.1\,\text{eV}$, drops to three, whereas the number of allowed transitions in the region, $0.1\,\text{eV} < E_t \leq 0.3\,\text{eV}$, increases to ninety four (although if one increases the criterion for an allowed transition to 5% of the largest oscillator strength, this drops to forty).

In Figure F.13, we show the effect of spin-orbit coupling on the absorption spectrum of a nanoplatelet with a thickness of 4 ML, using the 14-band $\mathbf{k}\cdot\mathbf{p}$ Hamiltonian. The inclusion of spin-orbit coupling has a negligible effect on the independent-particle band gap and the magnitude of the lowest transition appears to be relatively unaffected, however, its inclusion has changed the overall profile of the spectrum.

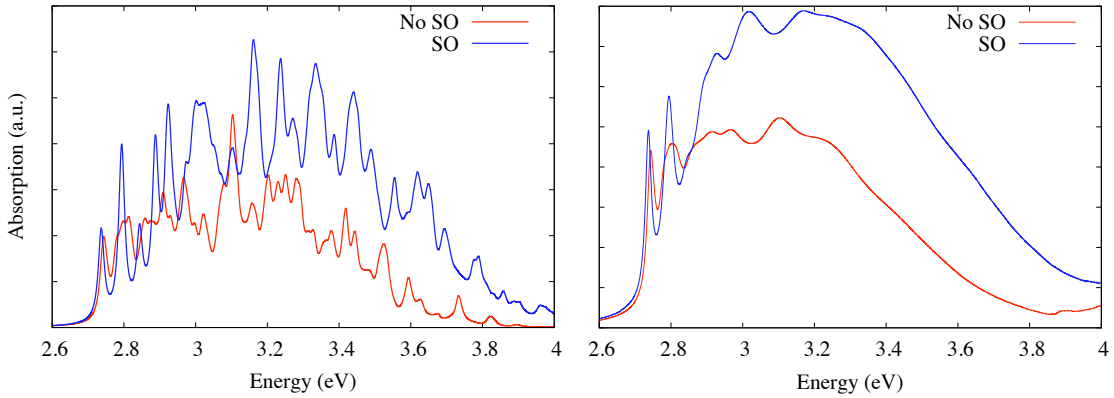

Figure F.13: A comparison of the absorption spectrum predicted by the 14-band $\mathbf{k} \cdot \mathbf{p}$ model with (blue) and without (red) the inclusion of spin-orbit coupling, for a platelet with a thickness of 4 ML. The panel on the left uses a fixed line width of 20 meV, whereas the panel on the right uses an energy-dependent line width, with a FWHM that increases from 20 meV to 340 meV between the onset and 4 eV.

Following the inclusion of spin-orbit coupling, two strong peaks are still present in the low-energy region of the spectrum. The width of the second peak has decreased, suggesting that the spin-orbit interaction redistributes spectral weight amongst transitions at ~ 2.8 eV, leading to an increase in the intensity of one whilst diminishing the others. We also observe that the addition of spin-orbit coupling has not changed the separation between the two lowest peaks and consequently will not improve the agreement with experiment. We therefore suggest that while its inclusion has a noticeable effect on the high-energy spectral profile, the inclusion of the electron-hole interaction is more important for an accurtate description of the low-energy features of the experimental spectrum.

Appendix G

Many-body Calculations Supporting Information

G.1 The Effect of the Two-Particle Basis on the Spectrum

In ab-initio Bethe-Salpeter calculations, the two-particle basis is defined such that the difference in energy between the HOMO and the lowest occupied state in the basis is approximately equal to the difference between the LUMO and the highest unoccupied state in the basis. As such, the two-particle basis is constructed using independent-particle states which span equivalent energy intervals (relative to the band extrema). In an analogous manner, we define the energy of the highest hole state relative to the lowest hole state and the energy of the highest electron state relative to the lowest electron state.

In this section, we investigate what effect using electron and hole states with different maximum energies has on the two-particle absorption spectrum. Specifically, we look at nanocrystals with diameters of 3 nm and 4 nm. CdSe nanocrystals exhibit a much higher density of states at the valance band edge than at the conduction band edge. A two-particle basis comprised of electrons and holes that span the same

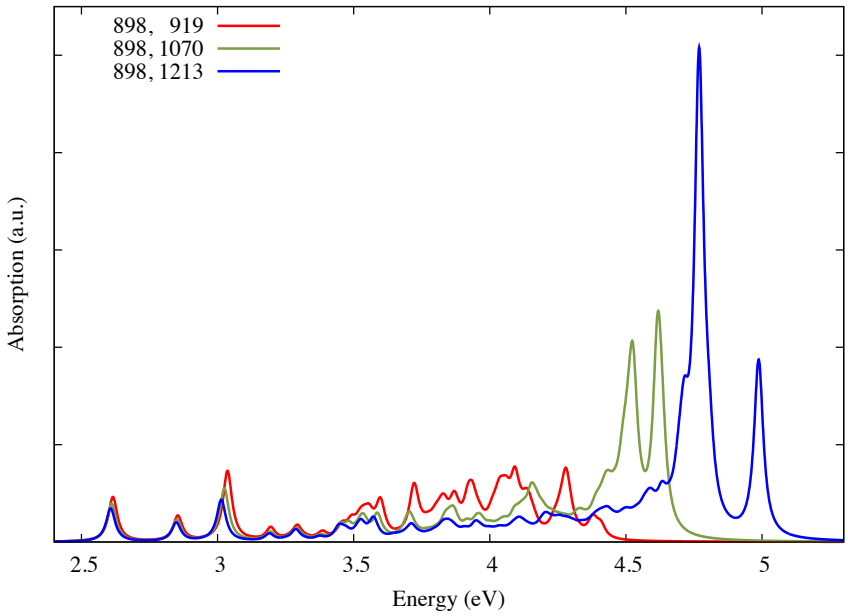

Figure G.1: Two-particle absorption spectrum as a function of maximum electron energy, for a nanocrystal with a diameter of 3 nm. The values in the key correspond to the energies of the largest hole and electron in the basis, $[E(h_{N_h}), E(e_{N_e})]$ (meV).

energetic range in their respective manifolds will therefore contain many more holes than electrons.

To investigate the effect of the basis on the absorption spectrum, we perform an initial calculation for which the energies of the largest hole and electrons states are approximately the same, $E(h_{N_h}) \approx E(e_{N_e})$. We then vary the maximum electron energy and observe what effect it has on the absorption spectrum. Finally, we do a calculation in which the hole energy is increased to equal the maximum electron energy. This is initially performed on a nanocrystal with a diameter of 3 nm and is shown in Figures G.1 and G.2.

Figure G.1 shows that the maximum electron energy is increased for a fixed hole basis, a resonance appears at a transition energy of 4.75 eV. The maximum energy at which a transition can occur in the two-particle spectrum corresponds to the transition energy of the largest electron-hole pair in the basis, $E(e_{N_e}) - E(h_{N_h})$. That is, as we increase the basis, we therefore also increase the maximum transition energy at which spectral features can be observed. Figure G.1 shows that there

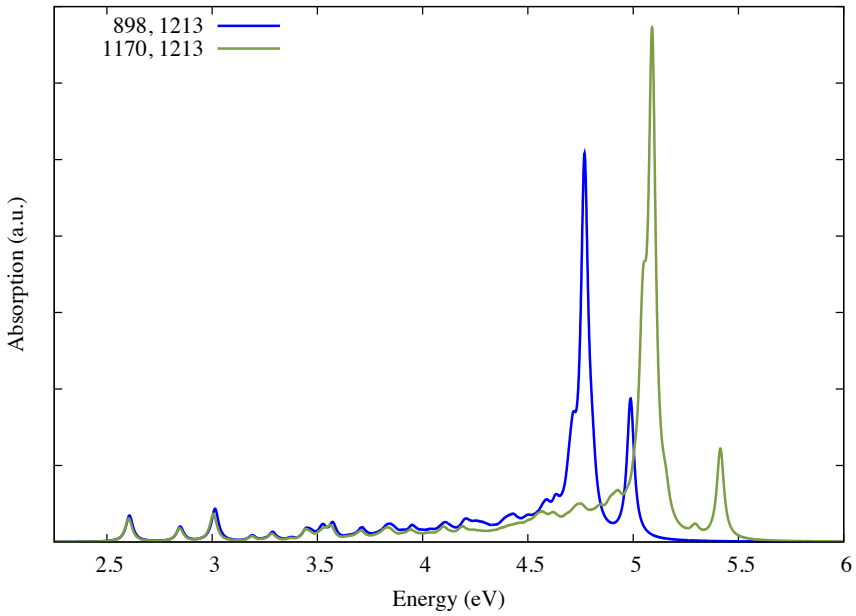

Figure G.2: Two-particle absorption spectrum for a nanocrystal with a diameter of 3 nm, computed with two basis sizes. The comparison shows the effect of a larger maximum energy cut-off for the hole state in the pair basis.

is also, however, a redistribution of oscillator strengths to high-energy transitions between 4.5 eV and 5 eV, else all of the spectra in the figure would agree in the range, 2.5 eV to $\sim$ 4 eV. The amount that the oscillator strengths are redistributed increases as a function of transition energy, and becomes more prominent as electrons with higher energies are introduced into the basis. Even the lowest exciton states can be seen to feel some effect of the additional pair states containing high-energy electrons.

When we subsequently increase the maximum energy of the hole states in the basis, such that $E(h_{N_h}) \approx E(e_{N_e})$, as shown in Figure G.2, we see a further redistribution in the oscillator strengths of the high-energy transitions but little change in the lowest spectral features. This suggests that pair states that contain a high-energy hole mix strongly with pair states of comparable energies but do not affect low-energy pair states.

We investigate the effect of the basis in the same manner for a larger nanocrystal, with a diameter of 4 nm. This system contains just over twice as many atoms as

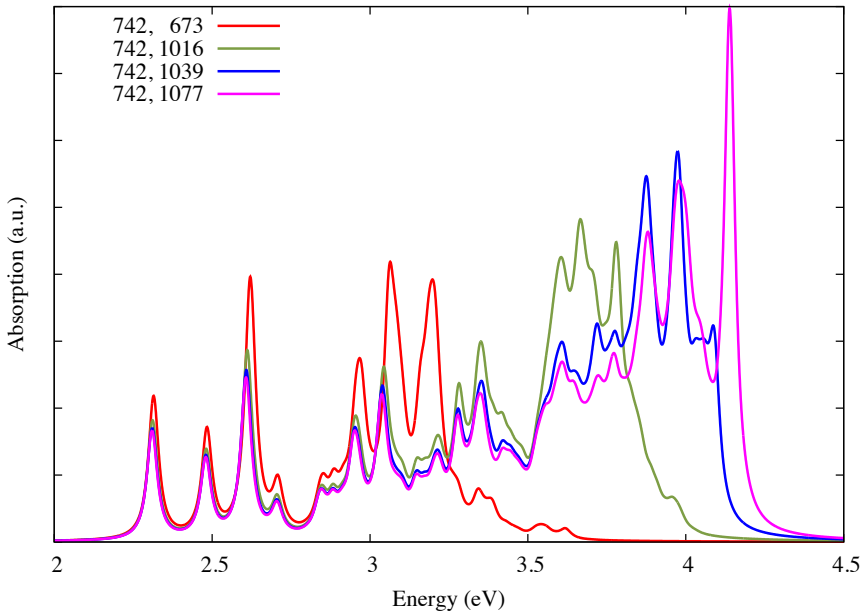

Figure G.3: Two-particle absorption spectrum as a function of maximum electron energy, for a nanocrystal with a diameter of 4 nm. The values in the key correspond to the energies of the largest hole and electron in the basis, $[E(h_{N_h}), E(e_{N_e})]$ (meV).

a nanocrystal with a diameter of 3 nm. The initial spectrum (red line) in Figure G.3 is not well-converged, even in the low-energy region of the spectrum and can be seen to converge as the electron energy cut-off is increased. We then see that as the maximum electron energy is increased from 1016 meV to 1077 meV, there is a small to negligible change in the oscillator strengths of transitions between 2 eV and 3.5 eV, whilst there is a large redistribution at higher energies. This suggests that pair states with high-energy electrons above a cut-off of 1 eV do not contribute to the lowest exciton states to the same extent that they do in a nanocrystal with a diameter of 3 nm. As the maximum hole energy is then increased for a fixed electron basis, shown in Figure G.4, the high-energy transitions are converged more so, whereas the effect on the low-energy region of the spectrum is negligible. This is essentially what is observed in the smaller system.

In summary, pair products with high-energy electrons contribute to low-energy exciton states more greatly than pair products containing high-energy holes and this effect is more pronounced in smaller systems, containing less than 1000 atoms.

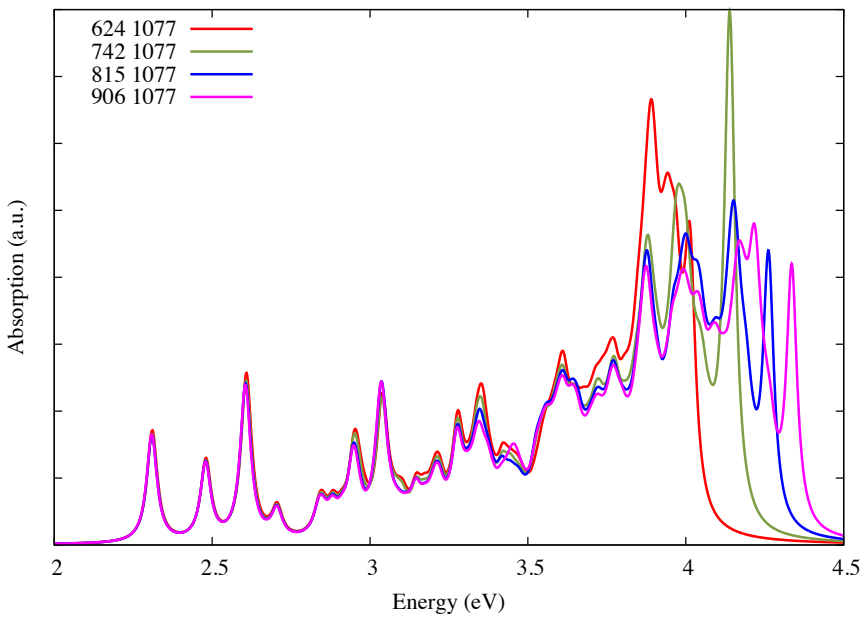

Figure G.4: Two-particle absorption spectrum as a function of maximum electron energy, for a nanocrystal with a diameter of 4 nm. The values in the key correspond to the energies of the largest hole and electron in the basis, $[E(h_{N_h}), E(e_{N_e})]$ (meV).

Secondly, pair products in which the energy of the electron exceeds 1 eV (relative to the lowest electron state) lead to a large redistribution of oscillator strengths to high-energy transitions. This effect is observed in nanocrystals with diameters of 2 nm (not shown here) and 3 nm but not in a nanocrystal with a diameter of 4 nm. This could either be a size-dependent effect or it may also occur in larger nanocrystals when one continues to increase the basis size. The latter is difficult to test give the expensiveness of the calculations.

If we look at Figure 10.3 in Chapter10, it is clear that this redistribution of oscillator strengths to high energies stems from the exchange term of the BSE kernel. It may therefore be the case that screening of the exchange term is necessary in small nanocrystals. The exchange term is not screened in either the BSE or TDDFT formalisms, however it has been argued that whilst the short-range exchange term is unscreened in the bulk, the long-range exchange is screened by the dielectric tensor, therefore motivating screening of the long-range exchange interaction in nanostructures[215].

Rabani and coworkers also observe shifts in oscillator strengths when modelling the absorption spectra of CdSe nanocrystals[212]. They use a Bethe-Salpeter implementation with a simple, size-dependent dielectric constant, however they use an empirical pseudo-potential model to generate the basis states. As it is often stated that pseudo-potential models are capable of LDA-quality wave functions[23], their results viewed in context with our own suggest that the features we observe occur at the level of the two-particle calculations. Rabani and coworkers suggest that it occurs because of an amplification of a plasmon resonance near 10 eV.

G.2 Nanocrystal Band gap as a Function of Size

The exact fit of the function for the band gap dependence on nanocrystal diameter can vary depending on the range of the data values used in the fit, the choice of the function and the free parameters which comprise it, such as the choice of bulk band gap, which varies quite considerably in the literature (see Table 6.2 in Chapter6). In this section we will therefore discuss the process used to fit the data presented in Figure 10.13 in Chapter10.

In Figure G.5, we observe that there is a lack of experimental data for nanocrystals with diameters less than 16 Å, whereas there are copious tight-binding data points. We therefore exclude tight-binding data for nanocrystals with diameters below 16 Å from the fit, such that both data sets are fit within a range in which data is available. We also remove a couple of anomalous experimental points in the large-size region of the plot (see those circled in Figure G.5). In doing so, the global agreement of the tight-binding fit relative to the experimental fit is improved.

Fitting functions to experimental and computational data defined over the same range still does not result in two functions that converge on the same value within 90 Å. This is achieved in Figure 3.2 of Chapter3, by initially fitting the tight-binding data. The parameters found from the tight-binding fit are then used in a modified

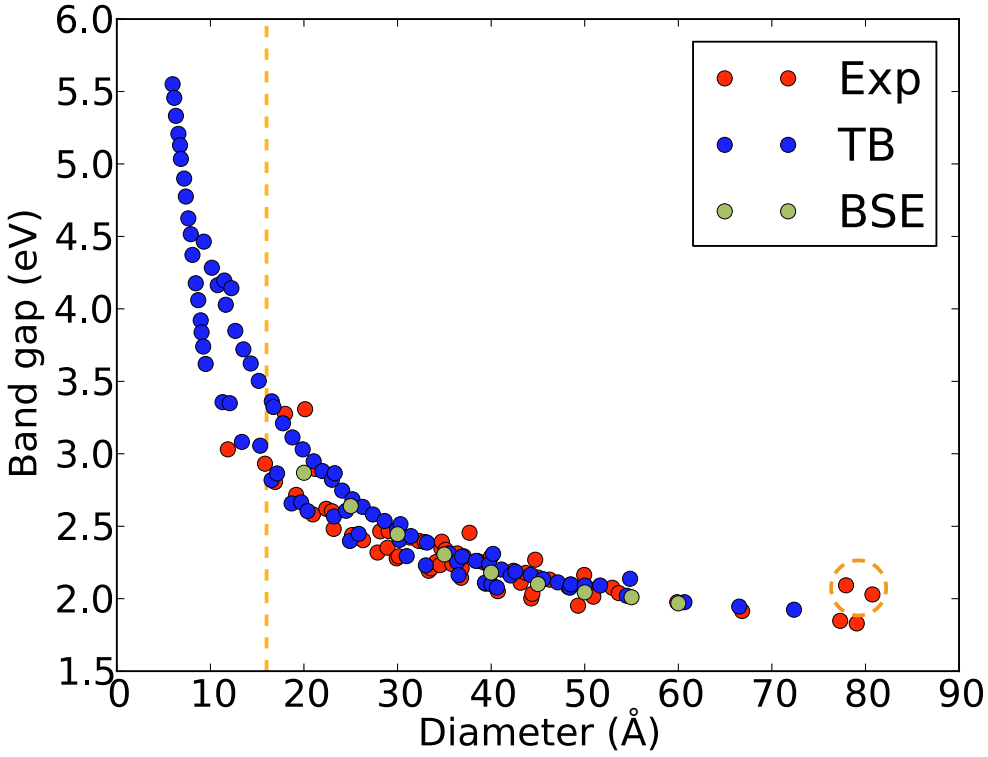

Figure G.5: Optical gap data for CdSe nanocrystals of varying diameters, taken from a range of experimental[11; 21; 100; 110–113] (red) and computational[24; 100; 102; 107] (blue) sources in the literature. All computational data is calculated using the sp^3s^* tight-binding model, although the methods used to compute the optical gap differ between sources. Our calculations of the optical gap using the Bethe-Salpeter equation are also presented in green. Data points to the left of the orange line are excluded in the fit shown in panel b) in the final fit.

function describing the experimental dependence. This is given by Equation (3.2) in Chapter3 and only contains one free parameter, representing the average uncertainty in the measured nanocrystal diameter. While constraining the fit in this manner may seem disingenuous, we stress that all fits to the band gap dependence are arbitrary. We choose our fit function such that it scales as $1/d^2$ (where d is the nanocrystal diameter) in the large-size limit: The scaling associated with quantum confinement in an infinitely deep, spherical potential well, and include the linear term to give some additional flexibility to the fit in the small size limit. Beyond that, any choice of function is no more or less valid.

In Figure G.6, we compare the functions fit to the experimental data using Equations

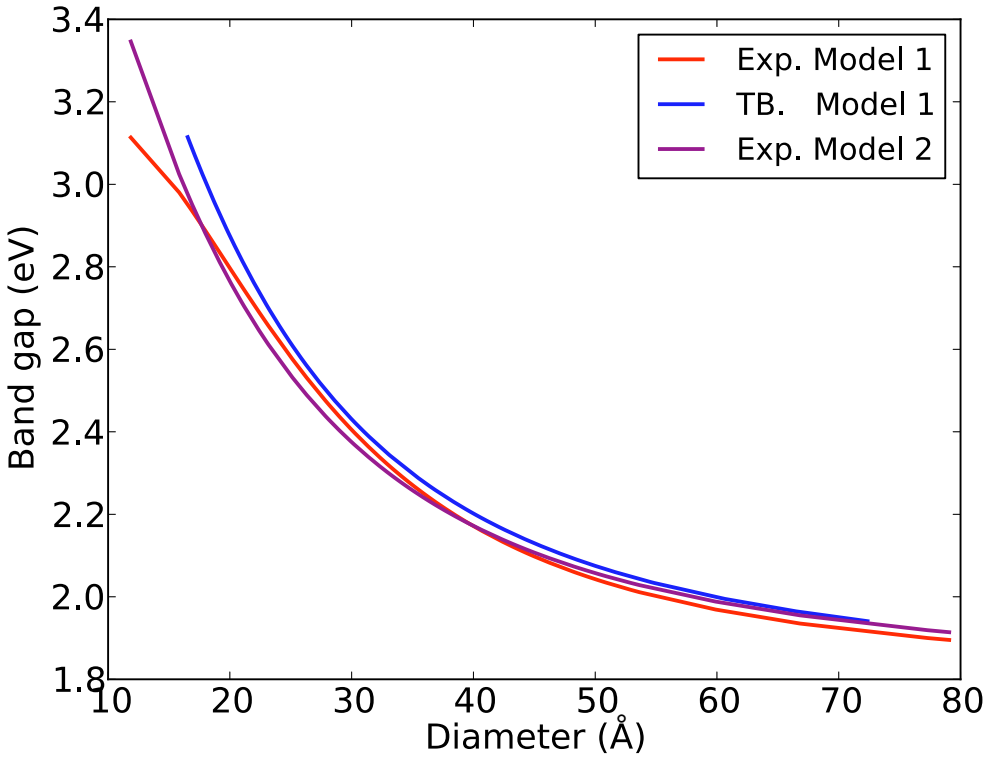

Figure G.6: Optical gap dependence on nanocrystal diameter. The tight-binding data and experimental data fit using Equation (10.3) are shown by the blue and red lines, respectively. A second fit to the experimental data is found by utilising Equation (3.2) and fixed parameters found from the tight-binding fit, along with an additional free parameter. This is shown by the purple line.

(3.2) and (10.3) (purple and red lines, respectively). We can see that the effect of constraining the experimental fit with the tight-binding parameters results in a curve (purple) which converges on the tight-binding best-fit much more quickly than the unconstrained experimental fit (red), at the expense of the agreement between 20 Å and 40 Å. Whilst fitting in this manner gives an nice estimate of the average uncertainty in the measured nanocrystal diameter, we compare our BSE calculations to the experimental dependence found by fitting to Equation (10.3), such that the same equation is used to fit each data set.

Figure G.7 compares the experimental and tight-binding data from the literature with our BSE calculations for the optical gap dependence on the diameter of CdSe nanocrystals. A bulk band gap of 1.8 eV is used (T=300 K) in all fits. The agreement

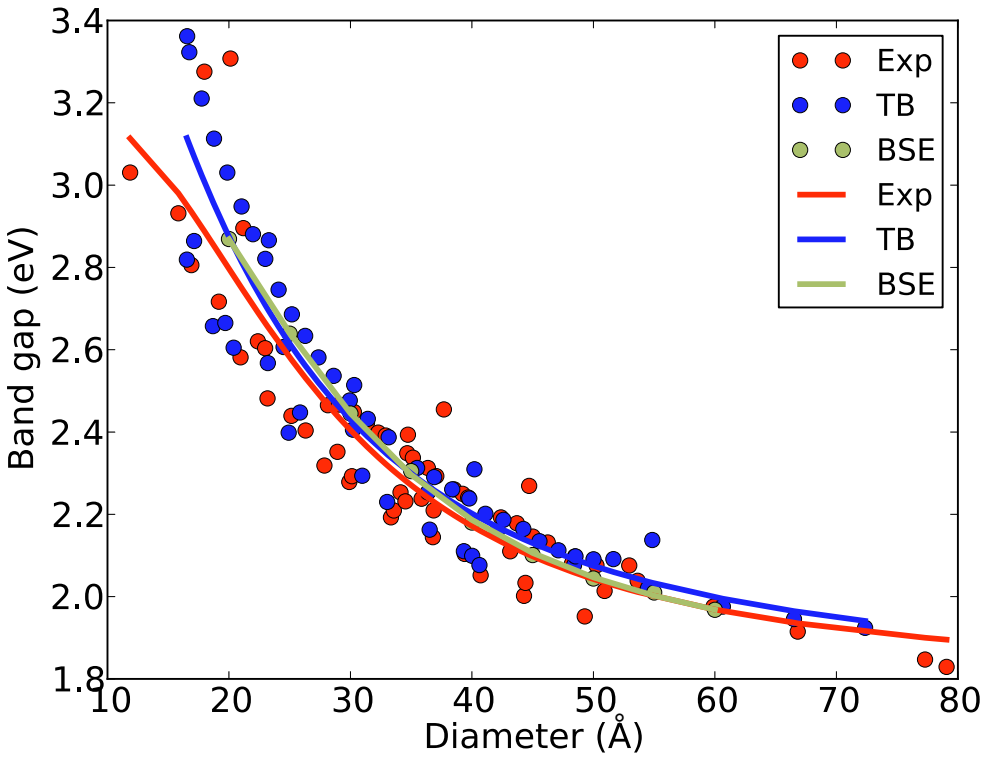

Figure G.7: Optical gap as a function of nanocrystal diameter. Data points taken from the literature (red and blue) are shown with our tight-binding+BSE results (green). Lines of best-fit, defined using Equation (10.3), are overlaid.

of the BSE calculations with the average optical gap as a function of diameter, is very good. This may be somewhat fortuitous due to the spread in the values of the experimental data, however the overall trend in the dependence is well-reproduced by our BSE calculations for a range of sizes. Agreement could further be improved below a diameter of 4 nm via the treatment of dielectric screening and the choice of basis, as discussed in section 10.3.1 in Chapter10.

Finally, one could raise the point that our tight-binding plus BSE model does not directly reproduce any of the experimental data shown here (only the average agreement is good), however the purpose of an empirical model in the first instance is to reproduce trends, and Figure G.7 demonstrates that our model does that. Parameters such as the bulk band gap and the passivating energy can then be adjusted in order to produce results consistent with one property of a specific set of

experimental data, such as the band gap dependence. The model can then be used to quantitatively investigate other physical properties. For example, the blue data points that closely match the red data points for the smallest set of optical gaps in Figure G.7 correspond to a tight-binding model with the same basis, that simply utilises a smaller bulk band gap and different passivation parameters to us[102].

G.3 Extensions to the Treatment of Dielectric Screening

In Chapter 10, we screen the electron-hole interaction with the modified Penn model, given by Equation 10.2. This accounts for the average reduction in the dielectric constant of the nanocrystal as its size decreases, however, it does not account for the spatial separation of the electron and hole. In general, we know that dielectric screening should be lower for electron-hole separations of the order of a bond length or less. This can be accounted for in a phenomenological manner using the Thomas-Fermi model of Resta[233]. In practice, this corresponds to multiplying the nanocrystal dielectric constant by a function that varies smoothly over $0.1 \leq f(|\mathbf{r}_1 - \mathbf{r}_2|) \leq 1$, in the range $0 \leq r \leq r_0$, where $r = |\mathbf{r}_1 - \mathbf{r}_2|$ is the electron-hole separation and r_0 is the screening radius. This leads to a dielectric constant of the form:

$$\epsilon(r, D) = \begin{cases} \epsilon_\infty(D) \frac{qr_0}{[\sinh(q(r_0 - r) + qr)]}, & \text{if } r < r_0 \\ \epsilon_\infty(D), & \text{if } r \geq r_0 \end{cases}, \tag{G.1}$$

where $q = (4\pi)^{1/2}(3\pi^2 n_0)^{1/6}$ is the Thomas-Fermi wave vector and $n_0 = 32/a_0^3$ is the valence electron density in a zincblende structure. The short-range variation in the dielectric constant, defined by Equation (G.1), is shown in Figure G.8 as a function of electron-hole separation, for several nanocrystal diameters. The screening radius is determined by satisfying the condition $\sinh(qr_0)/(qr_0) = \epsilon_\infty(D)$ and is found to vary from 2.8 Å to 2.95 Å as the nanocrystal diameter increases from 2 nm to 6 nm.

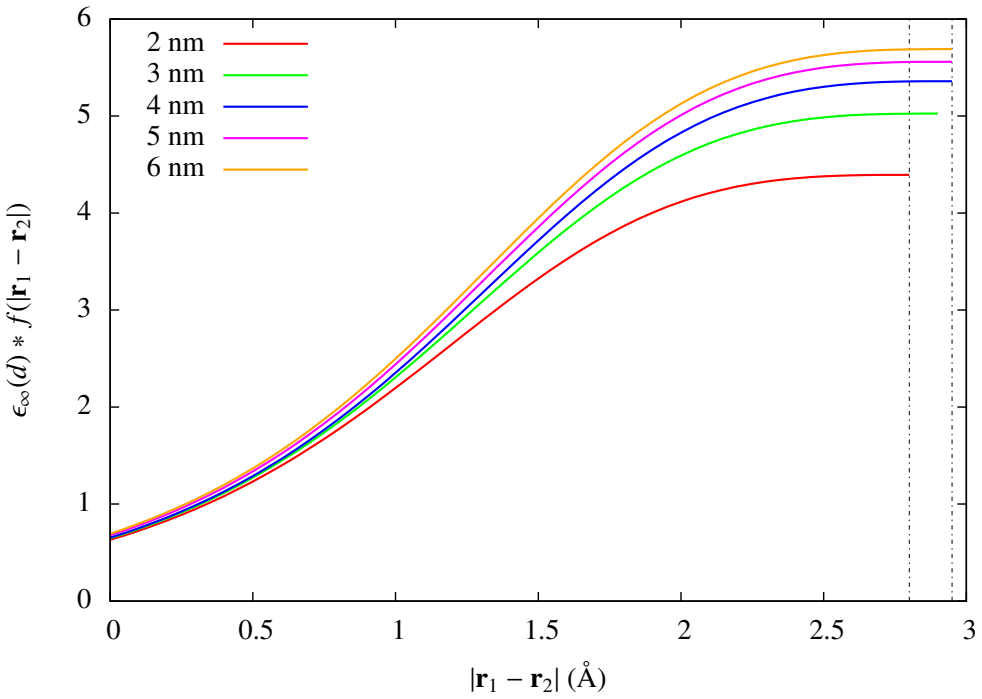

Figure G.8: Nanocrystal dielectric constant, given by Equation (G.1), as a function of electron-hole separation. The dashed, black lines correspond to the values of r_0 for nanocrystals with diameters of 2 nm and 6 nm.

Upon incorporation of separation dependence in the dielectric constant, one would need to compute an additional set of Coulomb-like and exchange-like orbital integrals, given by Equations (7.11) and (7.12), for which the screening is now explicitly included. It would then be straightforward to incorporate the changes into our BSE implementation, distinguishing between screened and unscreened integrals in the definition of the kernel, Equation (7.13). This was not included in the calculations presented in Chapter 10 due to time constraints, and would form the next step in improving the description of the nanocrystal dielectric function.

The Dielectric Environment

We model our nanocrystal in a vacuum, however in reality, the system is coated in ligands and suspended in a solvent. The environment in which the nanocrystal is suspended will therefore have a dielectric constant that differs from that of the nanocrystal interior. In principle, this should be accounted for in all orbital integrals

involving surface atoms, which would require us to compute another set of Coulomb-like and exchange like-integrals, defined by Equations (7.11) and (7.12), in addition to those described in the prior discussion. One would also need to consider the effect of the dielectric environment on the screening of the monopole interaction between two orbitals centred on interior and surface atoms, respectively.

We suggest that this could be accounted for in an approximate way by taking some average of the nanocrystal dielectric constant and the dielectric constant of the environment, both in the explicitly calculated orbital integrals and for those approximated with the monopole term. Although this is physically motivated, we believe that this makes the treatment of dielectric screening unnecessarily complicated given the uncertainty in the average nanocrystal dielectric constant predicted by the modified Penn model, and the experimental uncertainty associated with the value of the environmental dielectric constant. Hence it was not considered in the calculations presented in Chapter 10.

In general, we expect that consideration of the dielectric environment may lead to a slight increase in dielectric screening, which will consequently reduce the exciton binding energies presented in Chapter 10. We suggest that a quantum mechanical treatment of dielectric screening would therefore be an interesting area of study for future work.

G.4 Optical Gap as a Function of Nanoplatelet Thickness

Only two prior studies on the optical properties of CdSe nanoplatelets have been carried out in the literature using an atomistic model: one using tight-binding[95] and one using DFT[96]. The latter focuses on accurate self-energy corrections which are beyond the scope of this thesis. In the tight-binding binding study, Benchamekh and coworkers use an $sp^3d^5s^*$ tight-binding model including spin-orbit coupling, to

compute the independent-particle properties[95]. Electron and hole self-energies are treated classically, whilst exciton binding energies are computed using an effective mass formalism. This study therefore provides useful, first-order approximations for quasi-particle and exciton energies and how they scale as a function of thickness.

A direct comparison of our results with those of Benchamekh and coworkers is unfortunately hampered by their significantly different choice of bulk bang gap and periodic in-plane boundary conditions. At T=0 K, they fit to a bulk band gap of 1.76 eV, whereas our bulk band gap is fit to 1.9 eV. This leads to a systematic difference in their band gap dependence on nanoplatelet thickness with respective to ours. Consequently, Benchamekh and coworkers find good agreement with experiment by reducing the thicknesses assigned to measured optical gaps by one monolayer, whereas we find reasonable agreement with a reduction of two monolayers.

Which is correct is debatable. While it is possible that our parameterisation overestimates the bulk band gap, their choice of 1.76 eV seems too small when viewed in context with reported values[113; 116] (also see Table 6.2 in Chapter6). If we take a median bulk band gap of 1.83 eV[116] then the uncertainties in the parameterisations are comparable. One would expect that the use of a smaller bulk band gap would, however, lead to a reduction in the tight-binding band gap of the nanostructure, which is defined as the bulk band gap plus the confinement energies of the lowest electron and hole states.

We treat surface passivation in the same way as Benchamekh and coworkers, utilising a passivating parameter of 15 eV, while Benchamekh and coworkers use a similar value of 20 eV. We therefore assume that the difference in the predicted nanoplatelet band gaps must be due to their use of in-plane periodicity, in contrast to our finite simulations. However one would also expect the band gap to contract as a consequence of utilising periodic, in-plane boundary conditions, as this leads to

platelets with infinite lateral dimensions. As such, it is unclear as to what exactly causes Benchamekh and coworkers' model to produce systematically larger optical gaps in relation to ours.

The uncertainty regarding which is more accurate is compounded by differing suggestions in the literature regarding the amount by which the experimental thicknesses were initially overestimated. Assignments of thickness were initially made using 8-band $\mathbf{k} \cdot \mathbf{p}$ calculations[72], however later observations made using TEM revealed a systematic discrepancy between theory and experiment. High angle annular dark field STEM measurements made by Malher and coworkers suggest that theory had overestimated the nanoplatelet thicknesses by two monolayers[202], however this is contested by the group of Achtstein, who suggest that an overestimation of one monolayer is more consistent with their TEM measurements[87]. Our results are more consistent with Mauler and corworkers' assertion, which appears to be the consensus in the literature[75; 79; 80; 202; 205]. As a result, all experimental work from 2012 onwards should not require any adjustment in the assignments made to the nanoplatelet thickness (unless the group of Achtstein is being cited).

In Figure G.9 we compare Benchamekh and coworkers' optical gaps with our own calculations. We have also included experimental data with a systematic shift of one monolayer (solid squares/blue line) and two monolayers (hollow squares/dashed, blue line). Benchamekh and coworkers' results show strong agreement with experimental data (-1 ML). It is likely that this strong agreement with experiment is maximised through their choice of dielectric constant for the external medium, which could take one of several values. Our TB+BSE calculations do not yield quite as good agreement with experiment (- 2 ML), however our many-body calculations contain no empirical parameters.

Agreement between experiment and our BSE calculations can be improved in two

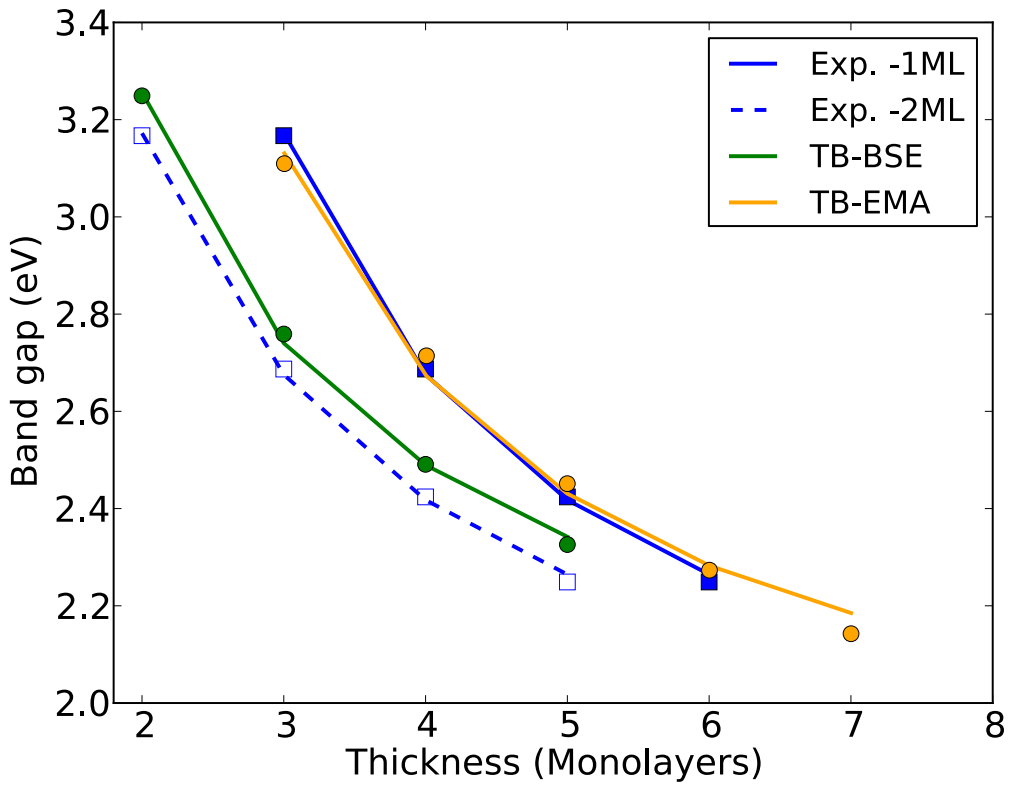

Figure G.9: Optical gap as a function of thickness for CdSe nanoplatelets. The tight-binding + effective mass results of Benchamekh and coworkers are plotted in yellow[95] whereas our tight-binding + BSE results are plotted in green. Two sets of experimental results with systematic reductions in their monolayer assignments, are given in blue. We note that from the year 2012 onwards, the open squares represent the adopted assignment of thicknesses for the optical gaps. The parameters for the lines of best-fit are given in Table G.5.

ways: Simulating nanoplatelets with larger, more realistic lateral dimensions and improving our description of dielectric screening. These are both discussed in more detail in the main text of Chapter10.

G.5 Best-Fit Parameters to Many-body Data

G.5.1 Fit Parameters for Nanocrystal Data

Table G.1 contains the best-fit parameters to the data in Figures 10.8 and 10.10, describing the dependence of the optical gap on nanocrystal diameter. This data is fit with Equation (10.3).

Data	a	b	c	σ_a	σ_b	σ_c
TB-CIS	0.00167	-0.0212	0.760	6.88×10^{-5}	4.83×10^{-3}	8.01×10^{-2}
BSE $\epsilon = 6.2$	0.002	-0.0416	0.859	8.47×10^{-5}	4.83×10^{-3}	$6.54 \times 1o^{-2}$
BSE $\epsilon = \epsilon(D)$	0.00213	-0.0450	0.986	9.09×10^{-5}	5.24×10^{-3}	7.15×10^{-2}

Table G.1: Parameters and standard deviations for the lines of best-fit plotted in Figures 10.8 and 10.10.

Table G.2 contains the best-fit parameters to the data in Figure 10.11, describing the dependence of the exciton binding energy on nanocrystal diameter. The data was fit to the equation, $E_X = a/\epsilon d^b$, where (a, b) are parameters and ϵ was either a constant or a function given by Equation (10.2).

Data	a	b	σ_a	σ_b
TB-CIS	3.97×10^4	0.973	4.18×10^3	2.97×10^{-2}
BSE $\epsilon = 6.2$	6.02×10^3	0.556	4.09×10^2	1.94×10^{-2}
BSE $\epsilon = \epsilon(D)$	1.31×10^4	0.744	3.90×10^2	8.79×10^{-3}

Table G.2: Parameters and standard deviations for the lines of best-fit plotted in Figure 10.11. The fits were performed on data given in meV.

Table G.3 contains the best-fit parameters to the experimental data, tight-binding data and our BSE calculations giving the optical gap dependence on nanocrystal diameter. All tight-binding data includes some approximation for the binding energy of the lowest exciton state. Functions defined with Equation (10.3) and the parameters in Table G.3 are shown in Figure 10.13.

Data	a	b	c	σ_a	σ_b	σ_c
Experiment	1.94×10^{-3}	-0.0322	0.87	4.81×10^{-4}	0.023	0.258
Tight-binding	1.23×10^{-3}	3.93×10^{-3}	0.359	5.55×10^{-4}	0.0284	0.343
BSE	2.13×10^{-3}	-0.045	0.986	9.09×10^{-5}	5.24×10^{-3}	0.0715

Table G.3: Parameters and standard deviations for the lines of best-fit plotted in Figures 10.13 and G.7. All fits were done using $E_{g,\text{bulk}} = 1.8$.

G.5.2 Fit Parameters for Nanoplatelet Data

Table G.4 contains best-fit parameters for the variation in the calculated nanoplatelet optical gap as a function of lateral dimensions. The parameters are used in Equation 10.3 to define the line of best-fit shown in Figure 11.2.

Data	a	b	c	σ_a	σ_b	σ_c
BSE	0.278	0.165	0.626	0.0299	0.153	0.167

Table G.4: Parameters and standard deviations for the lines of best-fit plotted in Figure 11.2.

Table G.5 contains the best-fit parameters to the data given in Figure G.9 above. The dependence of the nanoplatelet optical gap on thickness is fit with Equation (9.2).

Data	a	σ_a	b	σ_b
Experimental (- 1 ML)	7.64	0.359	1.56	0.0363
Experimental (- 2 ML)	3.07	0.152	1.16	0.0504
TB-EMA	6.67	0.717	1.47	0.0802
TB+BSE	3.07	0.0906	1.079	0.0295

Table G.5: Parameters and standard deviations for the lines of best-fit plotted in Figure G.9.

Table G.6 compares the ratio of surface atoms to total atoms for CdSe nanocrystals and nanoplatelets of varying dimensions.

Thickness (nm (ML))	$N^s_{\text{atoms}}/N_{\text{atoms}}(3\,s.f.)$	Diameter (nm)	$N^s_{\text{atoms}}/N_{\text{atoms}}(3\,s.f.)$
0.61 (2)	0.447	2	0.478
0.91 (3)	0.343	3	0.368
1.21 (4)	0.286	4	0.272
1.51 (5)	0.249	5	0.221
1.82 (6)	0.224	6	0.188

Table G.6: Surface to volume ratio for nanoplatelets (planar areas of 49 nm^2) and nanocrystals.

Bibliography

[1] Bawendi, M. G., Steigerwald, M. L. & Brus, L. E. The quantum mechanics of larger semiconductor clusters ("quantum dots"). *Ann. Rev. Phys. Chem.* **41**, 477–496 (1990).

[2] Ekimov, A. & Onushchenko, A., AA Tzehomskii. *Sov. Phys. Chem. Glass* **6**, 511–512 (1980).

[3] Henglein, A. Photo-degradation and fluorescence of colloidal cadmium sulfide in aqueous solution. *Berichte der Bunsengesellschaft für physikalische Chemie* **86**, 301–305 (1982).

[4] Wannier, G. H. The structure of electronic excitation levels in insulating crystals. *Phys. Rev* **52**, 191 (1937).

[5] Delerue, C., Lannoo, M. & Allan, G. Concept of dielectric constant for nanosized systems. *Phys. Rev. B* **68**, 115411 (2003).

[6] Cartoixa, X. & Wang, L.-W. Microscopic dielectric response functions in semiconductor quantum dots. *Phys. Rev. Lett.* **94**, 236804 (2005).

[7] Meulenberg, R. W. *et al.* Determination of the exciton binding energy in CdSe quantum dots. *ACS Nano* **3**, 325–330 (2009).

[8] Kovalenko, M. V. *et al.* Prospects of nanoscience with nanocrystals. *ACS Nano* **9**, 1012–1057 (2015).

[9] Bawendi, M., Kortan, A., Steigerwald, M. & Brus, L. X-ray structural characterization of larger CdSe semiconductor clusters. *J. Chem. Phys.* **91**, 7282–7290 (1989).

[10] Yang, Y. A., Wu, H., Williams, K. R. & Cao, Y. C. Synthesis of CdSe and CdTe nanocrystals without precursor injection. *Angew. Chem.* **117**, 6870–6873 (2005).

[11] Murray, C., Norris, D. J. & Bawendi, M. G. Synthesis and characterization of nearly monodisperse CdE (E= Sulfur, Selenium, Tellurium) semiconductor nanocrystallites. *J. Am. Chem. Soc.* **115**, 8706–8715 (1993).

[12] Medintz, I. L., Uyeda, H. T., Goldman, E. R. & Mattoussi, H. Quantum dot bioconjugates for imaging, labelling and sensing. *Nat. Mater* **4**, 435–446 (2005).

[13] Lo, S. S., Mirkovic, T., Chuang, C.-H., Burda, C. & Scholes, G. D. Emergent properties resulting from type-II band alignment in semiconductor nanoheterostructures. *Adv. Mater.* **23**, 180–197 (2011).

[14] Rogach, A. L. *et al.* Light-emitting diodes with semiconductor nanocrystals. *Angew. Chem. Int. Ed.* **47**, 6538–6549 (2008).

[15] Lee, J.-S., Kovalenko, M. V., Huang, J., Chung, D. S. & Talapin, D. V. Band-like transport, high electron mobility and high photoconductivity in all-inorganic nanocrystal arrays. *Nat. Nanotechnol.* **6**, 348–352 (2011).

[16] Kamat, P. V. Quantum dot solar cells. The next big thing in photovoltaics. *J. Phys. Chem. Lett.* **4**, 908–918 (2013).

[17] Saran, R. & Curry, R. J. Lead sulphide nanocrystal photodetector technologies. *Nat. Photon* **10**, 81–92 (2016).

[18] Lhuillier, E. *et al.* Two-dimensional colloidal metal chalcogenides semiconductors: Synthesis, spectroscopy, and applications. *Acc. Chem. Res.* (2015).

[19] Norris, D. & Bawendi, M. Structure in the lowest absorption feature of CdSe quantum dots. *J. Chem. Phys* **103**, 5260–5268 (1995).

[20] Norris, D., Efros, A. L., Rosen, M. & Bawendi, M. Size dependence of exciton fine structure in CdSe quantum dots. *Phys. Rev. B* **53**, 16347 (1996).

[21] Norris, D. & Bawendi, M. Measurement and assignment of the size-dependent optical spectrum in CdSe quantum dots. *Phys. Rev. B* **53**, 16338 (1996).

[22] Efros, A. L. *et al.* Band-edge exciton in quantum dots of semiconductors with a degenerate valence band: Dark and bright exciton states. *Phys. Rev. B* **54**, 4843 (1996).

[23] Franceschetti, A., Fu, H., Wang, L. & Zunger, A. Many-body pseudopotential theory of excitons in InP and CdSe quantum dots. *Phys. Rev. B* **60**, 1819 (1999).

[24] Lee, S., Jönsson, L., Wilkins, J. W., Bryant, G. W. & Klimeck, G. Electron-hole correlations in semiconductor quantum dots with tight-binding wave functions. *Phys. Rev. B* **63**, 195318 (2001).

[25] Chhowalla, M. *et al.* The chemistry of two-dimensional layered transition metal dichalcogenide nanosheets. *Nat. Chem.* **5**, 263–275 (2013).

[26] Bertrand, G. H., Polovitsyn, A., Christodoulou, S., Khan, A. H. & Moreels, I. Shape control of zincblende CdSe nanoplatelets. *Chem. Commun* (2016).

[27] Davies, J. H. *The physics of low-dimensional semiconductors: An introduction* (Cambridge university press, 1997).

[28] Pidgeon, C. R. & Brown, R. Interband magneto-absorption and faraday rotation in InSb. *Phys. Rev.* **146**, 575 (1966).

[29] Zitouni, O., Boujdaria, K. & Bouchriha, H. Band parameters for GaAs and Si in the 24-k·p model. *Semicond. Sci. Technol.* **20**, 908 (2005).

[30] Tomić, S. & Vukmirović, N. Symmetry reduction in multiband hamiltonians for semiconductor quantum dots: The role of interfaces and higher energy bands. *J. Appl. Phys.* **110**, 053710 (2011).

[31] Bester, G. Electronic excitations in nanostructures: An empirical pseudopotential based approach. *J. Phys. Condens. Matter.* **21**, 023202 (2009).

[32] Tomov, S., Langou, J., Canning, A., Wang, L.-W. & Dongarra, J. Comparison of nonlinear conjugate-gradient methods for computing the electronic properties of nanostructure architectures. In *ICCS*, 317–325 (Springer, 2005).

[33] Harrison, W. A. *Electronic Structure and the Properties of Solids* (Dover Books, 1989).

[34] Vogl, P., Hasjalmarson, H. P. & Dow, J. D. A semi-empirical tight-binding theory of the electronic structure of semiconductors. *J. Phys. Chem. Solids* **44**, 365–378 (1983).

[35] Fonseca, J. E. *et al.* Efficient and realistic device modeling from atomic detail to the nanoscale. *J. Comput. Electron.* **12**, 592–600 (2013).

[36] Hedin, L. New method for calculating the one-particle green's function with application to the electron-gas problem. *Phys. Rev.* **139**, A796 (1965).

[37] Hedin, L. & Lundqvist, S. Solid state physics, vol. 23. *Academic, New York* (1969).

[38] Strinati, G. Application of the greens functions method to the study of the optical properties of semiconductors. *La Rivista del Nuovo Cimento* **11**, 1–86 (1988).

[39] Leng, X., Jin, F., Wei, M. & Ma, Y. *GW* method and Bethe-Salpeter equation for calculating electronic excitations. *Wiley Interdiscip Rev Comput Mol Sci.* **6**, 532–550 (2016). URL `http://dx.doi.org/10.1002/wcms.1265`.

[40] Hirose, D., Noguchi, Y. & Sugino, O. All-electron $GW+$ Bethe-Salpeter calculations on small molecules. *Phys. Rev. B* **91**, 205111 (2015).

[41] Govoni, M. & Galli, G. Large scale *GW* calculations. *J. Chem. Theory Comput.* **11**, 2680–2696 (2015).

[42] Gilmore, K. *et al.* Efficient implementation of core-excitation Bethe–Salpeter equation calculations. *Comput. Phys. Commun.* **197**, 109–117 (2015).

[43] Duchemin, I., Deutsch, T. & Blase, X. Short-range to long-range charge-transfer excitations in the zincbacteriochlorin-bacteriochlorin complex: A Bethe-Salpeter study. *Phys. Rev. Lett.* **109**, 167801 (2012).

[44] Duchemin, I. & Blase, X. Resonant hot charge-transfer excitations in fullerene-porphyrin complexes: Many-body Bethe-Salpeter study. *Phys. Rev. B* **87**, 245412 (2013).

[45] Yin, H., Ma, Y., Mu, J., Liu, C. & Rohlfing, M. Charge-transfer excited states in aqueous DNA: Insights from many-body greens function theory. *Phys. Rev. Lett.* **112**, 228301 (2014).

[46] Prendergast, D. & Louie, S. G. Bloch-state-based interpolation: An efficient generalization of the shirley approach to interpolating electronic structure. *Phys. Rev. B* **80**, 235126 (2009).

[47] Boulanger, P., Jacquemin, D., Duchemin, I. & Blase, X. Fast and accurate electronic excitations in cyanines with the many-body Bethe-Salpeter approach. *J. Chem. Theory Comput.* **10**, 1212–1218 (2014).

[48] Ljungberg, M. P., Koval, P., Ferrari, F., Foerster, D. & Sanchez-Portal, D. Cubic-scaling iterative solution of the Bethe-Salpeter equation for finite systems. *Phys. Rev. B* **92**, 075422 (2015).

[49] Bruneval, F. & Gonze, X. Accurate *GW* self-energies in a plane-wave basis using only a few empty states: Towards large systems. *Phys. Rev. B* **78**, 085125 (2008).

[50] Lambert, H. & Giustino, F. Ab initio Sternheimer-GW method for quasiparticle calculations using plane waves. *Phys. Rev. B* **88**, 075117 (2013).

[51] Wang, L.-W., Califano, M., Zunger, A. & Franceschetti, A. Pseudopotential theory of Auger processes in CdSe quantum dots. *Phys. Rev. Lett* **91**, 056404 (2003).

[52] Bester, G. & Zunger, A. Cylindrically shaped zinc-blende semiconductor quantum dots do not have cylindrical symmetry: Atomistic symmetry, atomic relaxation, and piezoelectric effects. *Phys. Rev. B* **71**, 045318 (2005).

[53] Califano, M., Franceschetti, A. & Zunger, A. Temperature dependence of excitonic radiative decay in CdSe quantum dots: The role of surface hole traps. *Nano Lett.* **5**, 2360–2364 (2005).

[54] Sewall, S. L., Franceschetti, A., Cooney, R. R., Zunger, A. & Kambhampati, P. Direct observation of the structure of band-edge biexcitons in colloidal semiconductor CdSe quantum dots. *Phys. Rev. B* **80**, 081310 (2009).

[55] Onida, G., Reining, L. & Rubio, A. Electronic excitations: Density-functional versus many-body greens-function approaches. *Rev. Mod. Phys.* **74**, 601 (2002).

[56] Dreuw, A. & Head-Gordon, M. Single-reference ab initio methods for the calculation of excited states of large molecules. *Chem. Rev.* **105**, 4009–4037 (2005).

[57] Peng, X. *et al.* Shape control of CdSe nanocrystals. *Nature* **404**, 59–61 (2000).

[58] Manna, L., Scher, E. C. & Alivisatos, A. P. Synthesis of soluble and processable rod-, arrow-, teardrop-, and tetrapod-shaped CdSe nanocrystals. *J. Am. Chem. Soc.* **122**, 12700–12706 (2000).

[59] Murray, C. B., Kagan, C. & Bawendi, M. Synthesis and characterization of monodisperse nanocrystals and close-packed nanocrystal assemblies. *Ann. Rev. Mater. Sci* **30**, 545–610 (2000).

[60] Wang, W., Banerjee, S., Jia, S., Steigerwald, M. L. & Herman, I. P. Ligand control of growth, morphology, and capping structure of colloidal CdSe nanorods. *Chem. Mater* **19**, 2573–2580 (2007).

[61] Boles, M. A. & Talapin, D. V. Self-assembly of tetrahedral CdSe nanocrystals: Effective "patchiness" via anisotropic steric interaction. *J. Am. Chem. Soc* **136**, 5868–5871 (2014).

[62] Talapin, D. V. *et al.* Seeded growth of highly luminescent CdSe/CdS nanoheterostructures with rod and tetrapod morphologies. *Nano. Lett* **7**, 2951–2959 (2007).

[63] Joo, J., Son, J. S., Kwon, S. G., Yu, J. H. & Hyeon, T. Low-temperature solution-phase synthesis of quantum well structured CdSe nanoribbons. *J. Am. Chem. Soc.* **128**, 5632–5633 (2006).

[64] Ahn, J.-H. *et al.* Heterogeneous three-dimensional electronics by use of printed semiconductor nanomaterials. *Science* **314**, 1754–1757 (2006).

[65] Son, J. S. *et al.* Colloidal synthesis of ultrathin two-dimensional semiconductor nanocrystals. *Adv. Mater.* **23**, 3214–3219 (2011).

[66] Ithurria, S. & Dubertret, B. Quasi 2D colloidal CdSe platelets with thicknesses controlled at the atomic level. *J. Am. Chem. Soc.* **130**, 16504–16505 (2008).

[67] Tessier, M. D., Javaux, C., Maksimovic, I., Loriette, V. & Dubertret, B. Spectroscopy of single CdSe nanoplatelets. *ACS Nano.* **6**, 6751–6758 (2012).

[68] Son, J. S. *et al.* Large-scale soft colloidal template synthesis of 1.4 nm thick CdSe nanosheets. *Angew. Chem.* **121**, 6993–6996 (2009).

[69] Ithurria, S., Bousquet, G. & Dubertret, B. Continuous transition from 3d to 1D confinement observed during the formation of CdSe nanoplatelets. *J. Am. Chem. Soc.* **133**, 3070–3077 (2011).

[70] Bouet, C. *et al.* Two-dimensional growth of CdSe nanocrystals, from nanoplatelets to nanosheets. *Chem. Mater.* **25**, 639–645 (2013).

[71] Weisbuch, C. Applications of MBE-grown heterostructures and quantum wells in fundamental research and in advanced semiconductor devices. *J. Cryst. Growth* **127**, 742–751 (1993).

[72] Ithurria, S. *et al.* Colloidal nanoplatelets with two-dimensional electronic structure. *Nat. Mater.* **10**, 936–941 (2011).

[73] Tessier, M. D. *et al.* Spectroscopy of colloidal semiconductor core/shell nanoplatelets with high quantum yield. *Nano. Lett.* **13**, 3321–3328 (2013).

[74] Peng, X., Schlamp, M. C., Kadavanich, A. V. & Alivisatos, A. Epitaxial growth of highly luminescent CdSe/CdS core/shell nanocrystals with photostability and electronic accessibility. *J. Am. Chem. Soc.* **119**, 7019–7029 (1997).

[75] Pelton, M., Ithurria, S., Schaller, R. D., Dolzhnikov, D. S. & Talapin, D. V. Carrier cooling in colloidal quantum wells. *Nano. Lett.* **12**, 6158–6163 (2012).

[76] Sippel, P. *et al.* Femtosecond cooling of hot electrons in CdSe quantum-well platelets. *Nano. Lett* **15**, 2409–2416 (2015).

[77] Baghani, E., OLeary, S. K., Fedin, I., Talapin, D. V. & Pelton, M. Auger-limited carrier recombination and relaxation in CdSe colloidal quantum wells. *J. Phys. Chem. Lett.* **6**, 1032–1036 (2015).

[78] Htoon, H., Hollingsworth, J., Dickerson, R. & Klimov, V. Effect of zero-to one-dimensional transformation on multiparticle auger recombination in semiconductor quantum rods. *Phys. Rev. Lett.* **91**, 227401 (2003).

[79] Kunneman, L. T. *et al.* Bimolecular Auger recombination of electron–hole pairs in two-dimensional CdSe and CdSe/CdZnS core/shell nanoplatelets. *J. Phys. Chem. Lett.* **4**, 3574–3578 (2013).

[80] She, C. *et al.* Low-threshold stimulated emission using colloidal quantum wells. *Nano. Lett.* (2014).

[81] Hendry, E. *et al.* Direct observation of electron-to-hole energy transfer in CdSe quantum dots. *Phys. Rev. Lett* **96**, 057408 (2006).

[82] Cooney, R. R. *et al.* Unified picture of electron and hole relaxation pathways in semiconductor quantum dots. *Phys. Rev. B* **75**, 245311 (2007).

[83] Efros, A. L., Kharchenko, V. & Rosen, M. Breaking the phonon bottleneck in nanometer quantum dots: Role of Auger-like processes. *Solid State Commun.* **93**, 281–284 (1995).

[84] Taguchi, S., Saruyama, M., Teranishi, T. & Kanemitsu, Y. Quantized Auger recombination of biexcitons in CdSe nanorods studied by time-resolved photoluminescence and transient-absorption spectroscopy. *Phys. Rev. B* **83**, 155324 (2011).

[85] Kunneman, L. T. *et al.* Nature and decay pathways of photoexcited states in CdSe and CdSe/CdS nanoplatelets. *Nano. Lett* **14**, 7039–7045 (2014).

[86] Cragg, G. E. & Efros, A. L. Suppression of Auger processes in confined structures. *Nano. Lett.* **10**, 313–317 (2009).

[87] Achtstein, A. W. *et al.* Electronic structure and exciton–phonon interaction in two-dimensional colloidal CdSe nanosheets. *Nano. Lett.* **12**, 3151–3157 (2012).

[88] Gomez, D. E., van Embden, J., Mulvaney, P., Fernée, M. J. & Rubinsztein-Dunlop, H. Exciton-trion transitions in single CdSe–CdS core–shell nanocrystals. *ACS. Nano.* **3**, 2281–2287 (2009).

[89] de Mello Donegá, C., Bode, M. & Meijerink, A. Size-and temperature-dependence of exciton lifetimes in CdSe quantum dots. *Phys. Rev. B* **74**, 085320 (2006).

[90] Nirmal, M., Murray, C. & Bawendi, M. Fluorescence-line narrowing in CdSe quantum dots: Surface localization of the photogenerated exciton. *Phys. Rev. B* **50**, 2293 (1994).

[91] Naeem, A. *et al.* Giant exciton oscillator strength and radiatively limited dephasing in two-dimensional platelets. *Phys. Rev. B* **91**, 121302 (2015).

[92] Feldmann, J. *et al.* Linewidth dependence of radiative exciton lifetimes in quantum wells. *Phys. Rev. Lett.* **59**, 2337 (1987).

[93] Cassette, E., Pensack, R. D., Mahler, B. & Scholes, G. D. Room-temperature exciton coherence and dephasing in two-dimensional nanostructures. *Nat. Commun.* **6** (2015).

[94] Scholes, G. D. & Rumbles, G. Excitons in nanoscale systems. *Nat. Mater* **5**, 683–696 (2006).

[95] Benchamekh, R. *et al.* Tight-binding calculations of image-charge effects in colloidal nanoscale platelets of CdSe. *Phys. Rev. B* **89**, 035307 (2014).

[96] Even, J., Pedesseau, L. & Kepenekian, M. Electronic surface states and dielectric self-energy profiles in colloidal nanoscale platelets of CdSe. *Phys. Chem. Chem. Phys.* **16**, 25182–25190 (2014).

[97] Grim, J. Q. *et al.* Continuous-wave biexciton lasing at room temperature using solution-processed quantum wells. *Nat. Nano.* (2014).

[98] Papaconstantopoulos, D. & Mehl, M. The Slater–Koster tight-binding method: A computationally efficient and accurate approach. *J. Phys. Condens. Matter* **15**, R413 (2003).

[99] Lippens, P. & Lannoo, M. *Phys. Rev. B* **39**, 10935 (1989).

[100] Lippens, P. & Lannoo, M. *Phys. Rev. B* **41**, 6079 (1990).

[101] Lippens, P. & Lannoo, M. *Mater. Sci. Eng. B.* **9**, 485–487 (1991).

[102] Albe, V., Jouanin, C. & Bertho, D. Confinement and shape effects on the optical spectra of small CdSe nanocrystals. *Phys. Rev. B* **58**, 4713 (1998).

[103] Chamarro, M., Gourdon, C., Lavallard, P., Lublinskaya, O. & Ekimov, A. Enhancement of electron-hole exchange interaction in CdSe nanocrystals: A quantum confinement effect. *Phys. Rev. B* **53**, 1336 (1996).

[104] Diaz, J. & Planelles, J. Theoretical characterization of triangular CdS nanocrystals: A tight-binding approach. *Langmuir* **20**, 11278–11284 (2004).

[105] Diaz, J., Planelles, J., Bryant, G. & Aizpurua, J. Tight-binding method and multiband effective mass theory applied to CdS nanocrystals: Single-particle effects and optical spectra fine structure. *J. Phys. Chem. B* **108**, 17800–17804 (2004).

[106] Sapra, S. & Sarma, D. Evolution of the electronic structure with size in II-VI semiconductor nanocrystals. *Phys. Rev. B* **69**, 125304 (2004).

[107] Pérez-Conde, J. & Bhattacharjee, A. Exciton states and optical properties of CdSe nanocrystals. *Phys. Rev. B* **63**, 245318 (2001).

[108] Varshni, Y. Temperature dependence of the energy gap in semiconductors. *Physica* **34**, 149–154 (1967).

[109] Chia, C. *et al.* Temperature dependence of excitonic emission in cubic CdSe thin film. *JOL* **128**, 123–128 (2008).

[110] Rogach, A. L., Kornowski, A., Gao, M., Eychmüller, A. & Weller, H. Synthesis and characterization of a size series of extremely small thiol-stabilized CdSe nanocrystals. *J. Phys. Chem. B* **103**, 3065–3069 (1999).

[111] Dabbousi, B., Murray, C., Rubner, M. & Bawendi, M. Langmuir-blodgett manipulation of size-selected CdSe nanocrystallites. *Chem. Mater* **6**, 216–219 (1994).

[112] Gorer, S. & Hodes, G. Quantum size effects in the study of chemical solution deposition mechanisms of semiconductor films. *J. Phys. Chem* **98**, 5338–5346 (1994).

[113] Karel Capek, R. *et al.* Optical properties of zincblende cadmium selenide quantum dots. *J. Phys. Chem. C* **114**, 6371–6376 (2010).

[114] Tolbert, S. H., Herhold, A. B., Johnson, C. S. & Alivisatos, A. Comparison of quantum confinement effects on the electronic absorption spectra of direct and indirect gap semiconductor nanocrystals. *Phys. Rev. Lett.* **73**, 3266 (1994).

[115] Kaneta, A. & Adachi, S. Photoreflectance study of hexagonal CdSe. *J. Phys. D: Appl. Phys.* **32**, 2337 (1999).

[116] Wang, L.-W. & Zunger, A. High-energy excitonic transitions in CdSe quantum dots. *J. Phys. Chem. B.* **102**, 6449–6454 (1998).

[117] Landolt-Bornstein, H., Axford, W., Aller, L. H. & Biermann, P. *Numerical Data and Functional Relationships in Science and Technology: Group VI: Astronomy Astrophysics and Space Research* (Springer-Verlag, 1982).

[118] Fu, H., Wang, L.-W. & Zunger, A. Response to comment on comparison of the k·p and the direct diagonalization approaches for describing the electronic structure of quantum dots [appl. phys. lett. 73, 1155 (1998)]. *Appl. Phys. Lett.* **73**, 1157–1158 (1998). URL `http://scitation.aip.org/content/aip/journal/apl/73/8/10.1063/1.122155`.

[119] Allan, G. & Delerue, C. Tight-binding calculations of the optical properties of hgte nanocrystals. *Phys. Rev. B* **86**, 165437 (2012).

[120] Puzder, A., Williamson, A., Gygi, F. & Galli, G. Self-healing of CdSe nanocrystals: First-principles calculations. *Phys. Rev. Lett.* **92**, 217401 (2004).

[121] Manna, L., Wang, L. W., Cingolani, R. & Alivisatos, A. P. First-principles modeling of unpassivated and surfactant-passivated bulk facets of wurtzite CdSe: A model system for studying the anisotropic growth of CdSe nanocrystals. *J. Phys. Chem. B* **109**, 6183–6192 (2005).

[122] Diaz, J. & Bryant, G. W. Electronic and optical fine structure of GaAs nanocrystals: The role of d orbitals in a tight-binding approach. *Phys. Rev. B* **73**, 075329 (2006).

[123] Martin, E., Delerue, C., Allan, G. & Lannoo, M. Theory of excitonic exchange splitting and optical stokes shift in silicon nanocrystallites: Application to porous silicon. *Phys. Rev. B* **50**, 18258 (1994).

[124] Hill, N. A. & Whaley, K. B. Two-particle calculation of excitonic effects in semiconductor nanocrystals. *Chem. Phys* **210**, 117–133 (1996).

[125] Leung, K. & Whaley, K. Electron-hole interactions in silicon nanocrystals. *Phys. Rev. B* **56**, 7455 (1997).

[126] Leung, K., Pokrant, S. & Whaley, K. B. Exciton fine structure in CdSe nanoclusters. *Phys. Rev. B* **57**, 12291 (1998).

[127] Díaz, J., Zieliński, M., Jaskólski, W. & Bryant, G. W. Tight-binding theory of ZnS/CdS nanoscale heterostructures: Role of strain and *d* orbitals. *Phys. Rev. B* **74**, 205309 (2006).

[128] Leung, K. & Whaley, K. Surface relaxation in CdSe nanocrystals. *J. Chem. Phys.* **110**, 11012–11022 (1999).

[129] Kuno, M., Lee, J., Dabbousi, B., Mikulec, F. & Bawendi, M. The band edge luminescence of surface modified CdSe nanocrystallites: Probing the luminescing state. *J. Chem. Phys.* **106**, 9869–9882 (1997).

[130] Díaz, J., Bryant, G. & Jaskólski, W. Optical fine structure of II-VI and III-V nanocrystals: The role of *d* orbitals in a tight-binding approach. *Phys. Status Solidi C* **3**, 3823–3826 (2006).

[131] Boykin, T. B., Klimeck, G., Bowen, R. C. & Lake, R. Effective-mass reproducibility of the nearest-neighbor sp^3s^* models: Analytic results. *Phys. Rev. B* **56**, 4102 (1997).

[132] Jancu, J.-M., Scholz, R., Beltram, F. & Bassani, F. Empirical $spds^*$ tight-binding calculation for cubic semiconductors: General method and material parameters. *Phys. Rev. B* **57**, 6493 (1998).

[133] Giustino, F. *Materials Modelling Using Density Functional Theory: Properties and Predictions* (Oxford University Press, 2014).

[134] Hartree, D. R. The wave mechanics of an atom with a non-Coulomb central field. Part I. Theory and methods. In *Mathematical Proceedings of the Cambridge Philosophical Society*, vol. 24, 89–110 (Cambridge Univ Press, 1928).

[135] Slater, J. C. Note on hartree's method. *Phys. Rev* **35**, 210 (1930).

[136] Kohn, W. & Sham, L. J. Self-consistent equations including exchange and correlation effects. *Phys. Rev.* **140**, A1133 (1965).

[137] Goedecker, S. Linear scaling electronic structure methods. *Rev. Mod. Phys.* **71**, 1085 (1999).

[138] Tran, F. & Blaha, P. Accurate band gaps of semiconductors and insulators with a semilocal exchange-correlation potential. *Phys. Rev. Lett.* **102**, 226401 (2009).

[139] Soler, J. M. *et al.* The siesta method for ab initio order-n materials simulation. *J. Phys. Condens. Matter* **14**, 2745 (2002).

[140] Cardona, M. & Peter, Y. Y. *Fundamentals of semiconductors* (Springer, 2005).

[141] Martin, R. M. *Electronic structure: Basic theory and practical methods* (Cambridge university press, 2004).

[142] Chadi, D. & Cohen, M. L. Tight-binding calculations of the valence bands of diamond and zincblende crystals. *Phys. Status Solidi B* **68**, 405–419 (1975).

[143] Slater, J. C. & Koster, G. F. Simplified LCAO method for the periodic potential problem. *Phys. Rev.* **94**, 1498 (1954).

[144] Lee, S. *et al.* Many-body levels of optically excited and multiply charged InAs nanocrystals modeled by semiempirical tight binding. *Phys. Rev. B* **66**, 235307 (2002).

[145] Schulz, S., Schumacher, S. & Czycholl, G. Tight-binding model for semiconductor quantum dots with a wurtzite crystal structure: From one-particle properties to Coulomb correlations and optical spectra. *Phys. Rev. B* **73**, 245327 (2006).

[146] Salpeter, E. & Bethe, H. A. A relativistic equation for bound-state problems. *Phys. Rev.* **84**, 1232 (1951).

[147] Strinati, G. Effects of dynamical screening on resonances at inner-shell thresholds in semiconductors. *Phys. Rev. B* **29**, 5718 (1984).

[148] Rohlfing, M. & Louie, S. G. Electron-hole excitations and optical spectra from first principles. *Phys. Rev B* **62**, 4927 (2000).

[149] Gatti, M. *Correlation effects in valence electron spectroscopy of transition metal oxides: Many-body perturbation theory and alternative approaches.* Ph.D. thesis, PhD thesis, École Polytechnique, Palaiseau (2007).

[150] Rohlfing, M. & Louie, S. G. Electron-hole excitations in semiconductors and insulators. *Phys. Rev. Lett.* **81**, 2312 (1998).

[151] Fetter, A. L. & Walecka, J. D. *Quantum theory of many-particle systems* (Courier Corporation, 2003).

[152] Sottile, F. *Response functions of semiconductors and insulators: From the Bethe-Salpeter equation to time-dependent density functional theory.* Ph.D. thesis, Ecole Polytechnique X (2003).

[153] Hanke, W. & Sham, L. Local-field and excitonic effects in the optical spectrum of a covalent crystal. *Phys. Rev. B* **12**, 4501 (1975).

[154] Hanke, W. & Sham, L. Many-particle effects in the optical spectrum of a semiconductor. *Phys. Rev. B* **21**, 4656 (1980).

[155] Albrecht, S., Reining, L., Del Sole, R. & Onida, G. Ab initio calculation of excitonic effects in the optical spectra of semiconductors. *Phys. Rev. Lett.* **80**, 4510 (1998).

[156] Benedict, L. X., Shirley, E. L. & Bohn, R. B. Optical absorption of insulators and the electron-hole interaction: An ab initio calculation. *Phys. Rev. Lett.* **80**, 4514 (1998).

[157] Benedict, L. X., Shirley, E. L. & Bohn, R. B. Theory of optical absorption in diamond, Si, Ge, and GaAs. *Phys. Rev. B* **57**, R9385 (1998).

[158] Bechstedt, F., Tenelsen, K., Adolph, B. & Del Sole, R. Compensation of dynamical quasiparticle and vertex corrections in optical spectra. *Phys. Rev. Lett.* **78**, 1528 (1997).

[159] Saad, Y. *Numerical methods for large eigenvalue problems*, vol. 158 (SIAM, 1992).

[160] Hübener, H. & Giustino, F. Linear optical response of finite systems using multishift linear system solvers. *J. Chem. Phys.* **141**, 044117 (2014).

[161] Brillouin-zone database on the Bilbao crystallographic server. *Acta Cryst* **A70** (2014).

[162] Haug, H. & Koch, S. W. *Quantum theory of the optical and electronic properties of semiconductors*, vol. 5 (World Scientific, 1990).

[163] Schulz, S. & Czycholl, G. Tight-binding model for semiconductor nanostructures. *Phys. Rev. B* **72**, 165317 (2005).

[164] Norris, D., Sacra, A., Murray, C. & Bawendi, M. Measurement of the size dependent hole spectrum in CdSe quantum dots. *Phys. Rev. Lett* **72**, 2612 (1994).

[165] Kim, Y. D. *et al.* Optical properties of zinc-blende CdSe and $Zn_xCd_{1-x}Se$ films grown on GaAs. *Phys. Rev. B* **49**, 7262–7270 (1994).

[166] Shan, W., Song, J., Luo, H. & Furdyna, J. Determination of the fundamental and split-off band gaps in zinc-blende CdSe by photomodulation spectroscopy. *Phys. Rev. B* **50**, 8012 (1994).

[167] Dietze, W. *Landolt-Bornstein: Numerical data and functional relationships in science and technology* (Springer, 1984).

[168] Beard, M. C., Turner, G. M. & Schmuttenmaer, C. A. Size-dependent photoconductivity in CdSe nanoparticles as measured by time-resolved terahertz spectroscopy. *Nano Lett.* **2**, 983–987 (2002).

[169] Anderson, E. *et al. LAPACK Users' Guide* (Society for Industrial and Applied Mathematics, Philadelphia, PA, 1999), third edn.

[170] Polizzi, E. Density-matrix-based algorithm for solving eigenvalue problems. *Phys. Rev. B* **79**, 115112 (2009).

[171] Trefethen, L. N. & Bau III, D. *Numerical linear algebra*, vol. 50 (Siam, 1997).

[172] Krämer, L., Di Napoli, E., Galgon, M., Lang, B. & Bientinesi, P. Dissecting the feast algorithm for generalized eigenproblems. *J. Comput. Appl. Math.* **244**, 1–9 (2013).

[173] Sankey, O. F. & Niklewski, D. J. Ab initio multicenter tight-binding model for molecular-dynamics simulations and other applications in covalent systems. *Phys. Rev. B* **40**, 3979 (1989).

[174] Sánchez-Portal, D., Artacho, E. & Soler, J. M. Analysis of atomic orbital basis sets from the projection of plane-wave results. *J. Phys. Condens. Matter* **8**, 3859 (1996).

[175] Hill, N. A. & Whaley, K. B. A theoretical study of the influence of the surface on the electronic structure of CdSe nanoclusters. *J. Chem. Phys.* **100**, 2831–2837 (1994).

[176] Korkusinski, M., Voznyy, O. & Hawrylak, P. Fine structure and size dependence of exciton and biexciton optical spectra in CdSe nanocrystals. *Phys. Rev. B* **82**, 245304 (2010).

[177] Lee, S., Oyafuso, F., von Allmen, P. & Klimeck, G. Boundary conditions for the electronic structure of finite-extent embedded semiconductor nanostructures. *Phys. Rev. B* **69**, 045316 (2004).

[178] Lee, S., Jonsson, L., Wilkins, J. W., Bryant, G. W. & Klimeck, G. Electron-hole correlations in semiconductor quantum dots with tight-binding wave functions. *arXiv:cond-mat/0011246* (2000).

[179] Trani, F., Ninno, D. & Iadonisi, G. Role of local fields in the optical properties of silicon nanocrystals using the tight binding approach. *Phys. Rev. B* **75**, 033312 (2007).

[180] Trani, F., Ninno, D. & Iadonisi, G. Tight-binding formulation of the dielectric response in semiconductor nanocrystals. *Phys. Rev. B* **76**, 085326 (2007).

[181] Giustino, F. & Pasquarello, A. Theory of atomic-scale dielectric permittivity at insulator interfaces. *Phys. Rev. B* **71**, 144104 (2005).

[182] Pedersen, T. G. Density-functional-based tight-binding calculation of excitons in conjugated polymers. *Phys. Rev. B* **69**, 075207 (2004).

[183] Zieliński, M., Korkusiński, M. & Hawrylak, P. Atomistic tight-binding theory of multiexciton complexes in a self-assembled InAs quantum dot. *Phys. Rev. B* **81**, 085301–1 (2010).

[184] Jackson, J. D. *Classical electrodynamics* (Wiley, 1999).

[185] Jacobs, D. A. A generalization of the conjugate-gradient method to solve complex systems. *IMA J. Numer. Anal.* **6**, 447–452 (1986).

[186] Xie, R.-H., Bryant, G. W., Lee, S. & Jaskólski, W. Electron-hole correlations and optical excitonic gaps in quantum-dot quantum wells: Tight-binding approach. *Phys. Rev. B* **65**, 235306 (2002).

[187] Bryant, G. W. & Jaskólski, W. Tight-binding theory of quantum-dot quantum wells: Single-particle effects and near-band-edge structure. *Phys. Rev. B* **67**, 205320 (2003).

[188] Brus, L. E. Electron-electron and electron-hole interactions in small semiconductor crystallites: The size dependence of the lowest excited electronic state. *J. Chem. Phys.* **80**, 4403–4409 (1984).

[189] Hollingsworth, J. A. Heterostructuring nanocrystal quantum dots toward intentional suppression of blinking and auger recombination. *Chem. Mater.* **25**, 1318–1331 (2013).

[190] Boykin, T. Private correspondence. Unpublished.

[191] Shevchik, N., Tejeda, J., Cardona, M. & Langer, D. Photoemission and density of valence states of the II–VI compounds. i. ZnTe, CdSe, CdTe, HgSe, and HgTe. *Phys. Status Solidi B* **59**, 87–100 (1973).

[192] Persson, C. & Zunger, A. $s-d$ coupling in zinc-blende semiconductors. *Phys. Rev. B* **68**, 073205 (2003).

[193] Richard, T., Lefebvre, P., Mathieu, H. & Allégre, J. Effects of finite spin-orbit splitting on optical properties of spherical semiconductor quantum dots. *Phys. Rev. B* **53**, 7287 (1996).

[194] Klimov, V. I. *Nanocrystal quantum dots* (CRC Press, 2010).

[195] Ekimov, A. *et al.* Absorption and intensity-dependent photoluminescence measurements on CdSe quantum dots: Assignment of the first electronic transitions. *JOSA B* **10**, 100–107 (1993).

[196] Groeneveld, E., Delerue, C., Allan, G., Niquet, Y.-M. & de Mello Donega, C. Size dependence of the exciton transitions in colloidal CdTe quantum dots. *J. Chem. Phys. C.* **116**, 23160–23167 (2012).

[197] Delerue, C. & Lannoo, M. *Nanostructures: Theory and modelling* (Springer Science & Business Media, 2004).

[198] Leatherdale, C., Woo, W.-K., Mikulec, F. & Bawendi, M. On the absorption cross section of CdSe nanocrystal quantum dots. *J. Phys. Chem. B.* **106**, 7619–7622 (2002).

[199] Kittel, C., McEuen, P. & McEuen, P. *Introduction to solid state physics*, vol. 8 (Wiley New York, 1976).

[200] Chen, O. *et al.* Surface-functionalization-dependent optical properties of II–VI semiconductor nanocrystals. *J.Am. Chem. Soc.* **133**, 17504–17512 (2011).

[201] Szemjonov, A. *et al.* Ligand-stabilized CdSe nanoplatelet hybrid structures with tailored geometric and electronic properties. new insights from theory. *RSC Advances* **4**, 55980–55989 (2014).

[202] Mahler, B., Nadal, B., Bouet, C., Patriarche, G. & Dubertret, B. *J. Am. Chem. Soc.* **134**, 18591–18598 (2012).

[203] Efros, A. L. & Rosen, M. The electronic structure of semiconductor nanocrystals 1. *An. Rev. Mater. Sci* **30**, 475–521 (2000).

[204] Abécassis, B., Tessier, M. D., Davidson, P. & Dubertret, B. Self-assembly of CdSe nanoplatelets into giant micrometer-scale needles emitting polarized light. *Nano Lett.* **14**, 710–715 (2014).

[205] Biadala, L. *et al.* Recombination dynamics of band edge excitons in quasi-two-dimensional CdSe nanoplatelets. *Nano. Lett.* **14**, 1134–1139 (2014).

[206] Bristow, A. D., Zhang, T., Siemens, M. E., Cundiff, S. T. & Mirin, R. Separating homogeneous and inhomogeneous line widths of heavy-and light-hole excitons in weakly disordered semiconductor quantum wells. *J. Phys. Chem. B.* **115**, 5365–5371 (2011).

[207] Yeltik, A. *et al.* Experimental determination of the absorption cross-section and molar extinction coefficient of colloidal CdSe nanoplatelets. *J. Phys. Chem C.* **119**, 26768–26775 (2015).

[208] Pedetti, S., Ithurria, S., Heuclin, H., Patriarche, G. & Dubertret, B. Type-II core/crown CdSe/CdTe semiconductor nanoplatelets. *J. Am. Chem. Soc.* (2014).

[209] Kelestemur, Y. *et al.* Type-II colloidal quantum wells: CdSe/CdTe core/crown heteronanoplatelets. *J. Phys. Chem. C* (2015).

[210] Yang, L., Deslippe, J., Park, C.-H., Cohen, M. L. & Louie, S. G. Excitonic effects on the optical response of graphene and bilayer graphene. *Phys. Rev. Lett.* **103**, 186802 (2009).

[211] Öğüt, S., Chelikowsky, J. R. & Louie, S. G. Quantum confinement and optical gaps in Si nanocrystals. *Phys. Rev. Lett.* **79**, 1770 (1997).

[212] Rabani, E., Baer, R. & Neuhauser, D. Time-dependent stochastic Bethe-Salpeter approach. *Phys. Rev. B* **91**, 235302 (2015).

[213] Zakharov, O., Rubio, A., Blase, X., Cohen, M. L. & Louie, S. G. Quasiparticle band structures of six II-VI compounds: ZnS, ZnSe, ZnTe, CdS, CdSe, and CdTe. *Phys. Rev. B* **50**, 10780 (1994).

[214] Bruneval, F. Exchange and correlation in the electronic structure of solids, from silicon to cuprous oxide: *GW* approximation and beyond. *PhD Thesis* (2005).

[215] Franceschetti, A., Wang, L., Fu, H. & Zunger, A. Short-range versus long-range electron-hole exchange interactions in semiconductor quantum dots. *Phys. Rev. B* **58**, R13367 (1998).

[216] Penn, D. R. Wave-number-dependent dielectric function of semiconductors. *Phys. Rev* **128**, 2093 (1962).

[217] Wang, L.-W. & Zunger, A. Dielectric constants of silicon quantum dots. *Phys. Rev. Lett.* **73**, 1039 (1994).

[218] Wang, L.-W. & Zunger, A. Pseudopotential calculations of nanoscale CdSe quantum dots. *Phys. Rev. B* **53**, 9579 (1996).

[219] Janowitz, C. *et al.* Dielectric function and critical points of cubic and hexagonal CdSe. *Phys. Rev. B* **50**, 2181 (1994).

[220] Gruning, M., Marini, A. & Gonze, X. Exciton-plasmon states in nanoscale materials: Breakdown of the Tamm-Dancoff approximation. *Nano Lett.* **9**, 2820–2824 (2009).

[221] Ma, Y., Rohlfing, M. & Molteni, C. Excited states of biological chromophores studied using many-body perturbation theory: Effects of resonant-antiresonant coupling and dynamical screening. *Phys. Rev. B* **80**, 241405 (2009).

[222] Rocca, D., Lu, D. & Galli, G. Ab initio calculations of optical absorption spectra: Solution of the Bethe–Salpeter equation within density matrix perturbation theory. *J. Chem. Phys.* **133**, 164109 (2010).

[223] Nan, W. *et al.* Crystal structure control of zinc-blende CdSe/CdS core/shell nanocrystals: Synthesis and structure-dependent optical properties. *J. Am. Chem. Soc.* **134**, 19685–19693 (2012).

[224] Olutas, M. *et al.* Lateral size-dependent spontaneous and stimulated emission properties in colloidal CdSe nanoplatelets. *ACS Nano* **9**, 5041–5050 (2015).

[225] Qiu, D. Y., Felipe, H. & Louie, S. G. Optical spectrum of MoS_2: Many-body effects and diversity of exciton states. *Phys. Rev. Lett.* **111**, 216805 (2013).

[226] Chen, Z., Nadal, B., Mahler, B., Aubin, H. & Dubertret, B. Quasi-2D colloidal semiconductor nanoplatelets for narrow electroluminescence. *Adv. Funct. Mater.* **24**, 295–302 (2014).

[227] Cudazzo, P., Tokatly, I. V. & Rubio, A. Dielectric screening in two-dimensional insulators: Implications for excitonic and impurity states in graphane. *Phys. Rev. B* **84**, 085406 (2011).

[228] Achtstein, A. W. *et al.* Electroabsorption by 0D, 1D, and 2D nanocrystals: A comparative study of CdSe colloidal quantum dots, nanorods, and nanoplatelets. *ACS Nano* **8**, 7678–7686 (2014).

[229] Finnis, M. *Interatomic forces in condensed matter* (Oxford University Press, 2003).

[230] Inkson, J. C. *Many-body theory of solids: An introduction* (Plenum Press, New York, 1984).

[231] Strinati, G. Dynamical shift and broadening of core excitons in semiconductors. *Phys. Rev. Lett.* **49**, 1519 (1982).

[232] Achtstein, A. W. *et al.* p-state luminescence in CdSe nanoplatelets: Role of lateral confinement and a longitudinal optical phonon bottleneck. *Phys. Rev. Lett.* **116**, 116802 (2016).

[233] Resta, R. Thomas-fermi dielectric screening in semiconductors. *Phys. Rev. B.* **16**, 2717 (1977).

Acknowledgements

I would like to acknowledge the support of my supervisors, Jason Smith and Feliciano Giustino. I am tremendously grateful to Jason for providing me with the opportunity and privilege of studying at Oxford, and for proposing such a compelling project. His enthusiasm, patience and guidance in this endeavour have kept me motivated and stimulated. I am also indebted to Feliciano's thorough involvement and commitment to my development as a researcher. His physical insight and technical input have been essential throughout the project. Both have been invaluable in guiding me through what has been a marathon task.

A special thanks must be given to Hannes Hübener for numerous fruitful conversations and copious technical advice. I am enormously grateful for the amount of time and effort he has contributed. I would also like to thank our collaborator Stanko Tomić for performing $\mathbf{k} \cdot \mathbf{p}$ calculations and for having engaging discussions regarding the results. His simulations have greatly helped to elucidate our own findings. Finally, I'd also like to thank Mervyn Roy for stimulating conversations regarding this thesis.

Writing this thesis and completing this D.Phil has been far more challenging than I had initially anticipated, and there were many times when it felt like the hard work would not come to fruition. I am eternally grateful for the unconditional support of my family, particularly through the final phase of the project. I would specifically like to thank my father for constructing several diagrams for the thesis, many of which did not make the final cut, my sister, who on several occasions helped to tabulate data, and my mother, who meticulously proof-read key sections. They undoubtedly enabled me to complete this thesis. Finally I would like to thank the numerous members of the PNG and MML groups: Simon, Phil, Stefano, Ziyun, Helene, Alasdair, Matthew, Edward, Sam, Alex, Dave, Aurélien, Lucas, Larry and Robin; Chris, Keian, Harry, Tim, Henry, Miguel, Johnny, Sheena, Marina, Natalie, Charlotte, Marios, Carla, Kun, George, Fabio, Bi-Ching and Samuel, as well as Michael and all of the friends who have enriched my time at Oxford.

List of papers

[1] Flatten, Lucas; Christodoulou, Sotirios; Patel, Robin; Buccheri, Alexander; Coles, David; Reid, Ben; Taylor, Robert; Moreels, Iwan; Smith, Jason, *Strong exciton-photon coupling with colloidal nanoplatelets in an open microcavity*, Submitted to Nano Letters.

[2] Buccheri, Alexander; Hubener, Hannes; Tomić, Stanko; Smith, Jason; Giustino Feliciano, *Tight-binding and* $\mathbf{k} \cdot \mathbf{p}$ *calculations of CdSe nanoplatelets*, Manuscript in preparation.